

NORTHWESTERN UNIVERSITY

Elucidating the Nature of Active Sites in Heterogeneous Catalysts through the
Functionalization of Metal-Organic Frameworks

A DISSERTATION

SUBMITTED TO THE GRADUATE SCHOOL
IN PARTIAL FULFILLMENT OF THE REQUIREMENTS

for the degree

DOCTOR OF PHILOSOPHY

Field of Chemistry

By

Qining Wang

EVANSTON, ILLINOIS

September 2023

© Copyright by Qining Wang 2023
All Rights Reserved

Abstract

Heterogeneous catalysis is the pillar of chemical production and a crucial aspect for optimization toward a sustainable future. To improve the current design of heterogeneous catalysts of maximal activity and product selectivity, gaining fundamental understanding of the catalytic active sites is crucial. The nature of active sites has been the center of debate in the scientific community for the past few centuries due to the structural complexity of heterogeneous catalysts.

This Thesis compiles a few examples of simplifying active site structures by constructing different heterogeneous catalysts on a structurally well-defined porous support, metal-organic framework (MOF) NU-1000. Those heterogeneous catalysts include metal ion catalysts with tunable ligand environment, nuclearity, and composition. The functionalization of the MOF support was also explored.

For the modulation of the ligand environment, NU-1000-supported Ni-thiophenolate complexes were chosen to understand how changing the substituent on the thiophenolate groups can influence the electronics of Ni and how this modulation affects the reactivity of the Ni center for ethylene hydrogenation. The nuclearity of Ni in the same NU-1000-supported Ni system was modified by changing the available deposition sites in the framework. Experimental results showed that di-nuclear Ni^{2+} species are more reactive than single Ni ions for ethylene hydrogenation. Computational studies corroborate those observations, where ethylene hydrogenation is more enthalpically favorable on di-nuclear Ni sites.

The effect of catalyst composition was studied on a bimetallic catalyst, NiCu supported on NU-1000, where the Cu:Ni ratio of the catalytic species was modulated. The catalyst with

higher Ni concentration showed significantly lower activation energy than Cu-rich and Cu-only catalysts. Those results were rationalized through spectroscopic studies, which show the beneficial role of Ni in facilitating the rate-limiting β C-H bond scission and suppressing the reduction of reactive $\text{Cu}^{\delta+}$ species. Further exploration of the support modification was examined on thermally distorted NU-1000 nodes, where the sulfidation of the nodes was achieved with thiols bearing different functional groups.

Overall, this Thesis showcases various possibilities for functionalizing the nodes and the cavity of MOF NU-1000 to alter the properties of supported catalysts and realize the nature of catalytic active sites. The studies compiled in this Thesis would further inspire the utilization of MOF-based catalysts for low-temperature chemical productions and encourage the implementation of novel strategies in catalyst design.

Acknowledgments

It goes without saying that it takes a village to complete a Ph.D. degree, but for me, it's more like four villages.

For my science village, I owe my everlasting gratitude to my advisors, Prof. Joseph Hupp and Prof. Justin Notestein. Your seemingly different science personalities somehow complement different facets of my own: playful, creative, and expansive. I always enjoyed chatting with you about anything, from science to any random things our conversations lead us to. Joe always seemed to be able to give me the exact hints I needed to analyze my nonsensical data, and I genuinely appreciate Justin's critical and timely (and sometimes snarky) comments on my work. His feedback always leads me to look for potential pitfalls in my data interpretation. They both gave me tremendous trust, support, and freedom to pursue my scientific goals and other interests.

I also want to thank the two managers of the REACT facility, Prof. Neil Schweitzer and Prof. Selim Alayoglu. Neil has made my research journey so much smoother since I learned (almost) everything I needed to jumpstart my research from his heterogeneous catalysis course and XAS workshops. Selim has always been so helpful whenever I wanted to try new experiments. His expertise in spectroscopy, surface characterization, and reactor engineering has been an invaluable resource for my research.

I would not have been able to get this far without the support of my lab mates. Huppsters, I always enjoyed being surrounded by introverts with witty spirits. I loved chatting with you about science and anything and everything else in our lives during the coffee hours. Special thanks to Dr. Hyunho Noh for teaching me everything I need to know about ALD maintenance and MOF modifications. I greatly appreciate his patience and guidance when I needed help

figuring out where to start. Thanks, Dr. Timothy Goetjen, for all the constructive and insightful feedback on my research and for answering my questions and confusion navigating the graduate school requirements. Dr. Dawn Duan, thank you for being a great colleague, officemate, friend, and LGBTQ comrade who selflessly offer your help and lend your ears when I have something to vent. I also thank Nick Huryk and Greg Mandell, the two program assistants who made navigating the bureaucratic affairs much smoother.

The Notestein group has always been a fun crowd. I missed sitting with everyone at K231 pre-pandemic, and I always had so much fun during group hangouts. The most motivating and productive period of my grad school life was when I ran experiments with Dr. Emily Cheng, chatting about nothing during the downtimes around the XPS and Raman instruments. Dr. Kenton Hicks's sassiness has been contagious and cheerful, which has swept away much unhappiness in my life. Jordy Ramos has always gone out of his way to help me and the group when something went wrong in the lab. His knowledge of chemical engineering and selflessness have been priceless to the group. Lauren Cho has been an incredible social chair in the group who has done much to unite and keep us connected. Her candidness is precious and something I wish I could emulate.

My gratitude also extends to my undergraduate advisor, Prof. Jing Li, who introduced me to MOFs. I also thank my mentor, Dr. Hao Wang, for teaching me MOF synthesis and characterization. His love and dedication to research greatly inspired me to pursue my research journey.

The science communication village has been an inspiring one. I learned invaluable lessons on how to explain science from unconventional perspectives. Being a science writer has

also alleviated my fear of writing in a foreign language. Thank you, Prof. Patti Waltor, for introducing me to the wonder of turning science into intriguing stories, and Dr. John MacMullan, for offering me the opportunity to work at the Midwest Big Data Hub as a science writing intern. I learned so much about data science from interviewing data scientists, which inspired me to think about the intersection of data science and science at large with our daily life.

Music, especially classical music, has been a massive pillar of my life since a young age, and I cannot believe I could continue pursuing it seriously at Northwestern. Huge thanks to Dr. Robert Hasty, the conductor of the Northwestern Philharmonia and Northwestern University Chamber Orchestra, who made this happen. Dr. Hasty made me an exception to playing in the two orchestras for music-major students. The rehearsals gave me doses of high-quality intellectual stimuli outside of the lab, which helped me de-stress and gave me new inspirations in science.

I am forever grateful to my NUGW and NUBonD comrades for your resilience and single-mindedness in making Northwestern and the chemistry department a more inclusive and equitable place for all. Your visions of what Northwestern, or even the world, can become have been inspiring and hopeful. You made my voice heard, my struggles seen, and my needs centered when it seemed like no one could care less in a fast-paced workplace like Northwestern. I learned so much about the struggles of myself and other marginalized groups and what needs to change, and I was glad to be part of the effort in unionizing graduate workers at Northwestern. You made me feel less like an outsider in a country that doesn't welcome minority immigrants, and I wish more could join the effort and fight the good fight in the future.

Lastly, my most special thanks to my home base. My two best friends, Yunru Tang and Man Shi, have been there with me through thick and thin when we are all thousands of miles away from home. I am lucky to be born into a very supportive family. Thank you, Fan Wang and Lan Wang, for being the best parents I could ask for. Thank you for teaching me everything I need to know for my life adventures and providing financially so I could pursue my education in a costly country. Your unconditional love, care, patience, and encouragement have nurtured me to become the independent, resilient, and empathetic person I am today. Tantan, my precious big furry ball. You are probably curving up and napping peacefully on my couch right now. You are the best roommate I could ever ask for, even though you live with me rent-free and broke several of my CD records. I hope you keep living a happy cat life for as long as you want.

Table of Contents

Abstract	3
Acknowledgments	5
Table of Contents	9
List of Figures	12
List of Tables	16
List of Schemes	17
Chapter 1. Introduction	18
1.1 Heterogeneous Catalysts and A Sustainable Future	19
1.2 Enhancing the Functionality of Supported Catalysts	20
1.3 Structural Complexity in Heterogeneous Catalysts	21
1.4 Metal-Organic Frameworks	22
1.5 Perspective for Catalysts with Targeted Surface Functionality	27
1.5.1 Hydrogen Economy	27
1.5.2 Chemical Production from Sustainable Feedstock	30
1.6 Thesis Outline	32
Chapter 2. Investigating the Effect of Metal Nuclearity on Activity for Ethylene Hydrogenation by Metal-Organic-Framework-Supported oxy-Ni(II) Catalysts	34
2.1 Chapter Summary	35
2.2 The Appeals and Pitfalls of Single-Atom Catalysts	36
2.3 Metal-Organic Framework as A Model System for Tuning the Nuclearity of Metal Catalysts	36
2.4 Synthesis of NU-1000-Supported oxy-Ni(II) Catalysts of Various Nuclearities	39
2.5 Characterizations	40
2.5.1 Physical Properties	40
2.5.2 Structural Investigations	42
2.5.3 Proposed Active Site Structures	50
2.6 Reactivity Studies Using Ethylene Hydrogenation as the Model Reaction	51
2.7 Mechanistic Insights from Density Functional Studies	53
2.8 Mechanistic Investigation from an Enthalpic Perspective	56
2.9 Chapter Conclusions	58

	10
2.10 Additional Information.....	58
2.10.1 Materials	58
2.10.2 Synthesis.....	59
2.10.3 Catalytic Testing Details	60
2.10.4 Instrumentation.....	61
2.9.5 Computational Details	64
Chapter 3. Probing Structure-Activity Relationships of NU-1000-Supported Ni-Thiophenolate Catalysts for Gas-Phase Reductions	66
3.1 Chapter Summary.....	66
3.2 Ni-Based Chalcogenides in Hydrogenases	66
3.3 Constructing Biomimetic Hydrogenase Active Sites on Metal-Organic Framework.....	68
3.4 Studying NU-1000-Supported Ni-Thiophenolate Baring Various Functional Groups.....	69
3.5 Physical Characterizations	70
3.6 Spectroscopic Studies.....	72
3.7 Catalytic Testing	79
3.8 Chapter Conclusions	80
3.9 Additional Information.....	81
3.9.1 Materials	81
3.9.2 Synthesis.....	82
3.9.3 Catalytic Testing Details	83
3.9.4 Instrumentation.....	83
Chapter 4. Bimetallic NiCu Catalysts Supported on a Metal-Organic Framework for Non-oxidative Ethanol Dehydrogenation	86
4.1 Chapter Summary.....	87
4.2 Non-oxidative Ethanol Dehydrogenation as a Promising Route for Various Chemical Transformations	88
4.3 Metal-Organic Framework as A Well-Defined Support for Adjusting Catalyst Compositions.....	89
4.4 Synthesis of NU-1000-Supported NiCu Catalysts	89
4.5 Physical Characterizations	90
4.6 Spectroscopic Studies.....	96
4.7 Reactivity Testing	100

4.8 Active Site and Mechanistic Investigations	102
4.9 Mechanistic Insights.....	108
4.10 Study on a Comparative System	109
4.11 Post-Catalysis Characterizations	114
4.12 Chapter Conclusions	120
4.13 Additional Information.....	121
4.12.1 Materials	121
4.12.2 Synthesis.....	121
4.12.3 Catalytic Testing Details	124
4.12.4 Instrumentation.....	125
Chapter 5. Investigating the Heterolytic Splitting of S-Containing Molecules on A Thermally Distorted Zr-Based Metal-Organic Framework.....	128
5.1 Chapter Summary.....	129
5.2 Challenges in Elucidating the Sulfidation Mechanisms of Metal Oxides.....	129
5.3 Investigating Sulfidation through Heterolytic Splitting on Metal-Organic Framework ...	131
5.4 The Incorporation of S-Containing Molecules onto Thermally Distorted NU-1000 Nodes	132
5.5 Physical Characterizations	133
5.6 Thiolate Quantifications.....	134
5.7 Elucidating the Adsorption Modes of the Thiol Species.....	141
5.8 Reaction of Sulfides with the Distorted Zr ₆ Nodes	146
5.9 Computational Investigation on the Heterolytic Splitting Process	148
5.10 Chapter Conclusions	152
5.11 Additional Information.....	153
5.9.1 Materials	153
5.9.2 Synthesis.....	153
5.9.3 Instrumentation.....	155
Chapter 6. Conclusions and Future Directions	157
6.1 Conclusions	157
6.2 Looking Ahead.....	157
References.....	159

List of Figures

- Figure 1.1.** A selection of MOF crystal structures and their corresponding node and linker structures. The bold, three-letter sequence denotes the topology of the MOF. Adapted from ref. 15 with permission. Copyright 2022 Royal Chemical Society..... 24
- Figure 1.2.** Potential catalyst deposition sites in MOF. (top left, red) isolated nodes as catalysts, (top right, magenta) node supported catalysts, (bottom left, green) linker supported catalysts, (bottom right, yellow) cooperative behavior between linkers and nodes, and (middle, orange) MOF encapsulated or enshrouded catalysts. Adapted from ref. 15 with permission. Copyright 2022 Royal Chemical Society..... 25
- Figure 1.3.** Saturation H₂ uptake at 77K plotted against Langmuir surface area. Adapted with permission from ref 61. Copyright 2006 American Chemical Society. 30
- Figure 2.1.** Single crystal structure of Ni supported on NU-1000. The blue pyramids show Ni residing in the c-pores. 39
- Figure 2.2.** PXRD patterns of the as-made catalysts..... 40
- Figure 2.3.** (a-b) N₂ isotherms and DFT differential pore size distributions of 0Ni~3.4Ni. (c-d) N₂ isotherms and DFT differential pore size distributions of 3.8Ni and 4.9Ni-NDC..... 41
- Figure 2.4.** DRIFT spectra of 0Ni, 0.86Ni, 2.1Ni, 3.8Ni and 4.9Ni-NDC. Background spectra were collected following catalyst pretreatment in Ar at 200°C for 1 hour. The gas was then switched to 100 sccm 10% H₂/N₂ and difference spectra were collected until no further changes in spectra were observed. 43
- Figure 2.5.** (a) Thermogravimetric analysis from 25-600°C. (b) Derivative weight curves from 24-250°C showing weight loss from physisorbed water and aqua ligands below ~125°C, and amd ligands at higher temperatures..... 44
- Figure 2.6.** (a) XANES of 0.86Ni, 2.1Ni, 3.8Ni, 4.9Ni-NDC, and Ni(OH)₂ standard. (b) Pre-edge features at 8333.5 eV. (c) EXAFS in r-space with the fitting window shown in black. 46
- Figure 2.7.** EXAFS fittings in k-space. 47
- Figure 2.8.** EXAFS fitting in r-space. 48
- Figure 2.9.** XPS of (a) Ni and (b) Zr of the as-made samples. 50
- Figure 2.10.** Representative, average, structures of Ni ions in formate-free NU-1000 (left) and in NDC-NU-1000 (right). Each node of NU-1000 contains up to three additional Ni atoms in similar coordination environments. The nodes of NDC-NU-1000 contain only one other binding site due to blocking by the NDC ligands. For clarity, only dimer structure is presented. All Ni ions should be octahedrally coordinated; hydroxyl and/or precursor ligands on Ni ions are omitted for clarity. 51
- Figure 2.11.** (a) Conversion vs. time on stream (TOS) for 3.8Ni at five temperatures. Conditions: ~20 mg catalyst diluted in 1 g of SiC, pre-treated in 50 sccm 10% H₂/N₂, 12 h at 200°C, followed by 1:1 H₂:C₂H₄ (10 sccm 10% H₂/N₂ and 25 sccm 4% ethylene/N₂). (b) Ni-normalized reaction rates at 150°C. (c) Arrhenius plots of 3.8Ni and 4.9Ni-NDC from 50-90°C. 52
- Figure 2.12.** Reaction orders of H₂ and ethylene measured for (a)-(b) 3.8Ni, and (c)-(d) 4.9Ni-NDC at 100°C. H₂ reaction order measured at constant ethylene mole fraction of 0.01

- and H₂ mole fraction varied from 0.01-0.075. Ethylene reaction order measured at constant ethylene mole fraction of 0.01 and H₂ mole fraction varied from 0.01-0.075. The ethylene reaction order measured at constant H₂ mole fraction of 0.01 and ethylene mole fraction varied from 0.014-0.02. 53
- Figure 2.13.** DFT-calculated enthalpies (yellow) and free energies (gray) for intermediates and transition state structures. Energies given in kcal/mol relative to species 1. The lower portion of the node and linkers bound to the Zr₆ nodes are omitted for clarity. 55
- Figure 2.14.** Reaction enthalpies in associated with the ethylene activation reported for the mono-nickel (top) and calculated in this work for the dinickel (below). 57
- Figure 3.1.** (a) Simplified [NiFe] hydrogenase structure showing location of the metal species and the hydrophobic channels (blue cavities). The purple sphere represents Xe atoms used to probe the hydrophobic channel structures. (b) Active site structure of [NiFe] hydrogenase. The blue, red, black, and yellow spheres represent N, O, C, S, respectively. Figures adapted with permission from ref. 135. Copyright 2003 Royal Chemical Society. 67
- Figure 3.2.** (a) Powder X-ray diffraction (PXRD) patterns, (b) N₂ isotherms, and (c) DFT-calculated pore-size distributions of NU-1000, Ni-SIM, Ni-TP, Ni-OMe, and Ni-CF₃. ... 71
- Figure 3.3.** Ni XPS spectra for (a) Ni-SIM, (b) Ni-TP, (c) Ni-OMe, (d) Ni-CF₃, (e) Ni-NH₂ and (f) Ni-NO₂. 73
- Figure 3.4.** S XPS spectra for (a) Ni-TP, (b) Ni-OMe, (c) Ni-CF₃, (d) Ni-NH₂ and (e) Ni-NO₂. 74
- Figure 3.5.** The Hammett plots constructed with the binding energies of (a) Ni, and (b) S. 75
- Figure 3.6.** (a) Normalized Ni K-edge XANES spectra of Ni-SIM, Ni-TP, Ni-OMe, and Ni-CF₃. (b) Zoomed-in pre-edge region of the XANES spectra displaying the pre-edge features. 77
- Figure 3.7.** (a) Zoomed-in Raman spectra in the 100~400 cm⁻¹ region. The dash lines highlight the characteristic features observed for thiophenolate-containing samples. (b)-(c) Tetrahedral $\nu(A_1)$ and $\nu(T_2)$ vibrational modes. 78
- Figure 3.8.** (a) Proposed Ni-thiophenolate structure with one thiophenol binding. (b) Proposed Ni-thiophenolate structure with two thiophenols binding. The proton shown in blue originates from a thiophenol ligand. 79
- Figure 3.9.** Ethylene conversion in 10:1 H₂/ethylene at (a) 50-150°C and (b) 50-250°C for Ni-TP, Ni-OMe, and Ni-CF₃. 80
- Figure 4.1.** Single-crystal structure of MOF NU-1000 as viewed (a) along the c-axis and (b) facing the ab-plane. 90
- Figure 4.2.** (a) PXRD patterns, (b) N₂ isotherms, and (c) NL-DFT pore-size distributions of catalyst-free and catalyst-loaded NU-1000-FF. 91
- Figure 4.3.** TEM images of the as-made 2.4Cu0.1Ni catalyst prior to the NaBH₄ treatment. 93
- Figure 4.4.** TEM images of the as-made 1.7Cu2.1Ni catalyst prior to the NaBH₄ treatment. 93
- Figure 4.5.** TEM images of the as-made 1.7Cu2.1Ni catalyst prior to the NaBH₄ treatment. 94
- Figure 4.6.** (a)-(c) TEM images of 2.4Cu0.1Ni, 1.7Cu2.1Ni, and 0.8Cu2.4Ni, respectively, after the NaBH₄ treatment. (d)-(f) Particle size distributions of 2.4Cu0.1Ni, 1.7Cu2.1Ni, and 0.8Cu2.4Ni, respectively. Distributions were determined from measuring the diameters of at least 100 distinct NPs for all samples. (g) Lattice spacing measurement for one NP in 0.8Cu2.4Ni. 95

- Figure 4.7.** DED results for (a) 2.4Cu0.1Ni, (b) 1.7Cu2.1Ni, and (c) 0.8Cu2.4Ni presented along the c-axis. Their respective views along the b-axis are displayed in (d) – (f). The yellow blobs represent extra electron density from the metal species incorporated post-synthetically. (Green sphere = Zr, red spheres = O, brown spheres = C, white spheres = H) 96
- Figure 4.8.** XPS spectra for (a)-(c) Cu and (e)-(f) Ni. The Ni spectra for 2.4Cu0.1Ni are not shown here due to the low S/N ratio of the spectra. 99
- Figure 4.9.** (a) Example time-on-stream plot of all samples from 175-250°C. (b) Arrhenius plot for all samples in the temperature range of 200-250°C based on the initial rates at each temperature point. 101
- Figure 4.10.** TOS plot for 20.8 mg of 3.8Ni showing the background reactivity of Ni for non-oxidative ethanol dehydrogenation. 101
- Figure 4.11.** (a) Full in-situ ethanol DRIFTS spectra at 150°C and zoomed-in spectra of the (b) C-O stretching region, (c) C-H stretching region, and (d) O-H stretching region..... 104
- Figure 4.12.** Single-beam spectra recorded at 150°C for (a) 1.7Cu2.1Ni and (b) 2.4Cu0.1Ni.. 104
- Figure 4.13.** DRIFTS Spectra from 150 - 250°C for (a) NU-1000-FF, (b) 2.8Cu, (c) 3.8Ni, (d) 0.8Cu2.4Ni, (e)1.7Cu2.4Ni, and (f) 0.8Cu2.4Ni. All spectra are normalized to the highest peak intensities..... 107
- Figure 4.14.** Proposed reaction mechanism. The partial brown sphere represents the surface of a mixed oxide nanoparticle or sub-nm cluster species. Similar mechanism can take place with the Ni attached to the node and a neighboring Cu site. 109
- Figure 4.15.** PXRD patterns of ZrO₂ and 0.4Cu1.6Ni-ZrO₂. 110
- Figure 4.16.** TEM images of 0.4Cu1.6Ni-ZrO₂ after 2 hours of H₂ treatment at 200°C. 111
- Figure 4.17.** XPS of Ni and Cu of 0.4Cu1.6Ni-ZrO₂ compared to 0.8Cu2.4Ni..... 112
- Figure 4.18.** (a) Time-on-stream (TOS) plot of 0.4Cu1.6Ni-ZrO₂ from 175-350°C. (b) GC area plot of all products for 0.4Cu1.6Ni-ZrO₂. (c) GC area plots for 0.8Cu2.4Ni. 114
- Figure 4.19.** (a)-(c) TEM images of 2.4Cu0.1Ni, 1.7Cu2.1Ni, and 0.8Cu2.4Ni, respectively, after non-oxidative dehydrogenation from 175~300°C. (d)-(f) Particle size distributions before reactions of 2.4Cu0.1Ni, 1.7Cu2.1Ni, and 0.8Cu2.4Ni, respectively. (g)-(i) Particle size distributions after reactions of 2.4Cu0.1Ni, 1.7Cu2.1Ni, and 0.8Cu2.4Ni, respectively. 115
- Figure 4.20.** Thermogravimetric analysis of the fresh catalysts (top) and the catalysts after non-oxidative ethanol dehydrogenation (bottom) from 115-600°C..... 117
- Figure 4.21.** PXRD patterns of the post-catalysis samples. 118
- Figure 4.22.** (a) N₂ isotherms of 0.8Cu2.4Ni before and after catalysis. (b) Zoomed-in view of the N₂ isotherm of 0.8Cu2.4Ni after catalysis..... 119
- Figure 4.23.** N₂ isotherm of 2.4Cu0.1Ni after ethanol DRITS showing retained porosity..... 119
- Figure 4.24.** (a)-(c) Post-catalysis XPS of Cu in 2.4Cu0.1Ni, 1.7Cu2.1Ni, and 0.8Cu2.4Ni. (d)-(f) Post-catalysis XPS of Cu in 2.4Cu0.1Ni, 1.7Cu2.1Ni, and 0.8Cu2.4Ni. 120
- Figure 5.1.** (a) DFT-optimized node structures at 300°C. (b) The most stable node-NH₃ complex formed through the heterolytic splitting of NH₃. Color code: H-white, C-brown, N-cyan, O-red, and Zr-green. (c) Illustration of the node-H₂S complex formed through a similar heterolytic splitting mechanism. Color code: H-white, C-black, S-yellow, O-red, and Zr-

- brown. (a) and (b) are adapted with permission from ref 118. Copyright 2021 American Chemical Society. 132
- Figure 5.2.** (a) PXRD patterns of the as-made samples. (b) N₂ isotherms of NU-1000-FF, TP, and H₂S. (c) DFT pore-size distributions of NU-1000-FF, TP, and H₂S. 134
- Figure 5.3.** Acid-Digested NMR spectra for NU-1000-300C modified with ethanethiol (orange), hexanethiol (blue), and thiophenol (green) in the (a) alkyl region and (b) aromatic region. (c) A zoomed-in view of the spectrum for thiophenol in the 7.3~8.5 ppm region, showing the presence of additional aromatic features attributed to the presence of thiophenolate rings. 136
- Figure 5.4.** The NMR spectra for DES (top) and TPhen (bottom). Integration was not performed due to the low diethyl sulfide and thiophene loading in the acid-digested samples. 137
- Figure 5.5.** Fitted XPS S 2p spectra of NU-1000-FF-300C modified with (a) H₂S, (b) ethanethiol, (c) 1-hexanethiol, and (d) thiophenol. 139
- Figure 5.6.** Depth profiling XPS S 2p spectra of NU-1000-300C modified with (a) H₂S, (b) ethanethiol, (c) 1-hexanethiol, and (d) thiophenol. The black trace represents the spectrum of the surface, and the gray traces are spectra collected at increasing etch iterations. The peaks at *ca.* 161 eV and 166 eV are assigned to sulfides and sulfates, respectively. 141
- Figure 5.7.** (a) DRIFTS Spectra from 900~1250 cm⁻¹ of all samples modified with thiols collected at 29°C and 200°C. (b) DRIFTS Spectra from 2250~4000 cm⁻¹ of all samples modified with thiols collected at 29°C and 200°C. 145
- Figure 5.8.** (a) Two possible types of associative adsorption of 1-hexanethiol. (b) An illustration of the dissociative adsorption of 1-hexanethiol onto the distorted node. 145
- Figure 5.9.** Surface XPS S2p spectra for (a) DES and (b) TPhen, and the depth profiling spectra for (c) DES and (d) TPhen. 146
- Figure 5.10.** (a) DRIFTS Spectra from 900~1250 cm⁻¹ of all samples modified with sulfides collected at 29°C and 200°C. (b) DRIFTS Spectra from 2250~4000 cm⁻¹ of all samples modified with sulfides collected at 29°C and 200°C. 148
- Figure 5.11.** Reaction path for the H₂S splitting mechanism. 150
- Figure 5.12.** Reaction path for methanethiol (green) and dimethyl sulfide (red). Note two transition states for dimethyl sulfide splitting reaction. Dark red represents the more favored *rocking* mechanism, the light red is associated with higher-energy *transition* mechanism, see text for details. The numbers represent the Gibbs free energies with the unit of kJ/mol. 150
- Figure 5.13.** Two possible transition states in sulfide splitting reaction. 152

List of Tables

Table 2.1. Property table.	42
Table 2.2. Quantification of catalyst hydration and amd ligand remaining	45
Table 2.3. Ni K edge EXAFS fitting results.	48
Table 2.4. Complete EXAFS fitting results.	49
Table 2.5. Absolute energies of reaction species with corresponding corrections.	56
Table 3.1. BET surface areas and ICP-OES measurement results normalized to the number of Zr ₆ nodes for all Ni-containing samples.	72
Table 3.2. Binding energies of Ni and S for all samples.....	75
Table 3.3. Ni K-edge energies (E ₀) of Ni-SIM, Ni-TP, Ni-OMe, and Ni-CF ₃	77
Table 4.1. Property table.	92
Table 4.2. Binding energies of Cu and Ni before and after the complete reduction of Cu.....	99
Table 4.3. Weight loss quantifications based on TGA results.	116
Table 4.4. Synthetic condition screening at 10-mg scale.....	123
Table 4.5. Quantities of precursors used in 150-mg-scale syntheses.....	123
Table 5.1. S binding energies and thiolate quantifications for all samples.....	147
Table 5.2. Thiolate binding energies and quantifications for DES and TPhen.....	147
Table 5.3. Gibbs free energies of physisorption and splitting reaction of S-containing molecules.	148
Table 5.4. The amounts of thiols and sulfides used for liquid phase syntheses.....	154

List of Schemes

Scheme 1.1. An illustration of reversible hydrogen storage and release cycles coupled with CO ₂ and formic acid, promoted by heterogeneous catalysts.	29
Scheme 2.1. Synthesis of Ni supported on NU-1000-FF and NU-1000-NDC.	60
Scheme 3.1. Synthesis of Ni-SIM and Ni-thiophenolate.	83

Chapter 1. Introduction

Portions of this chapter appear in the following manuscript:

Liu, J.; Goetjen, T.A.; **Wang, Q.**; Knapp, J. G.; Wasson, M. C.; Yang, Y.; Syed, Z.; Delferro, M.; Notestein, J. M.; Farha, O. K.; Hupp, J.T. “MOF-Enabled Confinement and Related Effects for Chemical Catalyst Presentation and Utilization.” *Chem. Soc. Rev.* (2022), 51, 1045-1097

1.1 Heterogeneous Catalysts and A Sustainable Future

Catalysis is a ubiquitous phenomenon in industrial processes and biological reactions. Defined as accelerating a chemical reaction by reducing the activation energy without altering reaction equilibrium, catalysis plays a pivotal role in addressing challenges in climate change and moving towards a more sustainable world.¹⁻⁴

Catalysts can be broadly categorized into homogeneous and heterogeneous catalysts, where heterogeneous catalysts account for most fuels and chemicals currently produced at low cost, high conversion, and good product selectivity. Heterogeneous catalysts occupy a different physical phase from the reactants and products, where the catalysts are typically in the solid phase and substrates in the liquid or gas phase.² Due to the ease of recovery and high recyclability, heterogeneous catalysts eliminate secondary pollution, which leads to sustainable manufacturing practices -- an essential step in shifting to a renewable and circular society.⁴⁻⁶ One of the most used strategies to increase catalytic efficiencies of heterogeneous catalysts is to disperse catalytically active species onto a highly porous and high-surface-area catalyst support, typically a solid oxide (Al_2O_3 , SiO_2 , ZrO_2 , etc.). As will be discussed in section 1.2, not only do highly dispersed catalytic species increase the number of accessible active sites, but they also introduce unique surface functionality that can affect product selectivity.

A key to developing efficient and long-lasting supported catalysts is to study the surface species on heterogeneous catalysts and how they lead to various catalytic activities.⁷ Through identifying highly active and selective surface sites, we could further optimize current catalyst designs to replicate the active site structure, thereby improving the yield of various industrial processes.

1.2 Enhancing the Functionality of Supported Catalysts

Several strategies are commonly implemented to improve catalytic designs and modify surface functionalities for heterogeneous catalysts. Those strategies stem from three main types of surface effects, namely the geometric effects, electronic effects, and confinement effects.⁷ Geometric effects describe the local environment surrounding the active site. For instance, highly dispersed and undercoordinated metal species in supported metal catalysts are considered more catalytically relevant than aggregated clusters and nanoparticles. Geometric effects are inherently related to electronic effects, which determine how strongly a substrate binds to the active site, be it a reactant or a product.^{7, 8} Sabatier's principle is a prime example illustrating how electronic effects can serve as a predictor of the catalytic activity of transition metals, where the binding of the substrate should be neither too weak nor too strong to achieve the highest catalytic activity.⁹

The tuning of geometric and electronic effects often involves changing the size, morphology, and local coordination environments of the metal species and/or the support.¹⁰ Geometrically, reducing the size of the metal nanoparticles can increase catalyst dispersion on the support and the number of low-coordinated metal sites. This can often lead to an increase in catalytic activity.⁸ Similarly, changing the morphology of the nanoparticle catalysts and the catalyst support varies the number of low-coordination and defect sites, which can significantly affect the interaction of the catalyst with the support and the reactants.¹¹⁻¹³ Electronically, smaller nanoparticles would create discrete electronic states, in contrast to the continuous valence band of bulk metal, which can affect the charge transfer between the active site and the substrates and modulate the overall catalytic activity.^{11, 14}

Confinement effects can also greatly influence a catalyst's activity, stability, and selectivity, as the nanoconfinement surrounding an active site can prevent catalyst aggregation, discriminate

substrates of various sizes, and create transport effects relevant to catalytic activity and selectivity.¹⁵ Confinement effects are especially relevant to porous catalyst supports, where the pore shape and structure are crucial handles to tune their catalytic performances.

1.3 Structural Complexity in Heterogeneous Catalysts

Despite the ubiquitous presence of heterogeneous catalysts in industrial applications, the active site structure(s) responsible for the observed catalytic turnover can be highly complex. The structural-functional relationship of heterogeneous catalysts has been debated for over 100 years.¹⁶ Such complexity mainly stems from the non-well-defined surface structures of the catalyst supports, such as silica and alumina. The amorphous nature of the surfaces of those supports gives rise to various types of deposition sites, and depositing metal species on those sites often results in the formation of nanoparticles of different sizes and active sites of varied catalytic activities.

Another aspect of structural ambiguity arises from the catalyst evolution during the catalytic process. Active sites are dynamic, and their immediate surroundings can easily affect their behaviors. In some circumstances, active sites can cooperate or even communicate.^{7, 17, 18} Therefore, to capture those intricate subtleties during time-on-stream studies, various *in-situ* and operando spectroscopy techniques (Raman, infrared, fluorescence, X-ray-based, etc.) have been developed and continuously improved. However, even with advanced surface-sensitive analytic tools, the insights are often about the correlation between the overall average catalyst structure and the collective catalytic performance during catalysis. Probing the behavior of active sites on a molecular level remains a challenge.^{18, 19} Even with the development of *in-situ* scanning tunneling microscopy (STM) techniques that enables the direct observation of active sites in

contact with substrates,^{20, 21} the high resource and technical demands still prevents *in-situ* STM from being widely adopted in heterogeneous catalysis studies.

Model catalysts with simplified and uniform active site structures have been proposed to overcome the inherent complexity of heterogeneous catalysts to establish structural-functional relationships.¹⁹ Those model catalysts can be readily achieved in planar catalyst systems such as metal single crystals²²⁻²⁴ and oxide thin-film-supported catalysts.^{25, 26} Those planar model catalyst systems, in combination with ultra-high vacuum techniques, elucidated numerous elementary steps in catalysis such as adsorption and radical formation. However, those observations may not fully explain the observations in model catalysts dispersed on high-surface-area supports due to the unique geometric and electronic properties of the supported catalysts, such as the metal-support interface and the coordination to capping ligands.

Therefore, it is necessary to construct supported catalysts consisting of well-defined and simplified active sites to establish structural-functional relationships on systems reminiscent of industrially relevant catalysts.

1.4 Metal-Organic Frameworks

Metal-organic frameworks (MOFs) are highly porous and crystalline materials investigated for constructing highly dispersed, structurally homogeneous, and well-defined catalysts. MOFs are inherently crystalline due to the periodic arrangement of the metal clusters or ions (nodes) and the polytopic organic moieties (linkers). The crystallinity of MOFs allows for the visualization of the active-site structure using single-crystal X-ray diffraction (SCXRD). The crystal structure of MOF-based catalysts can then be used to establish structural-functional relationships with observed catalytic activities. Computational modeling via density-functional

theory (DFT) is also commonly implemented to unveil the reaction mechanisms through modeling a truncated secondary building unit (SBU).

As the combinations of nodes and linkers are virtually infinite, MOF systems are highly tunable, which gives rise to a wide array of crystal structures containing channels and cages of various sizes. A selection of those MOF structures can be found in **Figure 1.1**. This high degree of tunability is especially beneficial for heterogeneous catalysis since it allows for fine-tuning the chemical environment around the catalytic active sites. High-surface-area MOFs would facilitate the deposition of dispersed catalysts at high loadings as well as the mitigation of mass transfer limitation.^{27, 28} Popular emphasis has been placed on Zr-based MOFs for heterogeneous catalysis due to the strong interactions between Zr nodes and linkers, which contribute to their good thermal and chemical stability under catalytic conditions.

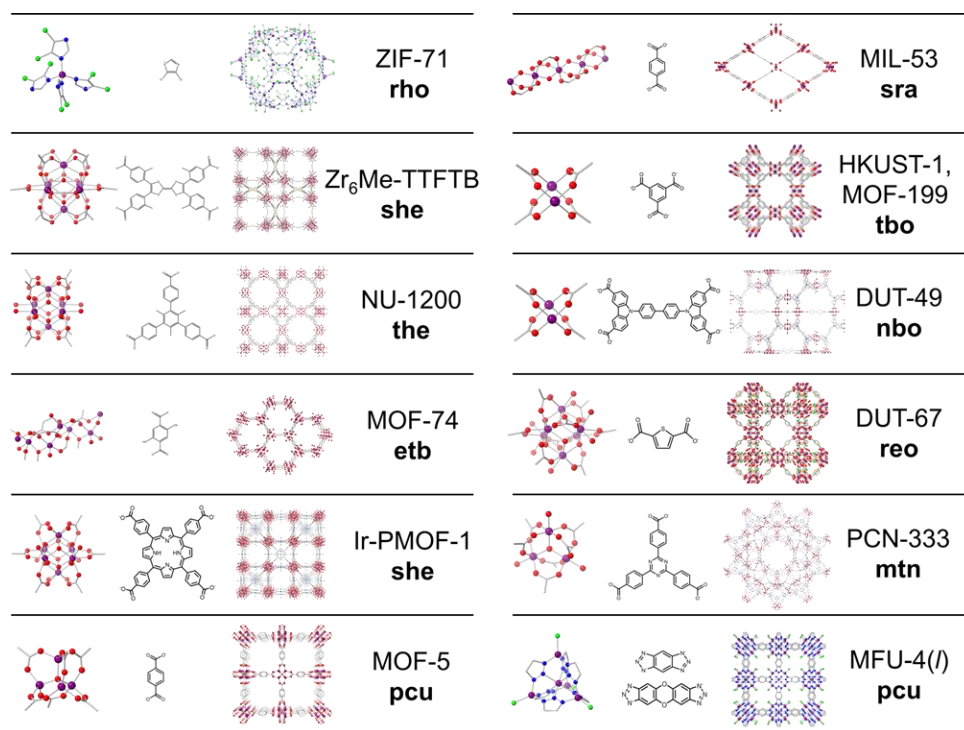


Figure 1.1. A selection of MOF crystal structures and their corresponding node and linker structures. The bold, three-letter sequence denotes the topology of the MOF. Adapted from ref. 15 with permission. Copyright 2022 Royal Chemical Society.

MOF catalysts can generally be constructed on the nodes, linkers, and within the MOF pores (**Figure 1.2**). MOF nodes containing open coordination sites can function as catalytic active sites (represented as red spheres in **Figure 1.2**) or as grafting sites for metal ions or clusters (depicted as blue and magenta in **Figure 1.2**). For Zr-MOFs, the connectivity of a commonly encountered Zr₆ node ($[\text{Zr}_6(\mu_3\text{-O})_4(\mu_3\text{-OH})_4]^{12+}$) can be 4-,²⁹ 5-,³⁰ 6-,³¹ 8-,³² 9-,³³ 10-,³⁴ or 12-connected³⁵ depending on synthesis conditions and the choice of polytopic carboxylate-based ligand. Open coordination sites are inherently built in for Zr-MOF with less than 12 linkers as bridging or terminal hydroxo and/or aqua ligands. In this regard, the Zr₆ nodes serve as isolated catalytic clusters or catalyst supports comprising crystallographically well-defined fragments of conventional metal oxide surfaces.³⁶ As for fully 12-connected Zr-MOFs,

open coordination sites can be randomly distributed throughout the crystallites as missing linker sites, which are also tunable and catalytically active as Brønsted acid sites.³⁷

Functionalization of MOF linkers, such as introducing N- and S-containing moieties, also enables the binding of metal ions to create single-site catalysts with tunable coordination environment (green spheres in **Figure 1.2**), reminiscent of organometallic complexes used in homogeneous catalysis. On top of realizing the high conversion and product selectivity of homogeneous catalysts, replicating the structures of organometallic complexes in MOF systems introduces additional benefits of the heterogeneous systems, such as the ease of separation and recyclability. The proximity of nodes and the functional groups on the linkers may also introduce synergetic effects during catalysis (yellow fragments in **Figure 1.2**).

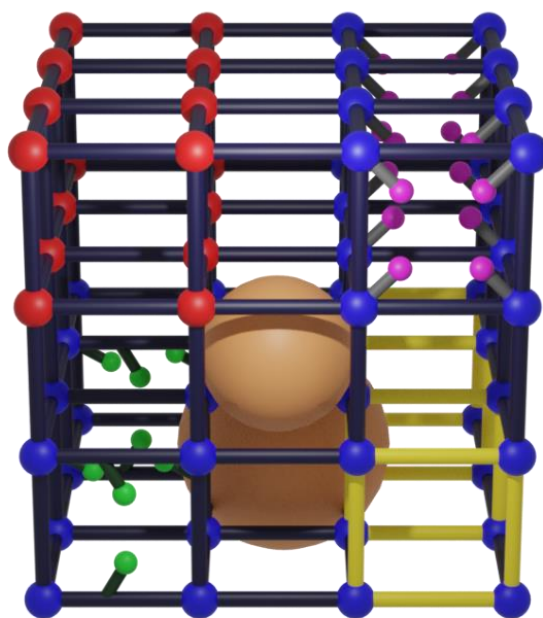


Figure 1.2. Potential catalyst deposition sites in MOF. (top left, red) isolated nodes as catalysts, (top right, magenta) node supported catalysts, (bottom left, green) linker supported catalysts, (bottom right, yellow) cooperative behavior between linkers and nodes, and (middle, orange) MOF encapsulated or enshrouded catalysts. Adapted from ref. 15 with permission. Copyright 2022 Royal Chemical Society.

Additionally, the pores or cages of MOFs can entrap catalytic species such as nanoparticles,³⁸ polyoxometalates (POMs),³⁹ and enzymes⁴⁰, as indicated by the brown spheres in **Figure 1.2**. One method for creating MOF-supported nanoparticle catalysts is to grow nanoparticles inside the MOF crystallites, where metal ions are first introduced onto the nodes or the linkers of the MOF, followed by reduction to induce the migration of metal ions to form nanoparticles. The porous framework can serve as a template to generate nanoparticles of controlled particle sizes.⁴¹ Those embedded nanoparticles can be essentially free of capping ligands typically required to stabilize and isolate nanoparticles. Non-innocent capping ligands could also introduce complications to the catalysis. Nanoparticles of various particle sizes can be located via a combination of techniques such as high-resolution transmission electron microscopy (HRTEM) and difference electron density (DED) mapping, which can provide a comprehensive view of various catalytic species in the system and further distinguish their respective reactivity.

In summary, MOFs are useful model systems to establish structural-functional relationships for various types of heterogeneous catalysts, including but not limited to single ions, small metal clusters, and nanoparticles. The high surface area and crystallinity of MOFs enable the construction of catalysts with less structural complexity and the elucidation of catalyst siting, structure, and behavior via various experimental and computational techniques. As will be alluded to in the following section, the fundamental understanding of structural-functional relationships will further guide the rational design of catalysts that will address some of the most urgent global issues.

1.5 Perspective for Catalysts with Targeted Surface Functionality

1.5.1 Hydrogen Economy

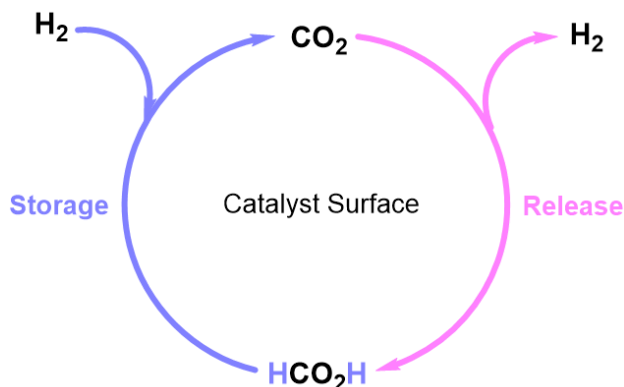
The hydrogen economy is a concept Lawrence W. Jones discussed extensively in 1970. Jones proposed that replacing fossil fuels with liquid hydrogen for air and vehicular transport can be a long-term solution to pollution from fossil fuel combustion and the ultimate depletion of fossil fuels.⁴² In the face of the exacerbating climate crisis, transitioning to a more sustainable and cleaner hydrogen-fueled economy is much needed. According to the International Energy Agency, the demand for pure hydrogen is projected to increase from 93.6 Mt in 2021 to 179.8 Mt by 2023 to achieve Net Zero Emissions by 2050 Scenario.^{43, 44} To meet the increasing demand, optimizing the current hydrogen production schemes as well as exploring other sustainable means of hydrogen production and utilization methods are of the utmost importance.

A promising route of hydrogen production is the thermal catalytic cracking of methane into carbon and hydrogen ($\text{CH}_4(\text{g}) \rightarrow \text{C}(\text{s}) + \text{H}_2(\text{g})$). Compared to the more widely used processes such as water-gas-shift reaction ($\text{CO} + \text{H}_2\text{O} \rightarrow \text{CO}_2 + \text{H}_2$), methane cracking avoids CO_2 emissions, and the solid carbon can be further transformed into value-added products.^{45, 46} Alternatively, the dry reforming of methane ($\text{CO}_2 + \text{CH}_4 \rightarrow 2\text{CO} + 2\text{H}_2$) is also attractive, as it converts the two potent greenhouse gas into synthesis gas. Ni-based catalysts have been widely investigated for both processes, yet the in-situ catalyst deactivation greatly limits their application through coking and the sintering of Ni species.⁴⁷ Efforts have been invested in stabilizing active Ni-species through support modification and introduction of a second metal, such as Ce, Ca, and Cu, as catalytic promoters.^{48, 49} However, there is still a lack of understanding of the exact deactivation mechanism of the catalysts beyond the general

description of “coking” and “aggregation.” Studying catalyst deactivation during time-on-stream studies could provide crucial perspectives on how to make highly active catalysts long-lasting.⁵⁰

Beyond hydrogen production, the rational design of heterogeneous catalysts is also critical for the chemical hydrogen storage and release processes. Compared to the physical hydrogen storage approach, where hydrogen gas is compressed up to 700 bar (40 g H₂/L) or cooled to liquid hydrogen temperature (-253°C, 70 g H₂/L), chemical hydrogen storage operates at much milder conditions through the reversible hydrogen storage and release on a catalyst surface.⁵¹

Reversible chemical hydrogen storage coupled with CO₂, i.e., CO₂ hydrogenation (CO₂ + H₂ → HCOOH), is a highly attractive route (**Scheme 1.1**). This process effectively utilizes an unwanted greenhouse gas, CO₂. In addition, this process is highly selective since the reverse reaction, the dehydrogenation of formic acid (FA) (HCOOH → CO₂ + H₂), is more thermodynamically favorable ($\Delta G_{298K} = -32.9$ kJ/mol) than the competing dehydration route (HCOOH → CO + H₂O, $\Delta G_{298K} = -23.4$ kJ/mol). To date, numerous studies have demonstrated the high catalytic turnover for either CO₂ hydrogenation or the dehydrogenation of FA on supported Pd and PdAg nanoparticles.⁵²⁻⁵⁴ However, only a handful of studies showed the two cycles working in conjunction.⁵⁵ In other words, to realize chemical hydrogen storage coupled with CO₂ on an industrial level, there is a need to further investigate if those highly active systems can carry out the hydrogen storage and release coupled with the CO₂-FA reversibly.



Scheme 1.1. An illustration of reversible hydrogen storage and release cycles coupled with CO₂ and formic acid, promoted by heterogeneous catalysts.

Meanwhile, many MOF systems, including MOF-5, MOF-74, HKUST-1, etc., have demonstrated impressive hydrogen storage capacity with reversible adsorption and desorption cycles.⁵⁶⁻⁵⁸ In addition to the high surface area of MOFs, the open metal sites that behave like Lewis acid sites for catalysis also contribute to the enhanced interaction between hydrogen molecules and the framework.^{59, 60} The hydrogen uptake of MOF materials generally trends with their surface areas, as depicted in **Figure 1.3**.⁶¹ However, the hydrogen storage capacity of MOFs was mainly studied at low temperatures,^{61, 62} and the development of MOF systems with enhanced room-temperature hydrogen storage capacity, perhaps with the incorporation of chemical storage through functionalization, is pivotal for their real-life applications. The activation of H₂ on MOF-based catalysts will be discussed extensively in Chapters 2 and 3.

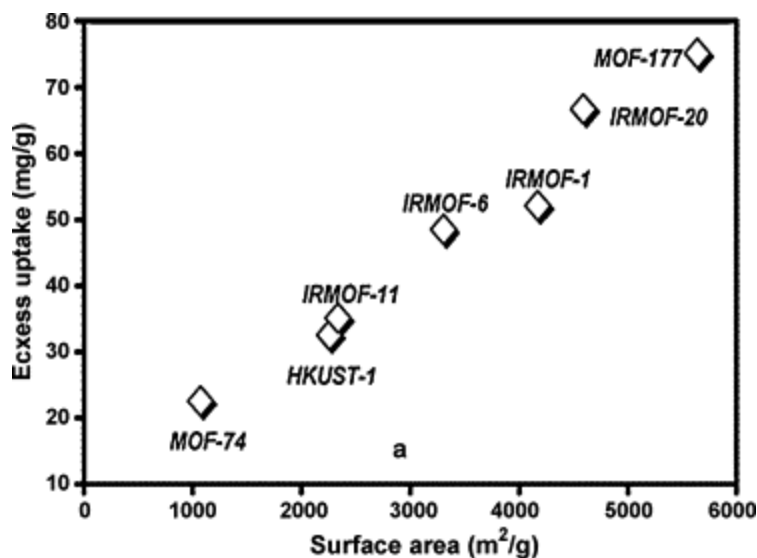


Figure 1.3. Saturation H₂ uptake at 77K plotted against Langmuir surface area. Adapted with permission from ref 61. Copyright 2006 American Chemical Society.

To summarize, engineering heterogeneous catalysts for hydrogen production and usage is crucial to eliminating fossil fuel usage and transitioning into a more sustainable hydrogen economy. Fundamentally speaking, understanding the catalyst deactivation phenomena under reaction conditions would be pivotal to improving the overall stability of active catalysts for hydrogen production. Regarding hydrogen utilization, MOF systems show several advantages over other chemical hydrogen storage materials, including the high surface area, enhanced interaction with adsorbed hydrogen molecules, and reversible hydrogen uptake and release cycles. Further optimization of MOF materials for hydrogen storage at room temperatures is required for real-life applications.

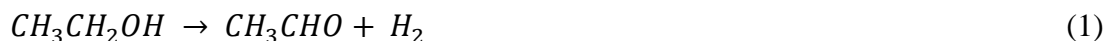
1.5.2 Chemical Production from Sustainable Feedstock

Moving away from fossil fuels also means a shift in feedstocks for chemical production. In 2018, chemical products accounted for approximately 12% and 8% of the global primary oil and natural gas demand, respectively.⁶³ More than 50% of those inputs were consumed as feedstocks to generate methanol, ammonia, butylene, and other chemical building blocks to

produce everyday products such as fuel, nitrogen fertilizers, plastic, and synthetic rubbers. This dependence on fossil carbon as feedstock and petrochemical products renders the chemical sector the most prominent industrial energy consumer. Therefore, It is necessary to develop and implement chemical production technologies that utilize sustainable feedstocks to reduce the CO₂ emissions from fossil fuel consumption and the accumulation of non-biodegradable wastes from petroleum-based products.⁶⁴

Heterogeneous catalysts are vital for sustainable feedstock consumption, especially in transforming biomass-derived feedstocks into other valuable chemical building blocks.⁶⁵⁻⁶⁷ In the United States, bioethanol derived from corn is the most significant renewable energy source. Compared to the production of 2.5 billion gallons of renewable diesel made of animal fats, waste oils, and greases, ethanol production in the U.S. totaled about 15 billion gallons in 2021.⁶⁸ Developing heterogeneous catalysts to efficiently transform bioethanol into high-value products such as the production of sustainable aviation fuel (SAF) could thus be a viable strategy for replacing many current processes that involve fossil fuels as the feedstock.^{69, 70}

The transformation of ethanol can give rise to various products, where hydrogen production is the most extensively studied. Some of those reactions include dehydrogenation (Eq. 1),^{71, 72} dehydration (Eq. 2), dry reforming with CO₂ (Eq. 3),^{73, 74} steam reforming (Eq. 4), partial oxidation (Eq. 5), and oxidative steam reforming (Eq. 6).





The reforming processes (Eq. 3-6) have been explored extensively and almost exclusively for hydrogen production from bioethanol. Those reactions typically require high energy input, operating at temperatures of 550~750°C, which also renders catalyst deactivation through coke formation a significant challenge. Meanwhile, hydrogen production through the dehydrogenation route requires lower temperatures, typically less than 400°C, and a value-adding byproduct, acetaldehyde.⁷⁵⁻⁷⁸ As long-temperature processes like the non-oxidative dehydrogenation of ethanol receive greater attention, high temperatures would no longer be the default operation conditions for chemical productions. As such, MOF-based catalysts would have great potential to be incorporated into alternative chemical production routes at milder conditions. Such a possibility has been explored and is detailed in Chapter 4 of this Thesis.

1.6 Thesis Outline

This Thesis is a compilation of work on generating various supported catalytic species through functionalizing the nodes and/or the cavities of MOF NU-1000.

The functionalization of the Zr₆ nodes of NU-1000 was mainly explored in Chapters 2, 3, and 5. Chapter 5 focuses on the functionalization of nodes by inducing thermal distortion of the Zr₆ node structure, which enables the binding of thiols containing different functional groups. The deposition mechanism was investigated, providing insights into the sulfidation mechanism of zirconia supports.

In Chapters 2 and 3, the empty coordination sites of the Zr₆ nodes were exploited for the deposition of Ni ions and clusters. The focus of Chapter 3 is the electronic effect on single-ion Ni

supported on NU-1000. Inspired by the active site structure in [NiFe] hydrogenase, thiophenols bearing various functional groups were grafted onto Ni ions supported on NU-1000, resulting in different electron densities on Ni and S. The differences were reflected in their varied reactivity for ethylene hydrogenation. The reactivity of node-supported single-ion Ni and multinuclear Ni²⁺ clusters for ethylene hydrogenation were compared in Chapter 2, where both experimental and computational tools were implemented to demonstrate that the activation energy for the rate-determining step, namely the heterolytic splitting of H₂, is lower for multinuclear Ni²⁺ species.

In Chapter 4, the open coordination sites on the Zr₆ nodes were enlisted along with the cavities of NU-1000 to investigate the roles of Ni as a catalytic promoter in bimetallic NiCu catalysts supported on MOF NU-1000 for non-oxidative ethanol dehydrogenation. The crystallinity of NU-1000 enables the implementation of difference electron density (DED) map, in combination with tunneled electronic microscope (TEM), to locate the NiCu species on the surface and within the interior of the NU-1000 crystallites. *In-situ* spectroscopic studies were also performed to further illustrate the role of Ni in reducing the activation barrier for non-oxidative ethanol dehydrogenation.

Chapter 2. Investigating the Effect of Metal Nuclearity on Activity for Ethylene Hydrogenation by Metal-Organic-Framework-Supported oxy-Ni(II) Catalysts

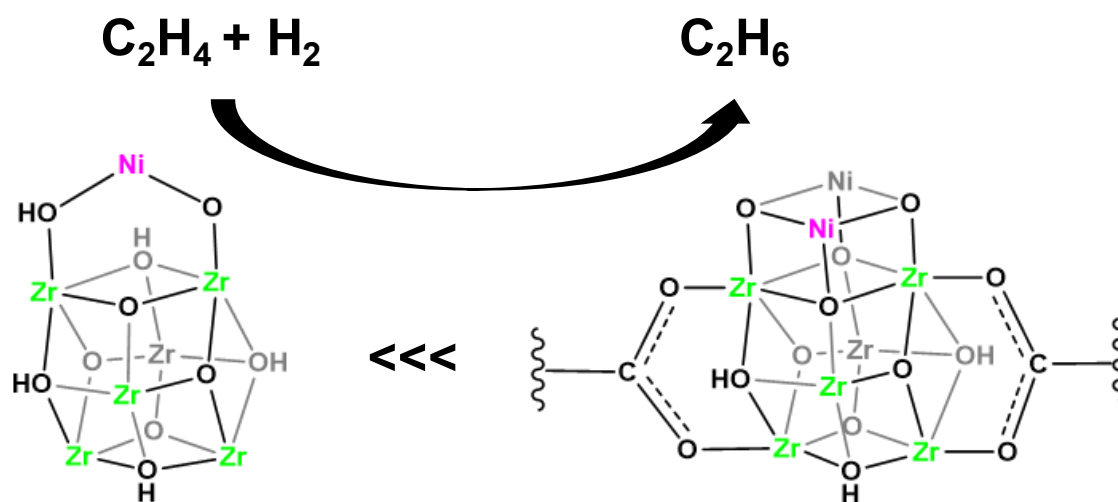
Portions of this chapter appear in the following manuscript:

Wang, Q.; Pengmei, Z.; Pandharkar, R.U.; Gagliardi, L.; Hupp, J.T.; Notestein, J.M.

“Investigating the Effect of Metal Nuclearity on Activity for Ethylene Hydrogenation by Metal-Organic-Framework-Supported oxy-Ni(II) Catalysts.” *J. Catal.* (2022), 407, 162-173

2.1 Chapter Summary

Metal-organic frameworks (MOFs), thanks to their well-defined coordination sites, are promising for studying catalytically active structures. To understand the effect of metal nuclearity in MOF-supported catalysts, we adjusted the nuclearity of oxy-Ni(II) supported on the zirconia-like nodes of MOF NU-1000 by modulating the Ni loading, where the organic linkers served to prevent node-to-node migration of grafted nickel ions. At the single-node level, we grafted auxiliary structural linkers, naphthalene dicarboxylate, to reduce the number of binding/grafting sites. We found higher catalytic rates at higher Ni loading for ethylene hydrogenation on a per-nickel-ion basis, despite the similar chemical environment of Ni(II) at different loadings; catalysts consisting mainly of pairs of nickel ions were more reactive than those of single nickel ions. These observations illustrate the need for at least two proximal nickel ions for effective catalysis – presumably one for hydrogen binding and heterolytic splitting and one for ethylene binding and activation.



2.2 The Appeals and Pitfalls of Single-Atom Catalysts

A widely implemented strategy to synthesize solid-state catalysts is to disperse catalytic species onto a solid support. Downsizing the particles of the catalytic species is generally desirable, as smaller particles and clusters present more defect sites that can increase catalytic activities.⁷⁹ Single-atom catalysts (SACs), the smallest achievable catalytic species, are thus of significant interest in realizing high catalytic activities. However, several underlying trade-offs can hinder SACs from achieving good catalytic performance. The high surface energies endow the SACs with high tendencies to aggregation and deactivation.⁸⁰ Also, SACs may be mechanistically prevented from certain types of catalysis. As a prominent example, single-atom Pt supported on α -MoC exhibits lower water-gas-shift activity than catalysts where sub-nanometer Pt clusters are present. It was found that the crowding of surface Pt species can more promptly remove surface oxygen species, preventing the support from deep oxidation and deactivation.^{80, 81} Those precedents illustrate the importance of understanding the interplay between the nuclearity of catalysts and catalytic activity, as it will provide crucial insights into optimizing catalytic systems.

2.3 Metal-Organic Framework as A Model System for Tuning the Nuclearity of Metal Catalysts

Metal-organic frameworks (MOFs) have been used as solid catalyst supports for dispersing catalytic species down to single ions. Constructed from metal ions or clusters (nodes) connected by polytopic organic moieties (linkers), MOFs typically possess high internal surface areas and porosities. Those features facilitate the uptake of reactants, diffusive transport of catalytic species, and the effective release of products. Moreover, thanks to the high tunability of MOFs, additional functionalities can be realized during synthesis or post-synthetically.³⁶ For instance, metal ions can be grafted to nodes via reactions with terminal nonstructural aqua and

hydroxo ligands or triply-bridging hydroxo ligands (μ_3 -OH), concomitant with the release of a fraction of the organic ligands from the metal precursor molecule.⁸² Thus, for node-grafted metal ions to be rendered capable of binding and activating candidate reactants, it is typically necessary to follow grafting with a step that releases/replaces unreacted ligand(s) from the precursor molecule. For remnant precursor alkyl or amidinate ligands, repetitive steam-dosing is a common removal/replacement strategy.⁸³

Alternatively, metal ions can be attached to MOF linkers by forming coordinate-covalent (typically chelating) metal-linker bonds.^{84, 85} Also known are variants where: a) catalytic metal ions are grafted via insertion between linker-node bonds, combined with recruitment of a nonstructural node ligand as a bridge between the added metal ion and the node (rarely encountered),^{86, 87} or b) intact catalytic complexes are node-tethered in fully molecular forms via reactive substituents at the periphery of the complex (often encountered).^{88, 89} Regardless of the catalyst immobilization scheme, the resistance of metal ions to transport across organic linkers, even at temperatures approaching MOF decomposition temperatures (*ca.* 350 to 450 °C for typical Zr-MOFs)^{90, 91} serves to prevent node-to-node metal ion migration and catalyst sintering. Thus, the initially synthetically defined metal-ion nuclearity tends to be preserved throughout catalyst operation.^{92, 93}

NU-1000 ($[\text{Zr}_6(\mu_3\text{-O})_4(\mu_3\text{-OH})_4(\text{OH})_4(\text{H}_2\text{O})_4(\text{TBAPy})_2]_\infty$ (TBAPy = 1,3,6,8-(*p*-benzoate)pyrene)) is a mesoporous MOF constructed from Zr_6 nodes and tetra-anionic TBAPy linkers. It has been used to support metal-oxy and metal-sulfur species to catalyze a wide range of reactions, including olefin hydrogenation,^{92, 94} alkene epoxidation,⁹⁵ oxidative propane dehydrogenation,⁹⁶ singlet-oxygen mediated dialkyl-sulfide oxygenation,^{97, 98} olefin dimerization,^{94, 99, 100} oligomerization,¹⁰¹⁻¹⁰³ or polymerization,^{104, 105} CO oxidation,^{83, 106}

xylene isomerization,^{107, 108} and electrochemically or photochemically driven water oxidation,¹⁰⁹⁻¹¹¹ water reduction,¹¹²⁻¹¹⁴ or aqueous nitrate reduction.^{115, 116} Each Zr_6 node connects to 8 linkers and presents four additional pairs of -OH/-H₂O ligands, suitable for grafting metal ions or carboxylate-terminated auxiliary ligands. Also present, regardless of node connectivity, are four Brønsted-acidic μ_3 -hydroxo ligands that can react with alcohols¹¹⁷ or ammonia,¹¹⁸ or that can participate independently or in cooperation with terminal node-aqua and/or -hydroxo ligands in metal-ion grafting.^{83, 119} NU-1000 possesses 3 nm diameter hexagonal channels and 1 nm diameter triangular channels down the *c*-axis of the particle, as well as small (~0.8 nm) openings, *c*-pores, and *c*₁-pores, that lie in the *ab*-plane and laterally interconnect the aforementioned channels (**Figure 2.1**).

While many MOF-node-supported metal ions are proficient catalysts for various gas-phase reactions, the interplay between metal nuclearity and reactivity is largely unexplored. On conventional metal oxide supports, SACs can be achieved at extremely low loading,¹²⁰ and the effect of catalyst coverage can be studied by gradually increasing the metal loading.¹²¹ However, studying the progression of metal nuclearity from monomer to dimer and above is challenging on metal oxide supports due to polydispersed metal binding sites. In some metal-oxide-supported catalysts, such as vanadium on zirconia, the target nuclearity is difficult to maintain due to the weak metal-support interactions. Vanadium species tend to migrate and form clusters of higher nuclearity.¹²² In the meantime, the uniform metal nodes in MOF provide monodispersed binding sites to realize the progression of increasing nuclearity, while the spatial isolation created by the linkers effectively prevents sintering.

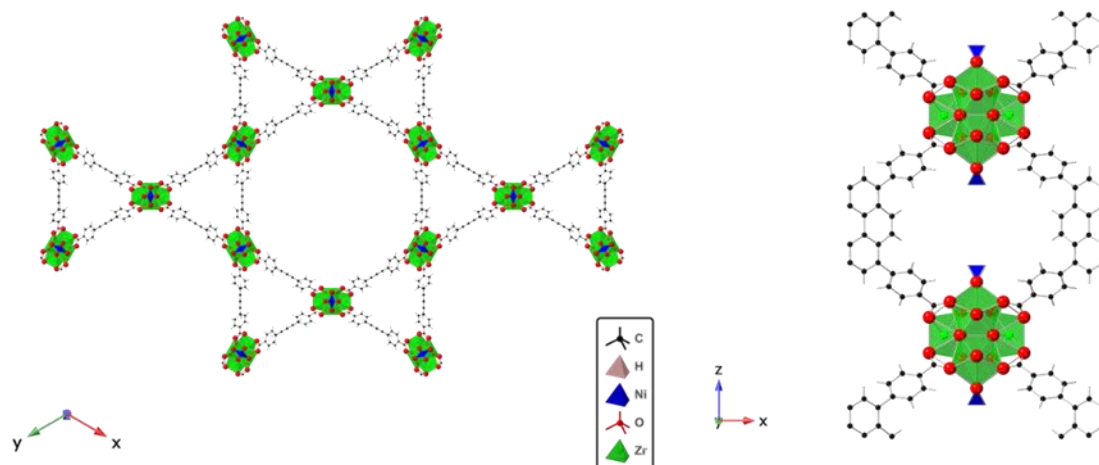


Figure 2.1. Single crystal structure of Ni supported on NU-1000. The blue pyramids show Ni residing in the c-pores.

2.4 Synthesis of NU-1000-Supported oxy-Ni(II) Catalysts of Various Nuclearities

In this work, Ni ions were deposited onto the Zr_6 nodes of formate-free NU-1000, and the effects of Ni nuclearity and siting were studied. According to the previously published single-crystal structure of Ni on NU-1000¹²³ (**Figure 2.1**), Ni ions preferentially reside in the c-pores of formate-containing NU-1000 single crystals. The effect of Ni residing in different locations in NU-1000 was therefore investigated by blocking the c-pores with naphthalenedicarboxylic acid (NDC), a ligand with similar aspect ratios as the c-pores. Using ethylene hydrogenation as the probe reaction, differences in reactivity arising from varied catalyst loadings and sitings were observed. The nature of the catalyst species was also studied with various spectroscopic techniques, where the presence of Ni-O-Ni sites was identified as crucial to the improved reactivity at high catalyst loadings.

2.5 Characterizations

2.5.1 Physical Properties

The retention of crystallinity and porosity of the MOF catalysts were confirmed by PXRD (**Figure 2.2**) and N₂ physisorption (**Figure 2.3**). Other properties, including the BET surface areas, Ni loading by weight and per Zr₆ node quantified by ICP-OES, are summarized in **Table 2.1**. In formate-free NU-1000, Ni loading increases with an increased amount of precursor in solution and reaches 3.8 Ni per node, close to the maximum number of single-site cation sites a Zr₆ node can accommodate (4). A decrease in BET surface area is generally observed with the incorporation of Ni. Different batches of formate-free NU-1000 were used during syntheses, which accounts for the variability in surface area.

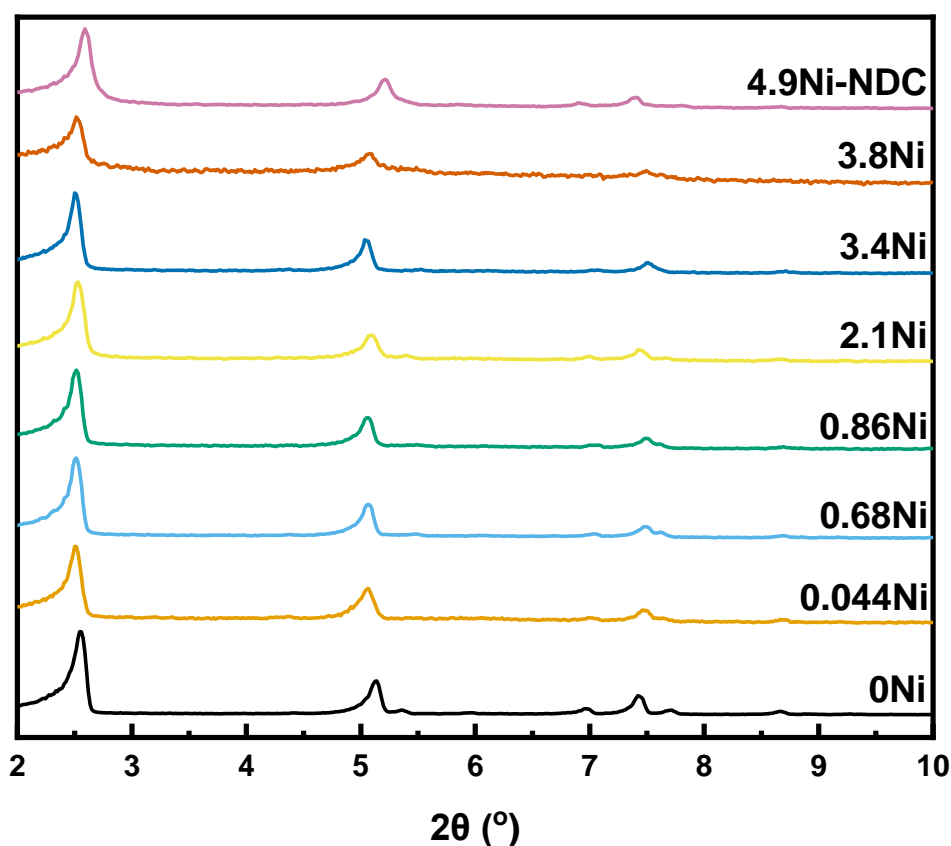


Figure 2.2. PXRD patterns of the as-made catalysts.

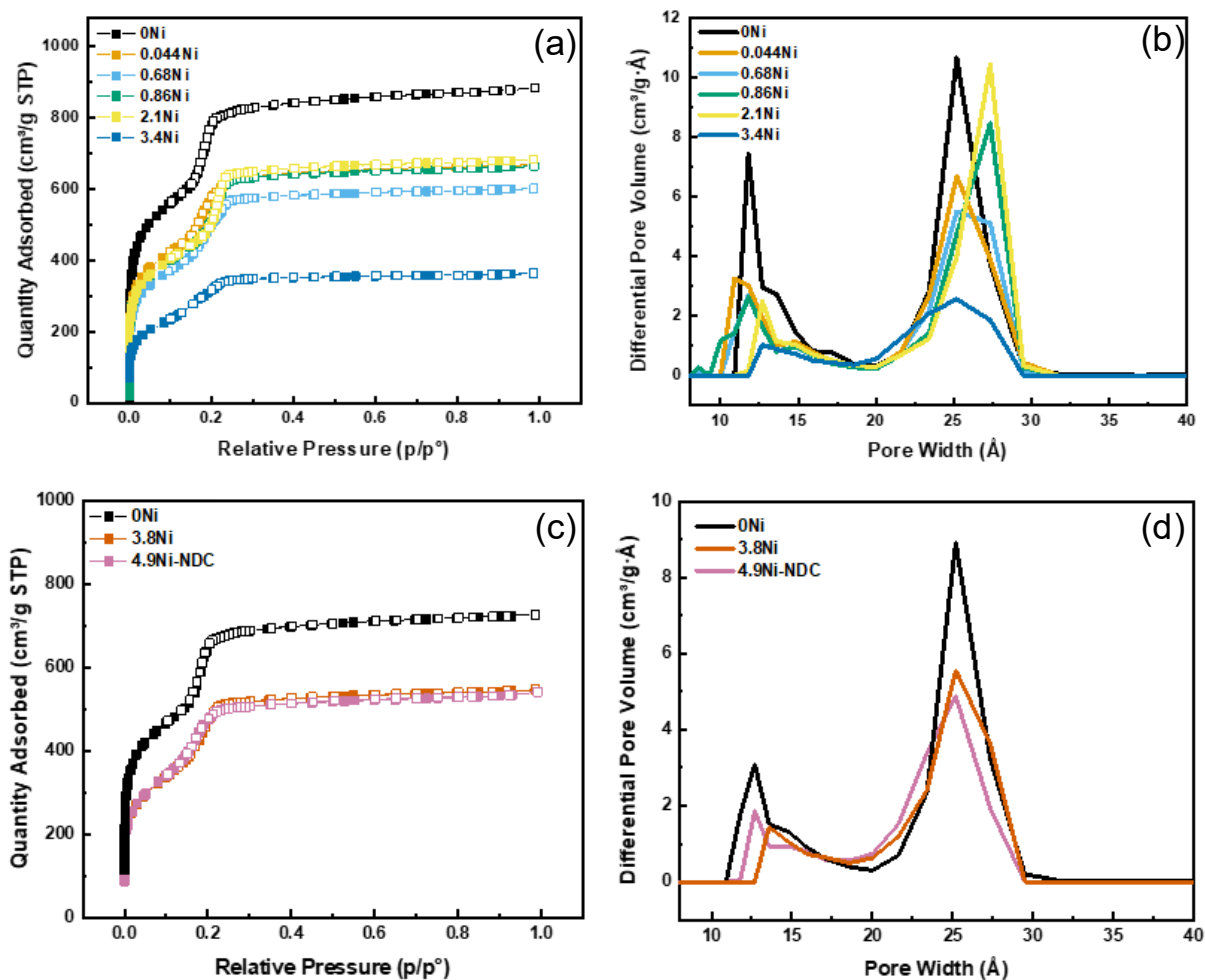


Figure 2.3. (a-b) N₂ isotherms and DFT differential pore size distributions of 0Ni~3.4Ni. (c-d) N₂ isotherms and DFT differential pore size distributions of 3.8Ni and 4.9Ni-NDC.

Table 2.1. Property table.

Catalyst	Ni(amd) ₂ added ^a	Ni (wt%)	Ni/node	Ni/site ^b	Surface Area (m ² /g)	Pore Volumes (cm ³ /g)
0Ni	n/a	0	0	0	2166	7.2, 10.4
0.044Ni	0.5	0.067%	0.044	0.01	1632	3.3, 6.7
0.68Ni	1	1.3%	0.68	0.17	1425	2.7, 5.5
0.86Ni	2	1.7%	0.86	0.22	1536	2.6, 8.5
1.4Ni	2	2.8%	1.4	0.35	1281	2.6, 5.5
2.1Ni	4	2.5%	2.1	0.53	1539	2.5, 10.3
3.8Ni	8	5.4%	3.8	0.95	1262	1.4, 5.6
0Ni-NDC	n/a	0	0	0	1790	1.8, 8.8
4.9Ni-NDC	8	6.2%	4.9	2.5	1274	1.8, 4.9

^a Molar equivalents Ni(amd)₂ per node added during synthesis

^b Based on a theoretical 4 cation binding sites per node of NU-1000-FF and 2 cation binding sites per node of NU-1000-NDC.

2.5.2 Structural Investigations

In-situ DRIFTS confirmed the presence of amd ligands from the Ni precursor in the as-made catalysts (**Figure 2.4**). The spectra were collected at 200°C under 10% H₂, mimicking reaction conditions. While the introduction of H₂ did not perturb the spectra of 0Ni, various negative features emerged for the Ni catalysts. The sharp negative peak at 1630 cm⁻¹ is present in all Ni-containing samples and is assigned to the loss of the bending vibration of aqua groups. The negative feature at 3645 cm⁻¹ in the spectra for 2.1Ni and 3.8Ni, and as a shoulder in 4.9Ni-NDC, is also attributed to the loss of aqua ligands. A negative feature centered at 3280 cm⁻¹ is present in all Ni-containing samples; the peak is broadened and blue-shifted for 4.9Ni-NDC. This feature arises from a combination of N-H from the amd ligands and O-H stretches on the nodes, both perturbed by the H₂ treatment. The negative 2970 cm⁻¹ peak is assigned to the C-H stretch of the t-butyl groups on the amd ligands. None of these features are present in the spectrum of 0Ni, showing that these aqua and hydroxyl groups affected by H₂ treatment at 200°C are associated with Ni atoms, as indicated in the structure shown in **Figure 2.4**. Overall, the

DRIFTS spectra confirmed the presence of amd ligands on Ni before catalysis and that the amd ligands and aqua ligands on the nodes are perturbed thermally under reducing environment.

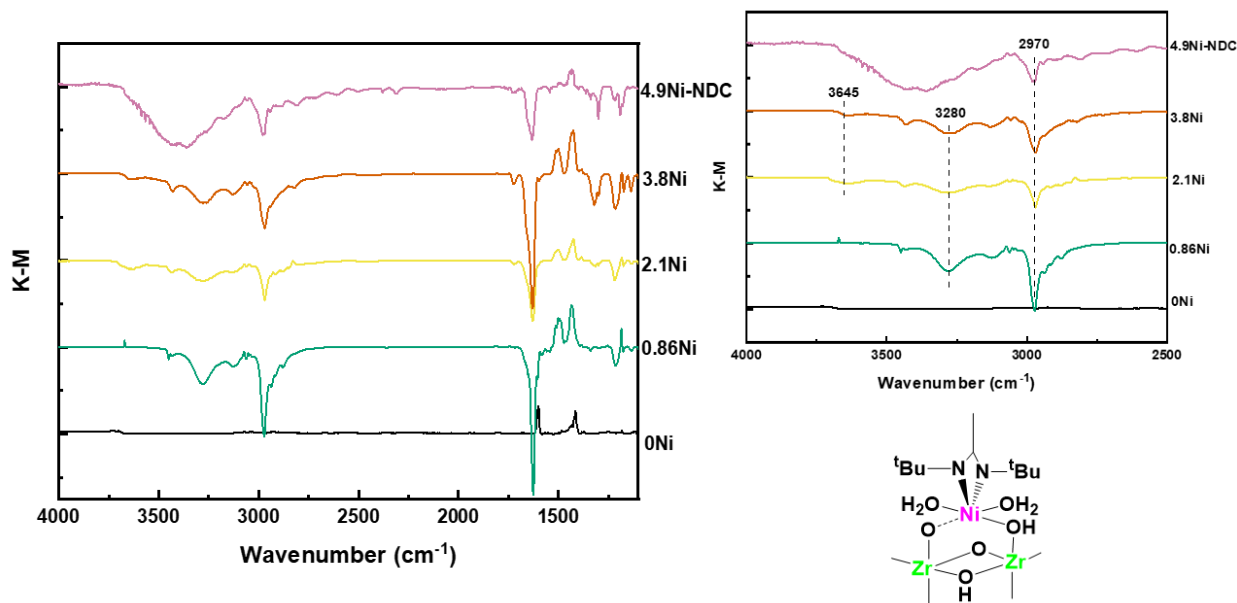


Figure 2.4. DRIFT spectra of 0Ni, 0.86Ni, 2.1Ni, 3.8Ni and 4.9Ni-NDC. Background spectra were collected following catalyst pretreatment in Ar at 200°C for 1 hour. The gas was then switched to 100 sccm 10% H₂/N₂, and difference spectra were collected until no further changes in spectra were observed.

The residual amd ligands and the degree of hydration of the catalysts were quantified with thermogravimetric analysis (TGA) in H₂ (**Figure 2.5**). Several stages of weight loss were observed in the TGA curves. Below 120°C, the weight losses originated from a combination of physisorbed water and the aqua ligands on the nodes, as suggested by the DRIFTS studies and TGA measurements on formate-free NU-1000.¹²⁴

For the 0Ni sample, three distinct peaks at 50, 91, and 113°C were observed. The peaks for Ni-containing samples were less resolved, possibly because the physisorbed water and the aqua ligands were removed rapidly and/or in a consecutive manner. In addition, the weight loss in the temperature range of 110~210°C only appeared in the Ni-containing samples and is assigned to the removal of the amd ligands, consistent with the amd ligand detachment

temperature observed for Ni(amd)₂ deposited on SiO₂ films.¹²⁵ For Ni supported on NU-1000-FF, one amd remained per Ni (**Table 2.2**), consistent with attachment reaction such that one of the two amd ligands in the precursor was replaced by the hydroxyl and bridging oxygens on the Zr₆ nodes, leaving the second amd ligand behind. 4.9Ni-NDC contains significantly fewer remaining amd ligands per Ni and is significantly less hydrated than the rest of the samples (**Table 2.2**). We interpret this as arising from a different Ni nuclearity, as illustrated in the proposed catalyst structures in **Figure 2.7**. Overall, the different degrees of catalyst hydricity points to the need to pre-treat the catalysts under elevated temperatures to remove physisorbed species within the MOF pores.

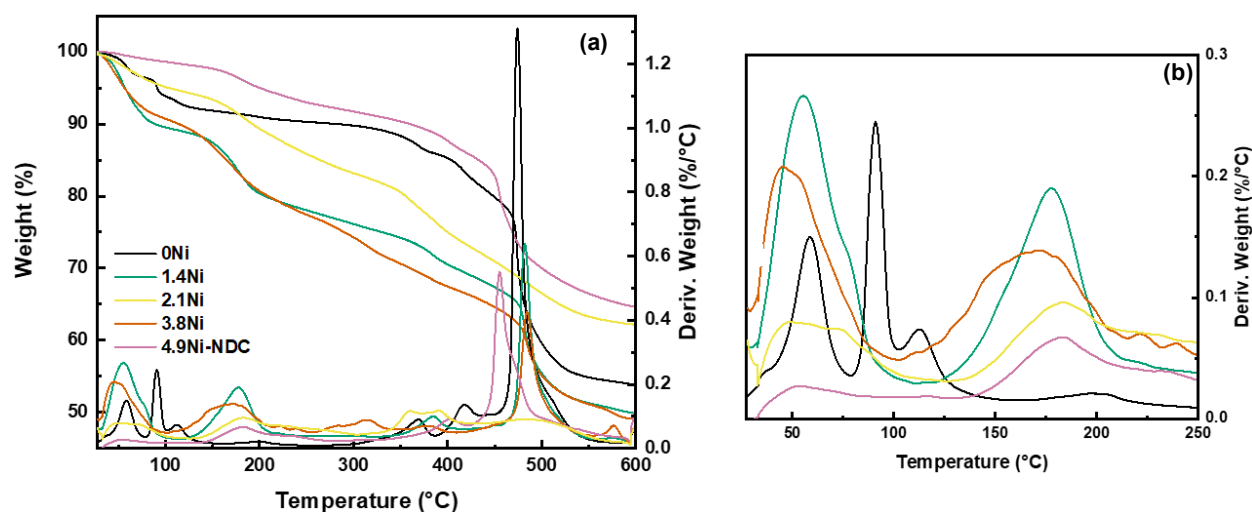


Figure 2.5. (a) Thermogravimetric analysis from 25-600°C. (b) Derivative weight curves from 24-250°C showing weight loss from physisorbed water and aqua ligands below ~125°C and amd ligands at higher temperatures.

Table 2.2. Quantification of catalyst hydration and amd ligand remaining.

Sample	Water (wt.%)^a	Ni (mmol/g)^b	amd (mmol /g)^a	amd:Ni
0Ni	7.70%	n/a	n/a	n/a
1.4Ni	10.2%	4.8	5.8	1.2
2.1Ni	5.35%	7.5	5.9	0.8
3.8Ni	9.70%	8.9	7.8	0.9
4.9Ni-NDC	1.29%	10.6	2.0	0.2

^a from TGA^b from ICP-OES

The local coordination environments of Ni in 0.86Ni, 2.1Ni, 3.8Ni, and NDC-4.9Ni were studied with X-ray absorption (XAS). The Ni edge energies extracted from the X-ray absorption near edge structure (XANES) are centered at 8345.3 ± 0.1 eV for all samples [Figure 2.6(a) and Table 2.3], shifted slightly from that of Ni(OH)₂ at 8346.9 eV. The pre-edge feature at 8333.5 eV is also present in all the spectra, which is assigned to the Ni 1s → 3d transition for octahedrally coordinated Ni²⁺ species [Figure 2.6(b)]. The octahedral coordination of Ni²⁺ in all Ni-containing samples is confirmed by the first-shell EXAFS fittings, where the Ni-X (X = N or O) coordination numbers were extracted from fitting against the Ni-O scattering path of the Ni(OH)₂ standard [Figure 2.6(c) and Table 2.3].

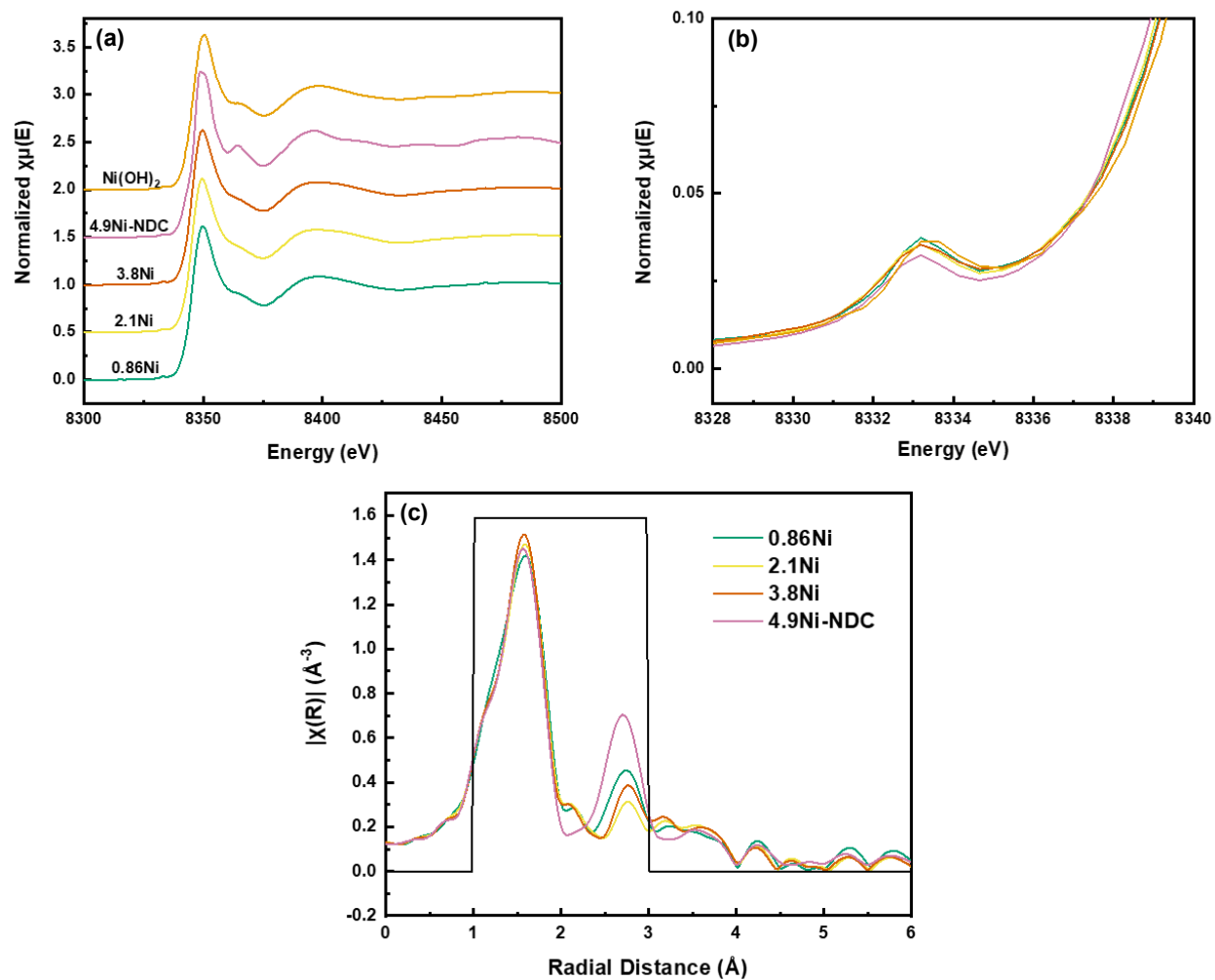


Figure 2.6. (a) XANES of 0.86Ni, 2.1Ni, 3.8Ni, 4.9Ni-NDC, and Ni(OH)₂ standard. (b) Pre-edge features at 8333.5 eV. (c) EXAFS in r-space with the fitting window shown in black.

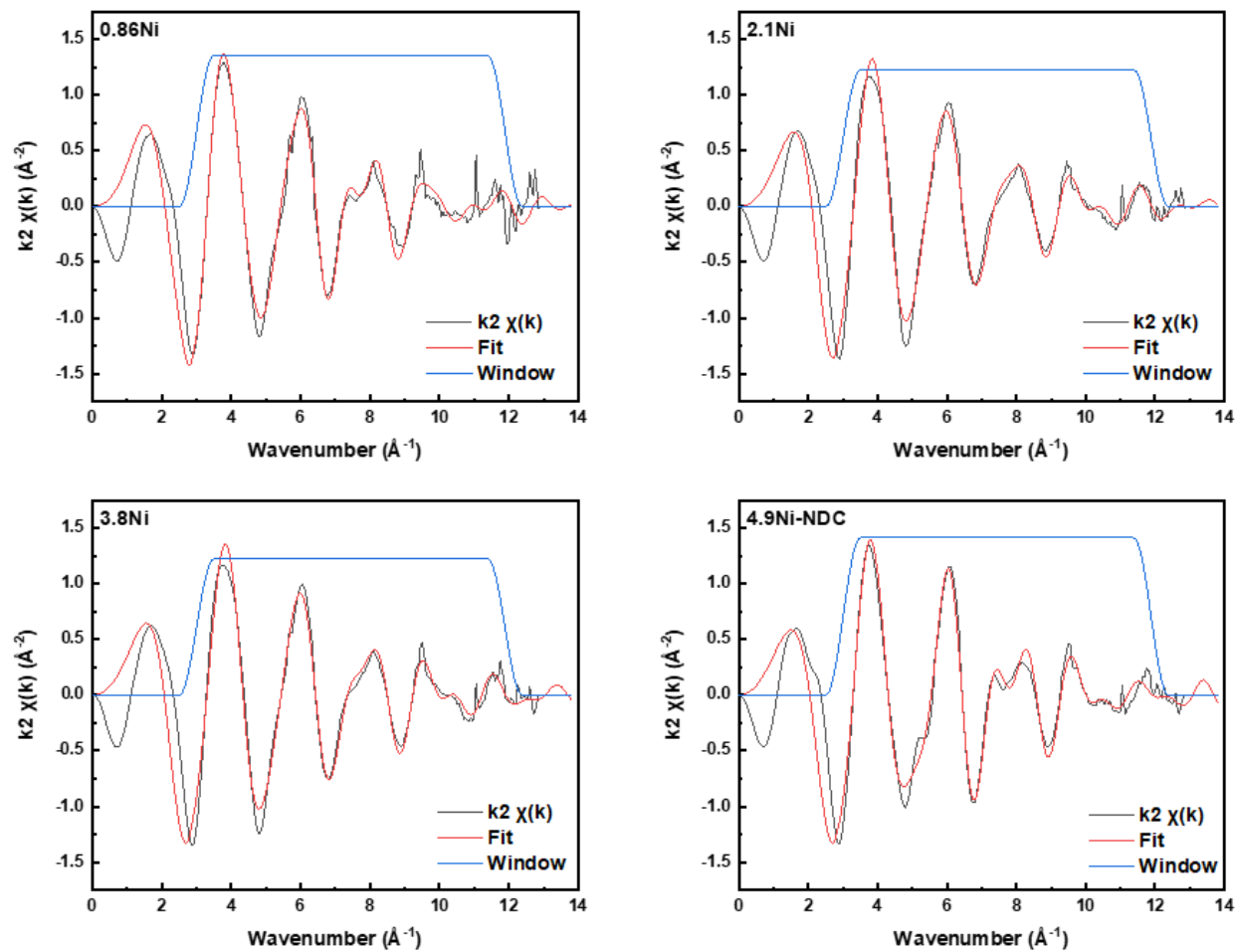


Figure 2.7. EXAFS fittings in k-space.

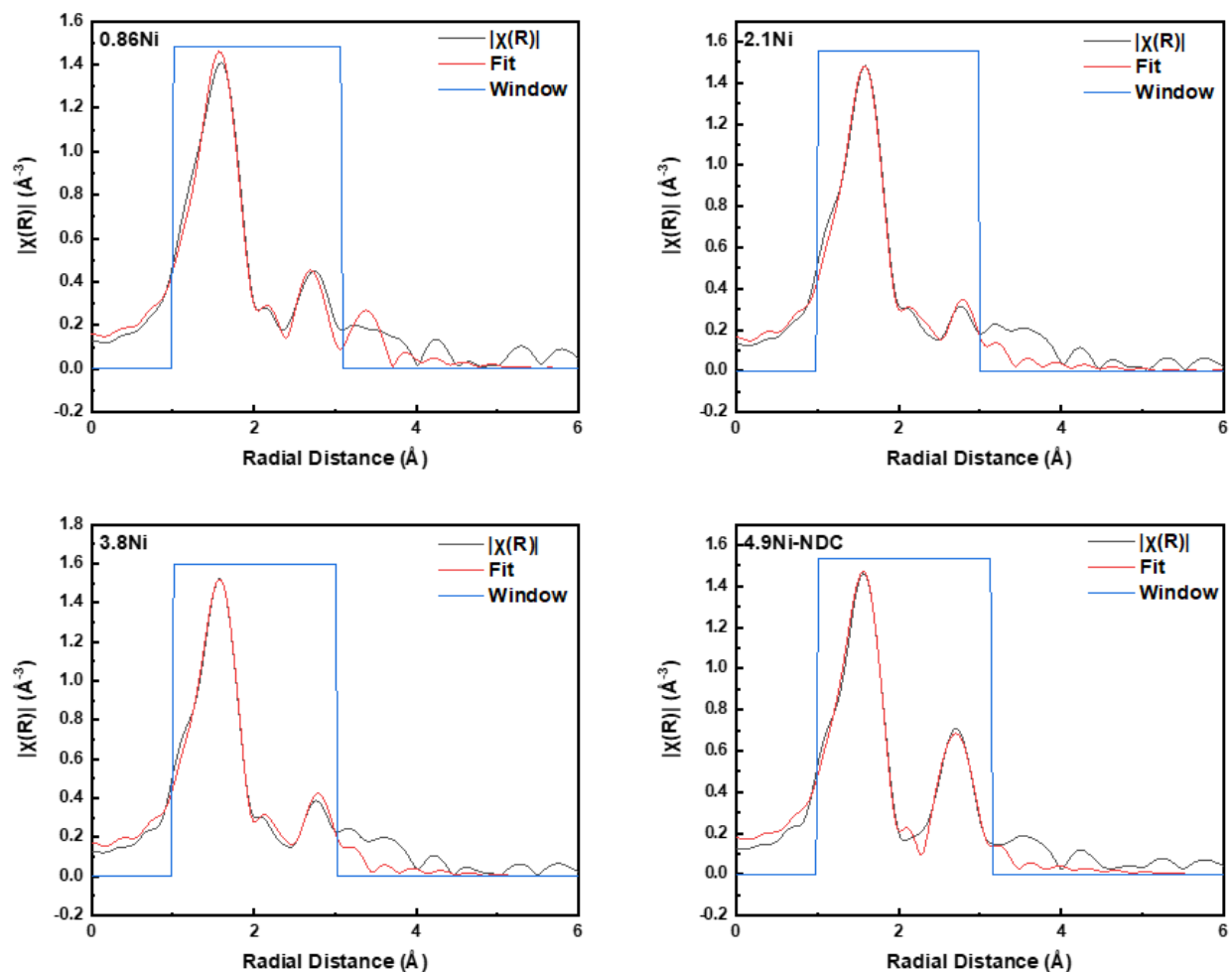


Figure 2.8. EXAFS fitting in r-space.

Table 2.3. Ni K edge EXAFS fitting results.

Sample	Edge Energy	Ni-X R (Å) ^a	Ni-X N ^a	Ni-X σ^{2a}	Ni..Ni R (Å) ^b	Ni..Ni N ^{b,c}	Ni..Ni σ^{2b}
0.86Ni	8345.36	2.052 ± 0.002	6.4 ± 0.3	0.0085 ± 0.0004	3.067 ± 0.009	1.4 ± 0.7	0.0053 ± 0.0010
2.1Ni	8345.27	2.047 ± 0.003	6.5 ± 0.2	0.0077 ± 0.0005	3.101 ± 0.038	0.4 ± 0.2	0.0085 ± 0.0039
3.8Ni	8345.38	2.043 ± 0.003	6.5 ± 0.2	0.0072 ± 0.0005	3.040 ± 0.021	0.3 ± 0.1	0.0011 ± 0.0023
4.9Ni-NDC	8345.59	2.038 ± 0.002	6.7 ± 0.2	0.0077 ± 0.0004	3.033 ± 0.006	2.4 ± 0.2	0.0072 ± 0.0007

^a Ni-X first shell bond distance (R), coordination number (N) and Debye-Waller factor

^b Ni..Ni second-shell distance (R), number of scattering paths (N) and Debye-Waller factor

^c possible contribution from Ni-O-Zr scattering in this low-loaded material

Table 2.4. Complete EXAFS fitting results.

Sample	Ni first shell bond distance (Å)	Ni first shell coordination number	Debye-Waller Factor (σ^2)
0.86Ni	2.052 \pm 0.002	6.9 \pm 0.2	0.0085 \pm 0.0004
2.1Ni	2.047 \pm 0.003	6.5 \pm 0.2	0.0077 \pm 0.0005
3.8Ni	2.043 \pm 0.003	6.5 \pm 0.2	0.0072 \pm 0.0005
4.9Ni-NDC	2.038 \pm 0.002	6.7 \pm 0.2	0.0077 \pm 0.0004
Sample	Ni...Ni distance (Å)	Ni...Ni coordination number	Debye-Waller Factor (σ^2)
0.86Ni	3.067 \pm 0.009	1.4 \pm 0.7	0.0053 \pm 0.0010
2.1Ni	3.101 \pm 0.038	0.4 \pm 0.2	0.0085 \pm 0.0039
3.8Ni	3.040 \pm 0.021	0.3 \pm 0.1	0.0011 \pm 0.0023
4.9Ni-NDC	3.033 \pm 0.006	2.4 \pm 0.2	0.0072 \pm 0.0007
Sample	Ni...Zr distance (Å)	Ni...Zr coordination number	Debye-Waller Factor (σ^2)
0.86Ni	3.709 \pm 0.016	2.4 \pm 0.6	0.0093 \pm 0.0019
2.1Ni	3.283 \pm 0.023	1.0 \pm 0.3	0.0059 \pm 0.0030
3.8Ni	3.308 \pm 0.014	0.8 \pm 0.2	0.0032 \pm 0.0015
4.9Ni-NDC	3.313 \pm 0.009	0.5 \pm 0.1	0.0015 \pm 0.0011

Overall, Ni exhibits a similar local chemical environment in all catalysts, consistent with the similar binding energies of Ni and Zr observed in XPS (**Figure 2.9**). However, the second-shell EXAFS fitting results reveal significant Ni-O-Ni contribution for 4.9Ni-NDC, where each Ni is bridged to approximately two other Ni by two oxygens. In contrast, Ni in the other catalysts remain isolated. Among all samples, 0.86Ni presents the highest uncertainty due to low loading. Detailed fitting parameters can be found in **Figures 2.7, 2.8**, and **Table 2.4**. This is consistent with the overall stoichiometry reported in **Table 2.1**.

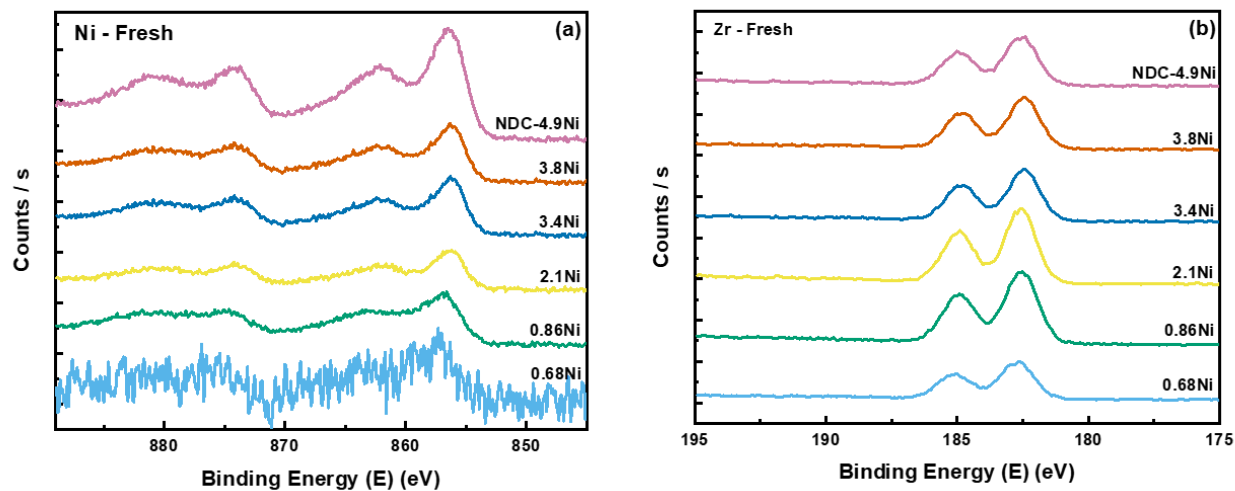


Figure 2.9. XPS of (a) Ni and (b) Zr of the as-made samples.

2.5.3 Proposed Active Site Structures

Based on the abovementioned characterization, two catalyst structures are proposed in **Figure 2.10**. For Ni on formate-free NU-1000, octahedrally coordinated Ni ions reside on the -OH/H₂O ligand pairs of the Zr₆ nodes. In the case of Ni on NDC-NU-1000, Ni ions recruit the μ_3 -O in addition to the -OH/H₂O ligands, forming Ni-O-Ni sites. Given a loading of 4.9 Ni per Zr₆ node on NDC-NU-1000, it is likely that there is also the presence of Ni species of nuclearities higher than 2.

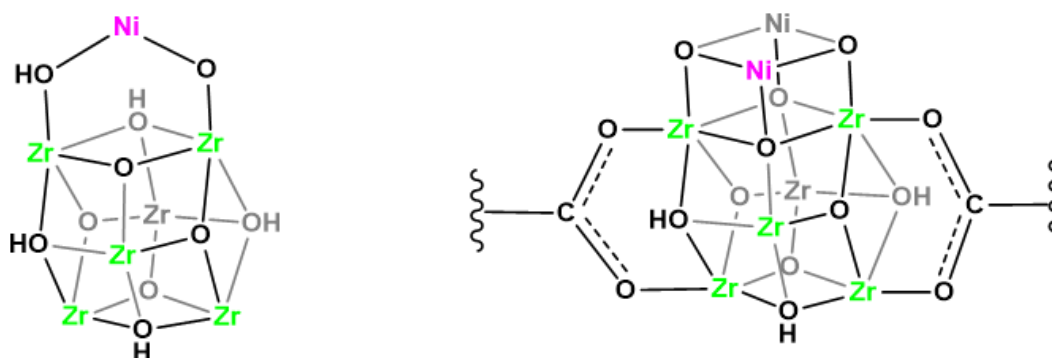


Figure 2.10. Representative, average, structures of Ni ions in formate-free NU-1000 (left) and NDC-NU-1000 (right). Each node of NU-1000 contains up to three additional Ni atoms in similar coordination environments. The nodes of NDC-NU-1000 contain only one other binding site due to blocking by the NDC ligands. For clarity, only dimer structure is presented. All Ni ions should be octahedrally coordinated; hydroxyl and/or precursor ligands on Ni ions are omitted for clarity.

2.6 Reactivity Studies Using Ethylene Hydrogenation as the Model Reaction

A representative conversion vs. time-on-stream plot is given for 3.8Ni in **Figure 2.11(a)**, where conversion steadily increases over the temperature range of 55~95°C. The initially high reactivity at 55°C is due to Ni being saturated with hydride species after the H₂ pre-treatment. As this step is found to be the rate-determining step from the subsequent studies, a decrease in reactivity approaching steady state is expected. **Figure 2.11(b)** shows the rate at 150 °C for the studied catalysts. At loadings below 1 Ni per node, the rates are low and close to that of the bare NU-1000. Rates per Ni atom increase when the loading reaches 2.1 Ni per node and continues to increase for 3.4 Ni per node. The rates for 4.9Ni-NDC are close to tenfold higher than those for 3.8Ni. However, further reactivity studies on 3.8Ni and 4.9Ni-NDC reveal reaction orders of 0.8 and ~0 for H₂ and ethylene, respectively (**Figure 2.12**), indicating that similar mechanisms operate on these two exemplar catalysts. Such mechanistic similarities are also reflected in the similar apparent activation energies extracted from the Arrhenius plots are 22 kcal/mol for 3.8Ni

and 17 kcal/mol for 4.9Ni-NDC. We hypothesize that the rate observed in 3.8Ni mainly arises from the small number of dimers in the system carrying out the catalytic turnovers.

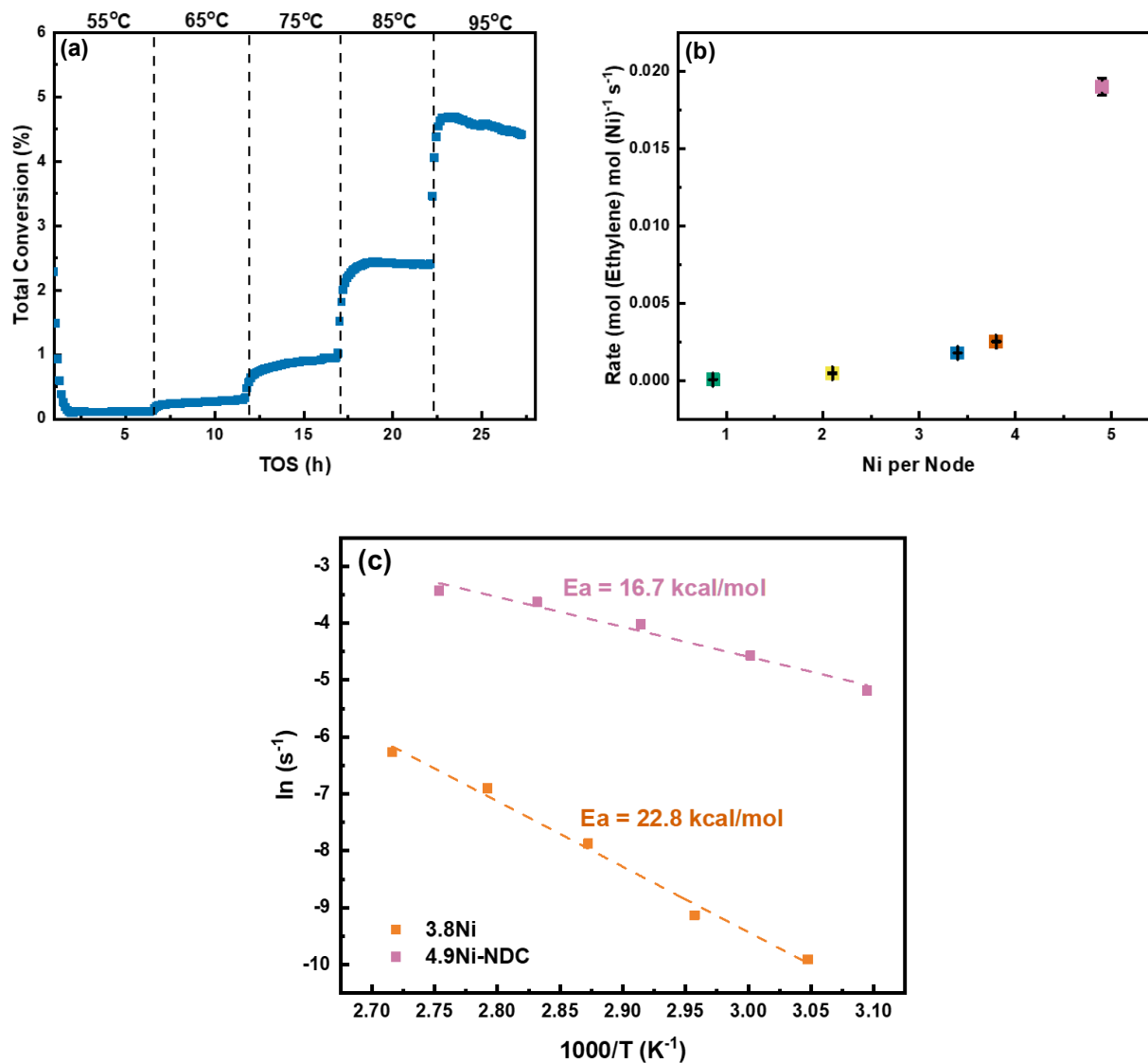


Figure 2.11. (a) Conversion vs. time on stream (TOS) for 3.8Ni at five temperatures. Conditions: ~20 mg catalyst diluted in 1 g of SiC, pre-treated in 50 sccm 10% H₂/N₂, 12 h at 200°C, followed by 1:1 H₂:C₂H₄ (10 sccm 10% H₂/N₂ and 25 sccm 4% ethylene/N₂). (b) Ni-normalized reaction rates at 150°C. (c) Arrhenius plots of 3.8Ni and 4.9Ni-NDC from 50-90°C.

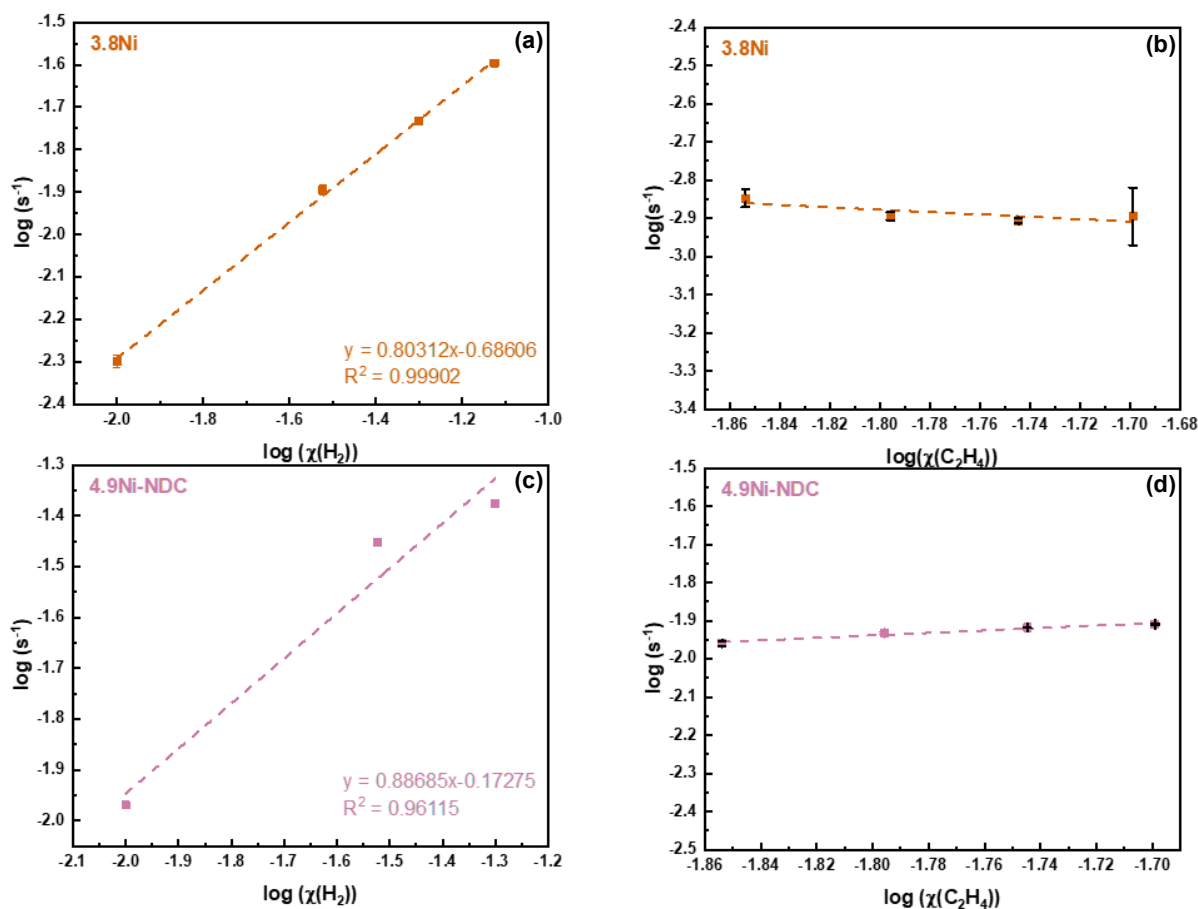


Figure 2.12. Reaction orders of H₂ and ethylene measured for (a)-(b) 3.8Ni, and (c)-(d) 4.9Ni-NDC at 100°C. H₂ reaction order measured at constant ethylene mole fraction of 0.01 and H₂ mole fraction varied from 0.01-0.075. Ethylene reaction order measured at constant ethylene mole fraction of 0.01 and H₂ mole fraction varied from 0.01-0.075. The ethylene reaction order measured at constant H₂ mole fraction of 0.01 and ethylene mole fraction varied from 0.014-0.02.

2.7 Mechanistic Insights from Density Functional Studies

The mechanism for ethylene hydrogenation that has been studied with DFT for the mono-nickel case involves the heterolytic splitting of the H₂ followed by the formation of the nickel-hydride activated species.^{92, 123} We explore a similar mechanism for the dinickel case. We only study the catalytic cycle of hydrogenation and the barriers involved in this reaction. The mechanisms for catalyst synthesis and catalyst activation are not studied. The relative free energies and enthalpies along the reaction are shown in **Figure 2.13** and the absolute energies are reported in **Table 2.5**.

Given the structure determined by EXAFS, we modeled an initial structure, such as might exist before the catalyst pretreatment, consisting of two Ni atoms linked by μ_3 -O bridges with three aqua ligands surrounding each Ni atom. Three elementary steps were then studied (**Figure 2.13**), namely the first C-H bond formation (step 1~2), and the second C-H bond formation (step 2~3) and catalyst regeneration/ H₂ splitting (step 5~6).

The Ni to the μ_3 -O distances for the two Ni are 1.96 Å in the pristine di-Ni structure, where both Ni are fully coordinated with water ligands. Those distances are comparable to the 2.04 Å determined from the EXAFS fitting for 4.9Ni-NDC. Meanwhile, this distance was found to be 2.12 Å for the mono-Ni structure. Considering the distance between Ni and the O of the aqua ligands being 2.00 Å, the average Ni-O distance is also close to the 2.05 Å extracted from the EXAFS fitting for 0.86Ni.

In the previously proposed mechanism for the mono-nickel case, the heterolytic splitting of H₂ and the protonation of the ethyl group to make ethane needed to occur in one step because there is no other place for a proton to bond upon splitting. The presence of Ni₂-O₂ moiety in the di-nickel case better accommodates this heterolytic splitting by forming a Ni-hydride and a hydroxy group. This is the active species of the catalyst. The reactant ethylene molecule adsorbs on the other Ni atom (that hasn't formed the hydride). Following the previous studies of the catalytic cycle,¹²³ this is used as the energy reference for the reported relative energies in Figure 11. The η_2 -bound ethylene is only weakly activated at this stage with dC-C = 1.35 Å, as compared to 1.33 Å in free ethylene. This is followed by the migratory insertion of the hydride to form a nickel-ethyl species. This step has a free energy of activation of 12.7 kcal/mol. The subsequent attack of the adjacent proton to form the ethane has an activation free energy of 2.4 kcal/mol. Ethane is only weakly adsorbed on the Ni atom. The Ni-hydride starting species is

regenerated when another H₂ molecule displaces the ethane and undergoes the subsequent heterolytic splitting of that has an apparent barrier – i.e. free energy of TS₅₆ with respect to the bare structure (species 4) – of about 24 kcal/mol. This high apparent barrier (partly entropic as H₂ molecule is first adsorbed and partly enthalpic because the H₂ is split) might justify the experimental dependence of the rate on the H₂ activity. This, however, needs to be verified with further studies and kinetic modeling.

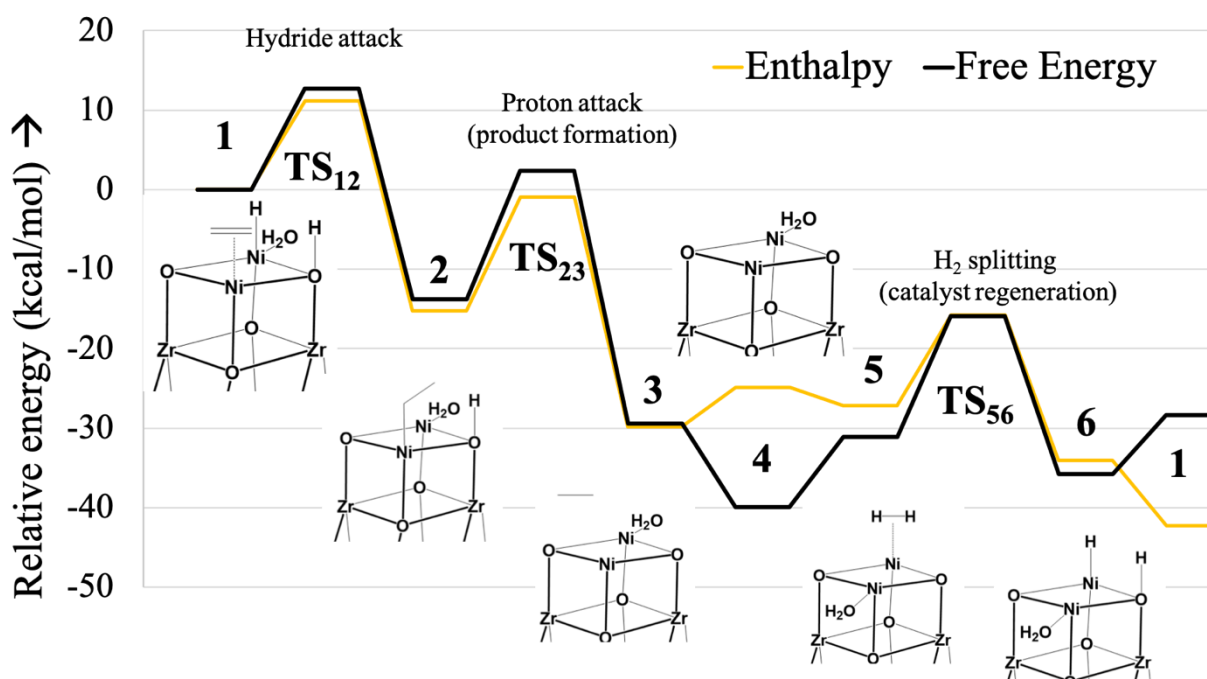


Figure 2.13. DFT-calculated enthalpies (yellow) and free energies (gray) for intermediates and transition state structures. Energies given in kcal/mol relative to species 1. The lower portion of the node and linkers bound to the Zr₆ nodes are omitted for clarity.

Table 2.5. Absolute energies of reaction species with corresponding corrections.

Species	E(a.u.)	H (a.u.)	G(a.u.)
1	-6182.48249	-6181.91223	-6182.21950
TS ₁₂	-6182.46224	-6181.89447	-6182.19926
2	-6182.50995	-6181.93647	-6182.24140
TS ₂₃	-6182.48214	-6181.91368	-6182.21567
3	-6182.53473	-6181.95969	-6182.26632
4	-6102.68046	-6102.18946	-6102.47544
5	-6103.85136	-6103.34345	-6103.63618
TS ₅₆	-6103.83043	-6103.32531	-6103.61205
6	-6103.86479	-6103.35444	-6103.64363

We also note that a mechanism exactly like the mono-nickel case was explored for the di-nickel catalyst – where one Ni is the active site, and the other Ni is a spectator. Intermediates for this mechanism were hard to obtain and would converge to one of the species reported mechanism. Another possibility of the H₂ splitting in a way to form Ni-hydride and protonating the the μ -O of the node (below the Ni) was also considered. This does not lead to product formation because the ethyl group (after the migratory insertion of the hydride) attaches to the other Ni and thus is too far from the proton for the reaction to complete. Both these mechanisms were thus discarded.

2.8 Mechanistic Investigation from an Enthalpic Perspective

To compare the catalytic activity in mono-nickel and di-nickel case, we compare the ΔH values calculated for the di-nickel case with the values reported in literature for the mono-nickel.⁹² We note that this reference uses a different basis set (bs1) for electronic energies. All the other details are consistent with our computational protocol.

Figure 2.14 below shows the enthalpy changes associated with ethylene adsorption, hydride attack, and the Ni-ethyl species formation. The enthalpy of activation for the hydride

attacking the adsorbed ethylene is ~ 4 kcal/mol in the mono-nickel case and 11.4 kcal/mol in the dinickel case. Both are low enough that they could show activity under the reaction conditions.

There is, however, a significant difference in the enthalpy of adsorption of ethylene. In the mono-nickel case the ethylene needs to adsorb on the nickel that has formed the hydride. This is an endergonic reaction with a ΔH of +15.9 kcal/mol. In the di-nickel case, however, it adsorbs on the other nickel, whose binding site is more available. This adsorption is exergonic with a ΔH of -8.2 kcal/mol. This is consistent with the experimental observation of lower catalytic activity from the mono-nickel case, where the reactivity likely arises from the trace amount of di-nickel species in the as-made samples or formed during the reaction.

We note that the ΔH values do not consider the entropic penalty for adsorption and that the ΔG for this step is uphill by 7 kcal/mol. The ΔG values for the mono-nickel case are not reported in the reference used.

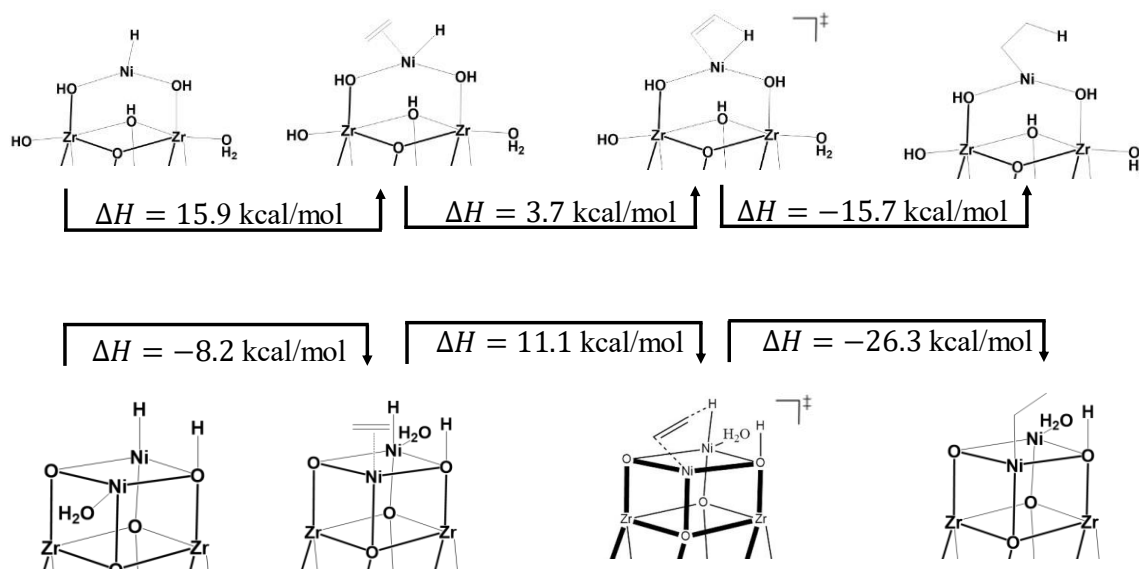


Figure 2.14. Reaction enthalpies in associated with the ethylene activation reported for the mono-nickel (top) and calculated in this work for the dinickel (below).

2.9 Chapter Conclusions

We found that the nuclearity of NiO_x supported on MOF NU-1000 can be controlled by systematically adjusting the overall Ni loading. We are also able to increase NiO_x nuclearity by introducing node-connecting auxiliary ligands (NDC anions) that change the Zr-MOF node from eight-connected to ten-connected and thus decrease the number of potential grafting sites presented by each node. The structural differences between mononuclear Ni cations and Ni-O-Ni sites are reflected in their different ethylene hydrogenation reactivities, where single-site Ni at loadings below 1 Ni per Zr₆ node is significantly less reactive. The most reactive catalyst is Ni supported on NDC-NU-1000, which is predominantly composed of Ni-O-Ni sites. Changing the catalyst loading and otherwise manipulating metal-ion nuclearity has a profound impact on the “per site” catalytic performance.

2.10 Additional Information

2.10.1 Materials

All chemicals for the NU-1000 synthesis, namely 1,3,6,8-tetrabromopyrene, (4-(methoxycarbonyl)phenyl)boronic acid, tripotassium phosphate, tetrakis(triphenylphosphine) palladium(0), zirconyl chloride octahydrate, benzoic acid, hydrochloric acid, 1,4-dioxane, acetone, N,N-dimethylformamide, were purchased from Sigma Aldrich Chemicals Company, Inc. (Milwaukee, WI) and were used as received. The linker, 1,3,6,8-(p-benzoate)pyrene, was synthesized according to a reported procedure and its purity was confirmed via its ¹H NMR spectrum. For chemicals used in the deposition of Ni, bis(N,N''-di-t-butylacetamidinato)nickel(II) [Ni(amd)₂] was purchased from Strem Chemicals (Newbury Port, MA), and the anhydrous heptane was purified from HPLC grade heptane from Sigma Aldrich in a solvent purification system. Nitric acid, Ni and Zr ICP standards were purchased from Sigma

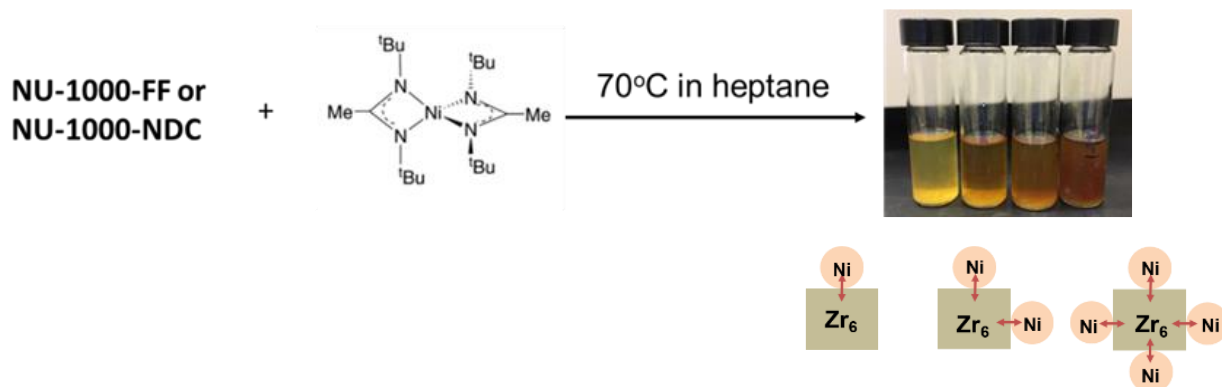
Aldrich. Ultrapure deionized water (18.2 MB•cm resistivity) was obtained from a Millipore Milli-Q-Biocel A10 instrument (Millipore Inc., Billerica, MA). Deuterium oxide, deuterated sulfuric acid, and deuterated dimethyl sulfoxide used for ^1H NMR characterization were purchased from Sigma Aldrich and used as received. Deuterated sodium hydroxide was purchased from Sigma Aldrich and diluted with deuterium oxide to 0.1 M for NMR sample digestion.

2.10.2 Synthesis

NU-1000, formate-free NU-1000 (NU-1000-FF). NU-1000 and NU-1000-FF were synthesized according to the published procedures.^{32, 124} Upon thermal activation, the crystallinity of the obtained materials was confirmed by N_2 isotherm measurements at 77 K and PXRD. NU-1000-NDC was synthesized according to Peters et al.¹²⁶ with minor modification. The mixture of NU-1000 and NDC in DMF was held at 65°C for 12 hours. In addition, the HCl wash at 90°C was replaced by repeated DMF wash at 65°C every 30 min until all excess NDC ligands were removed. The amount of formate and NDC ligands were monitored by integrating the corresponding peaks in the ^1H NMR spectra.

xNi (x= 0.044, 0.68, 0.86, 2.1, 3.6, 3.8) and 4.9Ni-NDC. Ni deposition was performed by adding NU-1000-FF to a heptane solution of $\text{Ni}(\text{amd})_2$. An overall synthesis scheme is displayed in Figure 2. The preparation of precursor solutions and the addition of NU-1000-FF and NU-1000-NDC were performed in an Ar-filled glovebox. The amounts of $\text{Ni}(\text{amd})_2$ added to 9.5 mL of heptane to achieve 0.5, 1, 2, 4, 6, 8 molar equivalence of 50 mg (0.021 mmol) FF-NU-1000 were 4.2 mg, 8.4 mg, 16.8 mg, 33.5 mg, 50.3 mg, and 67.2 mg, respectively. For 50 mg (0.021 mmol) NU-1000-NDC, 8 molar equivalence (67.2 mg) of $\text{Ni}(\text{amd})_2$ was used. The reaction mixtures were subsequently removed from the glovebox and transferred to a 70°C oven. After 16 hours,

the reaction mixtures were removed from the oven and allowed to cool to room temperature. The samples were then solvent exchanged with heptane five times over 24 hours. The catalysts were then dried in a vacuum oven at 70°C for one hour.



Scheme 2.1. Synthesis of Ni supported on NU-1000-FF and NU-1000-NDC.

2.10.3 Catalytic Testing Details

All reactivity studies were conducted using a packed bed reactor in the REACT core facility at Northwestern University. In a typical reaction, ~20 mg of catalyst was diluted with 1 g of silicon carbide (trace-metal grade) and packed in a quartz tube. The height of the bed was approximately 0.8 cm. The reaction temperature was controlled with a K-type thermocouple at the top of the catalyst bed. Pretreatments with 10% H₂/N₂ were carried out at 200°C for 12 h with a flow rate of 50 sccm, with a ramp rate of 10°C/min. Pressure in the reactor was monitored to be ~10 psig using a back-pressure regulator directly downstream from the reactor. To minimize the effect of the physisorbed water and residual and ligands, all catalysts were pre-treated in 50 sccm of 10% H₂ in N₂ at 200°C for 12 hours on stream prior to the introduction of reactant gases. After pretreatment, the temperatures were reduced to 50°C, and the reactant gases were then flowed over the sample. Reactant gases were 10% H₂/N₂ and 4% ethylene/N₂, and ethylene:H₂ was kept at 1:1. Products were analyzed via gas chromatography-flame ionization detection (GC-FID), and the gas mixture downstream were separated using a GS-Gaspro column (Agilent, 30m

length, 0.32 mm diameter). Reaction rate was calculated by multiplying the molar flow rate by the conversion under each reaction condition and then normalizing to the moles of Ni (mol ethane* mol^{-1} Ni).

2.10.4 Instrumentation

As-synthesized materials were first dried in a 70°C vacuum oven for one hour. The samples were then activated under high vacuum for 24 h using SmartVacPrep (Micromeritics, Norcross, GA) at 120 °C.

N₂ isotherms were measured afterwards using Micromeritics Tristar II 3020 at 77 K. Brunauer-Emmett-Teller (BET) surface area was determined at the range $P/P_0 = 0.005-0.1$ and pore size distribution was calculated via density function theory (DFT) calculations using a carbon slit-pore model with a N₂ kernel.

Inductively coupled plasma-optical emission spectroscopy (ICP-OES) was collected on Varian Vista-MDX model ICP-OES spectrometer (Varian, Walnut Creek, CA) with a CCD detector and Ar plasma that covers 175-785 nm range. MOF samples were prepared by dissolving 2-3 mg materials in 2 mL nitric acid in a 2-5 mL Biotage (Uppsala, Sweden) microwave vial. SPX microwave reactor (software version 2.3, build 6250) was used to heat the mixture at 150 °C for 15 min with stirring for complete digestion. 0.3 mL of the resulting mixtures were diluted to 10 mL with ultrapure deionized water and analyzed. For each sample, emissions at 231.604 and 221.647 nm for Ni, and 339.198, 343.823, and 327.305 nm for Zr, were compared to the standard solutions.

Powder X-ray diffraction (PXRD) patterns were recorded at room temperature on a STOESTADIMP powder diffractometer equipped with an asymmetric curved Germanium

monochromator (Cu K α 1 radiation, $\lambda = 1.54056 \text{ \AA}$) and one-dimensional silicon strip detector (MYTHEN2 1K from DECTRIS). The generator was set to be 40 kV and 40 mA. The activated powder was measured in transmission geometry in a rotating holder with the intensity data from 1 to 20°. The scan step was set to be $2\theta = 4^\circ/\text{min}$ with 0.05° step width.

X-ray photoelectron spectra (XPS) were measured at Keck-II/NUANCE facility at Northwestern University using a Thermo Scientific ESCALAB 250 Xi (Al K α radiation, 1486.6 eV). An equipped electron flood gun was utilized prior to any scans to minimize charging effect. Each spectrum was calibrated to C 1s peak at 284.8 eV.

X-ray absorption spectroscopy (XAS) measurements at the Ni K-edge (8777 eV) were performed on the insertion device beamline of DND-CAT (Sector 5-BMD), at the Advanced Photon Source (APS), Argonne National Laboratory. The beamline was detuned to 50% to minimize the presence of harmonics. Data were acquired in transmission in a step-scan mode in about 15 min using ionization chambers optimized for the maximum current with linear response (~ 1010 photons detected/sec) with 10% absorption in the incident ion chamber and 70% absorption in the transmission X-ray detector. A Ni foil spectrum was acquired simultaneously with each sample measurement for energy calibration. Samples were pressed into an aluminum plate holder with a thickness chosen to give an edge step of ~ 1.0 .

^1H nuclear magnetic resonance (NMR) spectra were collected on a Bruker S4 Avance III 500 MHz system equipped with DCH CryoProbe and automated with a BACS-60 autosampler. Chemical shifts for ^1H spectra were referenced using internal solvent resonances and reported relative to tetramethylsilane (TMS). For NDC quantification, ~ 2 mg of the sample was digested in 5 drops of D_2SO_4 followed by dilution in 0.6 mL d_6 -DMSO. The number of scans was set to

32. The peak at 8.53 ppm was integrated for NDC quantification. For formate quantification, 10 drops of 0.1 M NaOD/D₂O solution were added to ~2 mg of the sample, and the mixture was sonicated for 20 minutes. The mixture was then centrifuged, and the supernatant was further diluted with 0.5 mL of D₂O. The number of scans was set to 64. The peak at 8.38 ppm was integrated for formate quantification.

In-situ Diffuse Reflectance IR Fourier Transform Spectroscopy (DRIFTS) was performed at the Reactor Engineering and Catalyst Testing (REACT) core facility at Northwestern University. Approximately 10 mg of catalyst was diluted and ground with 100 mg of spectroscopic-grade KBr. The mixture was sealed into the praying mantis cell of a Thermo-iS50 infrared spectrometer. The sample was pretreated under an argon flow (100 sccm) at 200°C. A background spectrum was collected at this condition after one hour. The mixture was then cooled down to 150, 100, and 50°C. Background spectra were collected at each temperature point after one hour of stabilization. At 50°C, the mixture was exposed to 100 sccm 10% H₂/N₂, and difference spectra were recorded until there was no noticeable change from spectrum to spectrum. Then, the temperature was increased to 100, 150, and 200°C. 10 min of Ar purge was performed after each temperature ramp. At each temperature point, difference spectra were recorded until no noticeable change was observed.

Thermogravimetric Analysis (TGA) was performed on a TA Q500 TGA instrument in a 90 sccm 4% H₂/N₂ flow in high-res mode. The temperature was ramped from room temperature to 600°C at a ramp rate of 10°C/min.

2.10.5 Computational Details

Intermediates in the proposed reaction pathway were geometrically optimized in the electronic ground state using density functional theory (DFT) employing the M06-L functional¹²⁷ with the Gaussian 16 software package. Geometries were optimized using the def2-TZVP basis set^{128, 129} on the nickel and zirconium atoms, while the SDD pseudopotential¹³⁰ was applied on the zirconium atoms only. The def2-SVP basis set was assigned to the remaining C, H, and O atoms. Collectively, these basis sets are referred to as *bs1*.

With the same level of theory and basis set, the frequency analysis was performed. Since the quintet was assumed to be the ground state, open-shell DFT formalism was used. Harmonic vibrational frequencies were computed and confirmed to have no imaginary values. Grimme's entropy interpolation correction⁵⁴ was applied with the zero-point energy frequency correction factor of 0.97655 for low frequency vibration modes to achieve the correct molecular thermochemical parameters. Since electronic energy is sensitive to the basis set quality, def2-TZVPP basis sets were assigned on the nickel and zirconium atoms, while the SDD pseudopotential was applied on the zirconium atoms. The def2-TZVP basis set was assigned to the remaining C, H, and O atoms. Collectively, these basis sets are referred to as *bs2*. Final Gibbs free energy values of single species were obtained by adding electronic energies from the M06-L/*bs2* single point calculations and the corrected free energy correction under 473.15 K and 1.68 atm from M06-L/*bs1* frequency analyses. Reaction free energies were obtained from the difference of the summed free energies of the products and reactants. In searching and optimizing the transition state structures, the default Berny algorithm was applied with M06-L/*bs1*. After the procedure, a single imaginary frequency along the expected direction was

confirmed. Once a transition state was located, a single-point calculation was performed with M06-L/*bs2*.

Chapter 3. Probing Structure-Activity Relationships of NU-1000-Supported Ni-Thiophenolate Catalysts for Gas-Phase Reductions

3.1 Chapter Summary

Developing structural and functional models of enzymatic active sites has been a longstanding interest due to their high efficiency and selectivity. Herein, a series of tunable Ni-thiophenolate complexes were deposited onto a Zr-based metal-organic framework support, NU-1000, reminiscent of the active sites of the [NiFe] hydrogenases. We showed that different *para*-substituents on thiophenol can alter the electronic properties of Ni *via* Raman spectroscopy, X-ray absorption spectroscopy (XAS), and X-ray photoelectron spectroscopy (XPS). We subsequently showed that Ni-thiophenolate complexes with different substituents lead to varied rates and activation behaviors for ethylene hydrogenation. This study demonstrated that molecular catalysts with tunable ligand environment can be constructed in NU-1000 and further proved the potential of exploiting knowledge of enzymatic active sites for gas-phase catalysis.

3.2 Ni-Based Chalcogenides in Hydrogenases

Ni-containing chalcogenides, found in bacterial hydrogenases, are responsible for reversible proton reduction.^{131, 132} As many reversible proton reductions currently still rely on noble metals, such as Pt, as catalysts, chalcogenide-based catalysts using earth-abundant metals are of major environmental and potential industrial considerations for developing a clean and sustainable hydrogen economy.¹³³ To date, the most studied hydrogenase was found in *desulfovibrio gigas*, an enzyme that efficiently splits H₂ [turnover frequency (TOF): 1000 molecule H₂ s⁻¹ per site] and converts carbon dioxide to methane.¹³⁴ The active sites have been elucidated *via* single-crystal X-ray diffraction to be [NiFe] clusters coordinated to the thiol groups of the cysteines. Mechanistic

studies show that Ni is primarily responsible for the redox activities during hydrogen splitting and substrate binding, while Fe carries out electron transfer within the enzyme.¹³² Therefore, Ni coordination complexes constructed from sulfur-based ligands can be adopted as potential catalysts for hydrogenations at high efficiency.

The [NiFe] active site is buried 30 Å deep within the enzyme scaffold [**Figure 3.1(a)**]. The cysteines, cyanide, and carbonyl ligands isolate the active sites in a solvent-free environment within the enzyme [**Figure 3.1(b)**]. Hydrophobic channels were found to transport the gaseous species from one active site to another to keep the active sites from contact with water and oxygen. The oxygen- and water-sensitive nature of the [NiFe] clusters limits its use in condensed-phase systems but renders the structure relevant for gas-phase catalysis.^{132, 135} Since the [NiFe] cluster operates optimally in the absence of solvent, adopting structural mimics for gas-phase reductions can be a promising route for replacing noble-metal-based solid catalysts.

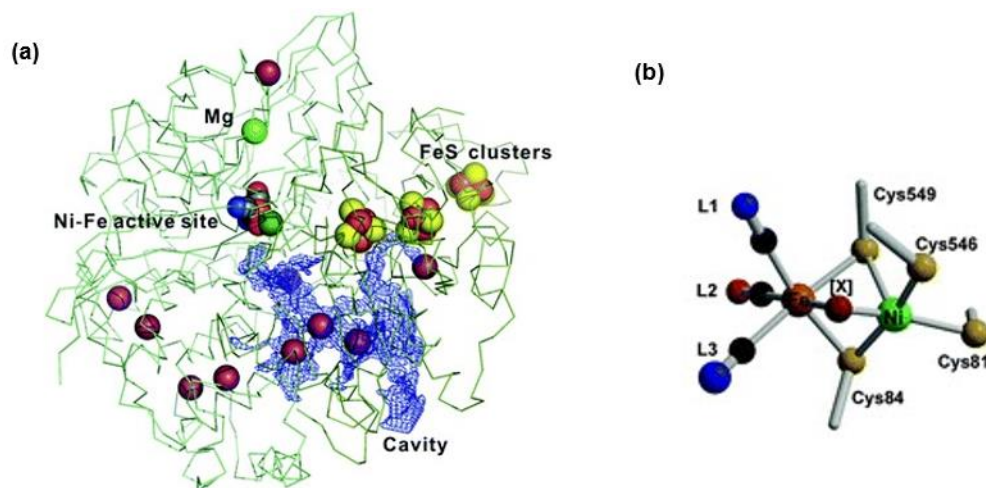


Figure 3.1. (a) Simplified [NiFe] hydrogenase structure showing location of the metal species and the hydrophobic channels (blue cavities). The purple sphere represents Xe atoms used to probe the hydrophobic channel structures. (b) Active site structure of [NiFe] hydrogenase. The blue, red, black, and yellow spheres represent N, O, C, S, respectively. Figures adapted with permission from ref. 135. Copyright 2003 Royal Chemical Society.

3.3 Constructing Biomimetic Hydrogenase Active Sites on Metal-Organic Framework

While enzyme encapsulation is optimal for stabilizing the active site structure, the enzymes must be preserved under physiological conditions (20-40°C, 1 atm, pH 6-8), which makes the encapsulation method incompatible with gas-phase reactions that typically require substantially higher temperatures and pressures. Therefore, to replicate and stabilize biomimetic hydrogenase active sites in a non-biological system that can tolerate harsher conditions, metal-organic frameworks (MOFs) are chosen as solid support for Ni-chalcogenide catalysts. MOFs are constructed from well-separated periodic metal oxide clusters (nodes) and carboxylate- or amine-based organic moieties (linkers).³² MOFs are ideal for supporting well-dispersed and structurally well-defined solid catalysts because compared to amorphous solid supports such as metal oxides and silica, the periodic arrangement of nodes and linkers endow MOFs with well-defined structures, which can significantly reduce the structural heterogeneity of the catalysts.¹³⁶⁻¹³⁸

Moreover, due to the high porosity and surface area of MOFs, catalytic active sites can be deposited in a well-dispersed fashion and are less likely to aggregate under reaction conditions. MOFs are also highly tunable and therefore amenable to various post-synthetic modification techniques while allowing for catalyst installation through grafting on the nodes or linkers or by being entrapped within the pores.¹³⁶ For MOF-node-supported catalysts, reactive hydroxyl and aqua groups, generated from defects or by reducing the connectivity of the nodes, serve as anchoring sites for metal ion deposition. Since the location of defect sites is unpredictable, reducing node connectivity is preferred to maximize the catalyst loading while ensuring the uniformity of deposition.

3.4 Studying NU-1000-Supported Ni-Thiophenolate Bearing Various Functional Groups

Taking inspiration from enzymatic metal chalcogenides, this study aims to explore heterogeneous, well-defined, MOF-based Ni-chalcogenide catalysts for gas-phase hydrogen activation reactions. Consisting of 8-coordinated oxo-Zr₆ clusters and 1,3,6,8-tetrakis(*p*-benzoate) pyrene (TBAPy) linkers, NU-1000 is chosen as the MOF support, as it presents well-separated, unsaturated oxo-Zr₆ nodes as catalyst grafting sites for Ni-thiophenolate complexes *via* post-synthetic modifications.^{32, 139, 140} The structure and electronics of NU-1000-supported Ni-thiophenolate complexes can be modulated by the electron-withdrawing/donating nature of the substituents at the *para* position of the thiophenol ligands. In these well-defined systems, structure-reactivity relationships can be constructed, from which we can extract design rules for synthesizing next-generation heterogeneous catalysts with higher efficiency and selectivity.

Structural investigation in this work involves probing the coordination environment of Ni, as well as the extent to which the electron-withdrawing/donating nature of the substituents on thiophenol affects the electronic properties of Ni and S. Further, the structure-function relationship of the catalysts is established by probing the gas-phase reactivity of NU-1000-supported Ni-thiophenolate complexes. Ethylene hydrogenation is chosen as a simple model hydrogenation reaction, where ethylene conversion at various temperatures is used to evaluate the reactivity of the complexes. Relating the reactivity of the complexes to the aforementioned structural investigations will provide further insights into improving ligand design and how different aspects of reaction (conversion, selectivity, etc.) are tuned by adjusting the complex and/or the MOF structures.

3.5 Physical Characterizations

The powder X-ray diffraction (PXRD) patterns of as-synthesized NU-1000, Ni-SIM, and thiophenolate-modified materials in the low-angle region [1-15°, **Figure 3.2(a)**] showed the bulk crystallinity of the MOF samples was retained after post-synthetic modifications. Here, Ni-SIM refers to NU-1000 modified with bis(N,N'-di-t-butylacetamidinato)nickel(II), and Ni-R refers to Ni-thiophenolate complexes bearing various functional groups grafted on NU-1000. For Ni-NO₂, peaks at 5° and 7.5° were broadened, and the peak at 1° and 5° both shifted to lower angles. Both suggest that the crystallinity of Ni-NO₂ was partially lost during the modifications.

Decreases in Brunauer-Emmett-Teller (BET) surface area were observed from the N₂ adsorption isotherms [**Figure 3.2(b)** and **Table 3.1**]. DFT calculated pore size distributions [**Figure 3.2(c)**] show the mesopore width and volume decreased after incorporating Ni and thiophenols into NU-1000. Both are evident for pore occupation by Ni and thiophenols.

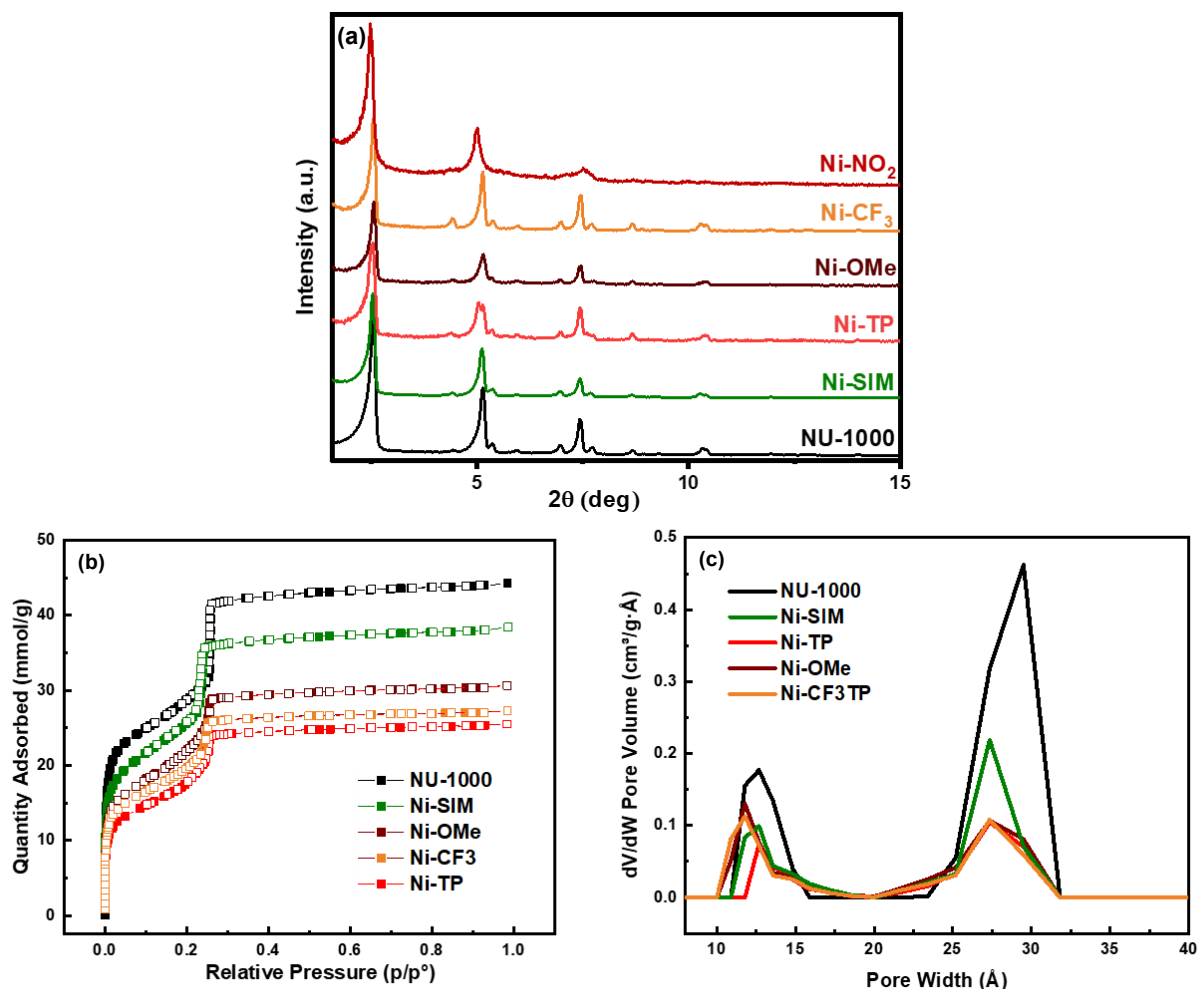


Figure 3.2. (a) Powder X-ray diffraction (PXRD) patterns, (b) N₂ isotherms, and (c) DFT-calculated pore-size distributions of NU-1000, Ni-SiM, Ni-TP, Ni-OMe, and Ni-CF₃.

Inductively coupled plasma optical emission spectrometry (ICP-OES) measurements further confirm the incorporation of Ni-thiophenolates. An average of 2.8 Ni per Zr₆ node were incorporated, and the amount of S varied for different substituents, ranging from 1.6-4.4 S per Zr₆ node (**Table 3.1**). The S/Ni ratios are less than 1 for all samples except for Ni-CF₃, where the ratio approaches 2, suggesting more than one CF₃-substituted thiophenol coordinating to Ni.

Table 3.1. BET surface areas and ICP-OES measurement results normalized to the number of Zr₆ nodes for all Ni-containing samples.

Sample ID	BET Surface Area (m ² /cm ³)	Ni per node	S per node	S/Ni
Ni-SIM	1801	2.8 ± 0.4	N/A	N/A
Ni-OMe	1501	4.1	1.6	0.39
Ni-TP	1229	4.4	3.2	0.72
Ni-CF ₃	1384	2.4	4.4	1.8
Ni-NH ₂	N/A	2.9	2.3	0.79
Ni-NO ₂	N/A	2.9	0.4	0.14

3.6 Spectroscopic Studies

X-ray photoelectron spectroscopy (XPS) was implemented to probe the electronic changes in Ni through binding energy, with the correlation between the binding energies (BEs) and the electronic properties of the substituents quantitatively assessed by Hammett parameters. **Figure 3.3(a)-(f)** display the Ni XPS for all Ni-containing NU-1000 samples. In general, the 2p 3/2 region can be deconvoluted to four peaks. Taking the 2p 3/2 transitions of Ni in Ni-SIM as an example, the peaks at 855.07 eV and 857.12 eV are assigned to Ni²⁺ and multiplet splitting, respectively, and the two peaks at 860.38 and 863.92 eV are assigned to satellite peaks.¹⁴¹⁻¹⁴³ The observed Ni²⁺ binding energies are higher than bulk Ni²⁺ materials due to the strong metal-support interaction between Ni and Zr₆ nodes.¹⁴⁴ The four peaks were observed in all samples, where the peaks generally shift to lower BE in thiophenolate-modified samples.

The S XPS for all thiophenolate samples are shown in **Figure 3.4(a)-(e)**. The Ni-TP, Ni-OMe, Ni-CF₃, and Ni-NH₂ spectra were deconvoluted into two peaks, corresponding to S 2p_{3/2} and S 2p_{1/2} of the thiophenolates.¹⁴⁵ No sulfur oxidation was observed except for Ni-NO₂, where an additional doublet at 167.9 and 168.1 eV appears. This set of doublet is assigned to phenyl

sulfate species. The BEs of the 2p_{3/2} peaks for both Ni and S are shown in **Table 3.2**. Those peak values are used for evaluating the electronic effects of the substituents.

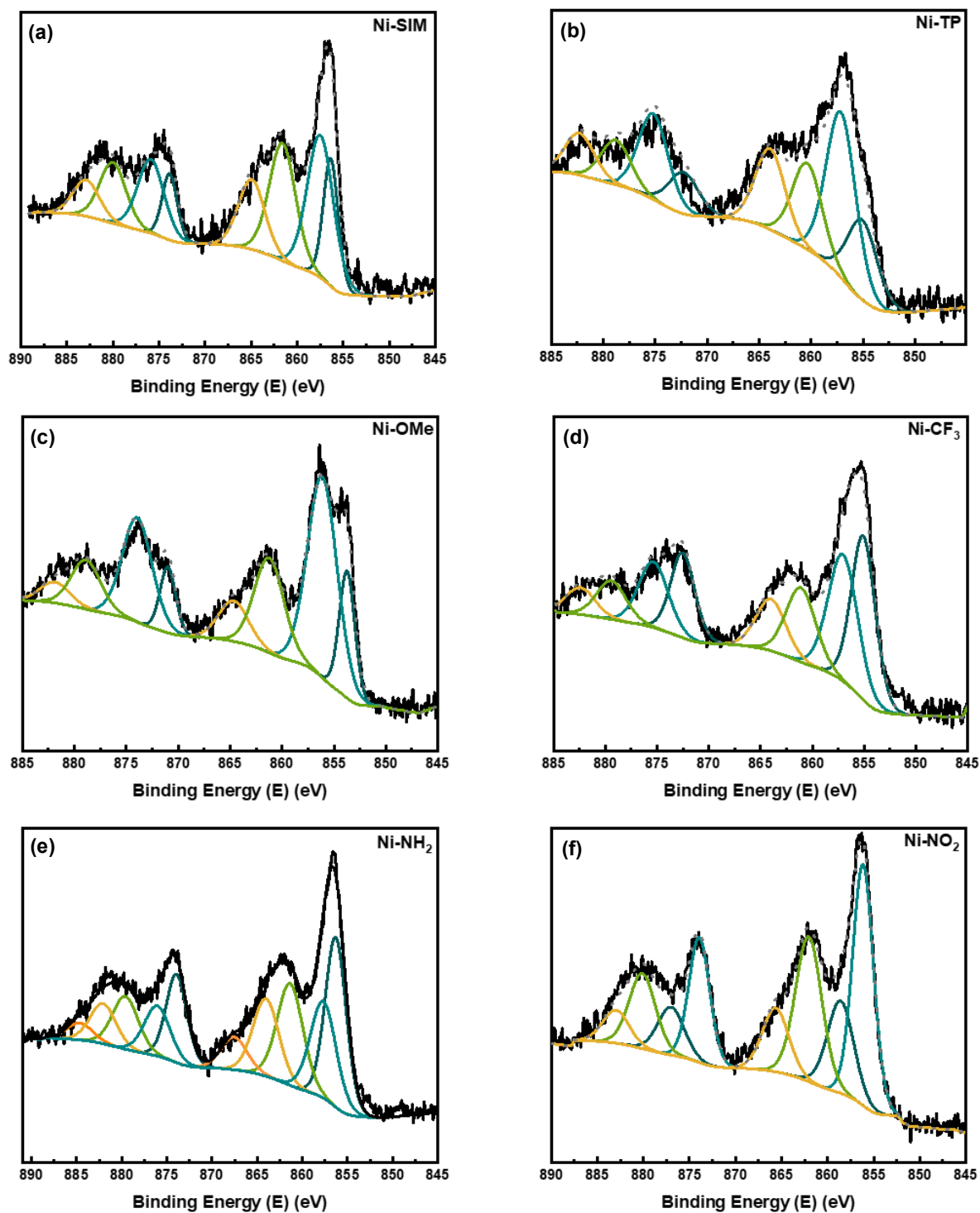


Figure 3.3. Ni XPS spectra for (a) Ni-SIM, (b) Ni-TP, (c) Ni-OMe, (d) Ni-CF₃, (e) Ni-NH₂ and (f) Ni-NO₂.

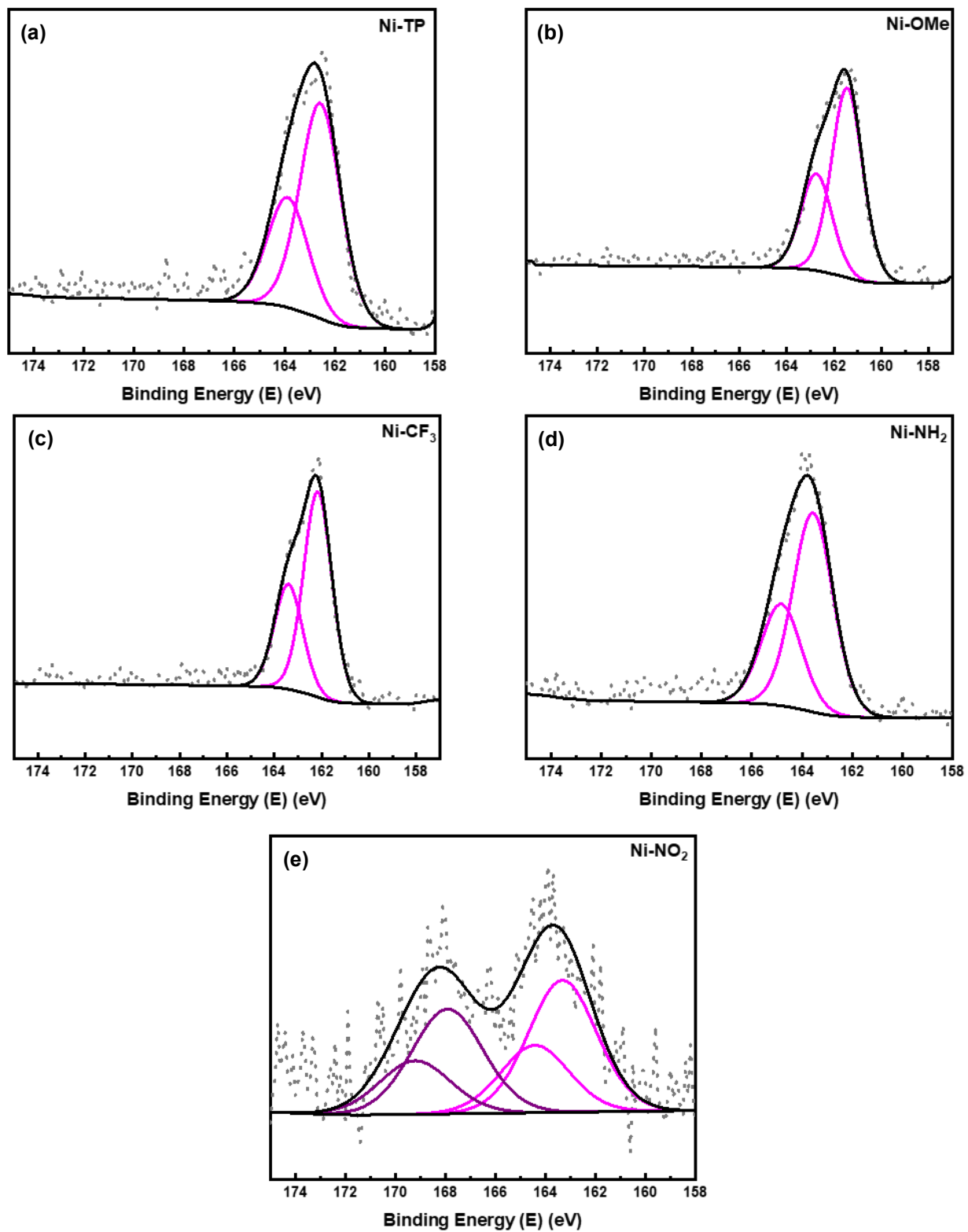
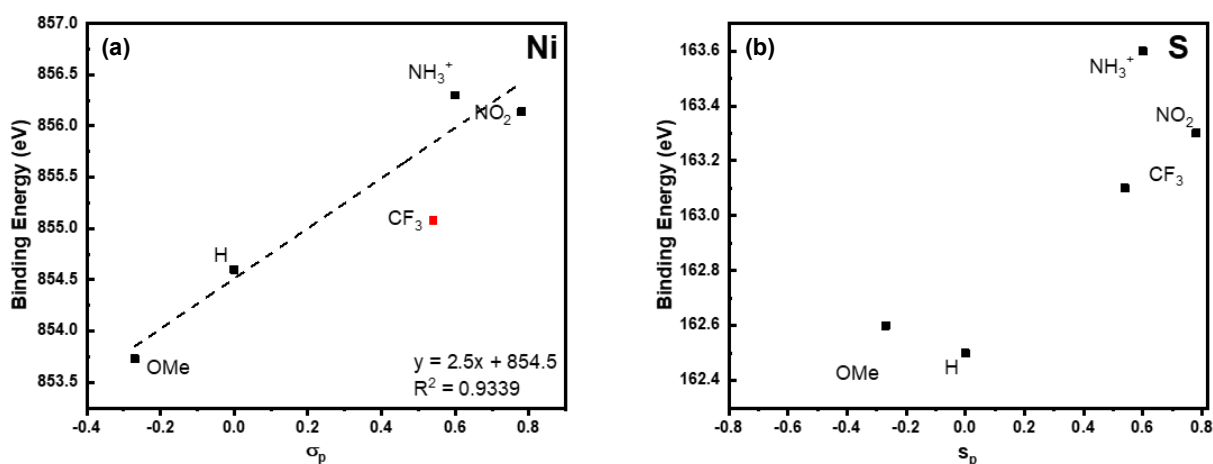


Figure 3.4. S XPS spectra for (a) Ni-TP, (b) Ni-OMe, (c) Ni-CF₃, (d) Ni-NH₂ and (e) Ni-NO₂.

Table 3.2. Binding energies of Ni and S for all samples.

Sample ID	Ni 2p3 BE (eV)	S 2p3 BE (eV)
Ni-SIM	856.3	N/A
Ni-OMe	853.7	162.6
Ni-TP	854.6	162.5
Ni-CF ₃	855.1	163.1
Ni-NH ₂	856.3	163.6
Ni-NO ₂	856.1	163.3, 167.9

Plotting the BEs of Ni against the Hammett constant σ_p , a positive correlation was observed from the best-fit analysis [Figure 3.5(a)]. This correlation shows that the more electron-donating substituent increases the electron density on Ni. Note that Ni-CF₃ was excluded from the analysis (highlighted in red) due to its higher S loading, which would reduce Ni to a greater degree, thus obscuring the substituent effect. Also noted that Ni-NH₂ adopted the σ_p of NH₃⁺, as the observed high Ni BE in Ni-NH₂ suggests that the substituent is electron-withdrawing. A similar plot was also constructed with the BEs of S. Although no clear trend can be discerned, a similar electronic effect on S can be observed, where the S BEs of Ni-thiophenolates containing electron-donating substituents are generally lower than those containing electron-withdrawing substituents.

**Figure 3.5.** The Hammett plots constructed with the binding energies of (a) Ni and (b) S.

To further investigate the local coordination environment of Ni, the Ni K-edge X-ray absorption spectra (XAS) were collected. **Figure 3.6(a)** displays the X-ray absorption near-edge structure (XANES) of Ni-SIM, Ni-CF₃, Ni-TP, and Ni-OMe. Qualitatively, the white line intensity decreases upon incorporating the thiophenols, and similar intensities were observed for Ni-TP and Ni-OMe. The white line refers to the sharp feature at the top of the edge (*ca.* 8350 eV) due to the strong x-ray absorption, and its intensity increases as the element becomes more oxidized.¹⁴⁶ Thus, the reduced white line intensities confirm the binding of the substituted thiophenols to Ni. The significantly lowered white line intensity for Ni-CF₃ is likely due to the higher S-content that reduces Ni to a higher degree than the other two complexes.¹⁴⁷

The energies at $\mu(E) = 0.5$ were taken as the edge energies (E_0) for comparison purposes (**Table 3.4**). Corresponding to the observations from the white line intensities, the E_0 decreases upon R-thiophenol deposition, where the E_0 of Ni-CF₃ is lower than those of Ni-TP and Ni-OMe. One possible explanation of the lowered E_0 from Ni-SIM to Ni-R is the increased metal-ligand covalency from the binding of S to Ni, and the more significant decrease of E_0 from Ni-TP and Ni-OMe to Ni-CF₃ suggests stronger ligand-to-metal charge transfer in Ni-CF₃.¹⁴⁸

The pre-edge features [**Figure 3.6(b)**] shed light on the coordination geometry of Ni. Ni-SIM possesses a low-intensity pre-edge feature at 8332 eV, whereas more profound pre-edge features at higher energy (8335 eV) are observed for the thiophenolate-containing samples. The pre-edge feature for Ni-SIM agrees with those observed for octahedrally-coordinated Ni complexes. In contrast, the pre-edge features of the thiophenolate-containing samples arise from Ni 3d-4d orbital mixing, which is largely promoted by tetrahedrally-coordinated Ni.¹⁴⁷⁻¹⁵⁰ The positions of the pre-edge are roughly the same for all thiophenolate complexes. Yet, the feature

is more intense for Ni-CF₃. This is likely due to the higher S content in the sample increasing the ligand field felt by the Ni center.

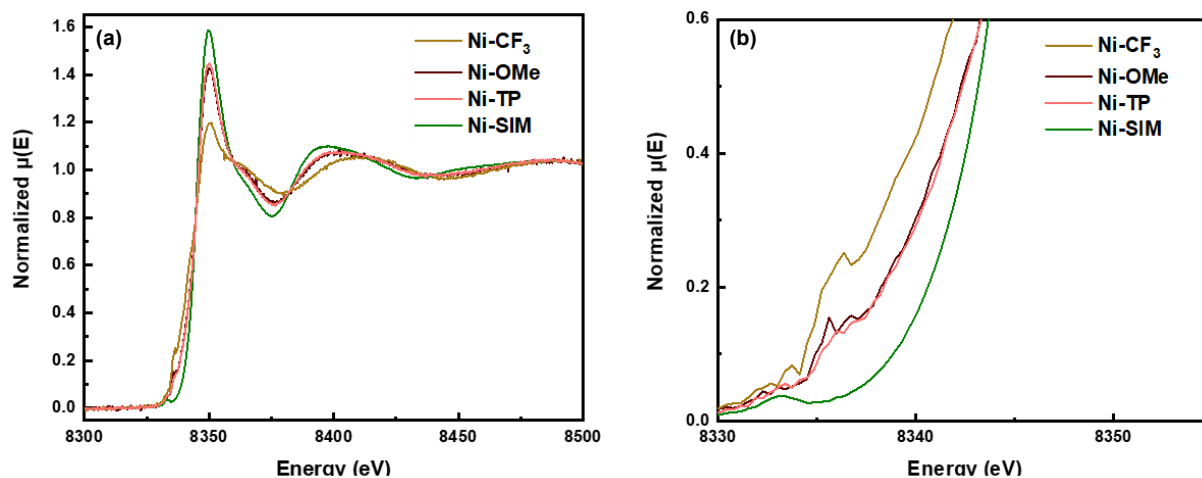


Figure 3.6. (a) Normalized Ni K-edge XANES spectra of Ni-SIM, Ni-TP, Ni-OMe, and Ni-CF₃. (b) Zoomed-in pre-edge region of the XANES spectra displaying the pre-edge features.

Table 3.3. Ni K-edge energies (E_0) of Ni-SIM, Ni-TP, Ni-OMe, and Ni-CF₃.

Sample	E_0 (eV)
Ni-SIM	8345.1
Ni-TP	8342.3
Ni-OMe	8342.3
Ni-CF ₃	8340.8

Raman spectra further confirm the tetrahedral coordination around Ni, as two distinct vibrations were observed in the 100-400 cm⁻¹ region for the thiophenolate-containing samples [Figure 3.7(a)]. One vibration found in the range of 170-230 cm⁻¹ is assigned to the $\nu(A_1)$ mode of tetrahedrally-coordinated Ni [Figure 3.7(b)], where the ligands surrounding Ni stretch out in all directions. The wavenumbers are roughly similar for Ni-TP (195 cm⁻¹) and Ni-NH₂ (198 cm⁻¹), yet blue-shifts significantly for Ni-CF₃ (212 cm⁻¹). This is likely because more charge is transferred from S to Ni as Ni coordinates to more than one CF₃-substituted thiophenol. The second feature is located at ~265 cm⁻¹ and is assigned to the $\nu(T_2)$ vibrational mode [Figure 3.7(c)]. Compared to the reference values observed for bulk Ni tetra-thiophenolate complexes,¹⁵¹

the wavenumbers that correspond to both vibrational modes for NU-1000-supported Ni-TP are systematically blue-shifted by 17 cm^{-1} . This blue shift can be rationalized by the bond-strengthening effect from the strong metal-support interaction between the acidic Zr_6 -nodes and the supported complexes.¹⁵² The peak position for the $\nu(\text{T}_2)$ mode is constant for all complexes, suggesting substituent has minimal effect on this mode.

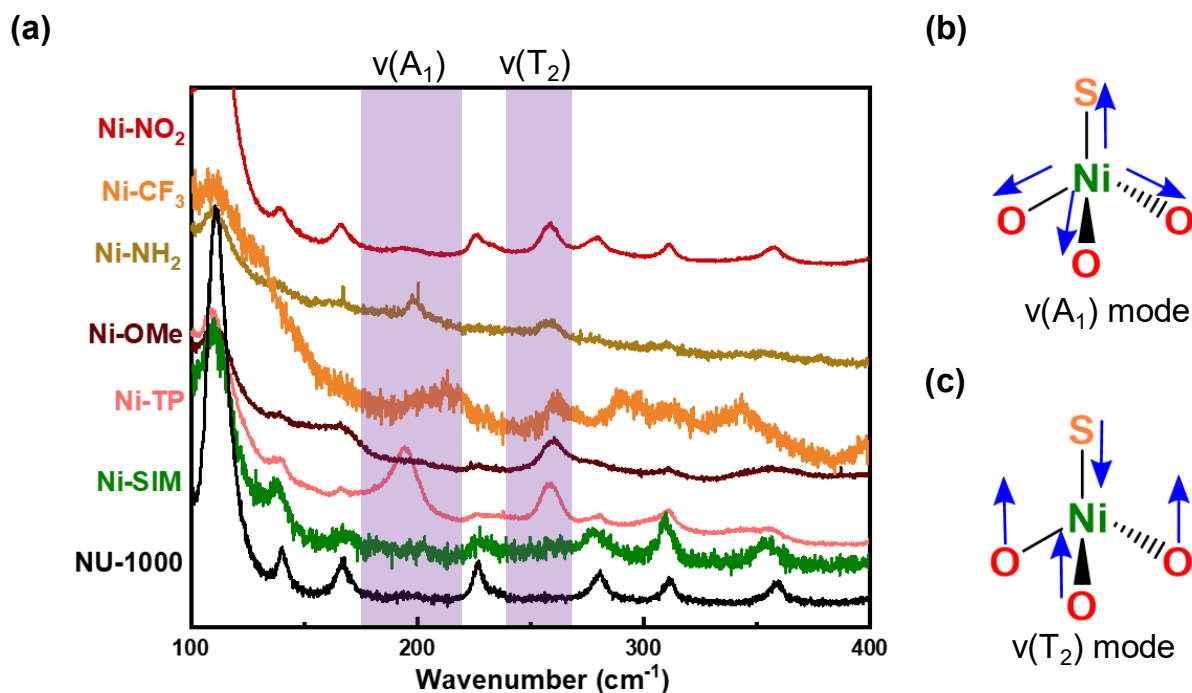


Figure 3.7. (a) Zoomed-in Raman spectra in the 100~400 cm^{-1} region. The dash lines highlight the characteristic features observed for thiophenolate-containing samples. (b)-(c) Tetrahedral $\nu(\text{A}_1)$ and $\nu(\text{T}_2)$ vibrational modes.

Both XAS and Raman spectroscopies reveal the coordination of Ni on NU-1000-supported Ni-thiophenolates complexes to be tetrahedral. Two possible structures are subsequently proposed in **Figure 3.8**. For Ni-TP, Ni-OMe, and Ni-NH₂, where the S/Ni ratio is roughly 1:1, Ni coordinates to a pair of -OH/H₂O sites on one side of the Zr_6 node while also binding to a $\mu_3\text{-O}$ and one thiophenolate ligand [**Figure 3.8(a)**]. For Ni-CF₃, where the S/Ni is 2:1, instead of coordinating to the $\mu_3\text{-O}$ on the node, Ni binds to two thiophenolates in a staggered fashion [**Figure 3.8(b)**].

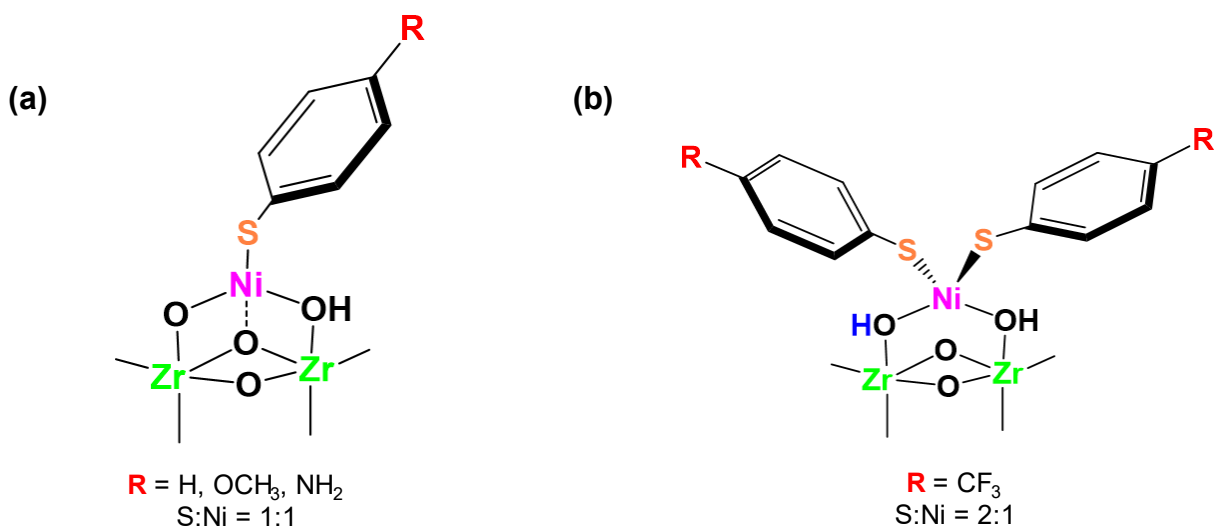


Figure 3.8. (a) Proposed Ni-thiophenolate structure with one thiophenol binding. (b) Proposed Ni-thiophenolate structure with two thiophenols binding. The proton shown in blue originates from a thiophenol ligand.

3.7 Catalytic Testing

With proposed catalyst structures supported by spectroscopic evidence, ethylene hydrogenation was then used to probe the reactivities of Ni-thiophenolates on NU-1000. Ni-TP showed initial reactivity starting from 50°C at 0.6% ethylene conversion [Figure 3.9(a)] and reached the highest reactivity among all three complexes starting from 200°C [Figure 3.9(b)]. The sudden increase in conversion suggests the catalyst undergoes reconstruction into a more active form. No reactivity was observed for Ni-OMe until the temperature reached 150°C, where the ethylene conversion was 0.1% [Figure 3.9(a)], with peak conversion observed at 200°C. The conversion gradually declined during the time on stream, and deactivation was accelerated when the temperature increased to 250°C [Figure 3.9(b)]. No reactivity was observed for Ni-CF₃ at any given temperature, possibly due to the steric hindrance created by Ni coordinating to two thiophenol ligands.

The sudden increase in reactivity for Ni-TP and Ni-OMe at 200°C suggests that the complexes undergo structural changes that activate the catalyst. One possibility is the detachment of thiophenol ligands that increase the number of undercoordinated sites on Ni, enhancing the reactivity. Another possibility is the aggregation of Ni ions into highly reactive species, such as multi-nuclear Ni²⁺ species (see [Chapter 2](#)).^{153, 154}

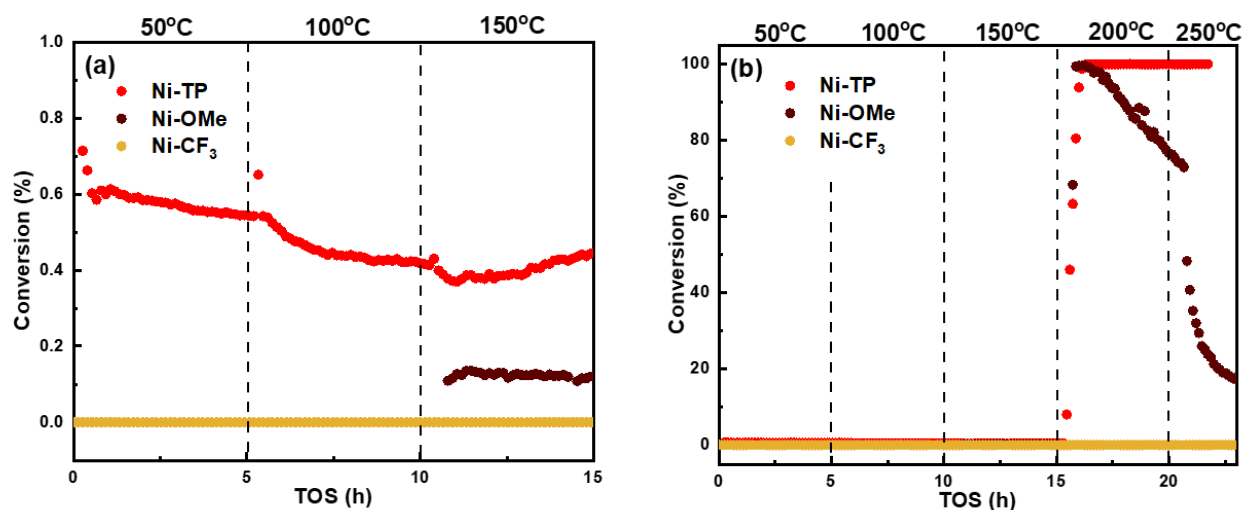


Figure 3.9. Ethylene conversion in 10:1 H₂/ethylene at (a) 50-150°C and (b) 50-250°C for Ni-TP, Ni-OMe, and Ni-CF₃.

3.8 Chapter Conclusions

A series of Ni-thiophenolate complexes with substituents of a range of electron-donating and electron-withdrawing nature were grafted onto the Zr₆ nodes of MOF NU-1000.

Spectroscopic investigations *via* Raman spectroscopy and XANES confirmed the formation of Ni-thiophenolate complexes and the Ni coordination to be tetrahedral. Based on the catalyst loading determined by ICP, two possible Ni-thiophenolate complexes were proposed, accounting for one and two thiophenol ligand incorporations. The binding energies of Ni and S determined by XPS were used to access the electron densities of the two elements in the complexes. A correlation was observed between the Ni binding energies and the Hammett constants of the

substituents. Lower reactivity for ethylene hydrogenation was observed for the Ni-thiophenolate complex with more electron-donating substituents, and no reactivity was observed when two thiophenol ligands coordinated to Ni.

Given the two possibilities proposed for the observed catalytic activities, as a future study, it is worth probing the structural evolution of the catalyst at different temperatures *via in-situ* XAS. More specifically, fitting the extended X-ray absorption fine structure (EXAFS) of the Ni-thiophenolate modified NU-1000 samples with those of Ni₃S₂ and Ni(OH)₂ standards can be particularly informative on the contributions from Ni-O and Ni-S coordinations. If thiophenol detachment occurs at a specific temperature, a decrease in Ni-S contribution would be expected. The formation of multi-nuclear Ni²⁺ species may also be observed as an increase in Ni-O-Ni contribution in EXAFS fitting results.

3.9 Additional Information

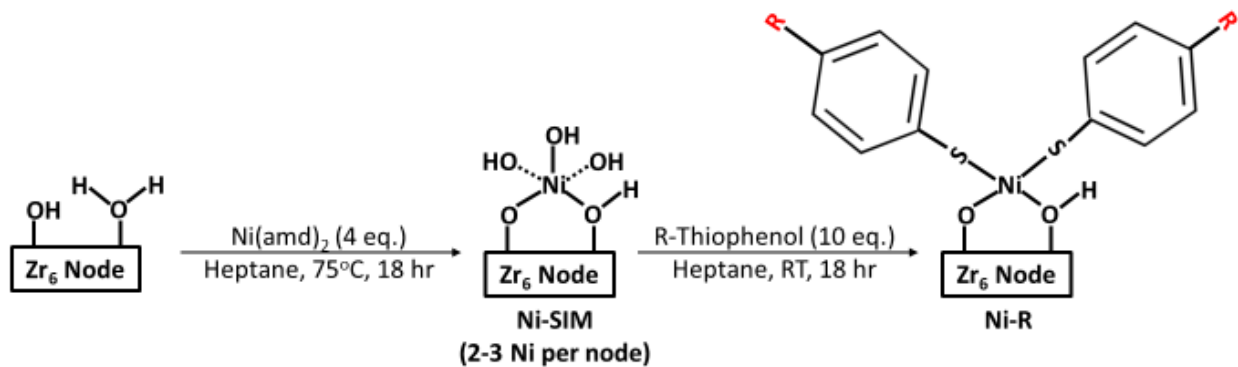
3.9.1 Materials

All chemicals for the NU-1000 synthesis were purchased from Sigma Aldrich Chemical Company, Inc. (Milwaukee, WI) and were used without further purification. R-thiophenols were also obtained from Sigma Aldrich and were used as received. NU-1000 linker, H₄TBAPy [1,3,6,8-(p-benzoate)pyrene], was synthesized according to a published procedure, and the purity was confirmed via ¹H NMR.¹⁵⁵ Bis(N,N''-di-t-butylacetamidinato)nickel(II) [Ni(amd)₂] used for Ni deposition was obtained from Strem Chemicals (Newbury Port, MA). Anhydrous heptane was purchased from Sigma Aldrich. Nitric acid, Ni, S, and Zr ICP standards were obtained from Sigma Aldrich. Ultrapure deionized water (18.2 MB•cm resistivity) was obtained from a Millipore Milli-Q-Biocel A10 instrument (Millipore Inc., Billerica, MA).

3.9.2 Synthesis

NU-1000 and Ni-SIM A 2 g batch of NU-1000 was synthesized and activated according to the published procedure.³² In an Ar-filled glovebox, Bis(N,N'-di-*t*-butylacetamidinato)nickel(II) (72 mg, 0.18 mmol) was dissolved in 20 mL anhydrous heptane in an 8-dram vial and activated NU-1000 (100 mg, 0.045 mmol) was added to the solution. The vial was then brought out of the glovebox and heated at 75°C in the oven for 18 hours. The resulting material, Ni-SIM, was washed with 20 mL heptane four times over the course of 8 hours before drying in a vacuum oven at 70°C overnight.

Ni-R (R = H, OCH₃, CF₃, NH₂, NO₂) 10 molar equivalence of 4-R-thiophenol (R = H, OCH₃, CF₃, NH₂), except for nitrothiophenol (R = NO₂), was dissolved in anhydrous heptane to make a 3 mM solution in an N₂ purged Biotage microwave vial. Due to the low solubility of 4-nitrothiophenol in heptane, the same synthetic procedure was carried out in anhydrous acetonitrile. The solution was then transferred to another N₂ purged microwave vial containing 50 mg Ni-SIM. Upon the addition of non-nitrogen-containing R-thiophenols, namely when the R group was H, OCH₃ and CF₃, the solution immediately turned dark red. For 4-nitrothiophenol and 4-aminothiophenol, the color of the solution remained yellow, which is the same color as NU-1000. The mixture was stirred at room temperature overnight. The resulting material, Ni-R, was washed with anhydrous heptane or acetonitrile five times, dried at 98°C for 24 hours under N₂ purge, and stored in the glovebox.



Scheme 3.1. Synthesis of Ni-SIM and Ni-thiophenolate.

3.9.3 Catalytic Testing Details

Ethylene hydrogenation was carried out using a packed bed reactor in the REACT core facility at Northwestern University. 20 mg of sample was mixed with 1 g of metal-trace-grade silica and packed in a quartz tube. The sample was first pretreated in 100 sccm of 10% H_2 balanced in N_2 for 2 hours. Then, 10:1 H_2 : C_2H_4 at a total flow rate of 100 sccm was introduced at 50, 100, 150, 200, and 250°C. The sample mixture was held at each temperature point for 5 hours except at 250°C, for which the temperature was held for 1 hour. A gas chromatography-flame ionization detection (GC-FID) was installed downstream to monitor product formation. The gas mixture downstream was separated using a GS-Gaspro column (Agilent, 30m length, 0.32 mm diameter). The catalytic conversion was calculated by dividing the GC area of the ethane peak by the total GC area of the ethane and ethylene peaks.

3.9.4 Instrumentation

Room-temperature powdered X-ray diffraction (PXRD) patterns were collected on a STOESTADIMP powder diffractometer equipped with an asymmetric curved Germanium monochromator (Cu $\text{K}\alpha 1$ radiation, $\lambda = 1.54056 \text{ \AA}$) and one-dimensional silicon strip detector (MYTHEN2 1K from DECTRIS). The generator was set to be 40 kV and 40 mA. The sample

measurements were carried out in transmission geometry in a rotating holder. The intensity data from 1 to 20° was recorded. The scan step was set to be $2\theta = 4^\circ/\text{min}$ with 0.05° step width.

As-synthesized materials were thermally activated for 16 hours under high vacuum at 80°C with SmartVacPrep (Micromeritics, Norcross, GA). Nitrogen isotherms at 77K were collected on Micromeritics Tristar II 3020. The materials' Brunauer-Emmett-Teller (BET) surface areas were determined at the range $P/P_0 = 0.005-0.1$. Pore size distribution was calculated based on density functional theory (DFT) calculations with a carbon slit-pore model with an N₂ kernel.

Inductively coupled plasma-optical emission spectroscopy (ICP-OES) was conducted on Varian Vista-MDX model ICP-OES spectrometer (Varian, Walnut Creek, CA) equipped with a CCD detector and Ar plasma in the 175-785 nm range. Samples for measurements were prepared by weighing and dissolving 2-3 mg materials in 2 mL metal trace grade nitric acid in a 2-5 mL Biotage (Uppsala, Sweden) microwave vial containing a magnetic stir bar. The sample vial was then transferred to the autosampler of the Biotage SPX microwave reactor (software version 2.3, build 6250). The mixture was microwaved at 150 °C for 15 minutes. 0.3 mL of the digested sample solution was diluted to 10 mL with millipore water for ICP-OES analysis. For each sample, emissions at 231.604 and 221.647 nm for Ni; 180.731, 182.034, and 182.624 nm for S; and 339.198, 343.823, and 327.305 nm for Zr, were compared to the standard solutions.

X-ray photoelectron spectra (XPS) were measured a Thermo Scientific ESCALAB 250 Xi using Al K α radiation (1486.6 eV) at Keck-II/NUANCE facility at Northwestern University. An electron flood gun equipped on the instrument was used during the measurements to minimize charging effect. All spectra were calibrated to C 1s peak at 284.8 eV for further processing and analyses.

Raman spectra in the 100–1300 cm^{-1} region was collected using a Horiba LabRAM HR Evolution Raman spectrometer system at SPID/NUANCE facility at Northwestern University. Sample powders were spread onto a glass slide and excited with a 633 nm Ar^+ laser at 5 mW power. A confocal microscope equipped with a long working distance objective lens of 100x magnification. The grating was set to 1800 grooves/mm, and each spectrum consists of 5 scans with a total exposure time of 30 s per scan.

X-ray absorption spectroscopy (XAS) measurements at the Ni K-edge (8777 eV) were performed on the insertion device beamline of DND-CAT (Sector 5-BMD), at Argonne National Laboratory's Advanced Photon Source (APS). To reduce the interference from harmonics, the X-ray beam was detuned to 50%. Sample powders were pressed into an aluminum plate holder. The thickness of the sample was determined so that the edge step would be ~ 1.0 . Ionization chambers were adjusted for maximal current with linear response (~ 101 photons detected/sec), 10% absorption in the incident ion chamber, and 70% absorption in the detector. Transmission spectra were collected in step-scan mode in about 15 min per scan. For each spectrum, a reference spectrum was collected with Ni foil simultaneously for energy calibration.

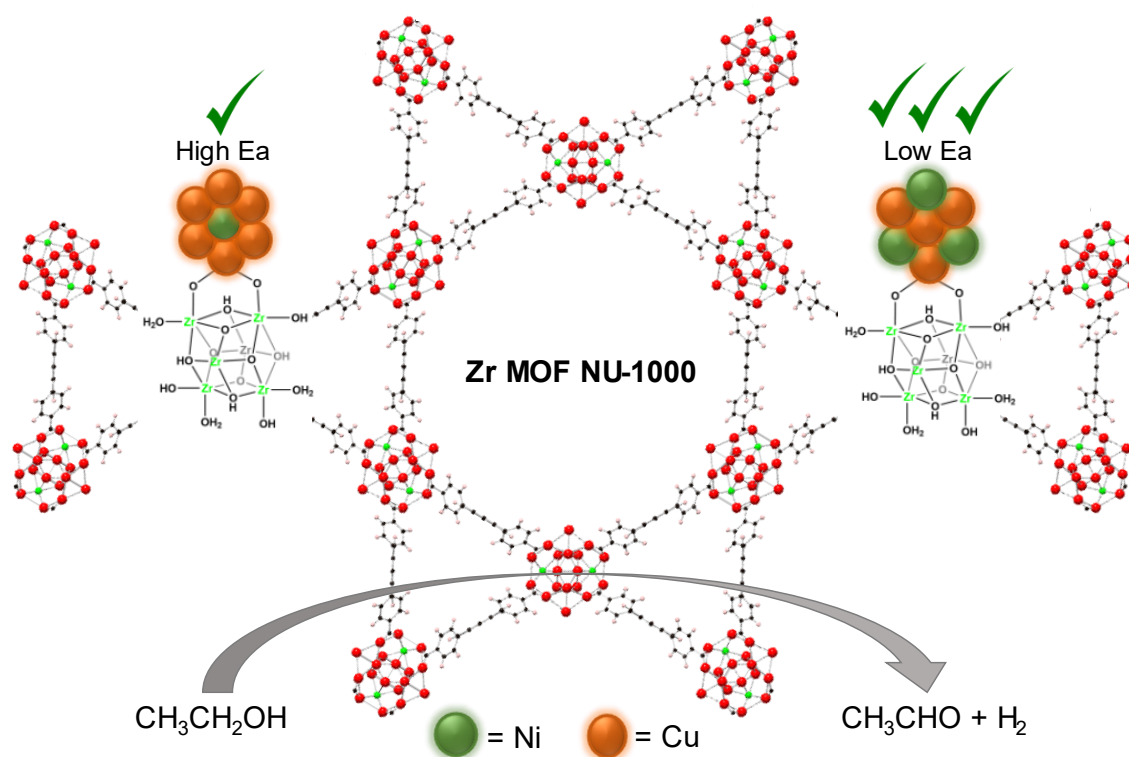
Chapter 4. Bimetallic NiCu Catalysts Supported on a Metal-Organic Framework for Non-oxidative Ethanol Dehydrogenation

Portions of this chapter appear in the following manuscript:

Wang, Q.; J., Duan; Goetjen, T.A.; Hupp, J.T.; Notestein, J.M. “Bimetallic NiCu Catalysts Supported on a Metal-Organic Framework for Non-oxidative Ethanol Dehydrogenation.” *J. Catal.*, 422 (2023) 86-98

4.1 Chapter Summary

Non-oxidative ethanol dehydrogenation is a promising route to produce acetaldehyde and hydrogen from sustainable feedstock. Bimetallic NiCu catalysts have shown high efficiency and selectivity for this chemical transformation. In this study, we leverage the high porosity and uniform catalyst deposition sites on a Zr-based metal-organic framework (MOF) catalyst support, NU-1000, to understand how the changes in Cu:Ni ratio affects the reactivity for non-oxidative ethanol dehydrogenation. We found that increasing the Ni²⁺ concentration significantly reduces the activation energy of the reaction due to the role of Ni²⁺ in suppressing the onset of Cu reduction. This study illustrates how MOFs can be used as catalyst supports to fine-tune the catalyst compositions and understand their effect on the overall catalytic performances.



4.2 Non-oxidative Ethanol Dehydrogenation as a Promising Route for Various Chemical Transformations

Ethanol derived from biomass and other biological processes (“bioethanol”) is a promising alternative to fossil hydrocarbons as a liquid fuel and chemical feedstock.^{156, 157, 158, 159} In particular, the dehydrogenation of ethanol is a crucial transformation that could be used for the bulk production of acetaldehyde, a vital commodity chemical with more than 10^6 metric tons being produced annually since 2015.¹⁶⁰ Not only can ethanol dehydrogenation potentially replace the current major acetaldehyde production route via ethylene oxidation (i.e., the Wacker process),¹⁶¹ but this transformation is also a crucial intermediate step for other alcohol-related transformations, such as the conversion of ethanol to propylene,^{162, 163} n-butanol,^{164, 165} 1,3-butadiene,^{166, 167} isobutene,^{168, 169} and aromatic compounds.^{170, 171} Non-oxidative ethanol dehydrogenation ($\text{CH}_3\text{CH}_2\text{OH} \rightarrow \text{CH}_3\text{CHO} + \text{H}_2$) also generates H_2 , a potentially desirable energy carrier that is absent if acetaldehyde is instead produced via ethanol or ethylene oxidation.

Copper-containing heterogeneous catalysts have been shown to be both active for non-oxidative ethanol dehydrogenation and highly selective towards acetaldehyde. However, oxidized Cu species can be readily reduced to Cu^0 and subsequently undergo sintering, especially at elevated temperatures required for non-oxidative ethanol dehydrogenation.¹⁷²⁻¹⁷⁴ Sintering leads to deactivation and shortens the lifespan of the catalysts.⁷⁸ Various strategies have been implemented to improve the structural stability of the Cu species, where promoting Cu with Ni has been shown to greatly improve the overall catalytic performance. On the one hand, it has been argued that Ni serves as a structural promotor by preventing Cu from aggregating under reaction conditions at high temperatures.¹⁷⁵ On the other hand, it has been proposed that

atomically dispersed Ni also serves as an effective electronic promotor in reducing the activation energy of the reaction.^{176, 177}

4.3 Metal-Organic Framework as A Well-Defined Support for Adjusting Catalyst Compositions

This study aims to further investigate the interplay between Ni and Cu in catalysts confined within a metal-organic framework (MOF). MOFs are a class of porous materials constructed from the self-assembly of inorganic metal ions or clusters (nodes) and polytopic organic moieties (linkers). Depending on the conditions, MOFs can template the formation of well-dispersed nanoparticles and clusters, limit their growth, and prevent leaching during catalytic transformations. The high crystallinity of MOF also enables structural characterization using various X-ray-based techniques, which provides further insights into the locations and structures of the active species. Those advantages have been showcased in MOF composites, including Au@ZIF-8,¹⁷⁸ Pt@MOF-808,¹⁷⁹ and Ag@MIL-101(Cr).¹⁸⁰ The growth of Cu in Zr-based MOF has also been widely investigated, and the tunability of MOF pore shapes and sizes can be leveraged to create Cu nanoparticles of various sizes and catalytic properties.⁴¹

4.4 Synthesis of NU-1000-Supported NiCu Catalysts

The MOF of interest here, NU-1000 ($[\text{Zr}_6(\mu_3\text{-O})_4(\mu_3\text{-OH})_4(\text{OH})_4(\text{H}_2\text{O})_4(\text{TBAPy})_2]_\infty$ (TBAPy = 1,3,6,8-(*p*-benzoate)pyrene)), has also been used to encapsulate Cu nanoparticles.¹⁸¹⁻¹⁸³ NU-1000 presents uniformly distributed Zr_6 nodes, each connected to eight pyrene-based linkers. NU-1000 feature 3 nm hexagonal channels, 1.2 nm triangular channels, and 0.8 nm side windows (c-pores), as defined by a **csq** topology. Notably, the nodes are isolated from each other by comparatively lengthy linkers (**Figure 4.1**). Cu nanoparticles enshrouded by NU-1000 have previously been investigated for acetylene semi-hydrogenation¹⁸⁴ and acetylene

oligomerization.⁹⁹ As such, we identify NU-1000 as a promising candidate to generate NiCu bimetallic NiCu nanoparticles at various Cu:Ni ratios and metal oxidation states. Adjusting the Cu:Ni ratio impacts the chemical state of Ni and Cu, the interaction between the two metals under reaction conditions, as well as how they might influence the catalytic activity for non-oxidative ethanol dehydrogenation in a Zr-MOF-based catalytic system.

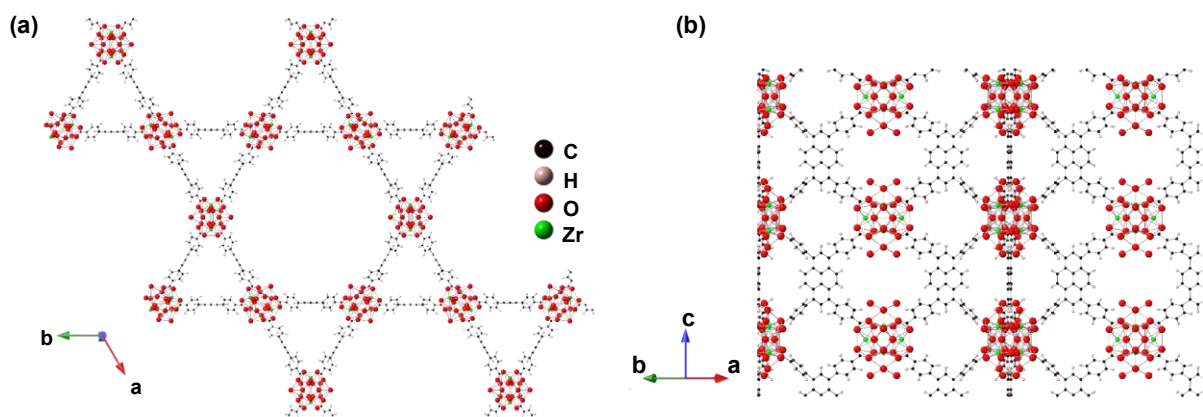


Figure 4.1. Single-crystal structure of MOF NU-1000 as viewed (a) along the c-axis and (b) facing the ab-plane.

4.5 Physical Characterizations

To confirm the retention of the bulk crystallinity and porosity, PXRD and N_2 isotherms were collected on the samples after metal loading and $NaBH_4$ treatment. **Figure 4.2(a)** displays the normalized PXRD patterns, where minimal changes are observed for all samples at different Cu and Ni loadings. The N_2 isotherms exhibited a slight decrease in the N_2 uptake for all samples, as shown in **Figure 4.2(b)**. Similar observations were made for related materials systems, where the added metals contribute mass without adding pore volume.¹⁷⁸ The pore distributions plotted in **Figure 4.2(c)** show little change in mesopore and micropore widths after metal loading and $NaBH_4$ treatment. The decrease in micropore volume corresponds to the catalytic species residing in the micropore, which is discussed further in the subsequent section on DED analysis. A slight increase in mesopore volume is also observed after metal

incorporation, likely due to the flexibility of the formate-free NU-1000 framework upon metal ion deposition.¹²⁴ Other properties of the catalysts, including the BET surface areas, total pore volumes, and metal loadings on both a per-Zr₆-node and a wt.% basis, are summarized in **Table 4.1**.

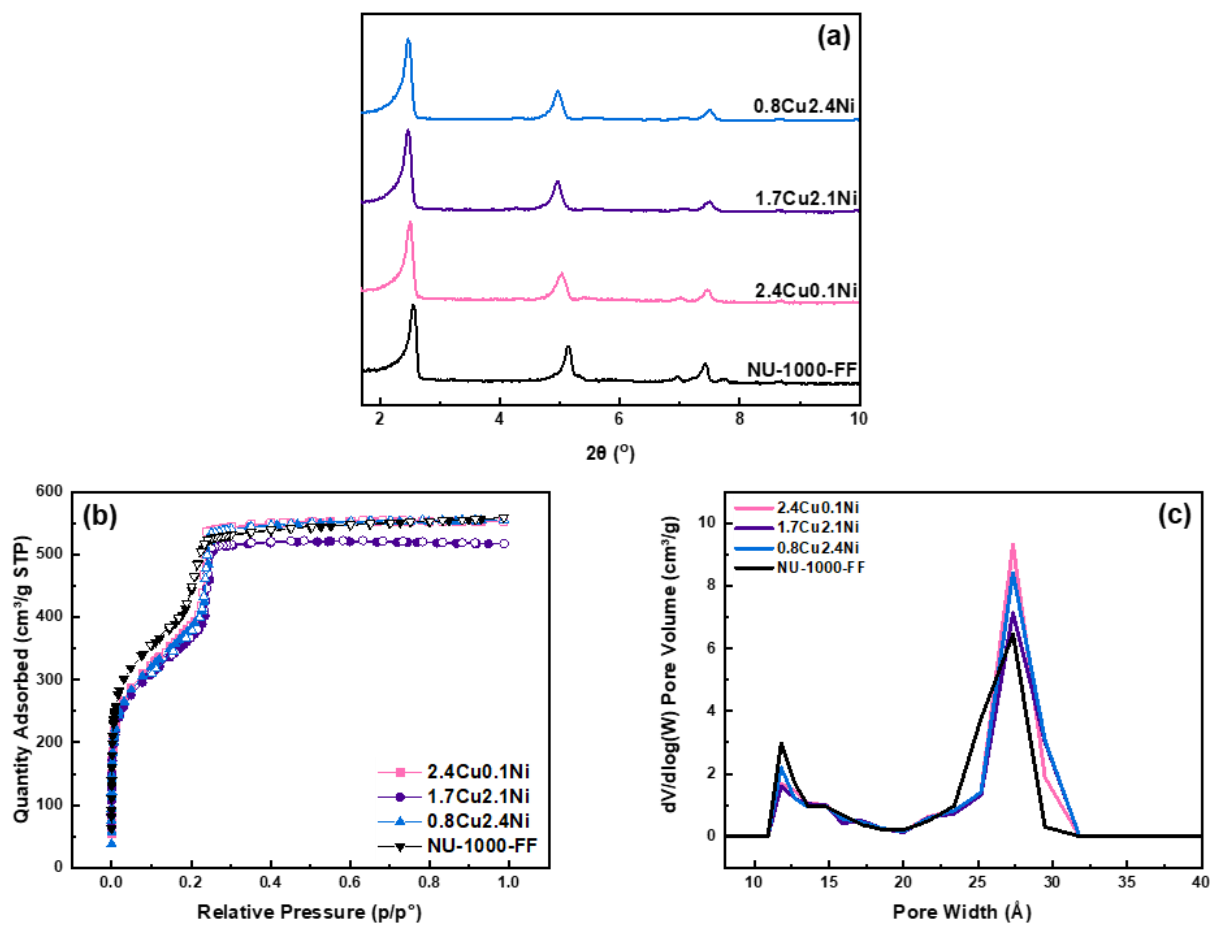


Figure 4.2. (a) PXRD patterns, (b) N₂ isotherms, and (c) NL-DFT pore-size distributions of catalyst-free and catalyst-loaded NU-1000-FF.

Table 4.1. Property table.

Catalyst	Cu(dmap) ₂ added ^a	Ni(amd) ₂ added ^a	Cu (wt%)	Ni (wt%)	Cu/node	Ni/node	Surface Area (m ² /g)	Micro- and Meso- pore Volumes (cm ³ /g)
NU-1000-FF	n/a	n/a	0	0	0	0	1365	3.0, 6.4
2.4Cu0.1Ni	7	1	6.1%	0.33%	2.4	0.1	1230	1.7, 9.3
1.7Cu2.1Ni	2	6	4.1%	3.5%	1.7	2.1	1180	1.6, 7.2
0.8Cu2.4Ni	1	7	3.7%	1.4%	0.8	2.4	1220	2.1, 8.4

^a Molar equivalents of Ni(amd)₂ and Cu(dmap)₂ per node added during synthesis.

The thermal stability of the samples after metal loading and NaBH₄ treatment was accessed with TGA, and the results are displayed in **Figure 4.20(a)-(b)**. During the ramping from 110 ~ 650 °C, two consecutive weight loss stages can be observed at 275 °C and 315 °C, respectively. The quantification reveals that the weight loss can be attributed to linker combustion.

The TEM images of the catalysts after metal loading and NaBH₄ treatment can be found in **Figure 4.6(a)-(c)**. While no nanoparticles were observed within the MOF crystallites in the as-made samples (**Figure 4.3-4.5**), the formation of spherical mixed-oxide NPs of sizes from 5 to 8 nm [**Figure 4.6(f)-(g)**] can be clearly discerned for 1.7Cu2.1Ni [**Figure 4.6(b)**] and 0.8Cu2.4Ni [**Figure 4.6(c)**] after the NaBH₄ treatment. The lattice spacing of one of the larger NPs in 0.8Cu2.4Ni was measured to be 0.21 nm [**Figure 4.6(g)**]. Due to resolution limitations, NPs in 2.4Cu0.1Ni [**Figure 4.6(a)**] are less visible. The presence of the NPs for this sample is indicated with white circles. The majority of NPs present in 2.4Cu0.1Ni is around 5~8 nm, yet around 25% NPs measured for this sample are larger than 8 nm, as shown in the particle size distribution in **Figure 4.6(d)**. Overall, the size of the NPs is found to be inversely proportional to Ni concentrations in the samples.

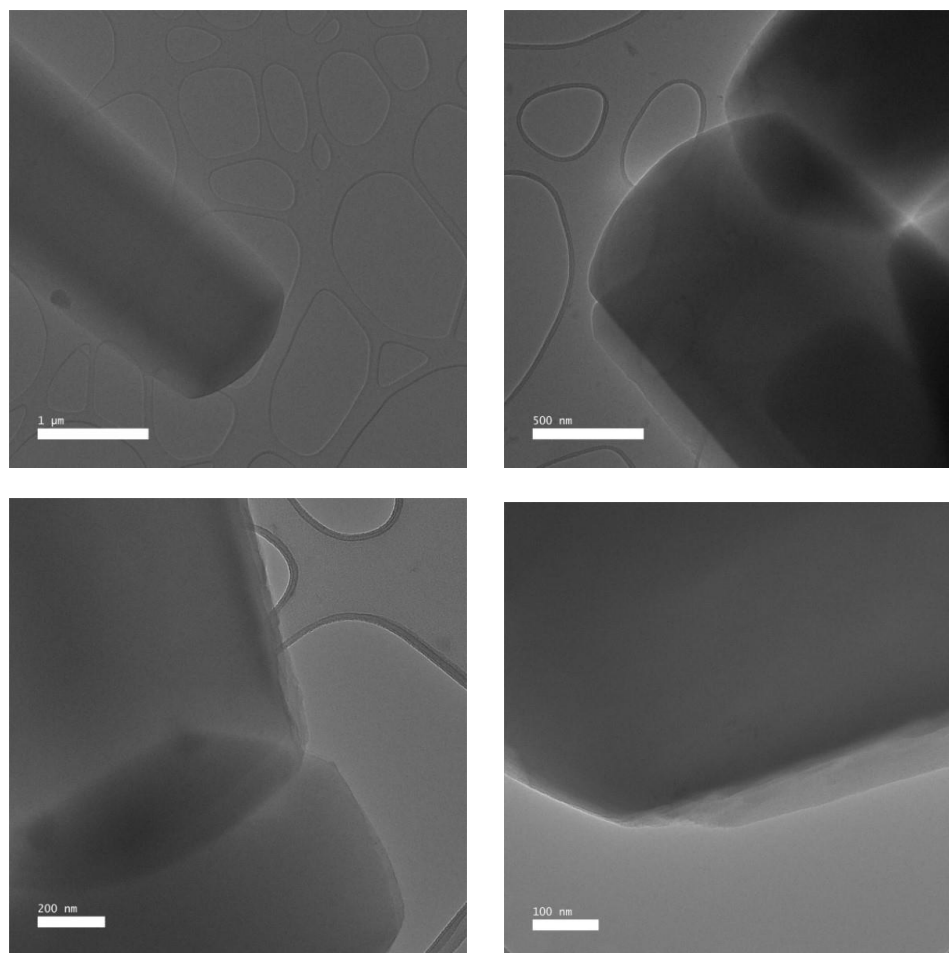


Figure 4.3. TEM images of the as-made 2.4Cu0.1Ni catalyst prior to the NaBH₄ treatment.

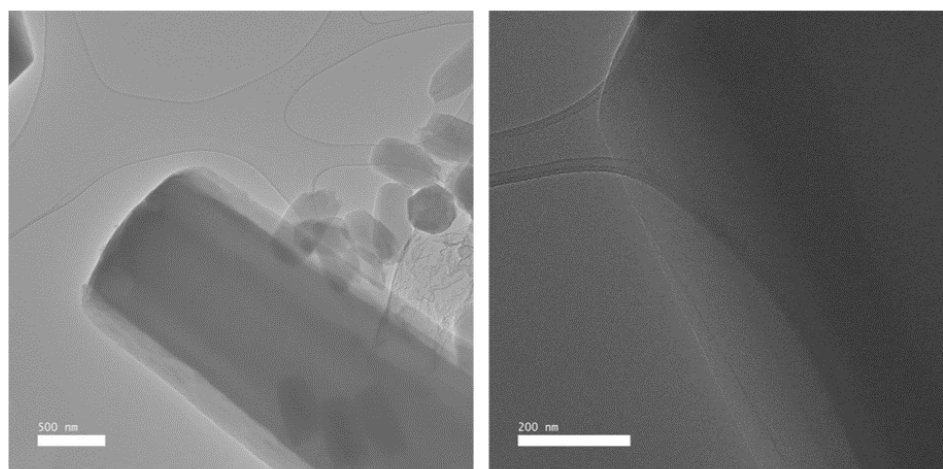


Figure 4.4. TEM images of the as-made 1.7Cu2.4Ni catalyst prior to the NaBH₄ treatment.

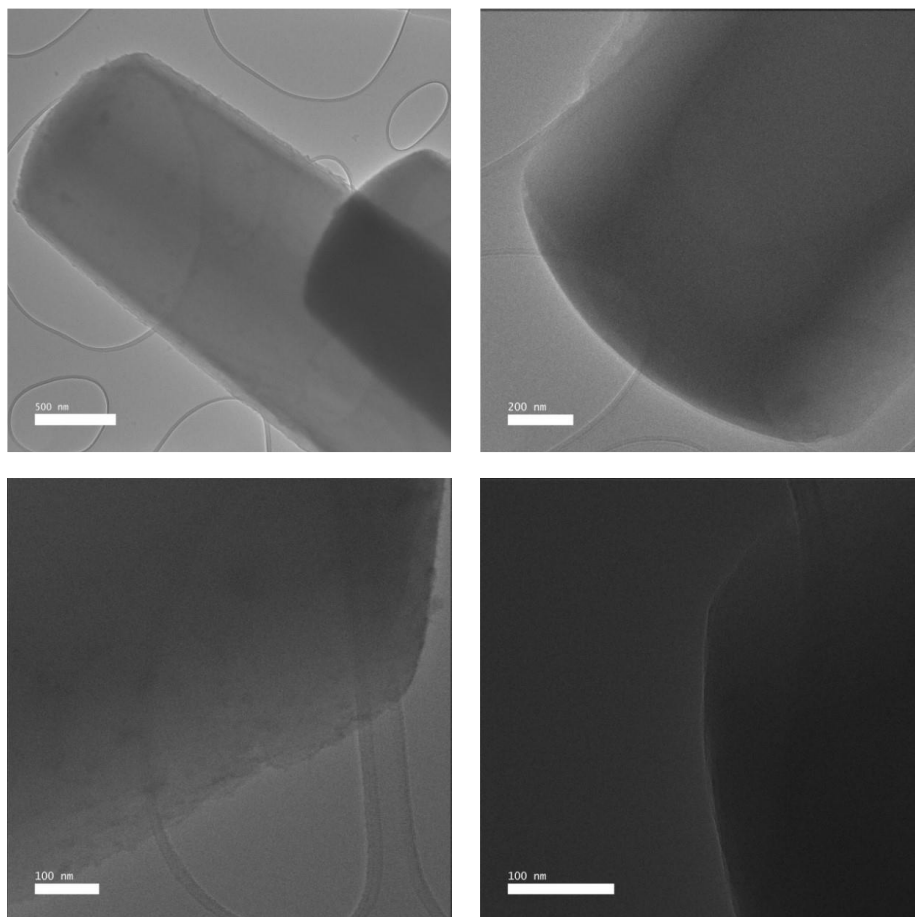


Figure 4.5. TEM images of the as-made 0.8Cu₂.4Ni catalyst prior to the NaBH₄ treatment.

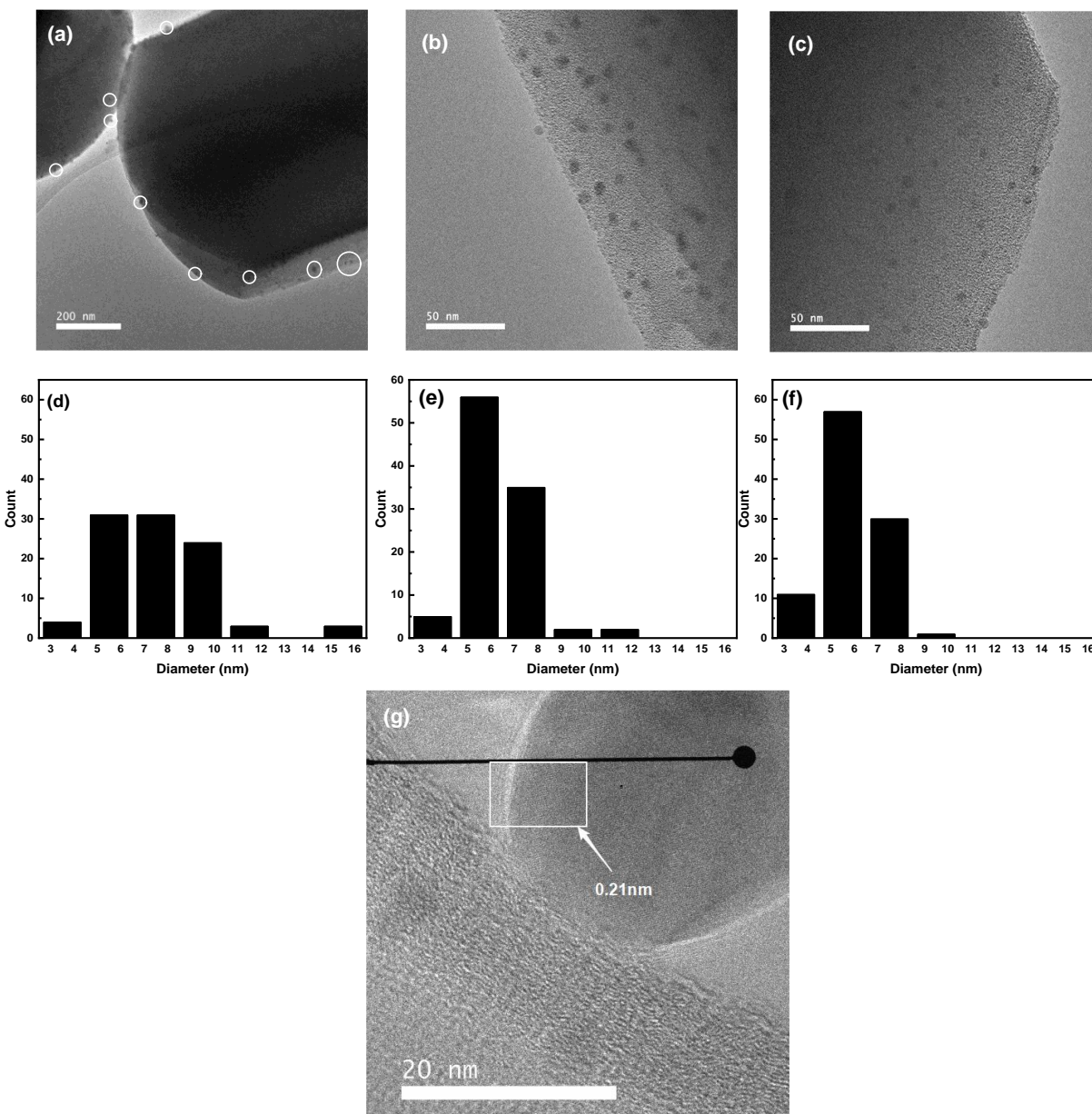


Figure 4.6. (a)-(c) TEM images of 2.4Cu0.1Ni, 1.7Cu2.1Ni, and 0.8Cu2.4Ni, respectively, after the NaBH₄ treatment. (d)-(f) Particle size distributions of 2.4Cu0.1Ni, 1.7Cu2.1Ni, and 0.8Cu2.4Ni, respectively. Distributions were determined from measuring the diameters of at least 100 distinct NPs for all samples. (g) Lattice spacing measurement for one NP in 0.8Cu2.4Ni.

Difference envelope density (DED) analyses were implemented to further investigate the metal species that cannot be directly observed in TEM. **Figure 4.7(a) – (f)** displays the DED maps of all three samples. For both 2.4Cu0.1Ni and 1.7Cu2.1Ni, electron densities can be observed in the mesopore and micropore channels and in the c-pores. No electron density is

found in the mesopore channel for $0.8\text{Cu}2.1\text{Ni}$. The DED analyses and the TEM images of the samples show that a mixture of larger TEM-visible nanoparticles and smaller metal clusters coexist in the MOF crystallites after the NaBH_4 treatment.

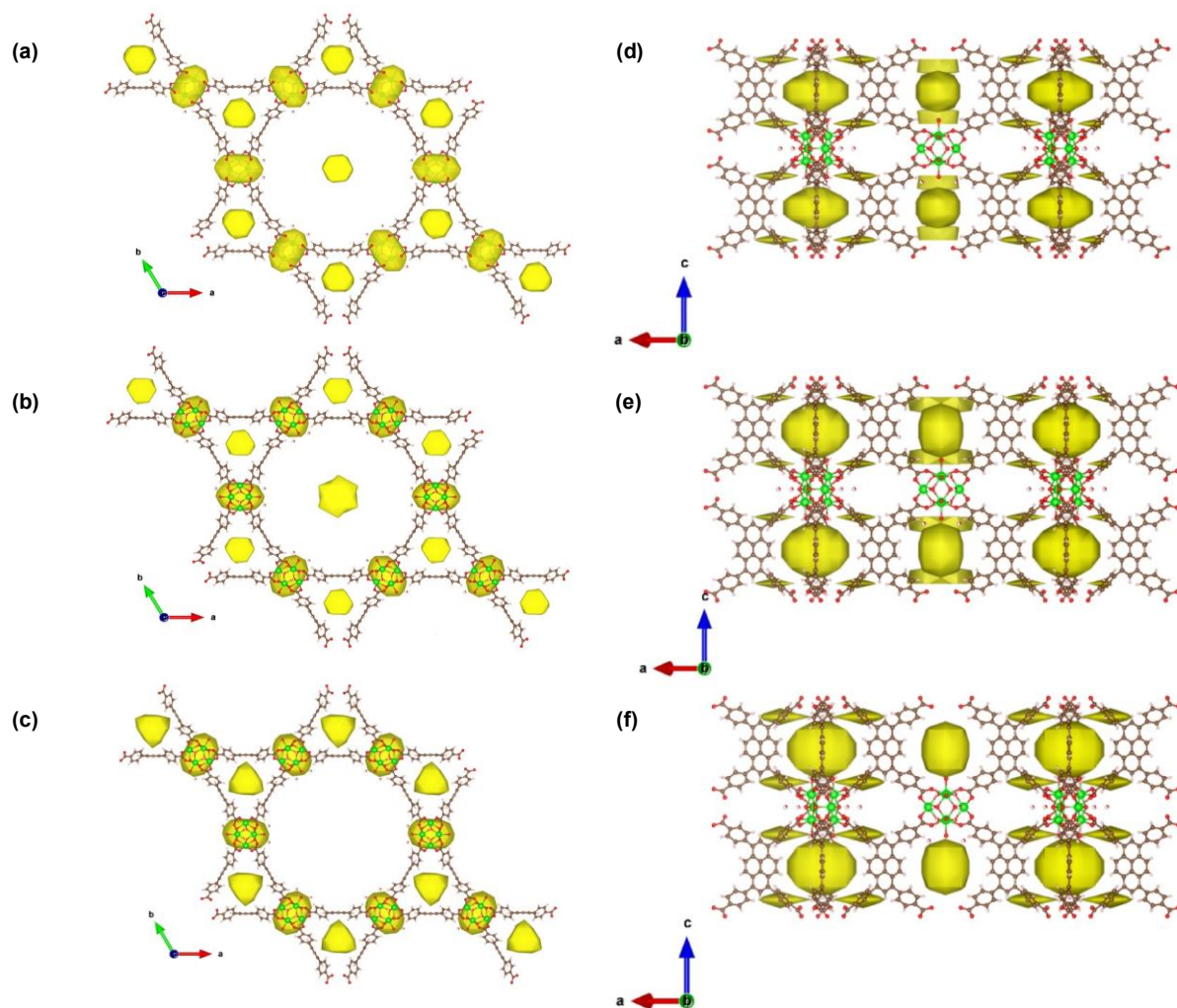


Figure 4.7. DED results for (a) $2.4\text{Cu}0.1\text{Ni}$, (b) $1.7\text{Cu}2.1\text{Ni}$, and (c) $0.8\text{Cu}2.4\text{Ni}$ presented along the c-axis. Their respective views along the b-axis are displayed in (d) – (f). The yellow blobs represent extra electron density from the metal species incorporated post-synthetically. (Green sphere = Zr, red spheres = O, brown spheres = C, white spheres = H)

4.6 Spectroscopic Studies

To monitor the chemical state of the Cu under different reducing conditions, XPS spectra of the samples after H_2 treatment were collected at temperatures ranging from $150\sim 300^\circ\text{C}$. XPS

spectra were collected after treatments in 5% H₂/N₂ for at least 2 h at temperatures from 150 ~ 300 °C. The initial NaBH₄-treated samples were treated without prior oxidation. A detailed experimental setup of these measurements can be found in Section 4.13.4. The resulting spectra for Cu and Ni at various temperatures are displayed in **Figure 4.8**.

In the Cu spectra [**Figure 4.8(a)-(c)**], two pairs of distinct peaks, with the 2p 3/2 binding energies (BEs) of 935 eV and 939 eV, respectively, can be discerned after the room temperatures pretreatment for all samples. As shown in the peak values tabulated in **Table 4.2**, the peaks at 935 ± 1 eV, denoted as peak 1, are assigned as Cu(0). The ones at 939 eV (peak 2) are assigned as Cu^{δ+} species. An increase in the binding energy of peak 2 is observed with increasing Ni loading. Those species can be either binding to the acidic Zr₆ nodes or interacting with the Ni²⁺ species, as the Ni²⁺ with higher positive charge withdraws electron density from the less positively charged Cu^{δ+} species. Additionally, satellite features shaded in purple are also present in all samples at low temperatures. The satellite feature is attributed to the presence of Cu²⁺ species within the Cu^{δ+} peak.^{185, 186}

For all catalysts, both peak 1 and peak 2 in all the Cu spectra shifted to lower BE when temperature was raised to 200°C and beyond, corresponding to the formation of more electron-rich Cu species. The satellite feature disappeared completely upon heating the samples in H₂ at 150°C for 2.4Cu0.1Ni, while it persisted till 250°C and 200°C for 1.7Cu2.1Ni and 0.8Cu2.4Ni, respectively. This clearly indicates that high levels of Ni delayed the onset of reduction of Cu²⁺ species to Cu⁺ or Cu⁰. Meanwhile, the main Ni peaks were found at 856.5 ± 0.5 eV below 250°C, corresponding to Ni²⁺ species in the systems [**Figure 4.8(d)-(e)** and **Table 4.2**]. Some Ni reduction was observed for 1.7Cu2.1Ni at above 250°C and for 0.8Cu2.4Ni at 300°C, as shown in the deconvoluted peaks shaded in green at 853.7 eV.

The higher-temperature onset of Cu^{2+} reduction for the Ni-rich samples signifies the two-fold effect of Ni in the catalytic systems. The presence of Ni resulted in the formation of smaller nanoparticles on average, and Cu reduction has previously been shown to be more difficult over smaller Cu nanoparticles.¹⁸⁷ This would suggest that the nanoparticles are mixed oxides, rather than metallic in nature. In addition to limiting the growth of larger nanoparticles, the electron deficient Ni^{2+} species can also withdraw electron density from Cu with minimal changes in its formal oxidation state, inhibiting Cu reduction. Overall, the XPS studies illustrate that CuNi bimetallic catalysts containing an appreciable amount of Ni result in a higher onset temperature for the reduction of Cu^{2+} , which could be beneficial for stabilizing the sub-nm clusters in the pores of NU-1000.

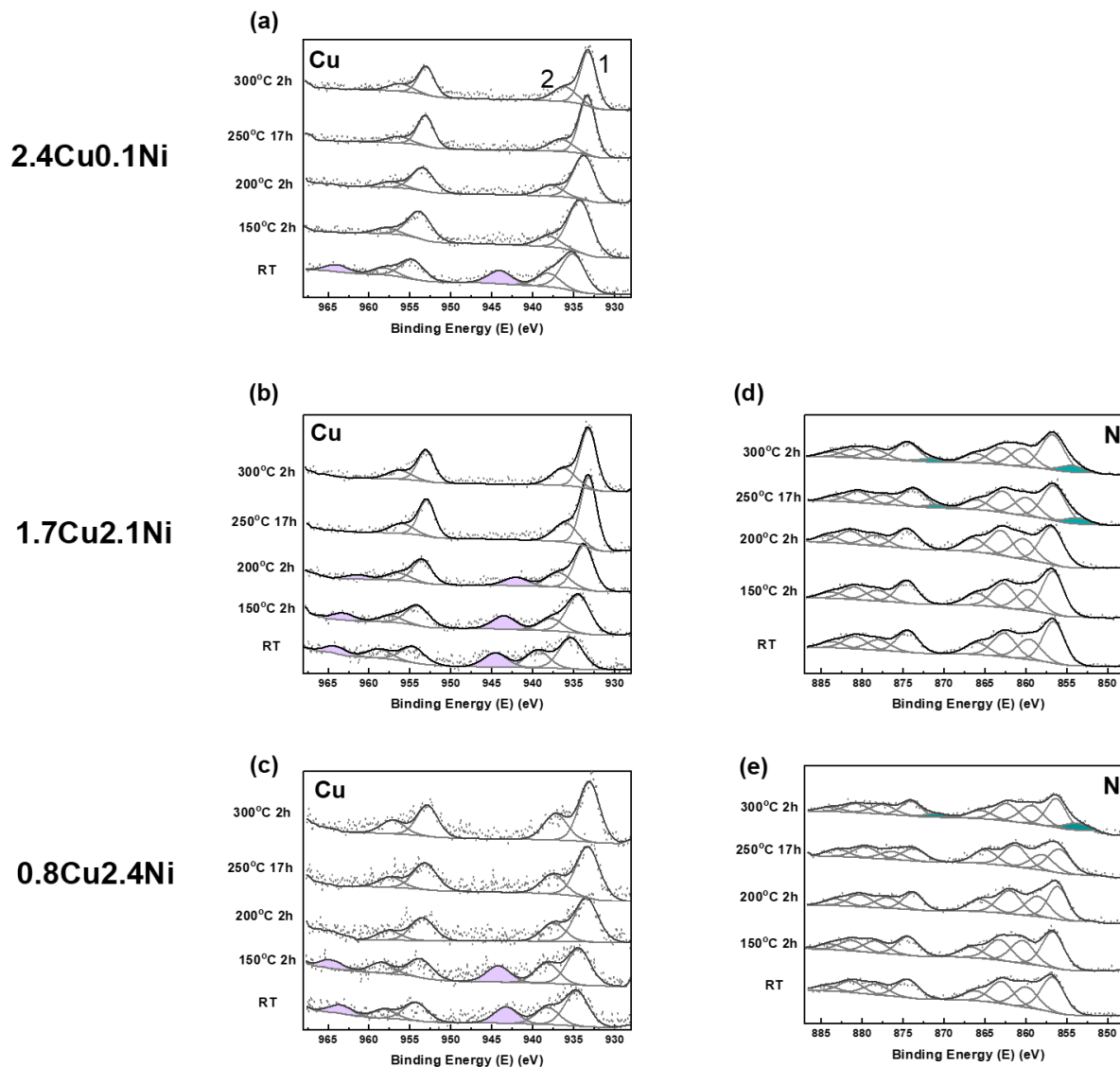


Figure 4.8. XPS spectra for (a)-(c) Cu and (e)-(f) Ni. The Ni spectra for 2.4Cu0.1Ni are not shown here due to the low S/N ratio of the spectra.

Table 4.2. Binding energies of Cu and Ni before and after the complete reduction of Cu.

Catalyst	Cu BE at room temperature ^a (eV)	Cu BE after reduction ^b (eV)	Ni BE at room temperature (eV)	Ni BE after reduction ^c (eV)
2.4Cu0.1Ni	935.1, 938.1	934.1, 937.9	N/A	N/A
1.7Cu2.1Ni	935.3, 939.4	933.1, 936.0	856.8	856.6 (853.7)
0.8Cu2.4Ni	934.6, 943.3	933.4, 937.4	856.7	856.0 (853.8)

^a After NaBH₄ treatment.

^b At the lowest temperature where the Cu satellite feature disappears.

^c At the lowest temperature where the Ni reduction peak appears. The reduction peak values are included in the parentheses.

4.7 Reactivity Testing

Non-oxidative ethanol dehydrogenation at varied temperatures was carried out for all samples in a plug-flow reactor. The amount of Cu was kept consistent across all samples, and the conversion was kept under 8%. Under these conditions, the NU-1000-supported NiCu catalysts are 100% selective towards acetaldehyde. **Figure 4.9(a)** shows an example time-on-stream (TOS) plot of all samples of ethanol conversion at increasing temperatures.

As can be observed at 250°C, all four catalysts all deactivated. TGA results [**Figure 4.20(c)-(d)**] indicate this is due to gradual linker decomposition and resultant framework collapse at the highest temperatures. Therefore, the first five data points at each temperature were used to calculate the initial reaction rates on a per Cu basis at each temperature point. The activation energies (E_a) for all samples are then extracted from the Arrhenius plots in the temperature range of 200 - 250°C, shown in **Figure 4.9(b)**. Some background reactivity was also observed for the Ni-only catalyst (**Figure 4.10**), suggesting that Ni can actively participate in ethanol dehydrogenation.

A small amount of Ni incorporation resulted in a slight increase in E_a , from 63 kJ/mol for 2.8Cu to 70 kJ/mol for 2.4Cu0.1Ni. Further increase in Ni loading results in a drastic decrease in E_a to 36 kJ/mol for 1.7Cu2.1Ni and 48 kJ/mol for 0.8Cu2.4Ni. Those observations signify the role of Ni^{2+} in promoting the non-oxidative ethanol dehydrogenation reaction.

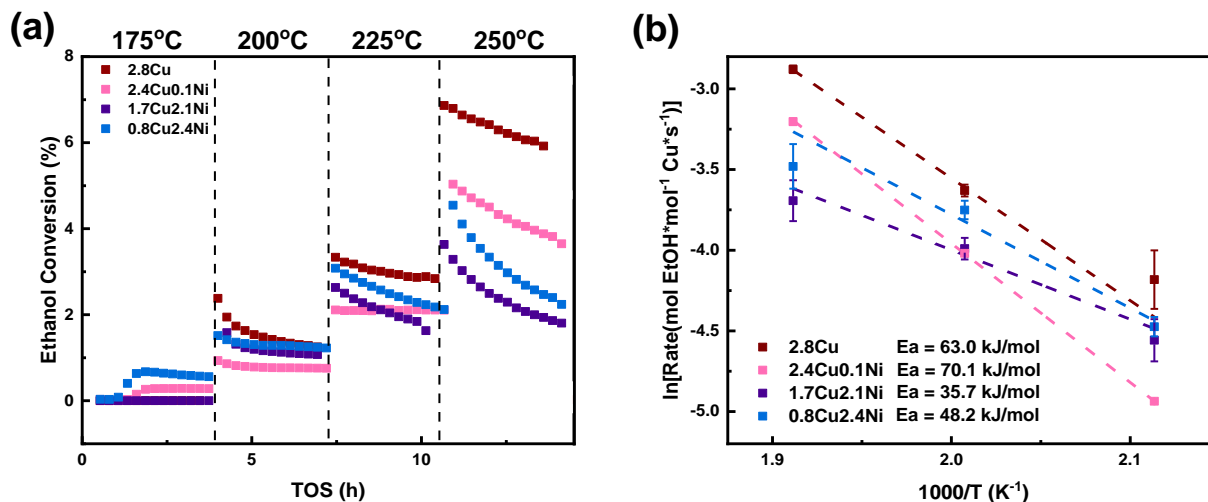


Figure 4.9. (a) Example time-on-stream plot of all samples from 175-250°C. (b) Arrhenius plot for all samples in the temperature range of 200-250°C based on the initial rates at each temperature point.

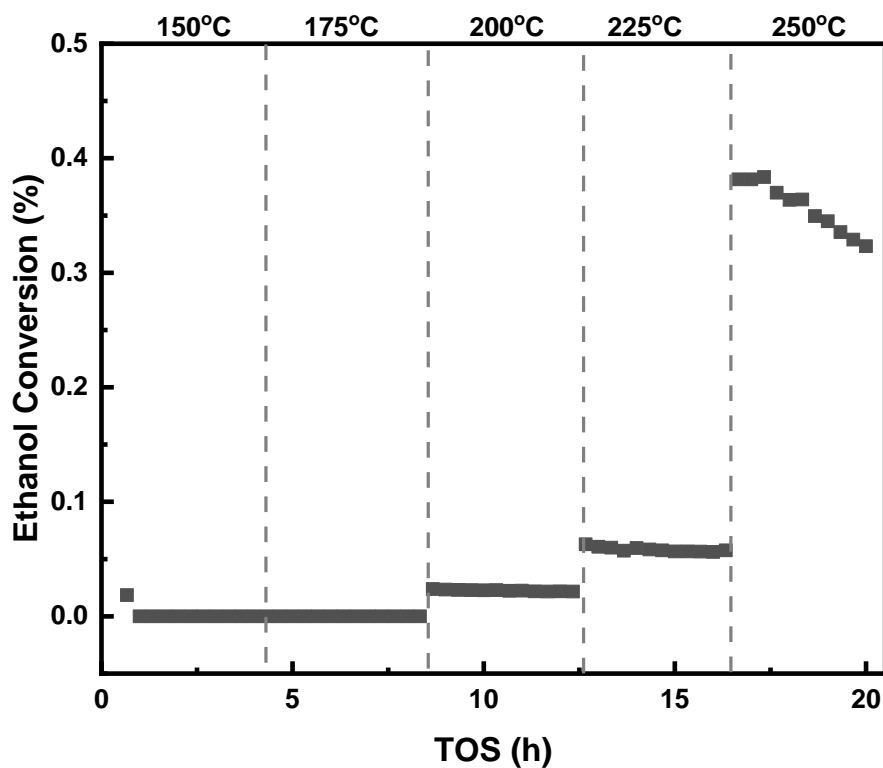


Figure 4.10. TOS plot for 20.8 mg of 3.8Ni showing the background reactivity of Ni for non-oxidative ethanol dehydrogenation.

4.8 Active Site and Mechanistic Investigations

To further explore the role of Ni during the catalytic process, *in-situ* ethanol DRIFTS studies from 150 – 250°C were performed. Conditions were kept consistent with the flow reaction conditions, where each sample was pre-treated under O₂ at 250°C for 2 hours, followed by the introduction of ethanol vapor at 150, 200, and 250°C. The spectra of the bare NU-1000-FF and catalysts at various Cu:Ni ratios at 150°C are displayed in **Figure 4.11(a)**. Characteristic features can be observed in the three shaded regions, namely the C-O bending region at 1000~1200 cm⁻¹ (orange), the C-H stretching region at 2650~3100 cm⁻¹ (green), and the O-H stretching region at 3000~3800 cm⁻¹ (blue).

The C-O stretching region [**Figure 4.11(b)**] revealed various adsorbed intermediates on the catalyst surfaces. Peaks are observed at around 1150 cm⁻¹, which are assigned to the $\nu(\text{C-CO})$ stretch of adsorbed acetaldehyde.¹⁸⁸ Other prominent features can be found in the range of 1025 ~ 1070 cm⁻¹, which could arise from the $\nu(\text{C-O})$ stretch of the adsorbed ethanol molecules and ethoxy species. A feature centered around 1100 cm⁻¹ was also observed for all samples except for 2.8Cu and 2.4Cu0.1Ni. This feature, showing no changes at increasing temperatures [**Figure 4.12**], is assigned to adsorbed CH₃CHO*/CH₃CO* as a result of multiple $\beta\text{C-H}$ bond scissions.¹⁸⁹

Spectra for the C-H stretching region are shown in **Figure 4.11(c)**, where a series of features associated with the alkyl C-H stretches on either ethanol or acetaldehyde are observed. Those features are of the lowest intensity for 3.8Ni, which is attributed to the low affinity of Ni²⁺ to ethanol. This observation is consistent with the low reactivity observed for this sample (**Figure 4.10**). A pair of peaks centered around 2710 cm⁻¹ and 2835 cm⁻¹ are present in the Cu-containing samples and NU-1000-FF, and are assigned to the Fermi resonance resulting from the

C-H stretch on the carbonyl group.¹⁹⁰ Those peaks, along with the peaks at around 1150 cm^{-1} in the C-O stretching region, signify that certain amount of product remained on the catalyst surfaces at 150°C .

The O-H stretching regions of the spectra are shown in **Figure 4.11(d)**, from where two types of negative features can be discerned. The sharp negative feature at 3670 cm^{-1} for NU-1000-FF originates from the loss of non-hydrogen-bonded aqua groups on the Zr_6 nodes.¹²⁴ This feature is greatly diminished in the metal-containing samples, consistent with metal ions binding to the aqua/hydroxyl pairs of the nodes. Meanwhile, a negative feature at 3710 cm^{-1} is present for all samples except for NU-1000-FF. This feature corresponds to the loss of hydroxyl groups on the sub-nm metal clusters. The loss of metal hydroxides can be attributed to the role of ethanol as a proton donor. During the course of the experiment, ethanol protonates the hydroxyl groups, resulting in the formation of adsorbed ethoxy species and water. Both 0.8Cu2.4Ni and 1.7Cu2.1Ni exhibit an intense negative feature at 3710 cm^{-1} , along with a broad peak centered around 3200 cm^{-1} . The broad peak corresponds to the presence of physisorbed water. Meanwhile, the intensity of this peak at 3710 cm^{-1} is much weaker for 3.8Ni, 2.8Cu, and 2.4Cu0.1Ni samples, which is consistent with the observation from the single-beam spectra [**Figure 4.12(b)**], where the O-H region is barely perturbed before and after the introduction of ethanol.

In summary, at 150°C , various adsorbed species, including chemisorbed ethanol, ethoxy, and acetaldehyde, are present. The formation of ethoxy results from ethanol deprotonation by reacting with metal hydroxyls on the sub-nm metal clusters, as illustrated by the loss of hydroxyl features in the spectra.

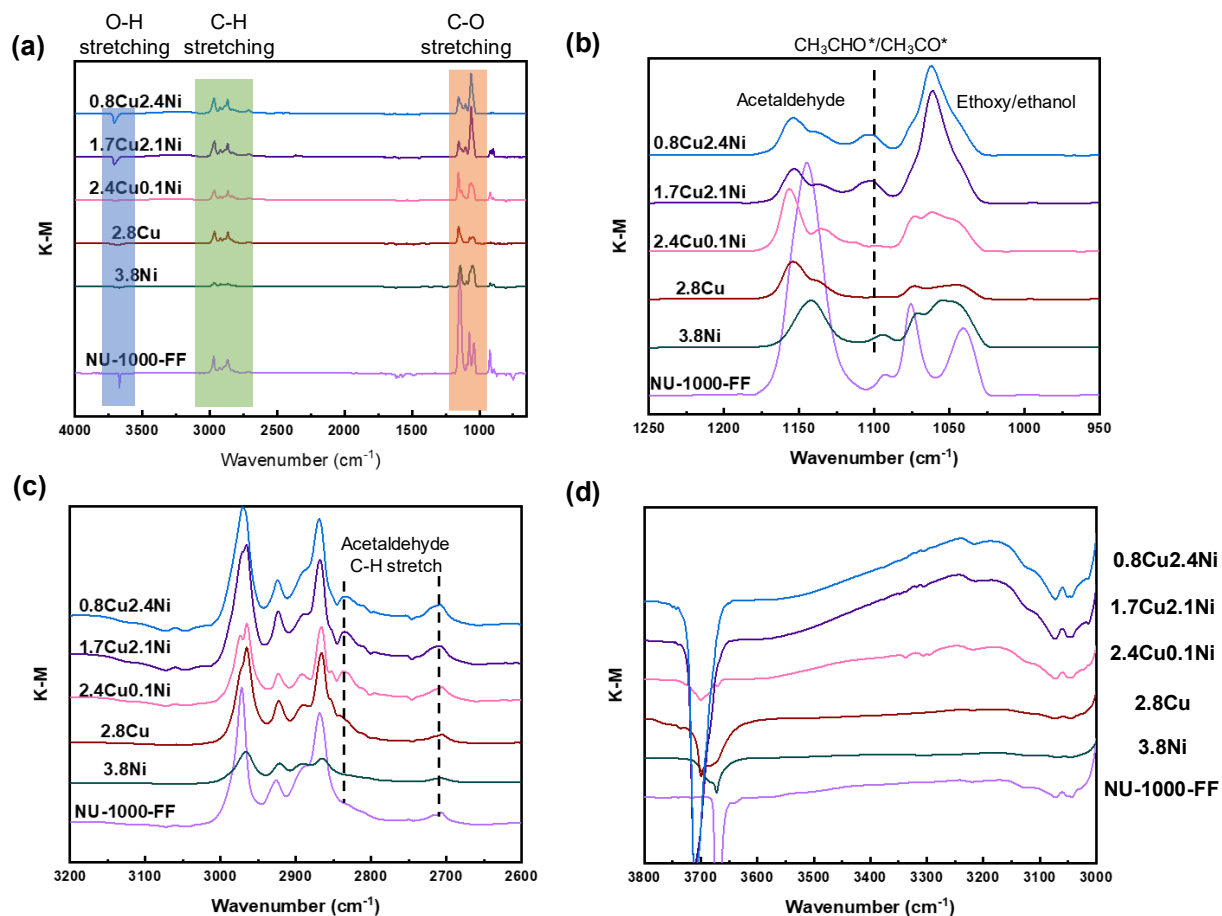


Figure 4.11. (a) Full in-situ ethanol DRIFTS spectra at 150°C and zoomed-in spectra of the (b) C-O stretching region, (c) C-H stretching region, and (d) O-H stretching region.

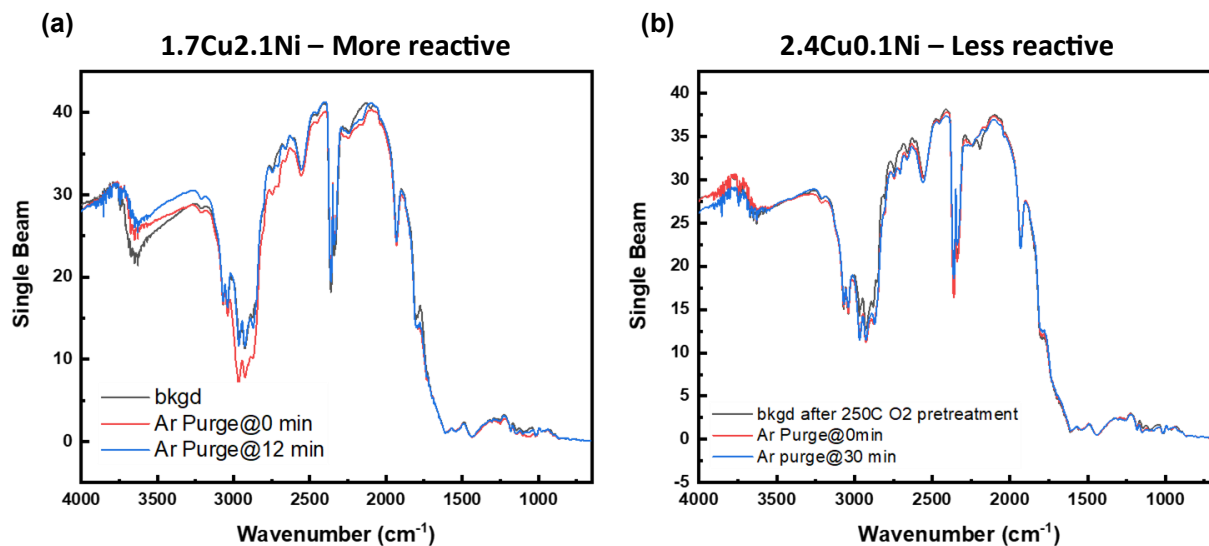


Figure 4.12. Single-beam spectra recorded at 150°C for (a) 1.7Cu2.1Ni and (b) 2.4Cu0.1Ni.

The spectra for all references and samples collected at various temperatures are displayed in **Figure 4.13(a)-(f)**. Starting with the C-O stretching region of NU-1000-FF and 3.8Ni, the intensity of the ethoxy peaks exhibits minimal changes at all temperatures, indicating that those adsorbed species are mostly spectators and there is minimal change in the structure of the adsorption sites. The intensities of the C-O stretches decreased significantly for 2.8Cu. The such decrease could arise from the formation of acetaldehyde from ethoxy and the direct desorption of ethanol, as Cu nanoparticles formed at high temperatures would have less affinity to ethanol and ethoxy binding with increasing temperatures.¹⁹¹ This also means that the adsorbed ethanol and ethoxy are no longer spectators for all Cu-containing samples with dynamic surface structures at increasing temperatures. For the spectra associated with 2.4Cu0.1Ni [**Figure 4.13(d)**], the adsorbed ethoxy/ethanol feature at 1050 cm^{-1} decreases with increasing temperature, suggesting the desorption and consumption of those surface species. A similar phenomenon is also seen in the C-O stretching regions for 1.7Cu2.1Ni [**Figure 4.13(e)**] and for 0.8Cu2.4Ni [**Figure 4.13(f)**]. The spectator species $\text{CH}_3\text{CHO}^*/\text{CH}_3\text{CO}^*$ at 1100 cm^{-1} is also barely perturbed for those two samples.

In the C-H stretching region, a decrease in intensity of the pair of peaks associated with acetaldehyde was observed at increasing temperatures in all samples, corresponding to product desorption. In the hydroxyl region, only a minimal loss of hydroxyl feature is observed at all temperatures for 2.4Cu0.1Ni. The raw spectra at 150°C prior to the introduction of ethanol show little hydroxyl feature [**Figure 4.12(b)**]. In contrast, significant hydroxyl peak loss is present for 1.7Cu2.1Ni and 0.8Cu2.4Ni. Both samples also started with an appreciable amount of hydroxyl features [**Figure 4.12(a)**]. These observations illustrate that the loss of Ni hydroxyl groups correlates with lowered activation barriers.

To summarize, the *in-situ* DRIFTS studies, along with the reactivity and XPS studies, demonstrated the differences in active sites with and without Ni. Combined with the XPS studies, these observations also suggest delaying Cu reduction by an appreciable amount of Ni is beneficial for realizing higher catalytic activity. As discussed in the subsequent section, this drastic decrease in E_a is due to the presence of Cu-Ni interfacial sites.

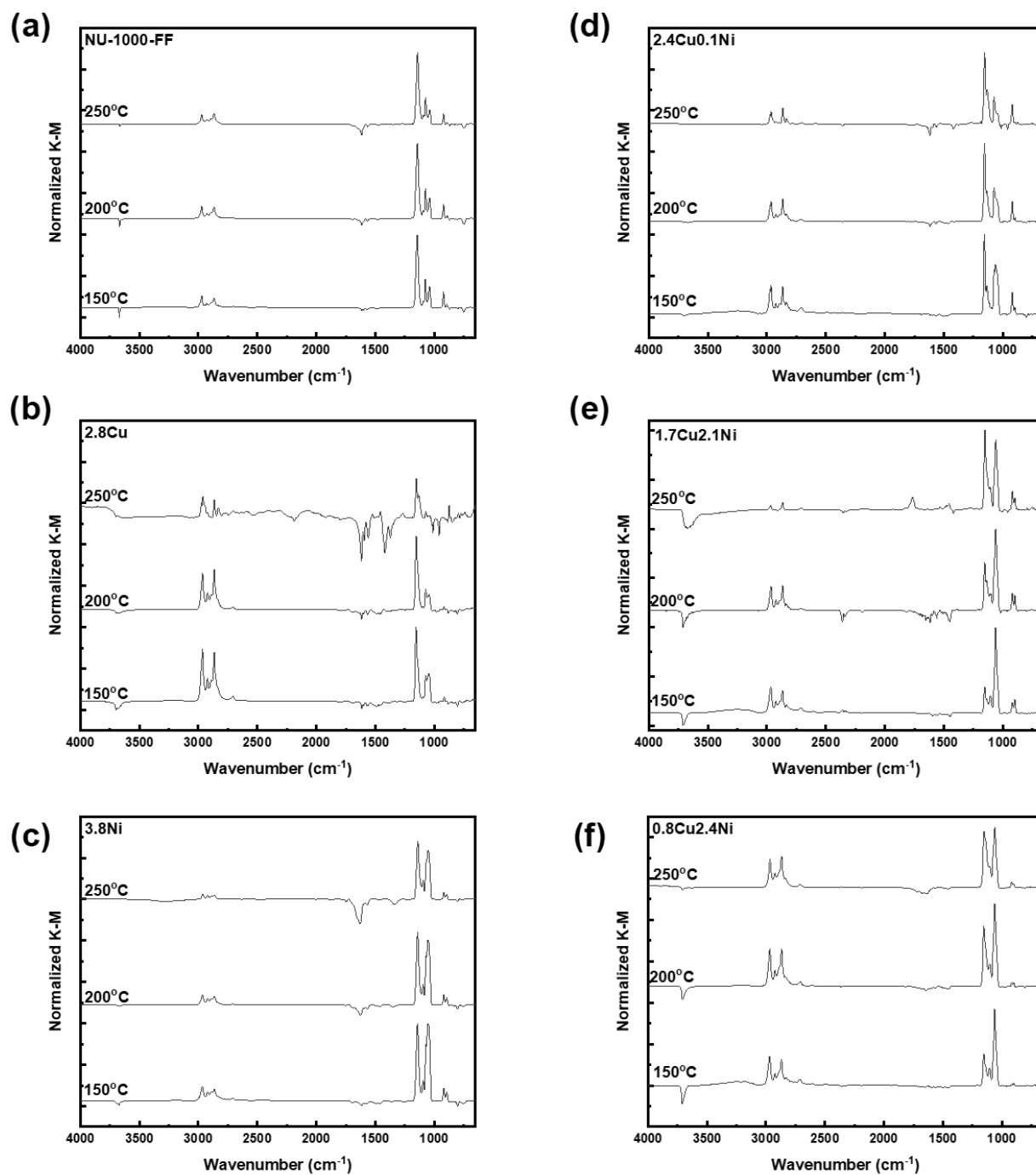


Figure 4.13. DRIFTS Spectra from 150 - 250°C for (a) NU-1000-FF, (b) 2.8Cu, (c) 3.8Ni, (d) 0.8Cu2.4Ni, (e) 1.7Cu2.4Ni, and (f) 0.8Cu2.4Ni. All spectra are normalized to the highest peak intensities.

4.9 Mechanistic Insights

Based on the observations from the DRIFTS spectra, we propose two possible mechanisms occurring either on the surface of the NPs or at the node-NP interfaces. **Figure 4.14** depicts the mechanism occurring at a Ni-Cu oxide interface. The cycle starts with a bare Cu and a hydroxylated Ni species. Upon contact with an ethanol molecule, one of the hydroxyl groups on Ni is protonated and leaves the surface as a water molecule. The resulting ethoxy fragment then binds to Cu. When the Ni-Cu interfacial sites are located adjacent to the Zr_6 nodes, the ethoxy fragment can bind the Zr Lewis acid sites and Cu in a bidentate fashion, as represented by the dotted line in the structure.

The ethoxy species then undergoes β C-H bond scission, which is proposed to be the rate-limiting step of the reaction. Considering that Ni supported on NU-1000 has been found by others to serve as a hydride acceptor for heterolytic hydrogen splitting,⁹² Ni could facilitate the β C-H bond scission on the ethoxy group, resulting in the formation of Ni-H species. The high activity of Ni for β C-H bond scission is also signified by the presence of CH_3CHO^*/CH_3CO^* species in the DRIFTS studies, and has also been reported by previous studies on similar systems.^{175-177, 192} We believe this activity may contribute to the faster deactivation of high-Ni-concentration catalysts due to the irreversible adsorption of these spectators during time-on-stream studies. The formation of Ni-H is also accompanied by the formation of a C=O bond on the acetaldehyde as the product. Upon introducing a second ethanol molecule, the ethanol molecule would be deprotonated, resulting in the formation of hydrogen and an adsorbed ethoxy species, restoring the catalytic cycle.

Considering that Ni-Cu interfacial sites are present in greater abundance in the 1.7Cu2.1Ni and 0.8Cu2.4Ni catalysts, the relative rates for β C-H bond scission could be higher

in those two cases. Meanwhile, for 2.4Cu0.1Ni, adjacent Cu-Cu sites are the dominant species. The lack of hydroxyl species on Cu, combined with the absence of Ni for accepting hydride, resulted in much higher apparent activation energy than the Ni-rich catalysts.

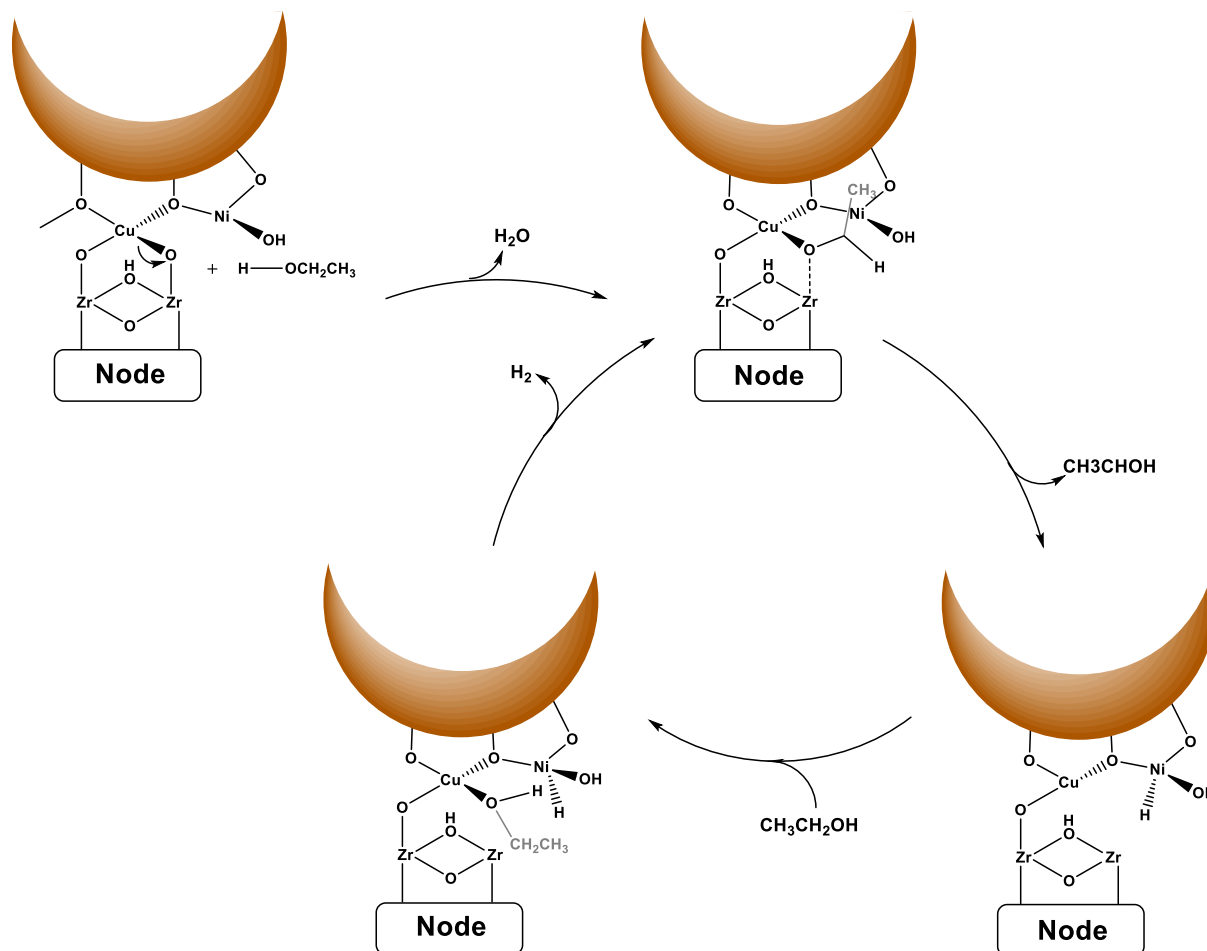


Figure 4.14. Proposed reaction mechanism. The partial brown sphere represents the surface of a mixed oxide nanoparticle or sub-nm cluster species. Similar mechanism can take place with the Ni attached to the node and a neighboring Cu site.

4.10 Study of a Comparative System

ZrO₂-supported NiCu, 0.4Cu1.6Ni-ZrO₂, has been reported previously to be active for non-oxidative ethanol dehydrogenation and was synthesized for this work as a comparative catalytic system. The synthesis is described in Section 4.13.2. The Cu and Ni loadings in the final catalyst were determined through ICP to be 0.4% and 1.6%, respectively, and are used in

the name. The PXRD patterns of the catalyst before and after NiCu deposition exhibit no appreciable differences, suggesting that no large nanoparticles were formed during the synthesis (**Figure 4.15**). TEM images (**Figure 4.16**) also show no nanoparticle formation on the bulk ZrO₂ surface. The XPS of Ni and Cu (**Figure 4.17**) shows similar binding energies to those supported on NU-1000, suggesting that the elements are in similar chemical states on ZrO₂ and NU-1000.

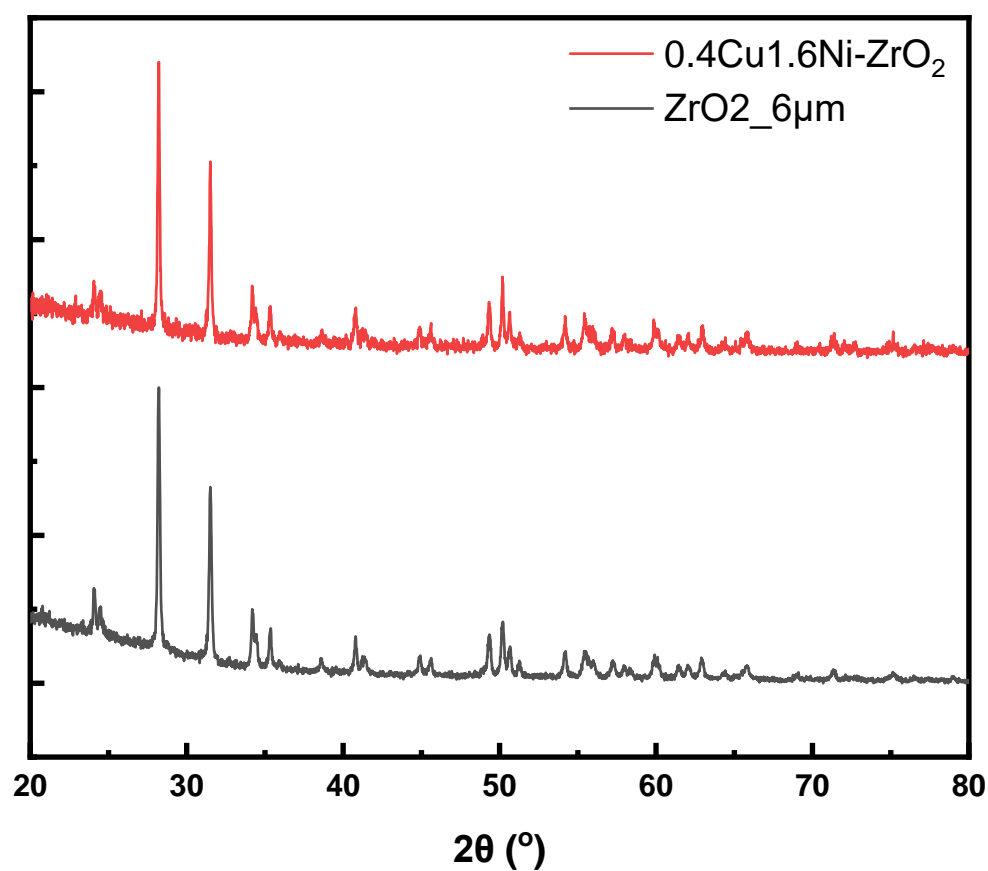


Figure 4.15. PXRD patterns of ZrO₂ and 0.4Cu1.6Ni-ZrO₂.

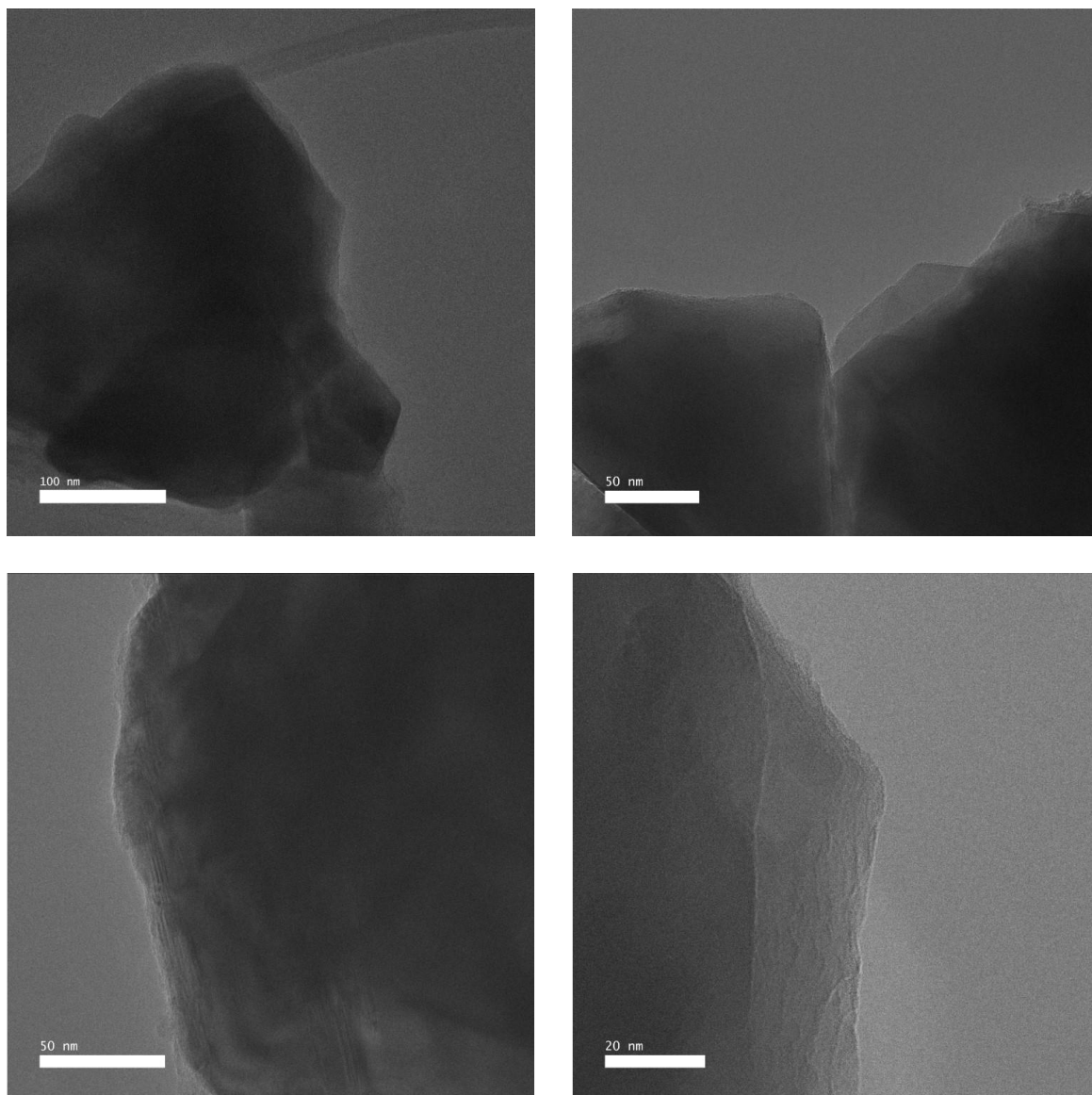


Figure 4.16. TEM images of $0.4\text{Cu}1.6\text{Ni-ZrO}_2$ after 2 hours of H_2 treatment at 200°C .

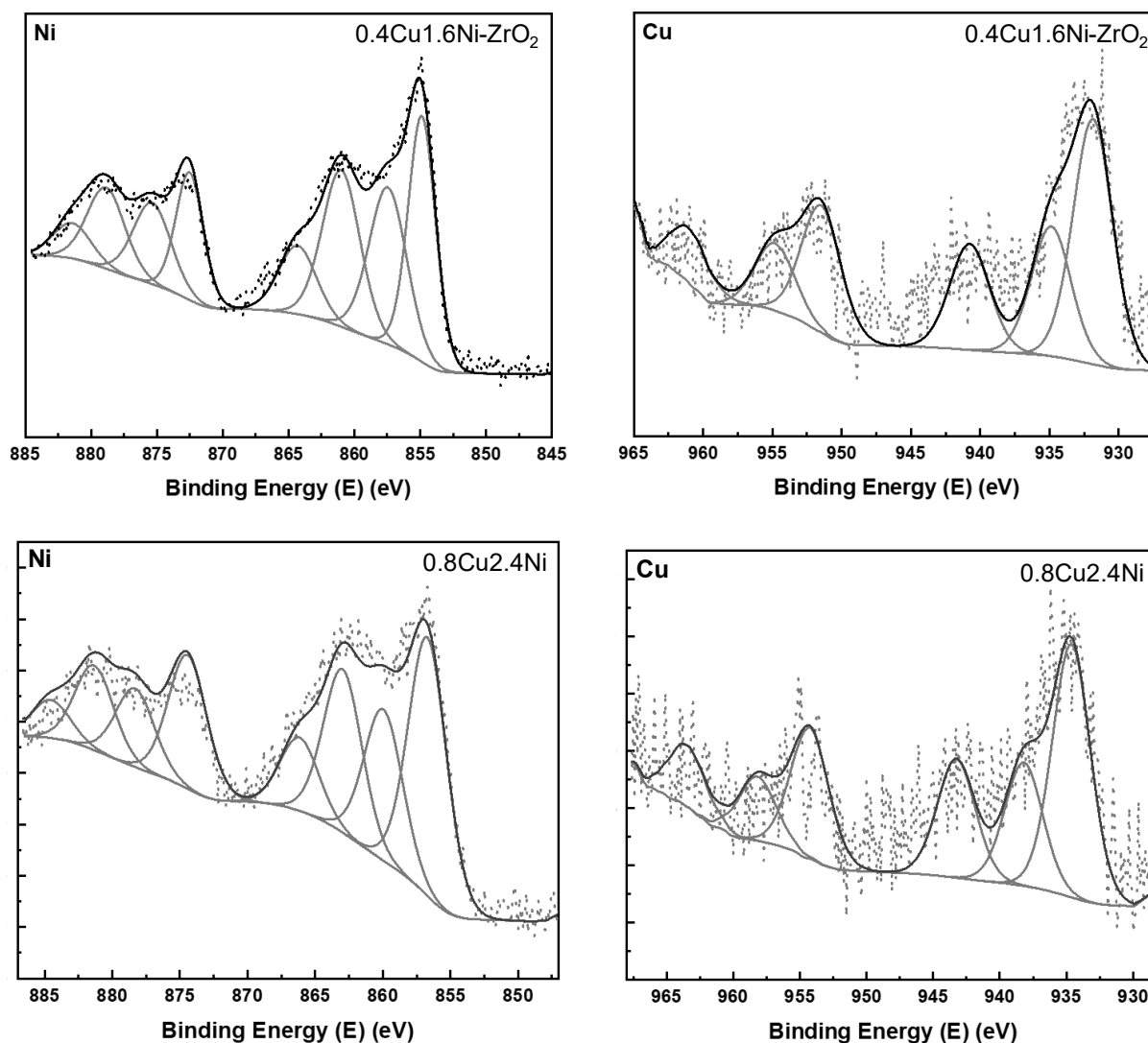


Figure 4.17. XPS of Ni and Cu of 0.4Cu1.6Ni-ZrO₂ compared to 0.8Cu₂.4Ni.

Non-oxidative ethanol dehydrogenation was performed with 118 mg of 0.4Cu1.6Ni-ZrO₂, which contains the same amount of Cu (0.007 mmol) used in the catalytic testing for all NU-1000-supported catalysts. Due to the higher thermal stability of ZrO₂, the reaction was performed from 175-350°C, and the resulting TOS plot is shown in **Figure 4.18(a)**. Compared to the TOS plot of 0.8Cu₂.4Ni [**Figure 4.9(a)**], the onset of the reaction occurs at a higher temperature of 225°C compared to that of 175°C in 0.8Cu₂.4Ni. The ethanol conversion for

0.4Cu1.6Ni-ZrO₂ below 350°C does not exceed 1.0%, while 0.8Cu2.4Ni achieves a conversion of 1.0-4.0% as the temperature increases from 175°C to 250°C.

A comparison of selectivity was also performed for the two systems, as shown in **Figure 4.18(b)-(c)**. For 0.8Cu2.4Ni [**Figure 4.18(c)**], the major product observed was acetaldehyde at all temperatures, with a negligible amount of ethylene and diethyl ether produced at above 250°C through the ethanol dehydration route. The production of CO and CH₄ was observed at all temperatures due to acetaldehyde decomposition, which originates from the acetaldehyde formation through the ethanol dehydrogenation route.⁷⁷ Meanwhile, 0.4Cu1.6Ni-ZrO₂ exhibits less selectivity towards acetaldehyde above 250°C, generating more significant amounts of diethyl ether and ethylene. Overall, the reactivity results show that NU-1000-supported NiCu catalysts exhibit higher reactivity for non-oxidative ethanol dehydrogenation and greater selectivity towards acetaldehyde than the ZrO₂-supported NiCu catalyst under the same catalytic conditions tested.

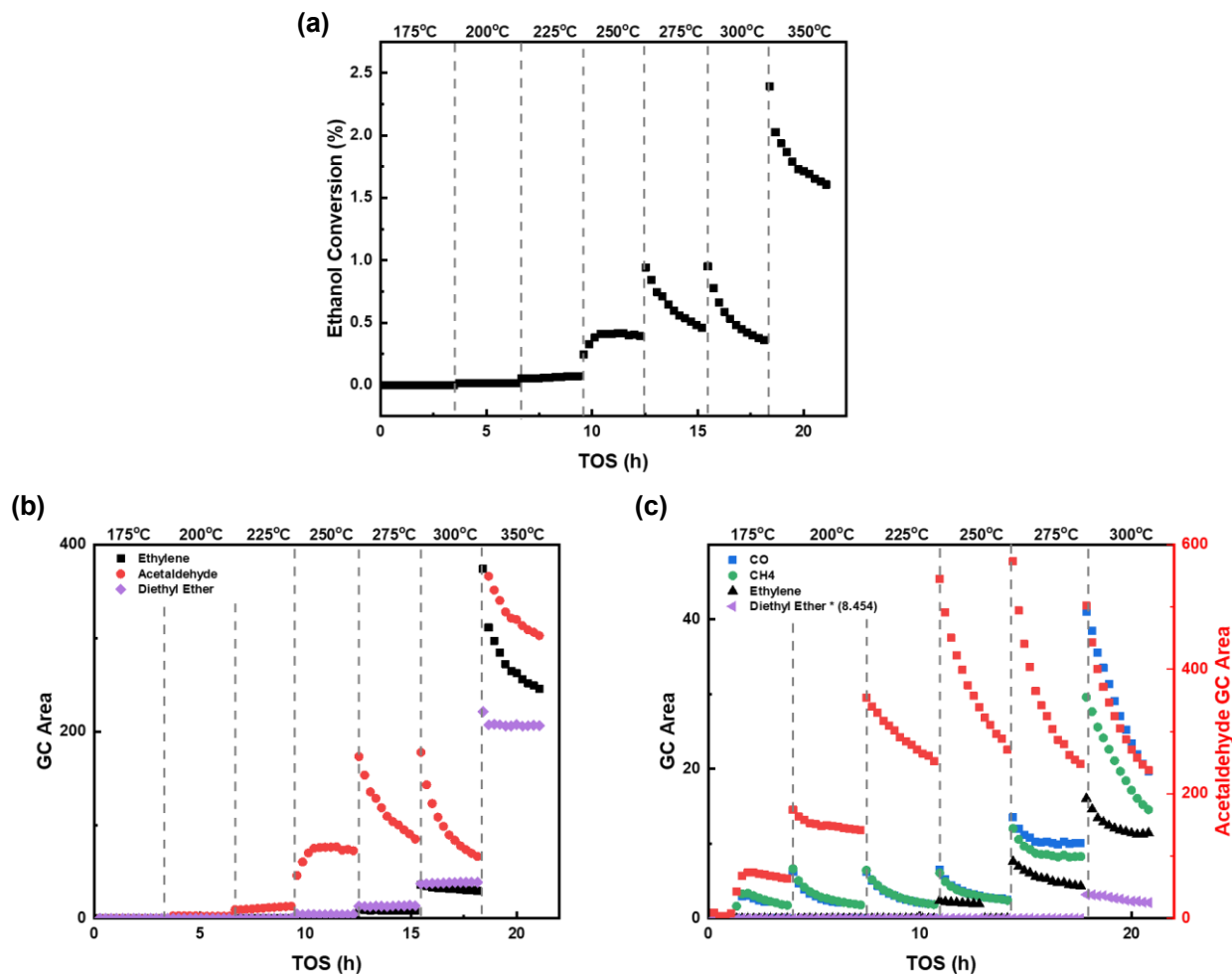


Figure 4.18. (a) Time-on-stream (TOS) plot of $0.4\text{Cu}1.6\text{Ni-ZrO}_2$ from 175-350°C. (b) GC area plot of all products for $0.4\text{Cu}1.6\text{Ni-ZrO}_2$. (c) GC area plots for $0.8\text{Cu}2.4\text{Ni}$.

4.11 Post-Catalysis Characterizations

Compared to the fresh catalysts after the NaBH_4 treatment, more nanoparticles appear on the NU-1000 crystallites after catalysis [Figure 4.19(a)-(c)] with broader size distributions, changing from 5~10 nm to 5~16 nm in diameters [Figure 4.19(d)-(i)]. These observations can be explained by the presence of sub-nm clusters within the micropores and c-pores of NU-1000-FF in the as-made samples, and some of those sub-nm clusters remained after the initial NaBH_4 treatment. However, under reaction conditions where H_2 is generated as a side product at elevated temperatures, those metal species became mobile, resulting in the formation of more

nanoparticles over extended times on stream. This increase in the number and size of nanoparticles, in conjunction with the catalyst deactivation at 250°C as seen in the TOS plot in **Figure 4.9(a)**, illustrates that the active species responsible for the catalytic turnover is the sub-nm clusters residing in the pores of NU-1000.¹⁹³

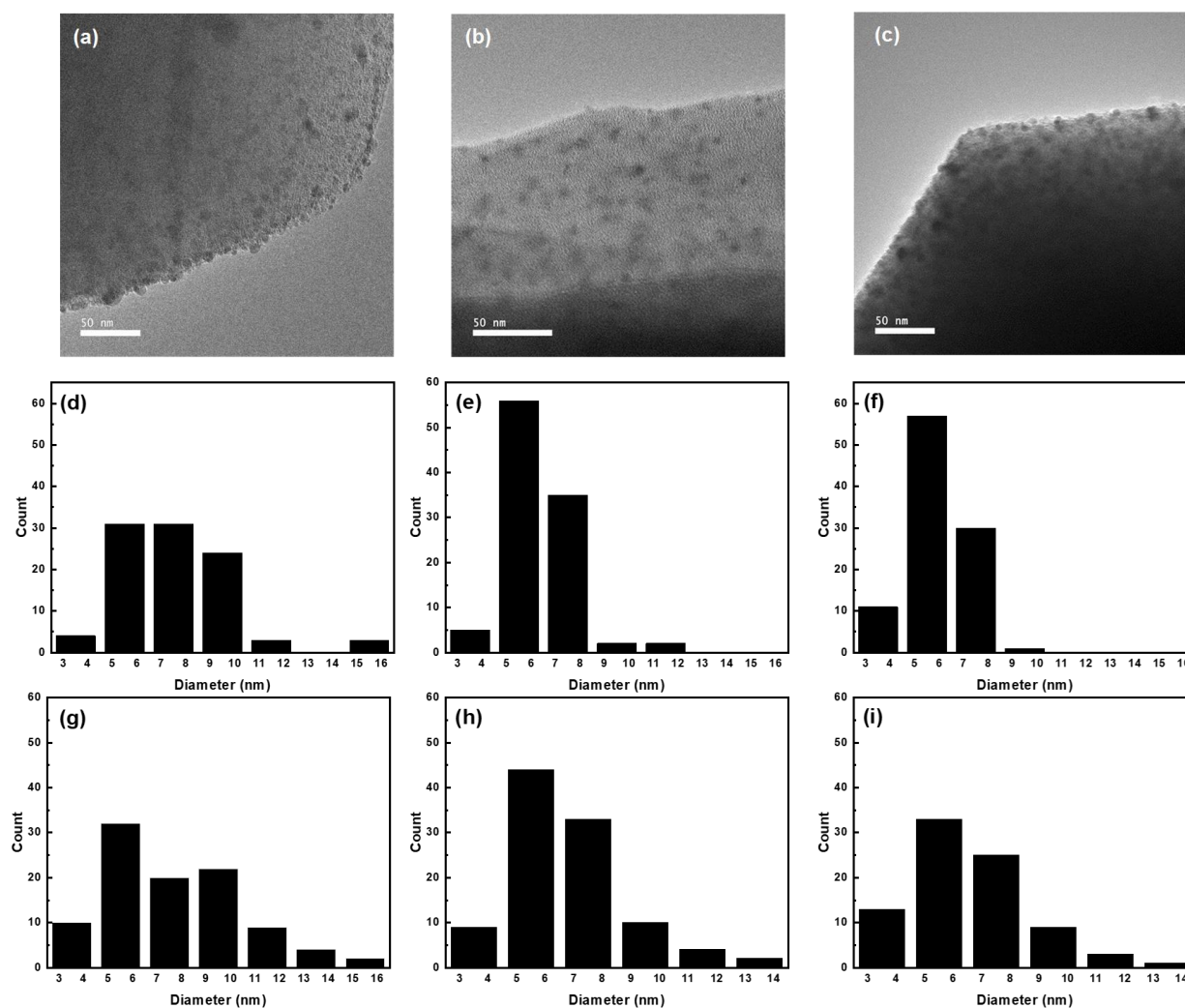


Figure 4.19. (a)-(c) TEM images of 2.4Cu0.1Ni, 1.7Cu2.1Ni, and 0.8Cu2.4Ni, respectively, after non-oxidative dehydrogenation from 175~300°C. (d)-(f) Particle size distributions before reactions of 2.4Cu0.1Ni, 1.7Cu2.1Ni, and 0.8Cu2.4Ni, respectively. (g)-(i) Particle size distributions after reactions of 2.4Cu0.1Ni, 1.7Cu2.1Ni, and 0.8Cu2.4Ni, respectively.

The thermal stability of the samples of the as-made catalysts after NaBH₄ treatment and after catalysis was compared with TGA, and the results are displayed in **Figure 4.20(a)-(d)**.

Before catalysis, two consecutive weight-loss stages can be observed at 275°C and 315°C, respectively. Quantification was performed to discern the origin of the weight loss, where the mass of the linker was calculated based on the starting mass and compared with the total weight loss. The quantification suggests that extra mass is present in 2.4Cu0.1Ni and 1.7Cu2.1Ni in addition to the Zr₆ nodes, NiCu species, and linkers, which could come from the hydroxyl and aqua ligands attached to the nodes and the NiCu species. Meanwhile, 0.8Cu2.4Ni showed some loss of linkers before catalysis. After catalysis, the first weight loss stage in all samples is less resolved [**Figure 4.20(d)**], suggesting that the catalysts have partially decomposed during the reaction steps above 200°C. The quantification also corroborates such observations, where 3-25% of the linker mass was lost during catalytic testing.

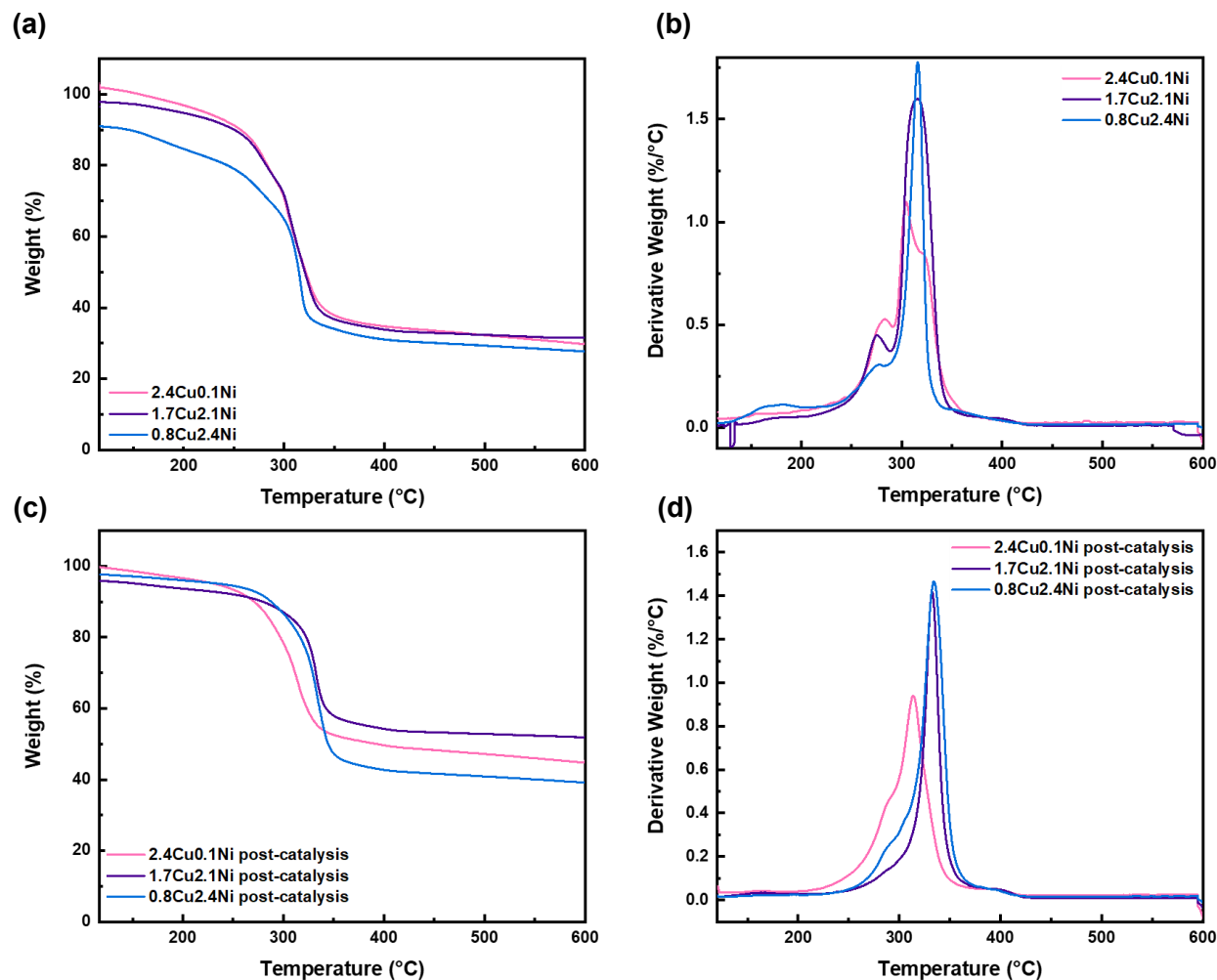


Figure 4.20. Thermogravimetric analysis of the fresh catalysts (top) and the catalysts after non-oxidative ethanol dehydrogenation (bottom) from 115-600°C.

Table 4.3. Weight loss quantifications based on TGA results.

Sample	Starting mass (mg)	Total mass loss (mg)	Stoich. linker mass (mg)	Excess mass (mg)	% linker lost during catalysis
2.4Cu0.1Ni_Fresh	2.105	1.381	1.172	0.209	N/A
1.7Cu2.1Ni_Fresh	5.899	3.785	3.239	0.546	N/A
0.8Cu2.4Ni_Fresh	7.111	3.805	4.013	N/A	5%
2.4Cu0.1Ni_post-catalysis	2.323	1.159	1.293	N/A	10%
1.7Cu2.1Ni_post-catalysis	5.516	2.266	3.029	N/A	25%
0.8Cu2.4Ni_post-catalysis	6.458	3.540	3.645	N/A	3%

Post-catalysis PXRD and N₂ isotherms (**Figure 4.21-4.22**) showed a complete loss of crystallinity and porosity of NU-100 after catalytic testing, consistent with the observed deactivation and TGA curves (**Figure 4.20**). However, all synthesis, characterization, and catalytic testing were conducted consistently across all catalysts, ensuring the validity of internal comparisons among the three catalysts, despite MOF decomposition during extended times on stream. In contrast to characterization after extended reaction times, catalyst porosity was retained after ethanol DRIFTS experiments at 250 °C, which exposed catalysts to high temperatures for shorter periods (**Figure 4.23**), confirming that loss of porosity is a slow process. We note that the lower N₂ uptake is due to the sample tested being a mixture of 2.4Cu0.1Ni and diluent used in the DRIFTS study.

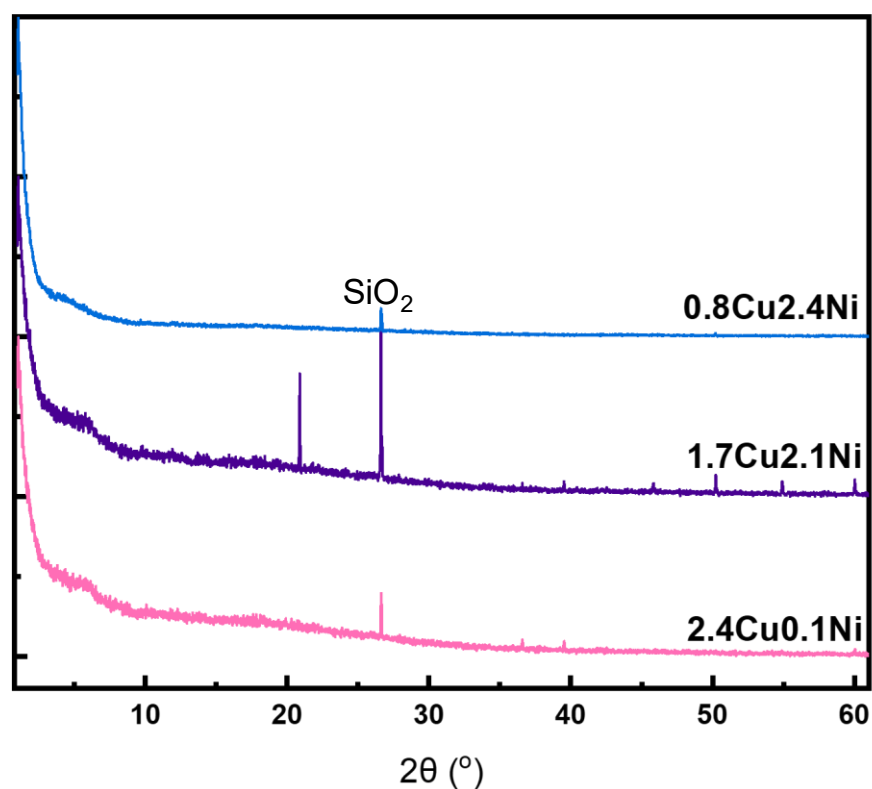


Figure 4.21. PXRD patterns of the post-catalysis samples.

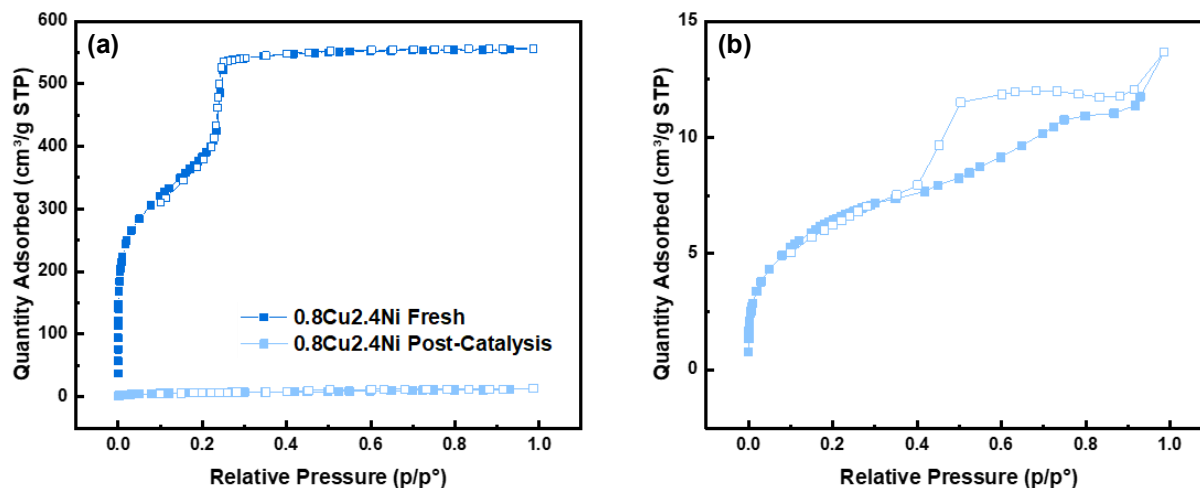


Figure 4.22. (a) N_2 isotherms of 0.8Cu2.4Ni before and after catalysis. (b) Zoomed-in view of the N_2 isotherm of 0.8Cu2.4Ni after catalysis.

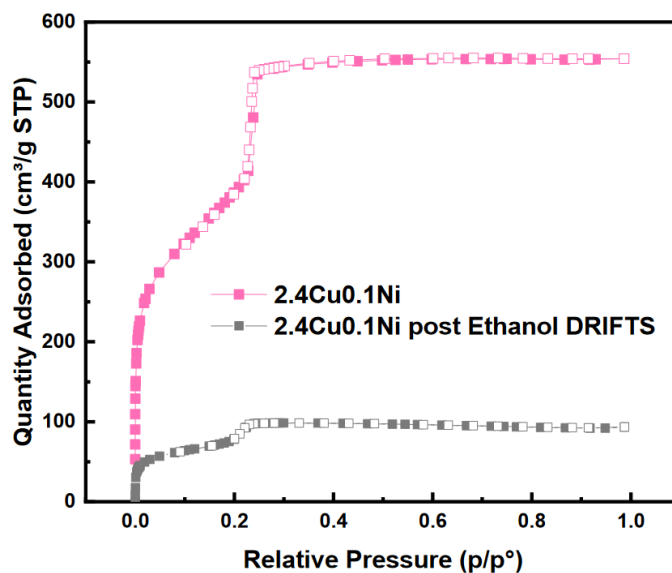


Figure 4.23. N_2 isotherm of 2.4Cu0.1Ni after ethanol DRITS showing retained porosity.

Post-catalysis XPS of 2.4Cu0.1Ni shows both Cu^0/Cu^+ and Cu^{2+} species after the reaction [Figure 4.24(a)], at energies characteristic of the bulk metal and oxides, consistent with the formation of large NPs in this sample. The Cu features in both 1.7Cu2.1Ni and 0.8Cu2.4Ni have also shifted to 933–934 eV, consistent with NP growth, but they cannot be readily separated into Cu^0/Cu^+ and Cu^{2+} species. This is in part due to the low signal-to-noise ratio. However, there is a strong satellite peak, suggesting that the detected Cu is predominantly in the Cu^{2+} state [Figure

4.24(b)-(c)].^{185, 186} Meanwhile, Ni remained in the 2+ state in all samples. Those results further signify the role of Ni²⁺ in suppressing Cu reduction during catalysis.

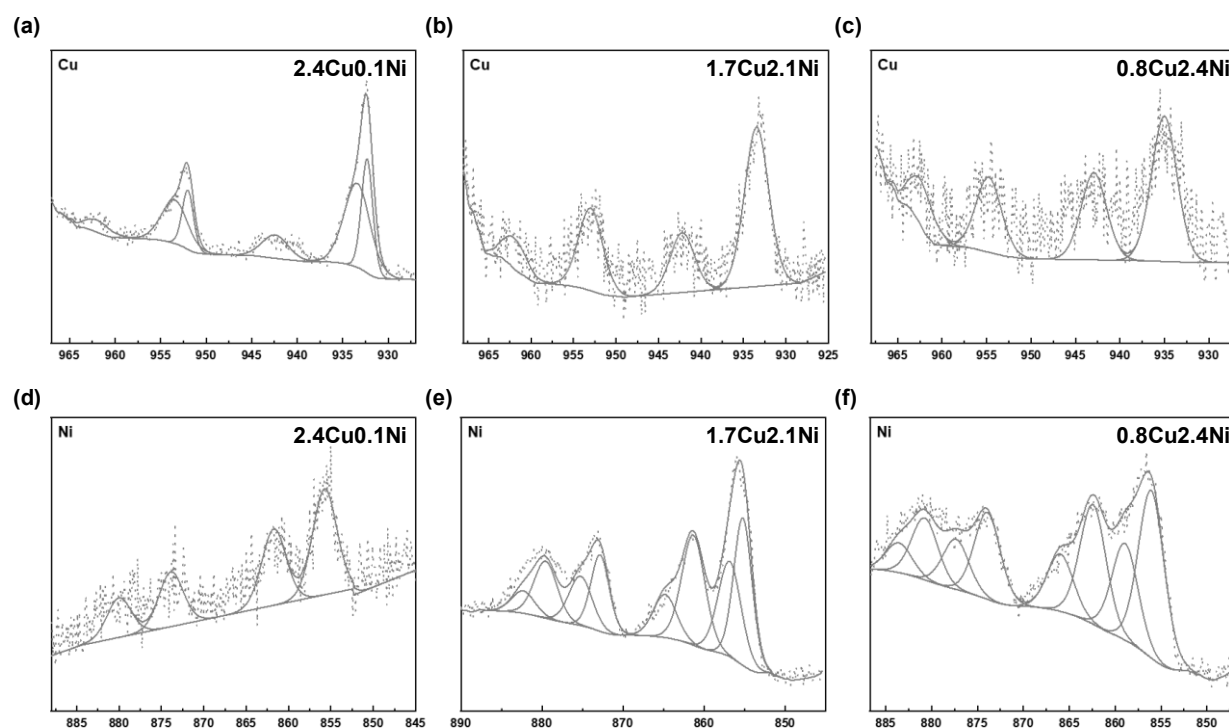


Figure 4.24. (a)-(c) Post-catalysis XPS of Cu in 2.4Cu0.1Ni, 1.7Cu2.1Ni, and 0.8Cu2.4Ni. (d)-(f) Post-catalysis XPS of Ni in 2.4Cu0.1Ni, 1.7Cu2.1Ni, and 0.8Cu2.4Ni.

4.12 Chapter Conclusions

In conclusion, we successfully achieved the synthesis of NiCu bimetallic catalysts at various Cu:Ni ratios using MOF NU-1000 as the support. Catalysts of higher Ni content reduce the activation energy for non-oxidative ethanol dehydrogenation. The possible roles of Ni²⁺ as a promoter in this system include suppressing the formation of large nanoparticles at the expense of the more active sub-nm cluster species under reaction conditions, delaying Cu²⁺ reduction, as well as decreasing the barrier of the β C-H bond scission at the interface of the Zr₆ nodes and the mixed-metal-oxide nanoparticle surfaces. This study illustrates how MOFs' structural uniformity

and pore confinement can be leveraged to systematically fine-tune catalyst compositions and realize the effects of such modifications on the nature of the catalytic active sites.

4.13 Additional Information

4.13.1 Materials

NU-1000 and its linker, 1,3,6,8-(p-benzoate)pyrene,¹⁵⁵ were synthesized according to prior procedures using 1,3,6,8-tetrabromopyrene, (4-(ethoxycarbonyl)phenyl)boronic acid, K₃PO₄, (PPh₃)₄Pd, ZrOCl₃·8H₂O, benzoic acid, HCl, dioxane, acetone, and DMF, which were purchased and used as received from Sigma Aldrich Chemicals Company, Inc. The Ni precursor, bis(N,N"-di-*t*-butylacetamidinato)nickel(II), Ni(amd)₂, and the Cu precursor, bis(dimethylamino-2-propoxy)copper(II), Cu(dmap)₂, were purchased from Strem Chemicals. Anhydrous heptane was prepared using a solvent purification system. Ultrapure water (18.2 MΩ•cm) was obtained from a Millipore Milli-Q-Biocel A10. All other species were obtained from Sigma Aldrich and used as received.

4.13.2 Synthesis

NU-1000, formate-free NU-1000 (NU-1000-FF). NU-1000 and NU-1000-FF were synthesized according to literature, and their structures were confirmed by ¹H NMR.^{32, 124} Powder XRD and N₂ physisorption at the normal boiling point confirmed that porosity and structure were retained after heat treatments. Residual formate on the nodes was quantified from ¹H NMR (**Figure S1**).

Synthesis condition optimizations. Small-scale (10 mg of NU-1000-FF) syntheses were first developed. In a typical 10 mg synthesis, an oven-dried 2-dram glass vial was first transferred into an Ar-filled glovebox. The metal precursors were then each weighted and transferred into the vial and dissolved in 6 mL of anhydrous heptane. A shaker plate inside the glovebox was

then used to facilitate precursor dissolution, which typically takes 1~2 hours. Upon complete dissolution of the precursors, 10 mg of activated NU-1000-FF was then added to the solution. For room-temperature syntheses, the vial was kept in the glovebox for 24 hours. Subsequently, five times of solvent exchange with fresh anhydrous heptane over the span of 24 hours. The vial was then transferred out of the glovebox, and the sample was washed with acetone three more times before transferring into a 70°C vacuum oven.

For syntheses at 70°C, the vial containing a mixture of NU-1000-FF and precursor solution was removed from the glovebox and transferred into a 70°C oven. The mixture was kept in the oven for 16 hours, followed by four times of solvent exchange with fresh heptane and three times of acetone washes. The sample was dried in a 70°C vacuum oven.

The resulting Cu and Ni loadings on a per-node basis show that the approximate Cu:Ni ratios incorporated in the MOF crystallites are relatively constant when the synthesis is performed with the same amount of Cu(dmap)₂ and Ni(amd)₂. However, the nodes were less saturated when syntheses were performed at room temperature. To ensure a more consistent total metal loading, we opted for syntheses at 70°C. The chosen synthetic conditions are boldened in **Table 4.4**.

Table 4.4. Synthetic condition screening at 10-mg scale.

Conditions	Mass of Cu(dmap) ₂ (mg)	Mass of Ni(amd) ₂ (mg)	Cu per node	Ni per node	Cu:Ni
7:1 Cu:Ni, RT	6.0	0.6	1.6	0.4	4.7
6:2 Cu:Ni, RT	5.1	1.2	1.5	0.5	2.7
4:4 Cu:Ni, RT	3.4	2.5	1.4	1.0	1.3
2:6 Cu:Ni, RT	1.7	3.7	0.5	1.3	0.3
1:7 Cu:Ni, RT	0.9	4.3	0.7	1.6	0.3
7:1 Cu:Ni, 70°C	6.0	0.6	3.8	0.7	4.8
4:4 Cu:Ni, 70°C	3.4	2.5	2.8	1.1	2.4
2:6 Cu:Ni, 70°C	1.7	3.7	1.7	2.1	0.7
1:7 Cu:Ni, 70°C	0.9	4.3	1.1	4.2	0.2

2.4Cu0.1Ni, 1.7Cu2.1Ni, 0.8Cu2.4Ni. Large-scale syntheses were then carried out using Cu(dmap)₂:Ni(amd)₂ precursor molar ratios of 1:7, 2:6, and 7:1 deposited at 70°C at the 150-mg scale. In a typical synthesis, Cu(dmap)₂ and Ni(amd)₂ were weighed and transferred into an over-dried 250 mL bottle inside an Ar-filled glovebox. The amount of the Cu and Ni precursors are summarized in **Table 4.5**. The precursors were dissolved in 90 mL anhydrous heptane, and 150 mg (0.047 mmol based on the NU-100-FF formula unit) of NU-1000-FF was added to the precursor solution. The bottle was sealed, transferred to a 70°C oven for 16 h, and cooled to room temperature. The liquid was then decanted, and the solids were washed four times with heptane and three times with acetone. The washed sample was dried at 70°C under dynamic vacuum for 1 h and stored in a desiccator.

Samples were reduced with NaBH₄ to create NiCu nanoparticles. 150 mg of the as-prepared sample was suspended in 15 mL methanol in a 100 mL round-bottom flask. 67 mg NaBH₄ and 67 mL methanol were added to a second 100 mL round bottom flask. Both flasks were purged with N₂, and the NaBH₄ solution was transferred into the flask with the solid. The mixture was stirred under N₂ for 1 h. The liquid was decanted, and the solid was washed three times with methanol and three times with acetone, dried at 70°C under dynamic vacuum, and stored in a desiccator.

Table 4.3. Quantities of precursors used in 150-mg-scale syntheses.

Sample ID	Cu:Ni precursor molar ratio	Mass of Cu(dmap) ₂ (mg)	Mass of Ni(amd) ₂ (mg)
2.4Cu0.1Ni	7:1	90	9
1.7Cu2.1Ni	2:6	26	56
0.8Cu2.4Ni	1:7	13	65

0.4Cu1.6Ni-ZrO₂. As a comparative system, the ZrO₂-supported NiCu catalyst was synthesized based on a modified procedure from the literature.¹⁹⁴ First, 5.0 mL of glycerol was added into a

100 mL round-bottom flask under vigorous stirring, followed by the addition of 174.5 mg (0.6 mmol) of $\text{Ni}(\text{NO}_3)_2 \cdot 6\text{H}_2\text{O}$ and 145 mg (0.6 mmol) of $\text{Cu}(\text{NO}_3)_2 \cdot 3\text{H}_2\text{O}$. The resultant mixture was stirred until completely dissolved. Then, 2.0 g of ZrO_2 was added, followed by adding 10 mL of buffer (pH = 7). The reduction was performed through the addition of 6.0 mL hydrazine monohydrate. The mixture was stirred overnight, and the solid was recovered through centrifugation. The solid was then washed several times with a mixture of acetone and water. After this, the solid was dried in a 70°C vacuum oven overnight and stored in a vacuum desiccator. Before catalytic testing, the sample was further reduced in a flow of H_2 at 200°C for 2 hours.

4.13.3 Catalytic Testing Details

Non-oxidative ethanol dehydrogenation was carried out using a quartz tube packed bed reactor in the Reactor Engineering and Catalyst Testing core facility at Northwestern. The reaction temperature was controlled with a K-type thermocouple at the top of the catalyst bed. Catalysts were typically diluted with 500 mg of trace-metal grade silica, and an additional 1 g of silica was added on top of the diluted catalyst bed to avoid cross-contamination on the thermocouple. All catalyst samples contained approximately 0.007 mmol Cu, and the bed height was approximately 0.8 cm. Catalysts were pre-treated under 20 sccm of 20% O_2/N_2 and a 10°C/min ramp to 250°C with a hold of 2 h. This removes water and prevents the autoreduction of Cu.⁸³ Pressure was ~10 psig using a back-pressure regulator directly downstream from the reactor. After pretreatment, the temperature was decreased to 150°C, and the catalyst was exposed to a combined stream of 100 sccm N_2 and 7 sccm EtOH introduced through a vaporizer. Products were analyzed with an Agilent GC-FID with a GS-Gaspro column (30 m x 0.32 mm). Ethanol reaction rates were normalized to total moles of Cu ($\text{mol}_{\text{EtOH}} \cdot \text{mol}_{\text{Cu}}^{-1} \cdot \text{s}^{-1}$).

4.13.4 Instrumentation

N₂ physisorption was carried out with a Micromeritics Tristar II 3020 at the normal boiling point of N₂. Brunauer-Emmett-Teller (BET) surface areas were determined from $P/P_0 = 0.005-0.1$, and pore size distributions were modeled with a DFT carbon slit-pore model and an N₂ kernel. Before measurement, materials were dried at 70°C in a vacuum oven, then further activated under dynamic vacuum in a Micromeritics SmartVacPrep at 80°C for 48 h for metal-containing samples and 120°C for 24 hours for NU-1000-FF.

Thermogravimetric Analysis (TGA) was conducted in high-res mode on a TA Q500 TGA instrument. The temperature was ramped from room temperature to 110°C at a ramp rate of 5°C/min in a flow of 90 sccm N₂. The sample was held at 110°C for 1 hour, and the gas was then switched to 90 sccm 10% O₂/N₂. The temperature ramp was resumed at a ramp rate of 5°C/min to 650°C.

Inductively coupled plasma-optical emission spectroscopy (ICP-OES) was run on a Varian Vista-MDX model ICP-OES spectrometer. 2-3 mg of the sample was digested in 2 mL nitric acid in a Biotage microwave reactor at 150 °C for 15 min. Portions were diluted 30-fold with ultrapure water for analysis, and emissions at 231.604 and 221.647 nm (Ni); 339.198, 343.823, and 327.305 nm (Zr); and 327.396, 324.754, 224.700, and 219.958 nm (Cu) were compared to standards.

X-ray diffraction used an STOE STADI P powder diffractometer set to 40 kV and 40 mA, an asymmetrically curved germanium monochromator (Cu K α 1 radiation, $\lambda = 1.54056 \text{ \AA}$), and a one-dimensional silicon strip detector (MYTHEN2 1K from DECTRIS). Sample crystallinity was assessed at room temperature in transmission mode in a rotating holder at $4^\circ 2\theta \text{ min}^{-1}$ and a 0.05° step width. Difference Envelope Density (DED) analyses used ~20 mg sample in a capillary tube

and collection from $1\sim 100^\circ 2\theta$. Envelope maps were generated via the procedure of Yakovenko et al.¹⁹⁵

X-ray photoelectron spectra (XPS) were acquired on a Thermo Scientific ESCALAB 250 Xi (Al K α radiation, 1486.6 eV) with an electron flood gun and spectra calibrated to the C 1s (284.8 eV). XPS characterization following H₂ treatment was carried out as follows to eliminate air exposure: Samples were loaded into an *in-situ* cell typically used infrared spectroscopy: The cell was purged with Ar at room temperature, ramped to the specified temperature under 5% H₂/N₂, held for at least 2 hours, then cooled to room temperature. Isolation valves were closed, and the entire cell transferred into an Ar-filled glovebox. Within the glovebox, the sample was removed and mounted inside an air-free transfer chamber for XPS measurements.

Transmission Electron Microscopy (TEM) used a JEOL ARM200CF Aberration-Corrected TEM at 200eV. Samples were suspended in acetone and then drop-cast on Holey carbon grids (400 mesh).

¹H nuclear magnetic resonance (NMR) spectra were collected on a 500 MHz Bruker S4 Avance III with a DCH CryoProbe. Chemical shifts are reported relative to tetramethylsilane. Formate (8.38 ppm) was quantified by digesting ~2 mg sample in ~0.5 mL 0.1 M NaOD/D₂O, centrifuging, removing the supernatant, and further diluting the supernatant with an additional 0.5 mL D₂O. After 64 scans, the integrated area was compared to prior calibrations.

In-situ Diffuse Reflectance IR Fourier Transform Spectroscopy (DRIFTS) was carried out with a Thermo-iS50 spectrometer. Powder samples were diluted 10:1 with ground KBr and loaded into the cell. The pretreatment consisted of a ramp to 250 °C under 100 sccm Ar, then 2 hr under 100 sccm 20% O₂/N₂. The gas was returned to Ar, and background spectra were collected at 250°C,

200°C, and 150°C in Ar after an hour of stabilization at each point. After background collection, 100 sccm Ar was flowed through a bubbler containing anhydrous ethanol and then into the DRIFTS cell. Spectra were collected every minute until no further changes were observed, indicating surface saturation. The gas was switched to pure Ar to purge the gas-phase and physisorbed surface specie, and difference spectra (with respect to the background in Ar) were collected each minute until no noticeable changes were observed. The procedure was then repeated at 200°C and 250°C.

Chapter 5. Investigating the Heterolytic Splitting of S-Containing Molecules on A Thermally Distorted Zr-Based Metal-Organic Framework

Portions of this chapter appear in the following manuscript:

Wang, Q.; Melix, P; Formalik, F.; Zhihengyu, C.; Vornholt, S.; Tufaro, L.; Chapman, K.W.; Snurr, R.; Hupp, J.T.; Notestein, J.M. “Experimental and Computational Insights into the Heterolytic Splitting of Sulfur-Containing Molecules on a Metal-Organic Framework.” *In preparation*

5.1 Chapter Summary

The sulfidation of metal oxides is a critical process to create catalysts for industrially relevant reactions. However, the exact sulfidation mechanism remains unclear. To investigate the sulfidation through the heterolytic splitting of S-containing molecules, we chose a structurally well-defined material, Zr-based metal-organic framework (MOF) NU-1000, as the model system to create partially sulfided Zr_6 clusters with well-defined structures through thermal treatment. Various spectroscopic characterizations and computational studies showed that thiols bearing different functional groups interact with the distorted Zr_6 nodes through dissociative adsorption, forming bridging Zr-S-Zr bonds at the expense of the heterolytic cleavage of the S-H bonds. This study provides crucial insights into the surface sites responsible for the sulfidation of metal oxide catalysts and offers a novel strategy for introducing S-bearing moieties to MOF scaffolds.

5.2 Challenges in Elucidating the Sulfidation Mechanisms of Metal Oxides

The sulfidation of metal oxide catalysts has been implemented to alter their catalytic activity. Many sulfide catalysts exhibit excellent activities for a variety of industrially relevant oxidation reactions, such as hydrodesulfurization (HDS) on supported MoS_2 and WS_2 slabs,¹⁹⁶⁻¹⁹⁸ isobutane dehydrogenation on bulk MoS_2 ,¹⁹⁹ and the oxidative coupling of methane (OCM) on supported PdS.²⁰⁰ Compared to those commonly investigated metal sulfides, sulfided ZrO_2 receives less attention due to the harsh conditions required to sulfide this highly acidic oxide. The synthesis of stable ZrS_2 or ZrS_3 phases from either the Zr metal or ZrO_2 requires temperatures up to 900-1000°C.²⁰¹ Meanwhile, numerous studies have shown sulfided ZrO_2 surfaces to have high propane selectivity for the oxidative dehydrogenation of propane using S_2 as the oxidant²⁰² and high methanethiol selectivity for the hydrodesulfurization of methanol.²⁰³

To further realize other interesting properties of sulfided ZrO_2 , it is therefore imperative to novel strategy to create sulfided ZrO_2 sites at milder conditions.

In addition, despite the feasibility of sulfiding metal oxide catalysts to improve the catalytic performance for various reactions, it remains unclear which surface sites are responsible for the sulfidation and if all surface sites give rise to sulfide species of the same catalytic activities. The very few speculations on the active metal sulfide species or phase have primarily been based on bulk characterization techniques, and the proposed active sulfide phases were thus averaged structures.^{204, 205} The understanding of metal sulfide formation on a molecular level is still insufficiently investigated, mostly likely due to the disordered metal sulfide phases and ambiguous surface structure of the catalyst supports, which make probing one single type of active phase a challenging task.¹⁹⁶

In the late 90s, Ziolk et al.²⁰³ and Sugioka et al.²⁰⁶ made an effort to elucidate the sulfidation mechanisms of metal oxides using H_2S as the precursor. Using various surface characterization techniques, they proposed three possible mechanisms, namely (1) the exchange of surface oxygen to sulfur in the presence of H_2S , (2) the dissociation of H_2S towards HS^- and H^+ at an undercoordinated metal site on the metal oxide surface, and (3) the coordinative binding of H_2S to an electron-deficient metal site. Nonetheless, on a metal oxide surface of ambiguous surface structures, all the surface sites mentioned above could be present, and none of these mechanisms could be entirely excluded.²⁰⁷

One way to fully understand the nature of different types of active sites is to construct a material of uniform structure that can reduce the complexity of the interactions between substrates and the surfaces of the material. Zr-based Metal-organic framework (MOF) provides such a possibility to realize the nature of a single type of zirconia active sites, thanks to the

periodic arrangement of the metal ions or clusters (nodes) isolated by organic moieties (linkers). However, high temperatures (340~600°C) are usually employed for sulfidation,²⁰⁸⁻²¹⁰ and MOFs tend to lose their bulk crystallinity or decompose at those harsh reaction conditions.²¹¹

To date, most reported literature on the sulfidation of MOF systems used MOF as a sacrificial scaffold to generate graphene-supported metal sulfides through MOF pyrolysis,²¹² resulting in the loss of the long-range order and structural uniformity of the materials. In cases where the bulk crystallinity of the material was retained, the sulfidation occurs on MOF-supported metal oxide clusters using atomic-layer deposition techniques at a lower temperature of 125°C than that used in the typical sulfidation processes.^{113, 116, 213, 214} While the functionalization of the nodes of MOFs with sulfate has been achieved on various Zr-MOFs,^{83, 215, 216} to our knowledge, decorating the Zr₆ nodes with sulfide moieties while preserving the structural integrity of the MOF crystallites has yet to be reported.

5.3 Investigating Sulfidation through Heterolytic Splitting on Metal-Organic Framework

Opportunity emerges from recent investigations on NU-1000 ($[\text{Zr}_6(\mu_3\text{-O})_4(\mu_3\text{-OH})_4(\text{OH})_4(\text{H}_2\text{O})_4(\text{TBAPy})_2]_\infty$ (TBAPy = 1,3,6,8-(*p*-benzoate)pyrene)), a Zr-MOF constructed from oxo-Zr₆ nodes combined with pyrene-based tetratopic linkers. Those Zr₆ nodes exhibit distortion behaviors under heat, which gives rise to interesting properties such as the negative thermal expansion of the NU-1000 lattice.^{217, 218}

Recently, density-functional theory (DFT) studies predicted the presence of distortion on the Zr₆ nodes upon thermal treatment at 300°C. These distortions occur through reducing the connectivity of a μ₃-O on the node to μ₁, which creates empty coordination sites and generates highly Lewis basic O sites. The two features combined are proposed to carry out the heterolytic

splitting of NH_3 .¹¹⁸ The DFT-predicted node distortion are depicted in **Figure 5.1(a)**, which shows the distortion created through the detachment of one $\mu_3\text{-O}$ and the generation of an undercoordinated site without changing the 4+ oxidation state of the Zr cations. Upon the adsorption of one NH_3 molecule [**Figure 5.1(b)**], NH_3 undergoes heterolytic splitting, generating NH_2^- that binds to the empty coordination site along with the protonation of the Lewis basic O. Experimentally, NU-1000 that underwent thermal treatment at 300°C exhibited irreversible uptakes of NH_3 upon exposure to the NH_3 vapor at room temperature.

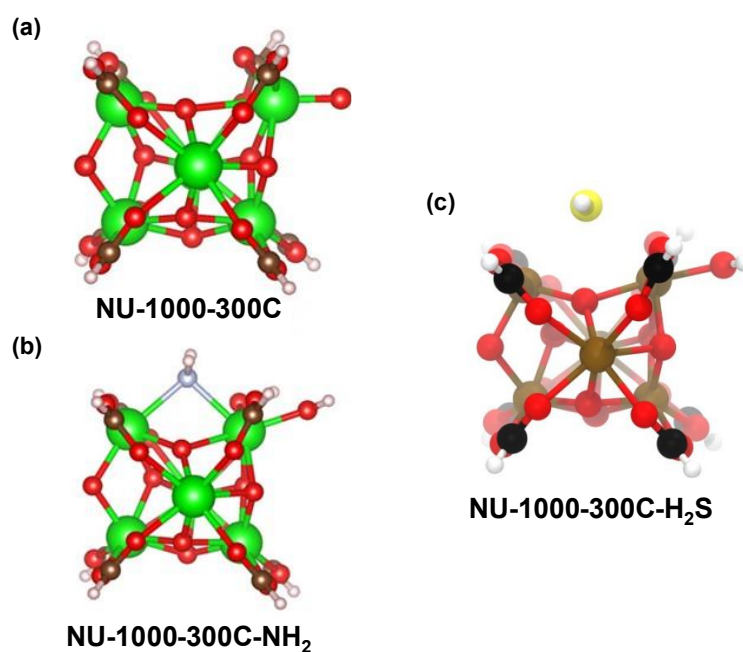


Figure 5.1. (a) DFT-optimized node structures at 300°C . (b) The most stable node- NH_3 complex formed through the heterolytic splitting of NH_3 . Color code: H-white, C-brown, N-cyan, O-red, and Zr-green. (c) Illustration of the node- H_2S complex formed through a similar heterolytic splitting mechanism. Color code: H-white, C-black, S-yellow, O-red, and Zr-brown. (a) and (b) are adapted with permission from ref 118. Copyright 2021 American Chemical Society.

5.4 The Incorporation of S-Containing Molecules onto Thermally Distorted NU-1000 Nodes

In this study, we aim to further explore the potential of those node distortion features in NU-1000 for the heterolytic splitting of S-containing molecules, including hydrogen sulfide [H_2S , as depicted in **Figure 5.1(c)**], alkyl thiols, aromatic thiols, and sulfides, through direct Zr-S bond

formation. In combination with computational modeling, this study would contribute to understanding sulfidation mechanism on zirconia surfaces on a molecular level. This work would also shed light on new possibilities in introducing functionality to MOF nodes.

5.5 Physical Characterizations

In this study, H₂S, ethanethiol (ET), 1-hexanethiol (1-HT), thiophenol (TP), diethylsulfide (DES), and thiophene (TPhen) were used to decorate the distorted Zr₆ nodes of NU-1000. The PXRD spectra of all samples were shown in **Figure 5.2(a)**, where the bulk crystallinity of the MOF was well retained for all samples that underwent liquid phase deposition. Both H₂S and thiophenol depositions resulted in some loss of long-range order of the MOF structure. However, the N₂ isotherms and the corresponding pore distributions of those two samples [**Figure 5.2(b)-(c)**] showed the porosity of modified NU-1000-FF-300C was retained. Despite the slight reduction of long-range crystallinity, NU-1000-FF-300C did not undergo significant degradation after the modifications.

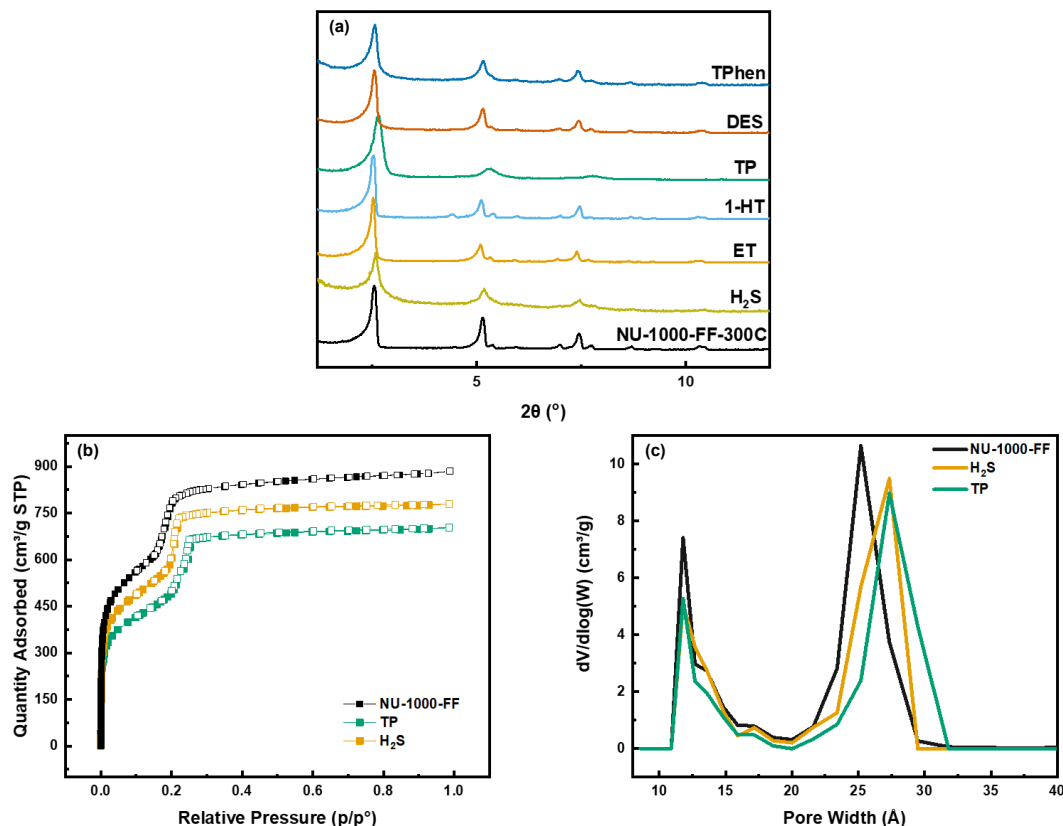


Figure 5.2. (a) PXRD patterns of the as-made samples. (b) N₂ isotherms of NU-1000-FF, TP, and H₂S. (c) DFT pore-size distributions of NU-1000-FF, TP, and H₂S.

5.6 Thiolate Quantifications

NMR integration was implemented for the quantification of thiolate species. Herein, the characteristic regions of the NMR spectra of the samples are shown in **Figure 5.3** for the thiol-containing samples. Upon examining the alkyl region of the spectra in **Figure 5.3(a)**, triplets originated from the terminal methyl group of the ethanethiol and 1-hexanethiol can be observed at 0.68 ppm and 0.82 ppm in the ET and 1-HT spectra, respectively. Those features are used to quantify the alkyl thiolates present in the samples, and the results are summarized in **Table 5.1**. Note that the quantifications are slightly overestimated due to the possibility of residual heptane from the synthesis, accounting for the terminal methyl groups on heptane molecules. Broad multiplet features at 1.05 ppm, 1.22 ppm, and 1.28 ppm are observed for ET, 1-HT, and TP,

respectively, which could originate from the methylene groups on either the alkyl thiols or the residual heptane solvent.

Figure 5.3(b) displays the aromatic regions of the ET, 1-HT, and TP NMR spectra. The most prominent features observed in this region are the different protons on the H₄TBAPy linkers of NU-1000. While no additional features are found in the spectra for ET and 1-HT, extra aromatic features can be observed in the 7.4~7.8 ppm region upon zooming in [**Figure 5.3(c)**], signifying the incorporation of thiophenol into NU-1000-FF-300C. The NMR spectra of the sulfide-containing samples are shown in **Figure 5.4**, where no characteristic features can be discerned due to the low sulfide loadings. Overall, the NMR spectra of the acid-digested samples confirmed the incorporation of the corresponding alkyl and aromatic thiols into NU-1000-FF-300C.

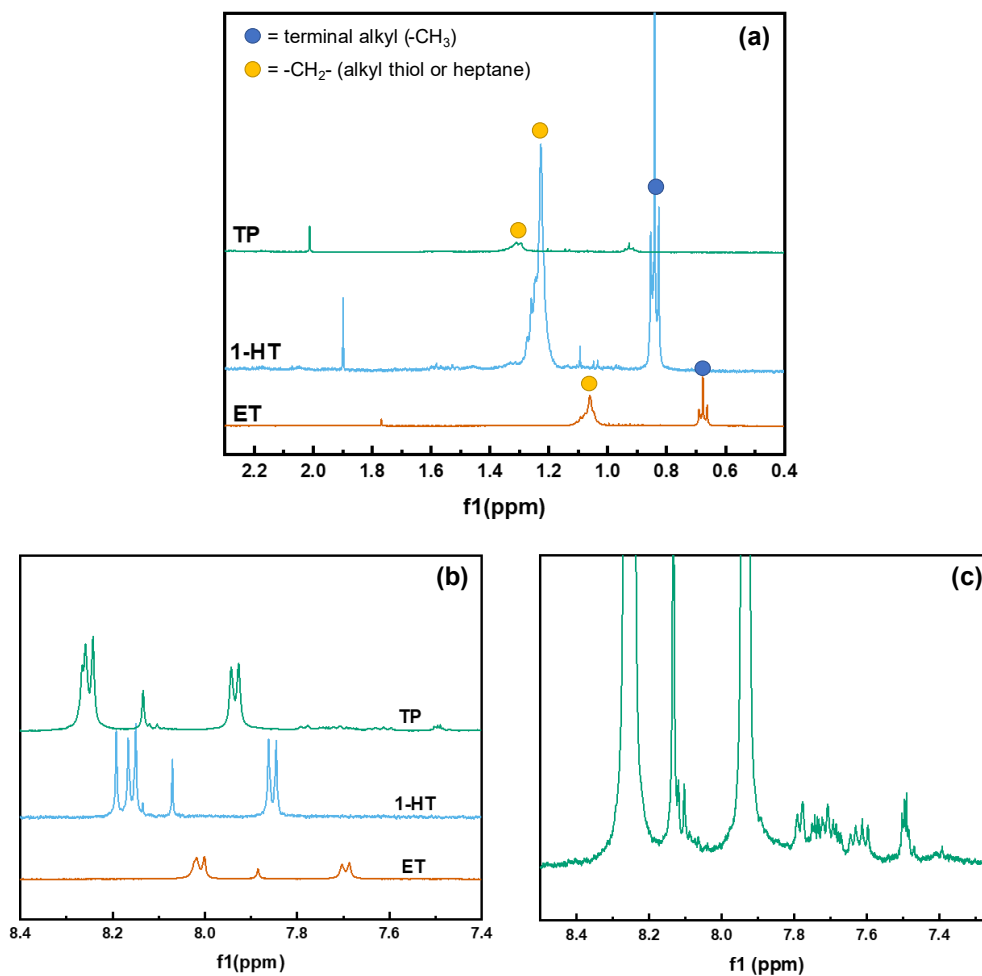


Figure 5.3. Acid-Digested NMR spectra for NU-1000-300C modified with ethanethiol (orange), hexanethiol (blue), and thiophenol (green) in the (a) alkyl region and (b) aromatic region. (c) A zoomed-in view of the spectrum for thiophenol in the 7.3~8.5 ppm region, showing the presence of additional aromatic features attributed to the presence of thiophenolate rings.

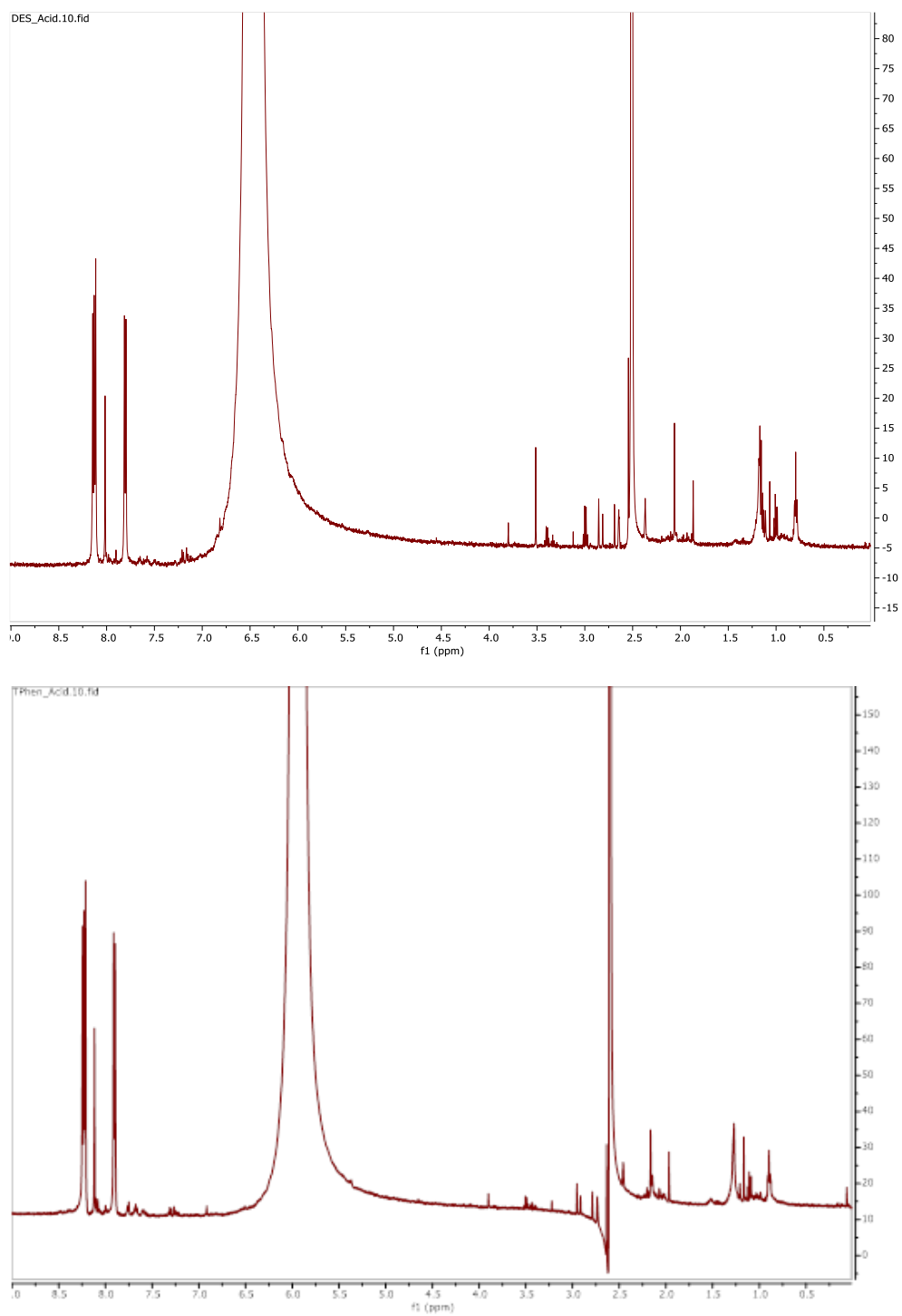


Figure 5.4. The NMR spectra for DES (top) and TPhen (bottom). Integration was not performed due to the low diethyl sulfide and thiophene loading in the acid-digested samples.

Sulfur XPS was performed to analyze the sulfur speciation and quantify the thiolate contents in the H₂S- and thiol-modified samples, as displayed in **Figure 5.5(a)-(d)**. On the surface of the MOF crystallites, two types of sulfur species are observed for all samples, as highlighted in green and pink, respectively. The two peaks at *ca.* 163 and 164.5 eV are assigned to the S 2p 3/2, and S 2p 1/2 transitions thiolate species originated from the heterolytic splitting of the S-containing molecule,²¹⁹ as depicted in the insert of **Figure 5.5(a)**. The two peaks at 167.6 and 168.9 eV are attributed to the S 2p 3/2 and S 2p 1/2 of the sulfate species from air oxidation after synthesis. The dominant species for all samples, except for H₂S and TP, are sulfates. All the BE values for the thiolate species are tabulated in **Table 5.1**, where the binding energies of the thiolate peak in all samples are around 163 eV, suggesting that the thiolate species are in the same oxidation states. Quantification was also performed for all samples using the thiolate peak areas in the S 2p XPS spectra. Comparing the quantification values obtained from XPS and NMR, the thiolate loadings are in good agreement.

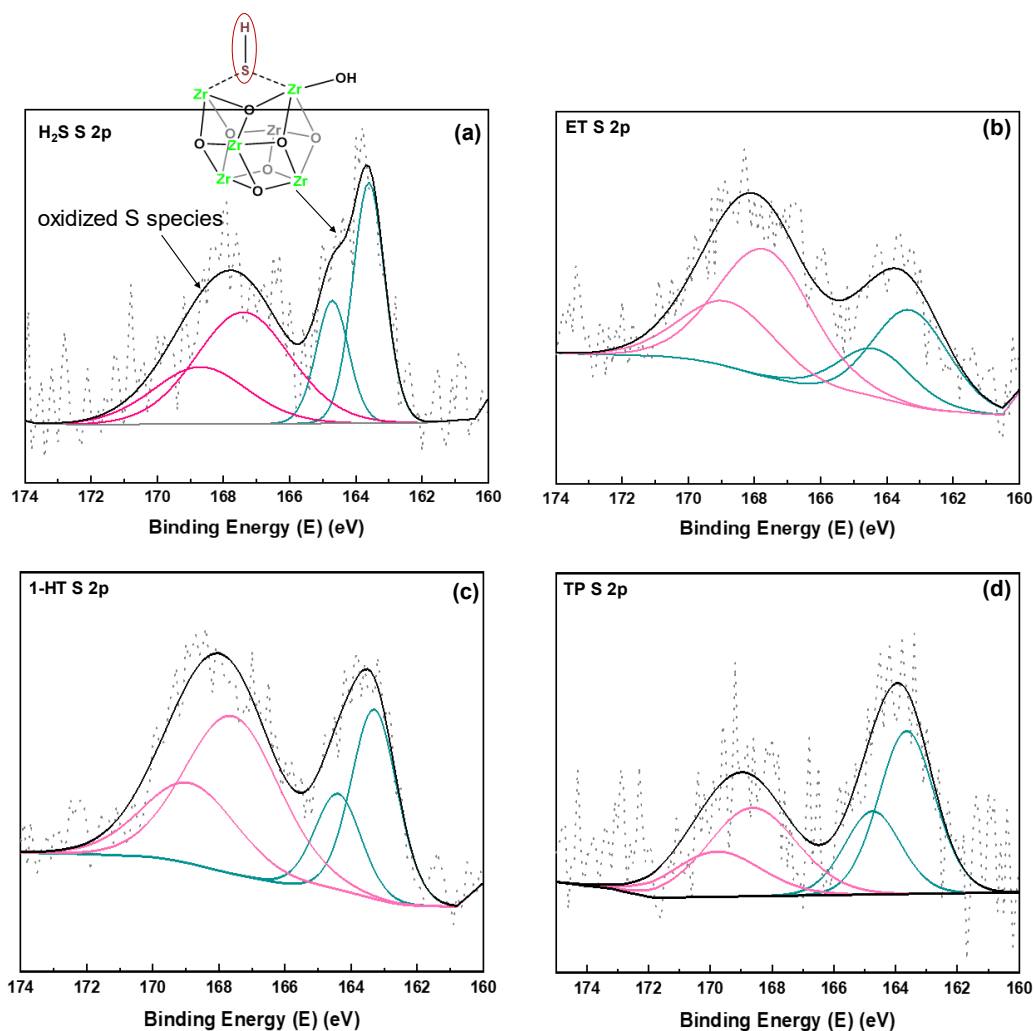


Figure 5.5. Fitted XPS S 2p spectra of NU-1000-FF-300C modified with (a) H₂S, (b) ethanethiol, (c) 1-hexanethiol, and (d) thiophenol.

Table 5.1. S binding energies and thiolate quantifications for all samples.

Sample	Thiolate S 2p _{3/2} BE (eV)	Thiolate per Zr ₆ node via XPS ^a	Thiolate per Zr ₆ node via NMR ^b
H ₂ S	163.2	0.3	-
ET	163.0	0.5	0.4
1-HT	163.3	0.9	1.3
TP	163.1	2.0	-

^aThe quantification of thiolates was performed based on the spectra after 60 seconds of etching, where most partially oxidized S is no longer present.

^bBased on the ratio of the number of CH₃ groups to the number of linkers. See supplementary material for a description of the calculation.

Depth-profiling XPS was also performed to evaluate the changes in S speciation at the interior of the NU-1000 crystallite. The resulting spectra are displayed in **Figure 5.6(a)-(d)**. With increasing etch time, the intensity of the features associated with sulfates decreases, showing that the deposition sites that result in the formation of sulfates are only present on the surface of the NU-1000 crystallites. Most of the deposition sites below the surface would induce the formation of thiolates.

Overall, the XPS results confirm the presence and the speciation of S in the NU-1000-FF-300C crystallites, where a significant amount of S exists as sulfate on the surface of the crystallites. Meanwhile, the dominant species below the surface level are thiolates created through the heterolytic splitting of the corresponding thiol molecules.

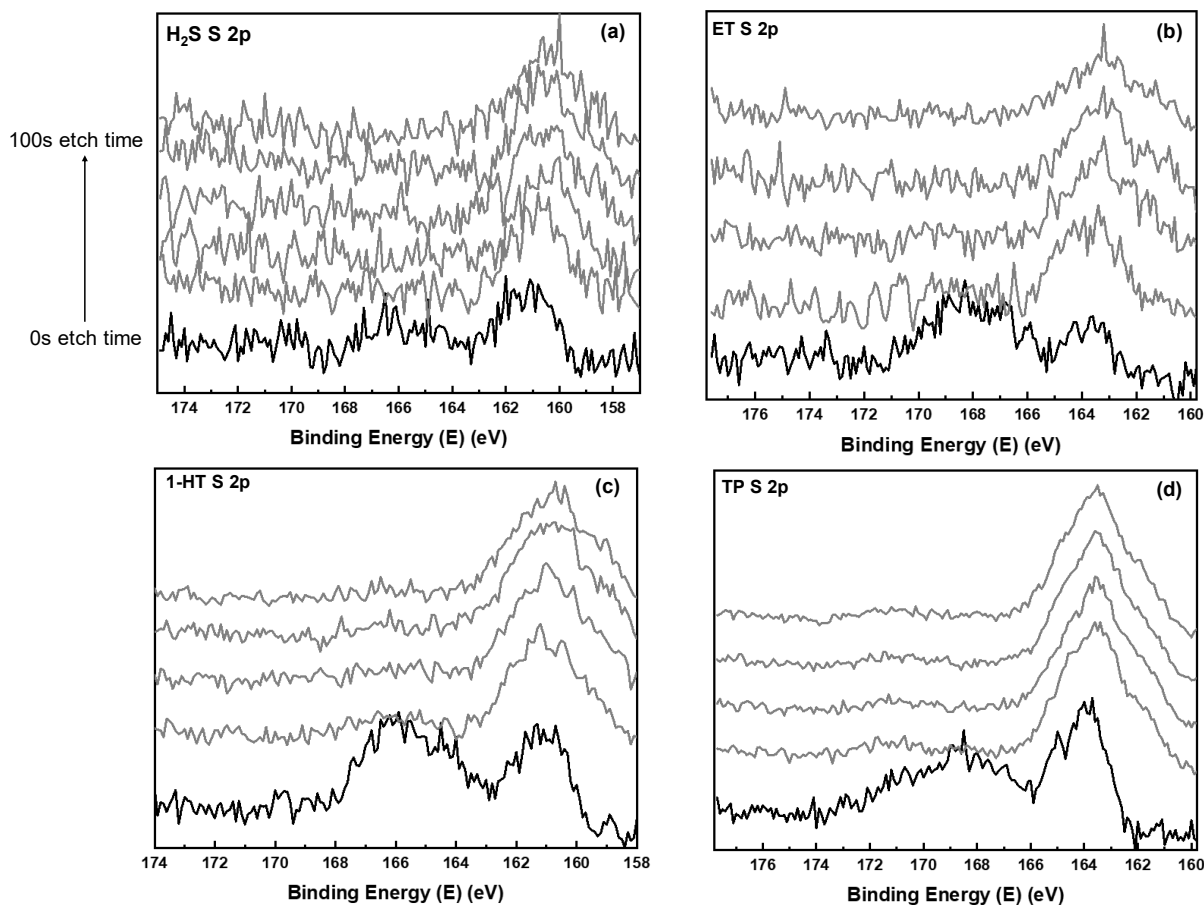


Figure 5.6. Depth profiling XPS S 2p spectra of NU-1000-300C modified with (a) H₂S, (b) ethanethiol, (c) 1-hexanethiol, and (d) thiophenol. The black trace represents the spectrum of the surface, and the gray traces are spectra collected at increasing etch iterations. The peaks at *ca.* 161 eV and 166 eV are assigned to sulfides and sulfates, respectively.

5.7 Elucidating the Adsorption Modes of the Thiol Species

Direct-reflectance infrared Fourier transform spectroscopy (DRIFTS) was performed to investigate the interaction between the S-containing and the distorted Zr₆ nodes, as well as to evaluate the stability of the adsorbed S-containing species. The characteristic regions of the spectra collected at 29°C and 200°C are displayed in **Figure 5.7(a)-(b)**.

In the 900~1250 cm⁻¹ region [**Figure 5.7(a)**], where aliphatic and aromatic C-H bending features are observed, no new features were observed for H₂S and ET at 29°C and 200°C compared to NU-1000-300C, likely due to the low S concentration in ET and the lack of

characteristic functional groups on H₂S in this region. Meanwhile, two alkyl C-H bending vibrations can be discerned in this region at 29°C for 1-HT. The peak at 1038 cm⁻¹ is assigned to the associatively adsorbed 1-hexanethiol species, where two types of associative adsorptions are possible. The first possibility is the thiol group on 1-hexanethiol interacting with the remaining oxygens on the nodes through hydrogen bonding, with the second being the direct coordination of 1-hexanethiol to the distorted site on the Zr₆ node without thiolate formation.^{203, 206} Both possibilities are depicted in **Figure 5.8(a)**. The feature at 969 cm⁻¹ is assigned to the dissociatively adsorbed hexanethiolates on the distorted node, as shown in **Figure 5.8(b)**. The associatively adsorbed 1-hexanethiol appears at a higher wavenumber because of the coupling of $\delta(\text{S-H})$ and $\nu(\text{C-H})$ vibrations,²²⁰ which is absent in heterolytically split species, as the S-H group is no longer present. After heating 1-HT at 200°C for one hour, the peak at 1038 cm⁻¹ corresponding to the associatively adsorbed hexanethiol disappears, while the dissociatively adsorbed thiolate species at 969 cm⁻¹ remains.

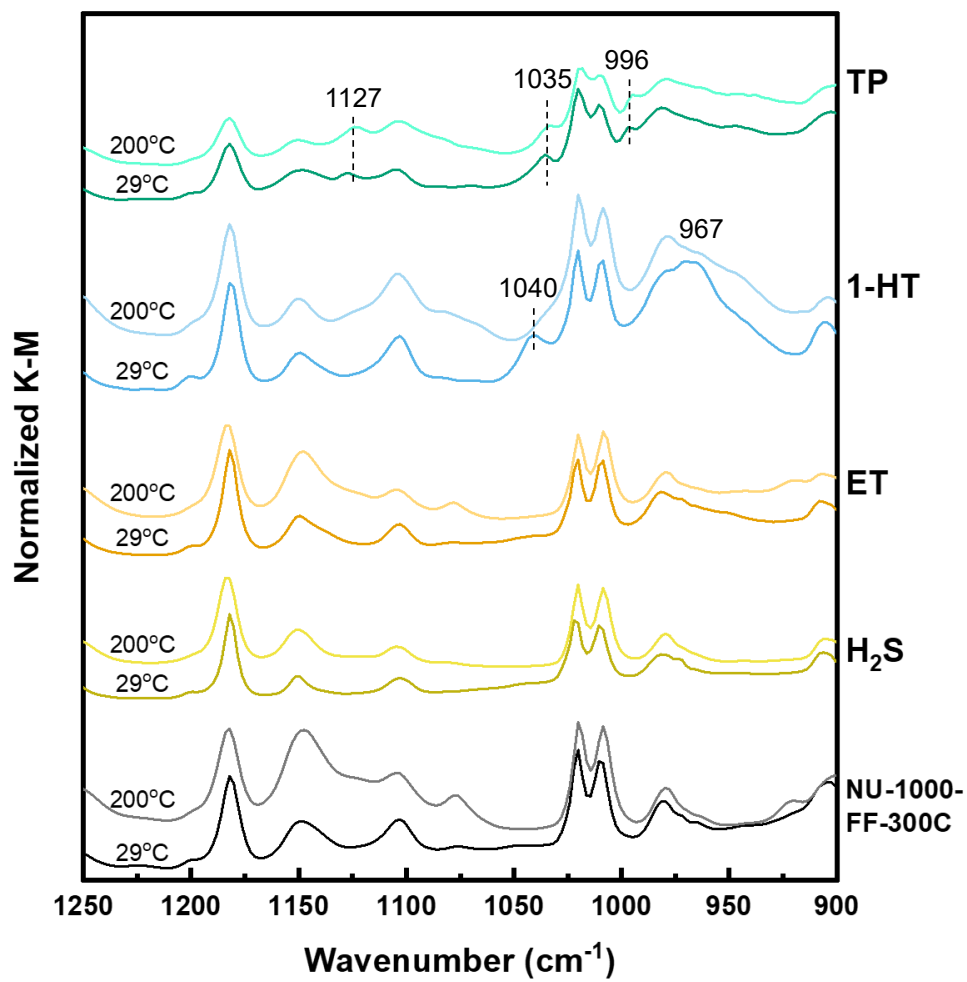
For TP, extra C-H bending features are also observed in the 900~1250 cm⁻¹ region. Aromatic C-H bending features characteristic of the thiophenyl rings are observed at 1145 cm⁻¹, 1028 cm⁻¹, and 978 cm⁻¹.²²¹ Those features remained after treating TP at 200°C, suggesting that the adsorbed thiophenol molecules underwent heterolytic splitting, resulting in the formation of the thiophenolate species that interact strongly with the distorted Zr₆ nodes.

In the 2250~4000 cm⁻¹ where mainly alkyl C-H and O-H stretching are present [**Figure 5.7(b)**], common features found in all samples at 29°C are the broad O-H stretching feature at *ca.* 3250 cm⁻¹ from the hydrogen bonding interactions of the physisorbed water in the pores, as well as the sharp O-H stretching at 3654 cm⁻¹ associated with node-bound OH species. Both features are typically observed in the DRIFTS spectra of NU-1000.^{83, 124}

In this region, a new feature at 2340 cm^{-1} was observed for H_2S at 29°C , which is assigned to the S-H stretching of the adsorbed H_2S molecules.²²² As the sample was heated to 200°C , the spectrum lost the S-H stretching peak at 2340 cm^{-1} and the broad O-H stretching feature at *ca.* 3250 cm^{-1} . Meanwhile, a new feature emerged at 3612 cm^{-1} , which appears in a similar region as the new features at 3640 cm^{-1} observed for ET and TP. Those new O-H features are evident in the heterolytic splitting of the thiols, resulting in the protonation of the highly Lewis basic O on the distorted Zr_6 node. Note that an extra O-H stretch is found for H_2S at 3774 cm^{-1} , which likely originates from trace water in the gas stream that underwent heterolytic dissociation. For ET and 1-HT, an extra feature emerges at 2855 cm^{-1} compared to the spectrum for NU-1000-FF-300C, which is assigned to the C-H stretching on the hydrocarbon chains. This feature partially diminishes after heating 1-HT at 200°C in Ar, consistent with the observation for 1-HT at the lower-wavenumber region where only the dissociatively adsorbed species remained after heating. As expected for aromatic molecules, no extra alkyl C-H stretching can be discerned for TP.

In summary, the DRIFTS studies unveil the presence of thiolates in both associative and dissociative adsorption modes, while the dissociatively adsorbed thiolates showed higher thermal stability. The emergence of new hydroxyl features upon removing the physisorbed water and dehydrating the nodes also demonstrates the occurrence of the dissociative adsorption of the thiols.

(a)



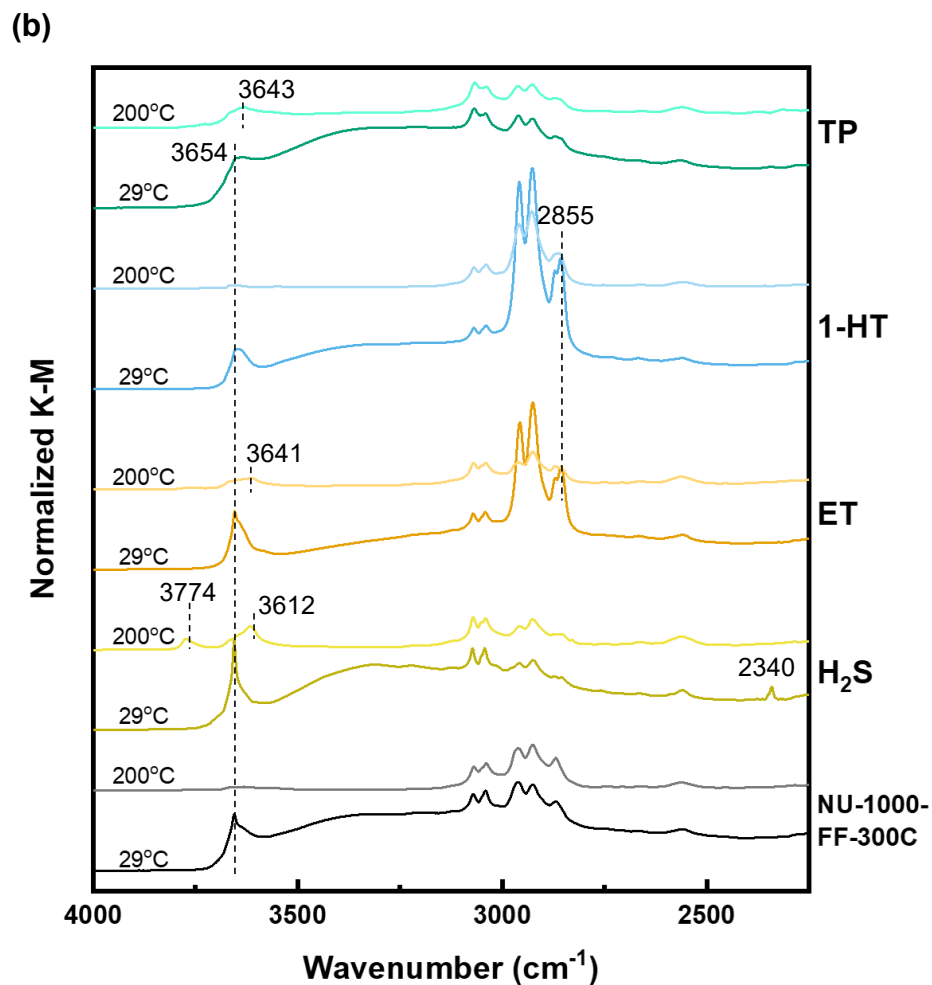


Figure 5.7. (a) DRIFTS Spectra from 900~1250 cm^{-1} of all samples modified with thiols collected at 29°C and 200°C. (b) DRIFTS Spectra from 2250~4000 cm^{-1} of all samples modified with thiols collected at 29°C and 200°C.

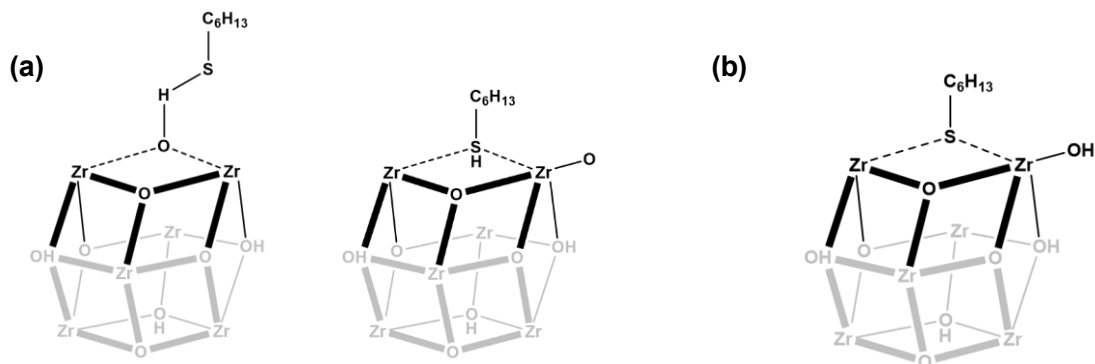


Figure 5.8. (a) Two possible types of associative adsorption of 1-hexanethiol. (b) An illustration of the dissociative adsorption of 1-hexanethiol onto the distorted node.

5.8 Reaction of Sulfides with the Distorted Zr_6 Nodes

The surface and depth-profiling XPS spectra for DES and TPhen are shown in **Figure 5.9(a)-(d)**, and the deconvoluted peak values are listed in **Table 5.2**. Similar to the spectra for the thiol-containing samples, surface S species are found in both sulfide-modified samples, although sulfates dominate the DES-modified surface. The depth-profiling XPS for DES is also similar to those for the sulfide-modified samples, where the sulfate peak gradually diminishes with increasing etch time. Meanwhile, the S signal is no longer detected for TPhen, due to the minimal interaction between thiophene and the Zr_6 nodes.

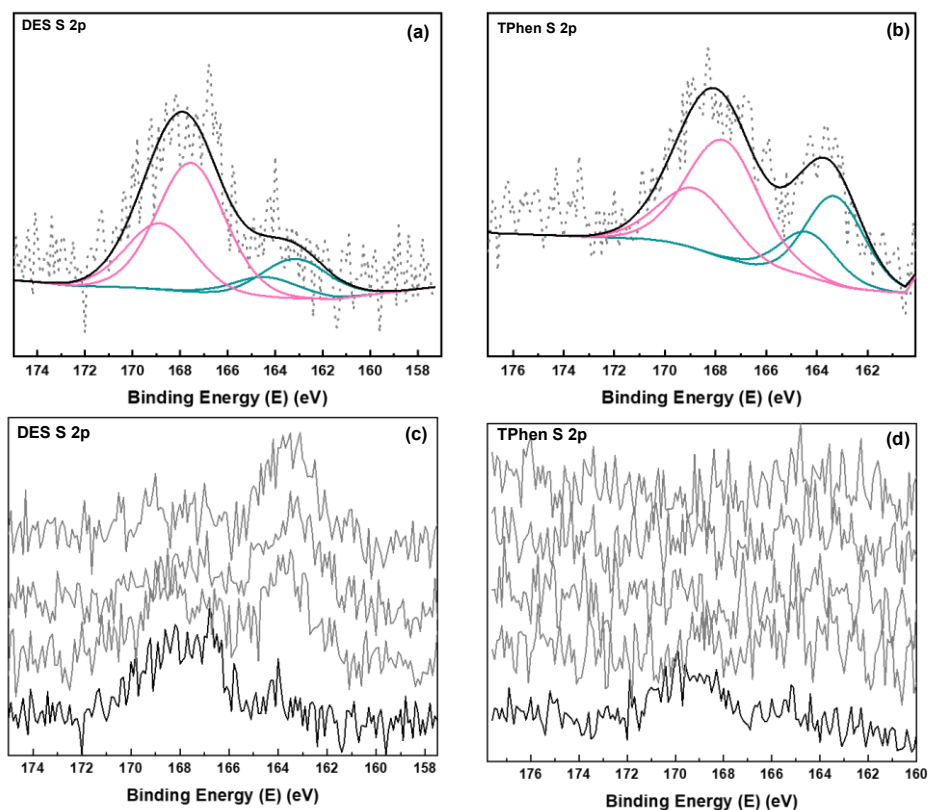


Figure 5.9. Surface XPS S2p spectra for (a) DES and (b) TPhen, and the depth profiling spectra for (c) DES and (d) TPhen.

Table 5.1. Thiolate binding energies and quantifications for DES and TPhen.

Sample	Thiolate S 2p3 BE (eV)	Sulfide per Zr ₆ node
DES	163.1	0.9
TPhen	164.3	-

In the 900~1250 cm⁻¹ region of the DRIFTS spectra [**Figure 5.10(a)**], a new peak at 1125 cm⁻¹ can be discerned in the spectrum for DES at 29°C. This peak diminished at 200°C and thus is assigned to diethyl sulfide species that weakly interact with the Zr₆ nodes. No feature indicates the breakage of the S-C bond that results in the formation of an ethyl thiolate fragment binding to the node and the formation of an ethoxy group. Meanwhile, no discernible features are found for TPhen due to the lack of interaction between thiophene and the defect sites, consistent with the depth-profiling XPS results. In the 2250~4000 cm⁻¹ region [**Figure 5.10(b)**], no extra C-H stretching features are found in DES and TPhen, and the node-bound -OH features remained after treatment at 200°C. The extra feature that appeared in TPhen at 3769 cm⁻¹ is likely the result of trace amount of water protonating the Lewis basic μ1-O, as no additional features that are associated with TPhen were observed. Similar observation was made for H₂S in **Figure 5.7**.

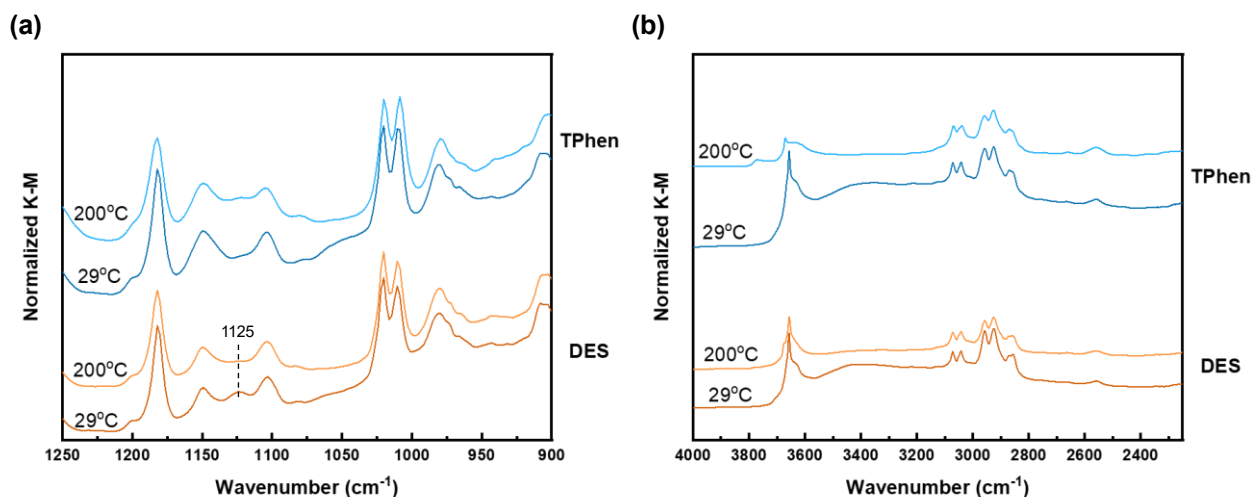


Figure 5.10. (a) DRIFTS Spectra from 900~1250 cm^{-1} of all samples modified with sulfides collected at 29°C and 200°C. (b) DRIFTS Spectra from 2250~4000 cm^{-1} of all samples modified with sulfides collected at 29°C and 200°C.

To summarize, the dissociative adsorption of sulfides was not observed NU-1000-FF-300C using the same synthetic conditions as the thiol modifications. Subsequent computational studies were carried out to rationalize this observation, as will be detailed in the next section.

5.9 Computational Investigation on the Heterolytic Splitting Process

To support the experimental findings and gain further atomistic-scale understanding of the mechanism of S-containing species splitting, we performed DFT analysis of the reaction. As a model for NU-1000-300C, we employed a fully dehydrated and distorted Zr_6O_8 node, with formate groups mimicking carboxylates of the linkers, as proposed by Platero-Prats *et al.*²¹⁷ and later applied by Liu *et al.*¹¹⁸ The catalytic active sites in this model are two Zr atoms which contribute to forming bridging species and the terminal oxygen. To understand how different molecules might react with this node, we calculated the Gibbs free energies (ΔG) of both the physisorption process and splitting reactions for a selected set of molecules (details are provided in **Table 5.3**). The free energies are calculated as a difference between the sum of energies of the reactants (S-containing

molecule and Zr_6O_8 node) and product (physisorbed or split S-containing molecule with Zr_6O_8 node).

Our calculations revealed that all the splitting reactions considered could occur spontaneously, as they had significantly negative Gibbs free energy changes (ΔG). Surprisingly, even the splitting of thiophene, which involves breaking an aromatic ring, shows a ΔG of -54 kJ/mol. Moreover, the free energy of heterolytic splitting is always favored over physisorption energy implying that this is the primary mechanism. Interestingly, even though these results support experimental findings about thiols, they contradict the observation that the distorted node does not react with sulfides. This discrepancy is likely due to the differences in breaking S-H and S-C bonds, which are involved in the reactions with thiols and sulfides, respectively.

Table 5.3. Gibbs free energies of physisorption and splitting reaction of S-containing molecules.

S-containing species	Gibbs free energy of physisorption (kJ/mol)	Gibbs free energy of splitting (kJ/mol)
H_2S	4.4	-157.0
Methanethiol	-4.8	-160.6
Ethanethiol	-8.9	-144.3
Thiophenol	0.3	-136.4
Dimethyl sulfide	-22.5	-122.5
Diethyl sulfide	-15.8	-118.8
Thiophene	8.6	-53.9

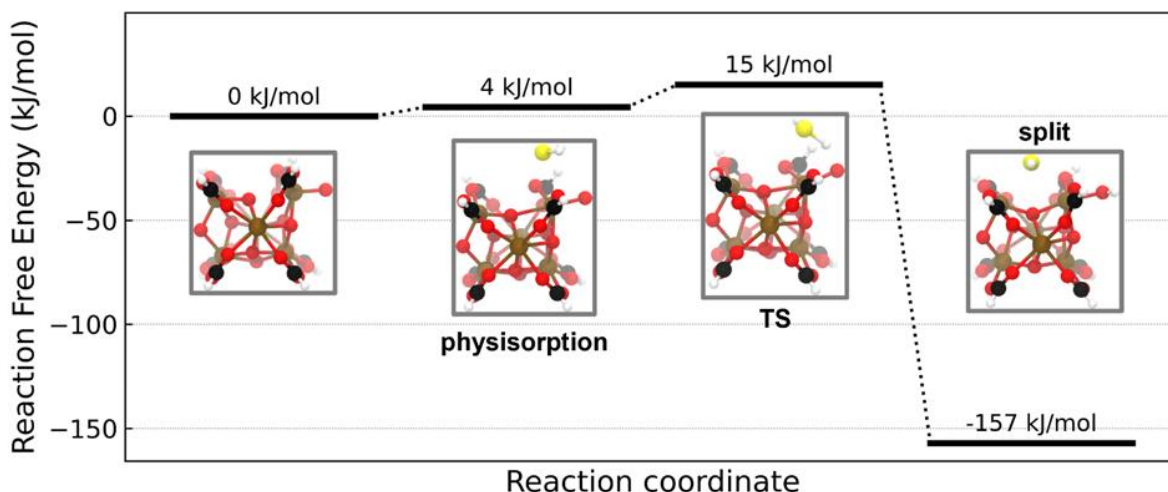


Figure 5.11. Reaction path for the H₂S splitting mechanism.

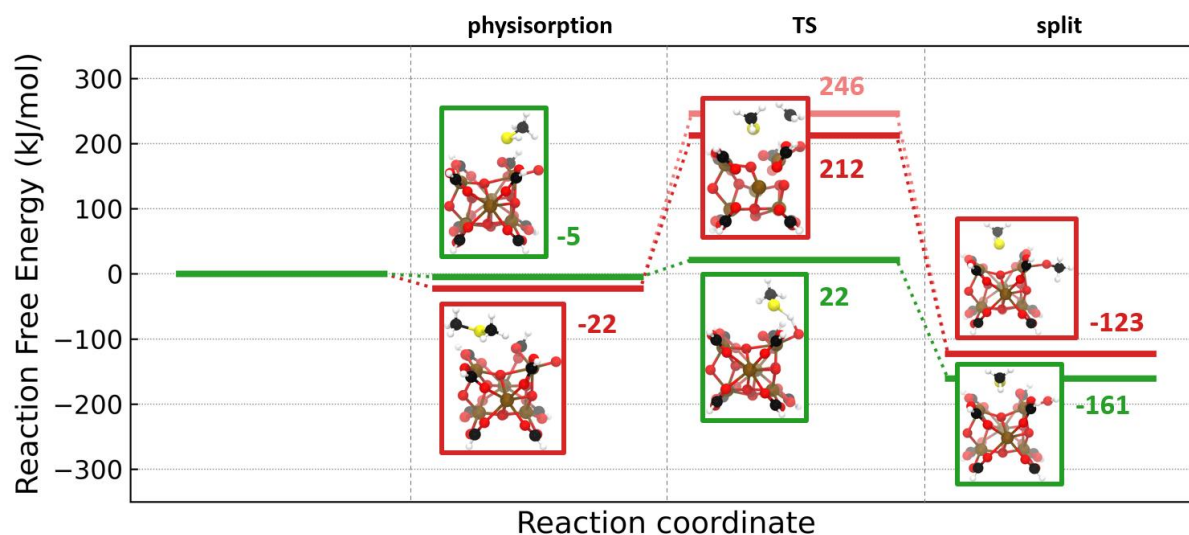


Figure 5.12. Reaction path for methanethiol (green) and dimethyl sulfide (red). Note two transition states for dimethyl sulfide splitting reaction. Dark red represents the more favored *rocking* mechanism, the light red is associated with higher-energy *transition* mechanism, see text for details. The numbers represent the Gibbs free energies with the unit of kJ/mol.

For a more comprehensive analysis, we explored the complete reaction pathway for three specific molecules – H₂S, ethanethiol, and dimethyl sulfide. Our selection was guided by the intention to maintain computational efficiency without losing the representativeness of the considered groups (thiols and sulfides). Thus, we focused on molecules with the shortest carbon chains, specifically those with a single carbon atom (C1, methyl).

The reaction diagram for H₂S splitting is illustrated in **Figure 5.11**. Initial steps involve the adsorption of the molecule on the Zr Lewis acid site, driven by the interaction with the lone pair of sulfur's electrons. Subsequently, a hydrogen atom from H₂S is transferred to a terminal oxygen atom, resulting in the formation of a transition state (TS). The energy barrier for this reaction is relatively low, just 15 kJ/mol, and with the final product stage exhibiting high stability (-157 kJ/mol), it aligns well with experimental findings.

The reaction diagram for methanethiol splitting, depicted in the green trace in **Figure 5.12**, follows a similar pathway. The TS stage, with a slightly higher but still considered to be very low energy barrier of 22 kJ/mol, follows the physisorption on open Zr site, and forms very stable product wherein hydrogen binds to the terminal oxygen, forming a hydroxyl group, and the methylthiolate (CH₃-S) radical bridges between two Zr Lewis acid sites, resulting in a Zr-S-Zr formation.

The reasons for the lack of experimental observation of sulfide splitting were elucidated through the TS calculations as well. The process of sulfide splitting significantly diverges from that of thiol splitting, marked by two critical distinctions. The initial step in the former, the physisorption, differs as sulfides tend to bridge between two Zr sites rather than adsorb on one open Zr site like thiols. This behavior increases the physisorption energy (-22 kJ/mol for dimethyl sulfide), marking a distinctive variance between those compounds. The most significant difference is related to the reaction barrier height which reaches 212 kJ/mol for sulfides, which likely prevents the reaction from occurring spontaneously in a reasonable timescale.

Interestingly, we identified two possible TS states associated with dimethyl sulfide splitting (**Figure 5.13**). In the first, the reaction proceeds through a *transition* TS, in which a planar methyl

radical forms and the orientation of 3 hydrogens changes significantly (initially, the hydrogens are oriented away from the sulfur atom; as the reaction proceeds, they must subsequently adjust their alignment to face away from the oxygen atom instead). This TS is restricted to a transition of terminal methyl group and cannot be considered for longer carbon chains (ethyl and larger). On the other hand, a second TS that involves *rocking* mechanism appears to be more universal as the hydrogen on methyl radical are not forced to change orientation significantly, and if one of them is replaced by another methyl group forming longer terminal group, it is still equally possible to be observed. Moreover, the *rocking* TS is associated with free energy lower by 34 kJ/mol. Even though these TS, due to high energy barrier do not occur in the experiments performed in this work, this analysis shed some light on the potential mechanism of transferring methyl group in harsher conditions (like higher temperature) or in the case of splitting other molecules involving methyl group cleavage.

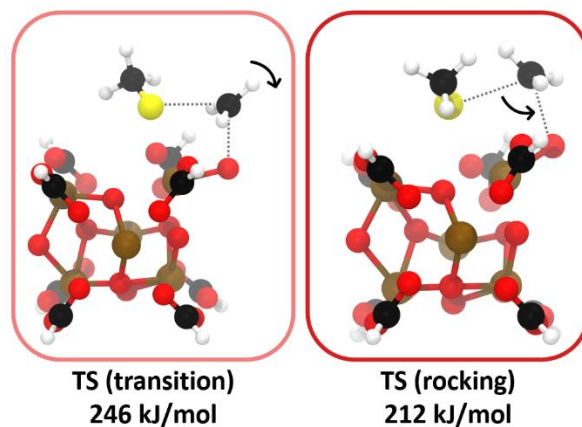


Figure 5.13. Two possible transition states in sulfide splitting reaction.

5.10 Chapter Conclusions

In this study, we attempted to incorporate thiols and sulfides onto the Zr_6 nodes of formate-free NU-1000 by leveraging the Zr_6 node distortion through high-temperature treatments. The grafting was successful for H_2S , alkyl, and aromatic thiols, where the binding

through heterolytic splitting was observed with various spectroscopy techniques. Meanwhile, diethyl sulfide and thiophene only bound to the node weakly without undergoing heterolytic splitting. The experimental observations were corroborated by computational studies, where a much higher activation barrier was found for C-S bond breakage at the undercoordinated sites of the distorted nodes. Through exploiting the structural uniformity of MOF NU-1000, our study provides crucial insights into the sulfidation mechanism on the defect sites of zirconia, as well as a handle to grafting sulfur-containing molecules bearing various functionalities on solid oxide surfaces.

5.11 Additional Information

5.11.1 Materials

The linkers for NU-1000 were synthesized according to a published procedure²²³ using 1,3,6,8-tetrabromopyrene, (4-(ethoxycarbonyl)phenyl)boronic acid, K_3PO_4 , $(PPh_3)_4Pd$, $ZrOCl_3 \cdot 8H_2O$, benzoic acid, HCl, dioxane, acetone, N,N-dimethylformamide. All chemicals were purchased from Sigma Aldrich Chemicals Company, Inc. and used without further purification. The chemicals used for the formate removal (dimethyl sulfoxide, ethanol, and triethyl amine) and for the thiol and sulfide depositions (1-ethanethiol, 1-hexanethiol, thiophenol, diethyl sulfide, and thiophene), were purchased and used as received from Sigma Aldrich Chemicals Company, Inc. 1% H_2S balanced in N_2 was purchased through Airgas.

5.11.2 Synthesis

NU-1000, formate-free NU-1000 (NU-1000-FF). NU-1000 was synthesized, followed by formate removal (NU-1000-FF) according to the published procedures.^{32, 124} The removal of residual formate from the synthesis was confirmed by 1H NMR. Powder XRD and N_2 isotherm confirmed the porosity and structure of the as-made NU-1000-FF.

As-synthesized NU-1000-FF went through two different synthetic routes for thiols and sulfides grafting, depending on the substrate.

The sulfidation using H₂S was performed in a Lindberg Blue M tube furnace purchased from Thermo Scientific Inc. 50 mg NU-1000-FF was placed in a quartz sample boat and was treated under a 20 sccm N₂ flow overnight to displace any physisorbed species inside the pores of NU-1000-FF. The temperature was then raised to 300°C at a ramp rate of 1°C/min and held at 300°C for 12 hours. Then the sample was cooled to room temperature inside the furnace, followed by introducing 20 sccm 4% H₂S balanced in N₂ for 4 hours. The system was then purged with 20 sccm N₂ for 2 hours before collecting the samples.

The sulfidations using other thiols and sulfides were performed in two steps, namely, the creation of the distorted Zr₆ nodes and the incorporation of the thiol or sulfide substrates. The thiols and sulfides of interest for this synthetic route are ethanethiol (ET), 1-hexanethiol (1-HT), thiophenol (TP), diethylsulfide (DES), and thiophene (TPhen). As-synthesized NU-1000-FF was first packed into a tube, and the sample was treated under dynamic vacuum at 300°C for 12 hours with Mitromeritics Smart VacPrep, generating NU-1000-FF-300C. The tube was then sealed with parafilm and transferred into an Ar-filled glovebox.

For the thiol or sulfide grafting, 30 mg (0.014 mmol) of NU-1000-300C and a stir bar were transferred into an oven-dried Biotage microwave vial (5-8 mL) in the glovebox. The vial was then capped with a septum and removed from the glovebox and kept under dynamic N₂ flow. Into a second microwave vial outside the glovebox, 10 molar equivalence (0.14 mmol, based on the molar mass of one unit cell of NU-1000, calculated to be 2139.32 g/mol) of the target sulfide or thiol was added. The amounts of sulfide and thiol used are listed in **Table 5.4**. Note that 100 molar equivalence was used for the incorporation of ET due to the high volatility of ethanethiol. The

second vial was also capped with a septum and kept under dynamic N₂ flow, followed by the addition of 4.4 mL anhydrous heptane to achieve a molar concentration of 0.032 M. Then, the thiol or sulfide solution was transferred into the vial containing NU-1000-FF-300C, and the mixture was stirred at room temperature overnight. The sample then underwent five times of solvent exchange with fresh anhydrous heptane for 36 hours, and the sample was then dried under N₂ purge in an oil bath made of nonflammable silicon oil at 100°C overnight. The microwave vial containing the sample was transferred to a vacuum desiccator for storage.

Table 5.4. The amounts of thiols and sulfides used for liquid phase syntheses.

Compound	Sample ID	Molecular Weight (g/mol)	Amount Used (μL)
ethanethiol	ET	62.1	101
1-hexanethiol	1-HT	118.2	19.7
thiophenol	TP	110.2	14.3
thiophene	TPhen	84.1	11.2

5.11.3 Instrumentation

Powder X-ray diffraction (PXRD) was performed on an STOE STADI P powder diffractometer set to 40 kV and 40 mA, equipped with an asymmetrically curved germanium monochromator with Cu K α 1 radiation ($\lambda = 1.54056 \text{ \AA}$), and a one-dimensional silicon strip detector (MYTHEN2 1K from DECTRIS). PXRD of all samples was measured in ambient conditions at room temperature in transmission mode in a rotating holder at $4^\circ 2\theta \text{ min}^{-1}$ and a 0.05° step width.

N₂ physisorption was performed with a Micromeritics Tristar II 3020 at 70K. Before measurement, samples were activated under dynamic vacuum in a Micromeritics SmartVacPrep at 80°C for 16 h for S-containing samples and 120°C for 16 hours for NU-1000-FF. Brunauer-Emmett-Teller (BET) surface areas were calculated in the P/P₀ range of 0.005-0.1. Pore size distributions were determined using a DFT carbon slit-pore model and an N₂ kernel.

^1H nuclear magnetic resonance (NMR) spectra of the acid-digested samples were collected on a 500 MHz Bruker S4 Avance III with a DCH CryoProbe. The internal reference compound used to assess all chemical shifts is tetramethylsilane. Acid digestion was performed in a glass vial by adding 3~5 drops of D_2SO_4 to around 2 mg of sample. Then, 0.7 mL of DMSO-d_6 was added, and the mixture was sonicated until all powders were fully digested.

Diffuse Reflectance IR Fourier Transform Spectroscopy (DRIFTS) measurements were performed using a Thermo-iS50 spectrometer. The sample cell was first filled with ground KBr, then around 7 mg of ground sample was added. The sample was then pressed down to form a flat surface. Spectra at room temperature were collected after the sample was kept under 100 sccm Ar flow for 30 minutes. The sample was then heated up to 200°C at a ramp rate of 10°C per minute in the same Ar flow and was kept at 200°C for 30 minutes, followed by spectra collection. All spectra were corrected with background spectra of KBr collected under the same conditions, namely at room temperature and 200°C in Ar, respectively.

X-ray photoelectron spectra (XPS) were acquired on a Thermo Scientific ESCALAB 250 Xi (Al $\text{K}\alpha$ radiation, 1486.6 eV) with an electron flood gun and spectra calibrated to the C 1s (284.8 eV). The pass energy of each spectrum was set to 20 eV and the dwell time 100 ms. Depth profiling was performed by etching the sample with an Ar^+ ion gun set to 2kV. Each level was etched at the same position for 15 seconds, and 4 levels of etching were performed for each sample.

Chapter 6. Conclusions and Future Directions

6.1 Conclusions

In conclusion, this Thesis details how the advantages of MOFs can be leveraged to gain fundamental insights into heterogeneous catalysts. Due to the high surface area and porosity, MOFs as catalysts and supports effectively reduce mass transport limitation during catalysis. When MOF nodes are used for the deposition of metal catalysts, the isolation created by the linkers can reduce structural complications during catalytic testing by preventing the sintering and aggregation of the metal species. The crystallinity of MOFs also renders various X-ray-based techniques, such as single-crystal X-ray diffraction (SCXRD) and difference electron density (DED) mapping, useful for locating and determining the structure of the catalytically relevant species.

The insights from this work could guide the rational construction of catalytic systems with higher efficiency and product selectivity, which directly relates to some of the most urgent steps we need to take to mitigate climate change, such as eliminating fossil fuel as the energy source and increasing the portion of sustainable feedstocks for chemical productions.

6.2 Looking Ahead

In recent years, MOFs have been primarily adopted as model systems for fundamental studies and modeling. The practicality of using MOF-based catalysts in industrial productions is limited mainly despite the high conversion and catalytic efficiency for many chemical reactions, as MOF and MOF-supported catalysts are not as robust as conventional catalysts and supports like metal oxides and zeolites under elevated temperatures and pressures required in many current chemical production processes. However, many high-temperature chemical productions,

such as the production of ethylene from ethane cracking and the generation of acetaldehyde from ethylene oxidation, rely on fossil fuels as feedstock. As fossil fuels and petroleum-based products are slowly phasing out from current industrial sectors, processes based on sustainable fuel and feedstock will be on the rise, providing new opportunities to incorporate MOF-based catalysts. In addition, the high tunability of MOF systems also enables high-throughput computational screening to determine the optimal MOF structure for a target application, which has also been an ongoing effort in numerous research groups. The possibilities for MOF catalysts are endless.

References

1. Weckhuysen, B. M., Solid catalysts under the spotlight. *Nature Catalysis* **2018**, *1* (2), 101-102.
2. Hagen, J., Introduction. In *Industrial Catalysis*, **2005**; pp 1-14.
3. Zhang, J.; Zeng, H., Intermolecular and Surface Interactions in Engineering Processes. *Engineering* **2021**, *7* (1), 63-83.
4. Hu, X.; Yip, A. C. K., Heterogeneous Catalysis: Enabling a Sustainable Future. *Frontiers in Catalysis* **2021**, *1*.
5. Thomas, J. M., Handbook Of Heterogeneous Catalysis. 2., completely revised and enlarged Edition. Vol. 1–8. Edited by G. Ertl, H. Knözinger, F. Schüth, and J. Weitkamp. *Angewandte Chemie International Edition* **2009**, *48* (19), 3390-3391.
6. Lin, L.; Ge, Y.; Zhang, H.; Wang, M.; Xiao, D.; Ma, D., Heterogeneous Catalysis in Water. *JACS Au* **2021**, *1* (11), 1834-1848.
7. Vogt, C.; Weckhuysen, B. M., The concept of active site in heterogeneous catalysis. *Nature Reviews Chemistry* **2022**, *6* (2), 89-111.
8. Wang, H.; Lu, J., A Review on Particle Size Effect in Metal-Catalyzed Heterogeneous Reactions. *Chinese Journal of Chemistry* **2020**, *38* (11), 1422-1444.
9. Medford, A. J.; Vojvodic, A.; Hummelshøj, J. S.; Voss, J.; Abild-Pedersen, F.; Studt, F.; Bligaard, T.; Nilsson, A.; Nørskov, J. K., From the Sabatier principle to a predictive theory of transition-metal heterogeneous catalysis. *Journal of Catalysis* **2015**, *328*, 36-42.
10. Rao, C. N. R.; Kulkarni, G. U.; Thomas, P. J.; Edwards, P. P., Size-Dependent Chemistry: Properties of Nanocrystals. *Chemistry – A European Journal* **2002**, *8* (1), 28-35.
11. Taketoshi, A.; Haruta, M., Size- and Structure-specificity in Catalysis by Gold Clusters. *Chemistry Letters* **2014**, *43* (4), 380-387.
12. Saveriede, L.; Nauert, S. L.; Roberts, C. A.; Notestein, J. M., The effect of support morphology on CoOX/CeO₂ catalysts for the reduction of NO by CO. *Journal of Catalysis* **2018**, *366*, 150-158.
13. Mansley, Z. R.; Paull, R. J.; Saveriede, L.; Tatro, S.; Greenstein, E. P.; Gosavi, A.; Cheng, E.; Wen, J.; Poepfelmeier, K. R.; Notestein, J. M.; Marks, L. D., Identifying Support Effects in Au-Catalyzed CO Oxidation. *ACS Catalysis* **2021**, *11* (19), 11921-11928.
14. Ferrando, R.; Jellinek, J.; Johnston, R. L., Nanoalloys: From Theory to Applications of Alloy Clusters and Nanoparticles. *Chemical Reviews* **2008**, *108* (3), 845-910.
15. Liu, J.; Goetjen, T. A.; Wang, Q.; Knapp, J. G.; Wasson, M. C.; Yang, Y.; Syed, Z. H.; Delferro, M.; Notestein, J. M.; Farha, O. K.; Hupp, J. T., MOF-enabled confinement and related effects for chemical catalyst presentation and utilization. *Chemical Society Reviews* **2022**, *51* (3), 1045-1097.
16. Nørskov, J. K.; Bligaard, T.; Hvolbæk, B.; Abild-Pedersen, F.; Chorkendorff, I.; Christensen, C. H., The nature of the active site in heterogeneous metal catalysis. *Chemical Society Reviews* **2008**, *37* (10), 2163-2171.
17. Zou, N.; Zhou, X.; Chen, G.; Andoy, N. M.; Jung, W.; Liu, G.; Chen, P., Cooperative communication within and between single nanocatalysts. *Nature Chemistry* **2018**, *10* (6), 607-614.
18. Najafshirtari, S.; Friedel Ortega, K.; Douthwaite, M.; Pattison, S.; Hutchings, G. J.; Bondué, C. J.; Tschulik, K.; Waffel, D.; Peng, B.; Deitermann, M.; Busser, G. W.; Muhler,

- M.; Behrens, M., A Perspective on Heterogeneous Catalysts for the Selective Oxidation of Alcohols. *Chemistry – A European Journal* **2021**, *27* (68), 16809-16833.
19. Gao, F.; Goodman, D. W., Model Catalysts: Simulating the Complexities of Heterogeneous Catalysts. *Annual Review of Physical Chemistry* **2012**, *63* (1), 265-286.
 20. Yuan, W.; Fang, K.; You, R.; Zhang, Z.; Wang, Y., Toward In Situ Atomistic Design of Catalytic Active Sites via Controlled Atmosphere Transmission Electron Microscopy. *Accounts of Materials Research* **2023**, *4* (3), 275-286.
 21. Golder, K. M.; Wintterlin, J., In Situ/Operando STM of the Fischer–Tropsch Synthesis on a Co(10 $\bar{1}$ 15) Surface—A Study to Bridge the Materials Gap between Single-Crystal Models and Supported Catalysts. *ACS Catalysis* **2022**, *12* (12), 7199-7209.
 22. Viswanathan, R.; Burgess, D. R.; Stair, P. C.; Weitz, E., Laser-induced thermal desorption of CO from clean polycrystalline copper: Time-of-flight and surface diffusion measurements. *Journal of Electron Spectroscopy and Related Phenomena* **1983**, *29* (1), 111.
 23. Smudde, G. H., Jr.; Peng, X. D.; Viswanathan, R.; Stair, P. C., Adsorption of gas phase methyl radicals on the oxygen modified Mo(100) single crystal surface. *Journal of Vacuum Science & Technology A* **1991**, *9* (3), 1885-1889.
 24. Koestner, R. J.; Frost, J. C.; Stair, P. C.; Van Hove, M. A.; Somorjai, G. A., Evidence for the formation of stable alkylidyne structures from C₃ and C₄ unsaturated hydrocarbons adsorbed on the pt(111) single crystal surface. *Surface Science* **1982**, *116* (1), 85-103.
 25. Santra, A. K.; Goodman, D. W., Oxide-supported metal clusters: models for heterogeneous catalysts. *Journal of Physics: Condensed Matter* **2003**, *15* (2), R31.
 26. Wu, M.-C.; Corneille, J. S.; Estrada, C. A.; He, J.-W.; Wayne Goodman, D., Synthesis and characterization of ultra-thin MgO films on Mo(100). *Chemical Physics Letters* **1991**, *182* (5), 472-478.
 27. Opelt, S.; Türk, S.; Dietzsch, E.; Henschel, A.; Kaskel, S.; Klemm, E., Preparation of palladium supported on MOF-5 and its use as hydrogenation catalyst. *Catalysis Communications* **2008**, *9* (6), 1286-1290.
 28. Sharp, C. H.; Bukowski, B. C.; Li, H.; Johnson, E. M.; Ilic, S.; Morris, A. J.; Gersappe, D.; Snurr, R. Q.; Morris, J. R., Nanoconfinement and mass transport in metal–organic frameworks. *Chemical Society Reviews* **2021**, *50* (20), 11530-11558.
 29. Zhang, Y.; Zhang, X.; Lyu, J.; Otake, K.-i.; Wang, X.; Redfern, L. R.; Malliakas, C. D.; Li, Z.; Islamoglu, T.; Wang, B.; Farha, O. K., A Flexible Metal–Organic Framework with 4-Connected Zr₆ Nodes. *Journal of the American Chemical Society* **2018**, *140* (36), 11179-11183.
 30. Chen, Y.; Zhang, X.; Mian, M. R.; Son, F. A.; Zhang, K.; Cao, R.; Chen, Z.; Lee, S.-J.; Idrees, K. B.; Goetjen, T. A.; Lyu, J.; Li, P.; Xia, Q.; Li, Z.; Hupp, J. T.; Islamoglu, T.; Napolitano, A.; Peterson, G. W.; Farha, O. K., Structural Diversity of Zirconium Metal–Organic Frameworks and Effect on Adsorption of Toxic Chemicals. *Journal of the American Chemical Society* **2020**, *142* (51), 21428-21438.
 31. Furukawa, H.; Gándara, F.; Zhang, Y.-B.; Jiang, J.; Queen, W. L.; Hudson, M. R.; Yaghi, O. M., Water Adsorption in Porous Metal–Organic Frameworks and Related Materials. *Journal of the American Chemical Society* **2014**, *136* (11), 4369-4381.
 32. Islamoglu, T.; Otake, K.-i.; Li, P.; Buru, C. T.; Peters, A. W.; Akpinar, I.; Garibay, S. J.; Farha, O. K., Revisiting the structural homogeneity of NU-1000, a Zr-based metal–organic framework. *CrystEngComm* **2018**, *20* (39), 5913-5918.

33. Zhao, Y.; Qi, S.; Niu, Z.; Peng, Y.; Shan, C.; Verma, G.; Wojtas, L.; Zhang, Z.; Zhang, B.; Feng, Y.; Chen, Y.-S.; Ma, S., Robust Corrole-Based Metal–Organic Frameworks with Rare 9-Connected Zr/Hf-Oxo Clusters. *Journal of the American Chemical Society* **2019**, *141* (36), 14443-14450.
34. Bon, V.; Senkowska, I.; Baburin, I. A.; Kaskel, S., Zr- and Hf-Based Metal–Organic Frameworks: Tracking Down the Polymorphism. *Crystal Growth & Design* **2013**, *13* (3), 1231-1237.
35. Cavka, J. H.; Jakobsen, S.; Olsbye, U.; Guillou, N.; Lamberti, C.; Bordiga, S.; Lillerud, K. P., A New Zirconium Inorganic Building Brick Forming Metal Organic Frameworks with Exceptional Stability. *Journal of the American Chemical Society* **2008**, *130* (42), 13850-13851.
36. Yang, D.; Gates, B. C., Catalysis by Metal Organic Frameworks: Perspective and Suggestions for Future Research. *ACS Catalysis* **2019**, *9* (3), 1779-1798.
37. Liang, W.; Wang, X.; Yang, W.; Zhao, S.; Wiley, D.; Haynes, B. S.; Jiang, Y.; Liu, P.; Huang, J., Tailoring and Identifying Brønsted Acid Sites on Metal Oxo-Clusters of Metal–Organic Frameworks for Catalytic Transformation. *ACS Central Science* **2023**, *9* (1), 27-35.
38. Zhang, Y.-Y.; Li, J.-X.; Ding, L.-L.; Liu, L.; Wang, S.-M.; Han, Z.-B., Palladium Nanoparticles Encapsulated in the MIL-101-Catalyzed One-Pot Reaction of Alcohol Oxidation and Aldimine Condensation. *Inorganic Chemistry* **2018**, *57* (21), 13586-13593.
39. Buru, C. T.; Lyu, J.; Liu, J.; Farha, O. K., Restricting Polyoxometalate Movement Within Metal–Organic Frameworks to Assess the Role of Residual Water in Catalytic Thioether Oxidation Using These Dynamic Composites. *Frontiers in Materials* **2019**, *6*.
40. Chen, Y.; Jiménez-Ángeles, F.; Qiao, B.; Krzyaniak, M. D.; Sha, F.; Kato, S.; Gong, X.; Buru, C. T.; Chen, Z.; Zhang, X.; Gianneschi, N. C.; Wasielewski, M. R.; Olvera de la Cruz, M.; Farha, O. K., Insights into the Enhanced Catalytic Activity of Cytochrome c When Encapsulated in a Metal–Organic Framework. *Journal of the American Chemical Society* **2020**, *142* (43), 18576-18582.
41. Mian, M. R.; Redfern, L. R.; Pratik, S. M.; Ray, D.; Liu, J.; Idrees, K. B.; Islamoglu, T.; Gagliardi, L.; Farha, O. K., Precise Control of Cu Nanoparticle Size and Catalytic Activity through Pore Templating in Zr Metal–Organic Frameworks. *Chemistry of Materials* **2020**, *32* (7), 3078-3086.
42. Jones, L. *Toward a liquid hydrogen fuel economy*; University of Michigan: Michigan, MI, **1970**.
43. IEA *Global Energy and Climate Model*; Paris, **2022**.
44. IEA *Hydrogen*; Paris, **2022**.
45. Gong, Y.; Yao, J.; Wang, P.; Li, Z.; Zhou, H.; Xu, C., Perspective of hydrogen energy and recent progress in electrocatalytic water splitting. *Chinese Journal of Chemical Engineering* **2022**, *43*, 282-296.
46. Chen, L.; Qi, Z.; Zhang, S.; Su, J.; Somorjai, G. A., Application of Single-Site Catalysts in the Hydrogen Economy. *Trends in Chemistry* **2020**, *2* (12), 1114-1125.
47. Shi, L.; Yang, G.; Tao, K.; Yoneyama, Y.; Tan, Y.; Tsubaki, N., An Introduction of CO₂ Conversion by Dry Reforming with Methane and New Route of Low-Temperature Methanol Synthesis. *Accounts of Chemical Research* **2013**, *46* (8), 1838-1847.
48. Abdullah, B.; Abd Ghani, N. A.; Vo, D.-V. N., Recent advances in dry reforming of methane over Ni-based catalysts. *Journal of Cleaner Production* **2017**, *162*, 170-185.

49. Peng, Z.; Qing, Z.; Jing, L. I. U.; Lian, G. A. O., Research Progress of Ni-based Composite Catalysts for Methane Dry Reforming. *Journal of Inorganic Materials* **2018**, *33*, 931.
50. Martín, A. J.; Mitchell, S.; Mondelli, C.; Jaydev, S.; Pérez-Ramírez, J., Unifying views on catalyst deactivation. *Nature Catalysis* **2022**, *5* (10), 854-866.
51. Wei, D.; Shi, X.; Qu, R.; Junge, K.; Junge, H.; Beller, M., Toward a Hydrogen Economy: Development of Heterogeneous Catalysts for Chemical Hydrogen Storage and Release Reactions. *ACS Energy Letters* **2022**, *7* (10), 3734-3752.
52. Lee, J. H.; Ryu, J.; Kim, J. Y.; Nam, S.-W.; Han, J. H.; Lim, T.-H.; Gautam, S.; Chae, K. H.; Yoon, C. W., Carbon dioxide mediated, reversible chemical hydrogen storage using a Pd nanocatalyst supported on mesoporous graphitic carbon nitride. *Journal of Materials Chemistry A* **2014**, *2* (25), 9490-9495.
53. Bi, Q.-Y.; Lin, J.-D.; Liu, Y.-M.; He, H.-Y.; Huang, F.-Q.; Cao, Y., Dehydrogenation of Formic Acid at Room Temperature: Boosting Palladium Nanoparticle Efficiency by Coupling with Pyridinic-Nitrogen-Doped Carbon. *Angewandte Chemie International Edition* **2016**, *55* (39), 11849-11853.
54. Mori, K.; Masuda, S.; Tanaka, H.; Yoshizawa, K.; Che, M.; Yamashita, H., Phenylamine-functionalized mesoporous silica supported PdAg nanoparticles: a dual heterogeneous catalyst for formic acid/CO₂-mediated chemical hydrogen delivery/storage. *Chemical Communications* **2017**, *53* (34), 4677-4680.
55. Lu, M.; Zhang, J.; Yao, Y.; Sun, J.; Wang, Y.; Lin, H., Renewable energy storage via efficient reversible hydrogenation of piperidine captured CO₂. *Green Chemistry* **2018**, *20* (18), 4292-4298.
56. Rowsell, J. L. C.; Yaghi, O. M., Effects of Functionalization, Catenation, and Variation of the Metal Oxide and Organic Linking Units on the Low-Pressure Hydrogen Adsorption Properties of Metal–Organic Frameworks. *Journal of the American Chemical Society* **2006**, *128* (4), 1304-1315.
57. Xiao, B.; Yuan, Q., Nanoporous metal organic framework materials for hydrogen storage. *Particuology* **2009**, *7* (2), 129-140.
58. Rowsell, J. L. C.; Millward, A. R.; Park, K. S.; Yaghi, O. M., Hydrogen Sorption in Functionalized Metal–Organic Frameworks. *Journal of the American Chemical Society* **2004**, *126* (18), 5666-5667.
59. Xiao, B.; Wheatley, P. S.; Zhao, X.; Fletcher, A. J.; Fox, S.; Rossi, A. G.; Megson, I. L.; Bordiga, S.; Regli, L.; Thomas, K. M., High-capacity hydrogen and nitric oxide adsorption and storage in a metal– organic framework. *Journal of the American Chemical Society* **2007**, *129* (5), 1203-1209.
60. Xiao, B.; Wheatley, P. S.; Morris, R. E., The adsorption, storage and release of nitric oxide using ion exchanged zeolites. In *Studies in surface science and catalysis*, Elsevier: **2007**; Vol. 170, pp 902-909.
61. Wong-Foy, A. G.; Matzger, A. J.; Yaghi, O. M., Exceptional H₂ saturation uptake in microporous metal– organic frameworks. *Journal of the American Chemical Society* **2006**, *128* (11), 3494-3495.
62. Duan, C.; Yu, Y.; Xiao, J.; Li, Y.; Yang, P.; Hu, F.; Xi, H., Recent advancements in metal–organic frameworks for green applications. *Green Energy & Environment* **2021**, *6* (1), 33-49.
63. IEA *From energy to chemicals*, <https://www.iea.org/commentaries/from-energy-to-chemicals>; Paris, **2018**.

64. IEA *The Future of Petrochemicals*, <https://www.iea.org/reports/the-future-of-petrochemicals>; Paris, **2018**.
65. Alsultan, A. G.; Asikin-Mijan, N.; Ibrahim, Z.; Yunus, R.; Razali, S. Z.; Mansir, N.; Islam, A.; Seenivasagam, S.; Taufiq-Yap, Y. H., A Short Review on Catalyst, Feedstock, Modernised Process, Current State and Challenges on Biodiesel Production. *Catalysts* **2021**, *11* (11), 1261.
66. Kim, S.; Tsang, Y. F.; Kwon, E. E.; Lin, K.-Y. A.; Lee, J., Recently developed methods to enhance stability of heterogeneous catalysts for conversion of biomass-derived feedstocks. *Korean Journal of Chemical Engineering* **2019**, *36* (1), 1-11.
67. Lang, M.; Li, H., Heterogeneous metal-based catalysts for cyclohexane synthesis from hydrodeoxygenation of lignin-derived phenolics. *Fuel* **2023**, *344*, 128084.
68. U.S. Bioenergy Statistics, <https://www.ers.usda.gov/data-products/u-s-bioenergy-statistics/> U.S. Department of Agriculture. **2023**.
69. Bozell, J. J.; Petersen, G. R., Technology development for the production of biobased products from biorefinery carbohydrates—the US Department of Energy’s “Top 10” revisited. *Green Chemistry* **2010**, *12* (4), 539-554.
70. Sanders, J.; Scott, E.; Weusthuis, R.; Mooibroek, H., Bio-Refinery as the Bio-Inspired Process to Bulk Chemicals. *Macromolecular Bioscience* **2007**, *7* (2), 105-117.
71. Abdulrazzaq, H. T.; Rahmani Chokanlu, A.; Frederick, B. G.; Schwartz, T. J., Reaction Kinetics Analysis of Ethanol Dehydrogenation Catalyzed by MgO–SiO₂. *ACS Catalysis* **2020**, *10* (11), 6318-6331.
72. Huang, Y.; Wang, B.; Yuan, H.; Sun, Y.; Yang, D.; Cui, X.; Shi, F., The catalytic dehydrogenation of ethanol by heterogeneous catalysts. *Catalysis Science & Technology* **2021**, *11* (5), 1652-1664.
73. De Oliveira-Vigier, K.; Abatzoglou, N.; Gitzhofer, F., Dry-reforming of ethanol in the presence of a 316 stainless steel catalyst. *Canadian Journal of Chemical Engineering* **2005**, *83* (6), 978-984.
74. Tsiakaras, P.; Demin, A., Thermodynamic analysis of a solid oxide fuel cell system fuelled by ethanol. *Journal of Power Sources* **2001**, *102* (1-2), 210-217.
75. Adkins, H.; Kommers, C. E.; Struss, E. F.; Dasler, W., The Preparation of Aldehydes and Ketones by Dehydrogenation of Alcohols over Copper—Chromium Oxide. *Journal of the American Chemical Society* **1933**, *55* (7), 2992-2994.
76. Lazier, W. A.; Adkins, H., DEHYDROGENATION AND DEHYDRATION OF ALCOHOLS OVER A ZINC OXIDE CATALYST. *Journal of the American Chemical Society* **1925**, *47* (6), 1719-1722.
77. Pasel, J.; Häusler, J.; Schmitt, D.; Valencia, H.; Meledina, M.; Mayer, J.; Peters, R., Ethanol Dehydrogenation: A Reaction Path Study by Means of Temporal Analysis of Products. *Catalysts* **2020**, *10* (10), 1151.
78. Ob-eye, J.; Praserthdam, P.; Jongsomjit, B., Dehydrogenation of Ethanol to Acetaldehyde over Different Metals Supported on Carbon Catalysts. *Catalysts* **2019**, *9* (1), 66.
79. Rong, H.; Ji, S.; Zhang, J.; Wang, D.; Li, Y., Synthetic strategies of supported atomic clusters for heterogeneous catalysis. *Nature Communications* **2020**, *11* (1), 5884.
80. Zhang, X.; Zhang, M.; Deng, Y.; Xu, M.; Artiglia, L.; Wen, W.; Gao, R.; Chen, B.; Yao, S.; Zhang, X.; Peng, M.; Yan, J.; Li, A.; Jiang, Z.; Gao, X.; Cao, S.; Yang, C.; Kropf, A. J.; Shi, J.; Xie, J.; Bi, M.; van Bokhoven, J. A.; Li, Y.-W.; Wen, X.; Flytzani-

- Stephanopoulos, M.; Shi, C.; Zhou, W.; Ma, D., A stable low-temperature H₂-production catalyst by crowding Pt on α -MoC. *Nature* **2021**, *589* (7842), 396-401.
81. Ding, K.; Gulec, A.; Johnson, A. M.; Schweitzer, N. M.; Stucky, G. D.; Marks, L. D.; Stair, P. C., Identification of active sites in CO oxidation and water-gas shift over supported Pt catalysts. *Science* **2015**, *350* (6257), 189-192.
82. Otake, K.-i.; Ahn, S.; Knapp, J.; Hupp, J. T.; Notestein, J. M.; Farha, O. K., Vapor-Phase Cyclohexene Epoxidation by Single-Ion Fe(III) Sites in Metal–Organic Frameworks. *Inorganic Chemistry* **2021**, *60* (4), 2457-2463.
83. Yang, Y.; Zhang, X.; Kanchanakungwankul, S.; Lu, Z.; Noh, H.; Syed, Z. H.; Farha, O. K.; Truhlar, D. G.; Hupp, J. T., Unexpected “Spontaneous” Evolution of Catalytic, MOF-Supported Single Cu(II) Cations to Catalytic, MOF-Supported Cu(0) Nanoparticles. *Journal of the American Chemical Society* **2020**, *142* (50), 21169-21177.
84. Wang, C.; Xie, Z.; deKrafft, K. E.; Lin, W., Doping Metal–Organic Frameworks for Water Oxidation, Carbon Dioxide Reduction, and Organic Photocatalysis. *Journal of the American Chemical Society* **2011**, *133* (34), 13445-13454.
85. Manna, K.; Zhang, T.; Carboni, M.; Abney, C. W.; Lin, W., Salicylaldimine-Based Metal–Organic Framework Enabling Highly Active Olefin Hydrogenation with Iron and Cobalt Catalysts. *Journal of the American Chemical Society* **2014**, *136* (38), 13182-13185.
86. Liu, J.; Li, Z.; Zhang, X.; Otake, K.-i.; Zhang, L.; Peters, A. W.; Young, M. J.; Bedford, N. M.; Letourneau, S. P.; Mandia, D. J.; Elam, J. W.; Farha, O. K.; Hupp, J. T., Introducing Nonstructural Ligands to Zirconia-like Metal–Organic Framework Nodes To Tune the Activity of Node-Supported Nickel Catalysts for Ethylene Hydrogenation. *ACS Catalysis* **2019**, *9* (4), 3198-3207.
87. Yuan, S.; Chen, Y.-P.; Qin, J.; Lu, W.; Wang, X.; Zhang, Q.; Bosch, M.; Liu, T.-F.; Lian, X.; Zhou, H.-C., Cooperative Cluster Metalation and Ligand Migration in Zirconium Metal–Organic Frameworks. *Angewandte Chemie International Edition* **2015**, *54* (49), 14696-14700.
88. Peralta, R. A.; Huxley, M. T.; Evans, J. D.; Fallon, T.; Cao, H.; He, M.; Zhao, X. S.; Agnoli, S.; Sumbly, C. J.; Doonan, C. J., Highly Active Gas Phase Organometallic Catalysis Supported Within Metal–Organic Framework Pores. *Journal of the American Chemical Society* **2020**, *142* (31), 13533-13543.
89. Momeni, M. R.; Pahls, D. R.; Yang, D.; Wang, T. C.; Farha, O. K.; Hupp, J. T.; Cramer, C. J.; Gagliardi, L.; Gates, B. C., Correction to “Metal–Organic Framework Nodes as Nearly Ideal Supports for Molecular Catalysts: NU-1000- and UiO-66-Supported Iridium Complexes”. *Journal of the American Chemical Society* **2017**, *139* (50), 18406-18406.
90. Nguyen, L. H. T.; Nguyen, T. T. T.; Dang, Y. T.; Tran, P. H.; Le Hoang Doan, T., Microwave-Assisted Synthesis as an Efficient Method to Enhance the Catalytic Activity of Zr-Based Metal Organic Framework UiO-66 in a Heterocyclization Reaction. *Asian Journal of Organic Chemistry* **2019**, *8* (12), 2276-2281.
91. Ramezanzadeh, M.; Tati, A.; Bahlakeh, G.; Ramezanzadeh, B., Construction of an epoxy composite coating with exceptional thermo-mechanical properties using Zr-based NH₂-UiO-66 metal-organic framework (MOF): Experimental and DFT-D theoretical explorations. *Chemical Engineering Journal* **2021**, *408*, 127366.
92. Li, Z.; Schweitzer, N. M.; League, A. B.; Bernales, V.; Peters, A. W.; Getsoian, A. B.; Wang, T. C.; Miller, J. T.; Vjunov, A.; Fulton, J. L.; Lercher, J. A.; Cramer, C. J.; Gagliardi, L.; Hupp, J. T.; Farha, O. K., Sintering-Resistant Single-Site Nickel Catalyst Supported by

- Metal–Organic Framework. *Journal of the American Chemical Society* **2016**, *138* (6), 1977-1982.
93. Wu, X.; Zhang, H.; Zuo, S.; Dong, J.; Li, Y.; Zhang, J.; Han, Y., Engineering the Coordination Sphere of Isolated Active Sites to Explore the Intrinsic Activity in Single-Atom Catalysts. *Nano-Micro Letters* **2021**, *13* (1), 136.
94. Bernales, V.; Yang, D.; Yu, J.; Gümüşlü, G.; Cramer, C. J.; Gates, B. C.; Gagliardi, L., Molecular Rhodium Complexes Supported on the Metal-Oxide-Like Nodes of Metal Organic Frameworks and on Zeolite HY: Catalysts for Ethylene Hydrogenation and Dimerization. *ACS Applied Materials & Interfaces* **2017**, *9* (39), 33511-33520.
95. Ahn, S.; Thornburg, N. E.; Li, Z.; Wang, T. C.; Gallington, L. C.; Chapman, K. W.; Notestein, J. M.; Hupp, J. T.; Farha, O. K., Stable Metal–Organic Framework-Supported Niobium Catalysts. *Inorganic Chemistry* **2016**, *55* (22), 11954-11961.
96. Li, Z.; Peters, A. W.; Bernales, V.; Ortuño, M. A.; Schweitzer, N. M.; DeStefano, M. R.; Gallington, L. C.; Platero-Prats, A. E.; Chapman, K. W.; Cramer, C. J.; Gagliardi, L.; Hupp, J. T.; Farha, O. K., Metal–Organic Framework Supported Cobalt Catalysts for the Oxidative Dehydrogenation of Propane at Low Temperature. *ACS Central Science* **2017**, *3* (1), 31-38.
97. Hwang, Y. K.; Hong, D.-Y.; Chang, J.-S.; Seo, H.; Yoon, M.; Kim, J.; Jung, S. H.; Serre, C.; Férey, G., Selective sulfoxidation of aryl sulfides by coordinatively unsaturated metal centers in chromium carboxylate MIL-101. *Applied Catalysis A: General* **2009**, *358* (2), 249-253.
98. Xie, M.-H.; Yang, X.-L.; Zou, C.; Wu, C.-D., A SnIV–Porphyrin-Based Metal–Organic Framework for the Selective Photo-Oxygenation of Phenol and Sulfides. *Inorganic Chemistry* **2011**, *50* (12), 5318-5320.
99. Redfern, L. R.; Lo, W.-S.; Dillingham, I. J.; Eatman, J. G.; Mian, M. R.; Tsung, C.-K.; Farha, O. K., Enhancing Four-Carbon Olefin Production from Acetylene over Copper Nanoparticles in Metal–Organic Frameworks. *ACS Applied Materials & Interfaces* **2020**, *12* (28), 31496-31502.
100. Chen, C.; Alalouni, M. R.; Dong, X.; Cao, Z.; Cheng, Q.; Zheng, L.; Meng, L.; Guan, C.; Liu, L.; Abou-Hamad, E.; Wang, J.; Shi, Z.; Huang, K.-W.; Cavallo, L.; Han, Y., Highly Active Heterogeneous Catalyst for Ethylene Dimerization Prepared by Selectively Doping Ni on the Surface of a Zeolitic Imidazolate Framework. *Journal of the American Chemical Society* **2021**, *143* (18), 7144-7153.
101. Joshi, R.; Saxena, A.; Gounder, R., Mechanistic insights into alkene chain growth reactions catalyzed by nickel active sites on ordered microporous and mesoporous supports. *Catalysis Science & Technology* **2020**, *10* (21), 7101-7123.
102. Liu, P.; Redekop, E.; Gao, X.; Liu, W.-C.; Olsbye, U.; Somorjai, G. A., Oligomerization of Light Olefins Catalyzed by Brønsted-Acidic Metal–Organic Framework-808. *Journal of the American Chemical Society* **2019**, *141* (29), 11557-11564.
103. Goetjen, T. A.; Zhang, X.; Liu, J.; Hupp, J. T.; Farha, O. K., Metal–Organic Framework Supported Single Site Chromium(III) Catalyst for Ethylene Oligomerization at Low Pressure and Temperature. *ACS Sustainable Chemistry & Engineering* **2019**, *7* (2), 2553-2557.
104. Rivera-Torrente, M.; Pletcher, P. D.; Jongkind, M. K.; Nikolopoulos, N.; Weckhuysen, B. M., Ethylene Polymerization over Metal–Organic Framework Crystallites and the Influence of Linkers on Their Fracturing Process. *ACS Catalysis* **2019**, *9* (4), 3059-3069.

105. Comito, R. J.; Wu, Z.; Zhang, G.; Lawrence III, J. A.; Korzyński, M. D.; Kehl, J. A.; Miller, J. T.; Dincă, M., Stabilized Vanadium Catalyst for Olefin Polymerization by Site Isolation in a Metal–Organic Framework. *Angewandte Chemie International Edition* **2018**, *57* (27), 8135-8139.
106. Noei, H.; Amirjalayer, S.; Müller, M.; Zhang, X.; Schmid, R.; Muhler, M.; Fischer, R. A.; Wang, Y., Low-Temperature CO Oxidation over Cu-Based Metal–Organic Frameworks Monitored by using FTIR Spectroscopy. *ChemCatChem* **2012**, *4* (6), 755-759.
107. Yousefzadeh Borzehandani, M.; Abdulmalek, E.; Abdul Rahman, M. B.; Mohammad Latif, M. A., First-principles investigation of dimethyl-functionalized MIL-53(Al) metal–organic framework for adsorption and separation of xylene isomers. *Journal of Porous Materials* **2021**, *28* (2), 579-591.
108. Ahn, S.; Nauert, S. L.; Buru, C. T.; Rimoldi, M.; Choi, H.; Schweitzer, N. M.; Hupp, J. T.; Farha, O. K.; Notestein, J. M., Pushing the Limits on Metal–Organic Frameworks as a Catalyst Support: NU-1000 Supported Tungsten Catalysts for o-Xylene Isomerization and Disproportionation. *Journal of the American Chemical Society* **2018**, *140* (27), 8535-8543.
109. Nepal, B.; Das, S., Sustained Water Oxidation by a Catalyst Cage-Isolated in a Metal–Organic Framework. *Angewandte Chemie International Edition* **2013**, *52* (28), 7224-7227.
110. Wang, L.; Wu, Y.; Cao, R.; Ren, L.; Chen, M.; Feng, X.; Zhou, J.; Wang, B., Fe/Ni Metal–Organic Frameworks and Their Binder-Free Thin Films for Efficient Oxygen Evolution with Low Overpotential. *ACS Applied Materials & Interfaces* **2016**, *8* (26), 16736-16743.
111. Kung, C.-W.; Mondloch, J. E.; Wang, T. C.; Bury, W.; Hoffeditz, W.; Klahr, B. M.; Klet, R. C.; Pellin, M. J.; Farha, O. K.; Hupp, J. T., Metal–Organic Framework Thin Films as Platforms for Atomic Layer Deposition of Cobalt Ions To Enable Electrocatalytic Water Oxidation. *ACS Applied Materials & Interfaces* **2015**, *7* (51), 28223-28230.
112. Han, W.; Li, M.; Ma, Y.; Yang, J., Cobalt-Based Metal-Organic Frameworks and Their Derivatives for Hydrogen Evolution Reaction. *Frontiers in Chemistry* **2020**, *8* (1025).
113. Peters, A. W.; Li, Z.; Farha, O. K.; Hupp, J. T., Toward Inexpensive Photocatalytic Hydrogen Evolution: A Nickel Sulfide Catalyst Supported on a High-Stability Metal–Organic Framework. *ACS Applied Materials & Interfaces* **2016**, *8* (32), 20675-20681.
114. Huang, N.-Y.; He, H.; Li, H.; Liao, P.-Q.; Chen, X.-M., A metal–organic framework with in situ generated low-coordinate binuclear Cu(i) units as a highly effective catalyst for photodriven hydrogen production. *Chemical Communications* **2020**, *56* (49), 6700-6703.
115. He, J.; Yang, H.; Chen, Y.; Yan, Z.; Zeng, Y.; Luo, Z.; Gao, W.; Wang, J., Solar Light Photocatalytic Degradation of Nitrite in Aqueous Solution Over CdS Embedded on Metal–Organic Frameworks. *Water, Air, & Soil Pollution* **2015**, *226* (6), 197.
116. Choi, H.; Peters, A. W.; Noh, H.; Gallington, L. C.; Platero-Prats, A. E.; DeStefano, M. R.; Rimoldi, M.; Goswami, S.; Chapman, K. W.; Farha, O. K.; Hupp, J. T., Vapor-Phase Fabrication and Condensed-Phase Application of a MOF-Node-Supported Iron Thiolate Photocatalyst for Nitrate Conversion to Ammonium. *ACS Applied Energy Materials* **2019**, *2* (12), 8695-8700.
117. Yang, D.; Ortuño, M. A.; Bernales, V.; Cramer, C. J.; Gagliardi, L.; Gates, B. C., Structure and Dynamics of Zr6O8 Metal–Organic Framework Node Surfaces Probed with Ethanol Dehydration as a Catalytic Test Reaction. *Journal of the American Chemical Society* **2018**, *140* (10), 3751-3759.
118. Liu, J.; Lu, Z.; Chen, Z.; Rimoldi, M.; Howarth, A. J.; Chen, H.; Alayoglu, S.; Snurr, R. Q.; Farha, O. K.; Hupp, J. T., Ammonia Capture within Zirconium Metal–Organic

- Frameworks: Reversible and Irreversible Uptake. *ACS Applied Materials & Interfaces* **2021**, *13* (17), 20081-20093.
119. Larabi, C.; Quadrelli, E. A., Titration of Zr₃(μ-OH) Hydroxy Groups at the Cornerstones of Bulk MOF UiO-67, [Zr₆O₄(OH)₄(biphenyldicarboxylate)₆], and Their Reaction with [AuMe(PMe₃)]. *European Journal of Inorganic Chemistry* **2012**, *2012* (18), 3014-3022.
120. Ouyang, M.; Cao, S.; Yang, S.; Li, M.; Flytzani-Stephanopoulos, M., Atomically Dispersed Pd Supported on Zinc Oxide for Selective Nonoxidative Ethanol Dehydrogenation. *Industrial & Engineering Chemistry Research* **2020**, *59* (6), 2648-2656.
121. Cheng, E.; Notestein, J., Catalytic dehydrogenation of isobutane over supported MoO_x/K-Al₂O₃. *Journal of Catalysis* **2021**, *397*, 212-222.
122. Benomar, S.; Massó, A.; Solsona, B.; Issaadi, R.; López Nieto, J. M., Vanadium Supported on Alumina and/or Zirconia Catalysts for the Selective Transformation of Ethane and Methanol. *Catalysts* **2018**, *8* (4), 126.
123. Wang, X.; Zhang, X.; Pandharkar, R.; Lyu, J.; Ray, D.; Yang, Y.; Kato, S.; Liu, J.; Wasson, M. C.; Islamoglu, T.; Li, Z.; Hupp, J. T.; Cramer, C. J.; Gagliardi, L.; Farha, O. K., Insights into the Structure–Activity Relationships in Metal–Organic Framework-Supported Nickel Catalysts for Ethylene Hydrogenation. *ACS Catalysis* **2020**, *10* (16), 8995-9005.
124. Lu, Z.; Liu, J.; Zhang, X.; Liao, Y.; Wang, R.; Zhang, K.; Lyu, J.; Farha, O. K.; Hupp, J. T., Node-Accessible Zirconium MOFs. *Journal of the American Chemical Society* **2020**, *142* (50), 21110-21121.
125. Zhao, R.; Xiao, S.; Yang, S.; Wang, X., Surface Thermolytic Behavior of Nickel Amidinate and Its Implication on the Atomic Layer Deposition of Nickel Compounds. *Chemistry of Materials* **2019**, *31* (14), 5172-5180.
126. Peters, A. W.; Otake, K.; Platero-Prats, A. E.; Li, Z.; DeStefano, M. R.; Chapman, K. W.; Farha, O. K.; Hupp, J. T., Site-Directed Synthesis of Cobalt Oxide Clusters in a Metal–Organic Framework. *ACS Applied Materials & Interfaces* **2018**, *10* (17), 15073-15078.
127. Zhao, Y.; Truhlar, D. G., A new local density functional for main-group thermochemistry, transition metal bonding, thermochemical kinetics, and noncovalent interactions. *The Journal of Chemical Physics* **2006**, *125* (19), 194101.
128. Weigend, F.; Ahlrichs, R., Balanced basis sets of split valence, triple zeta valence and quadruple zeta valence quality for H to Rn: Design and assessment of accuracy. *Physical Chemistry Chemical Physics* **2005**, *7* (18), 3297-3305.
129. Weigend, F., Accurate Coulomb-fitting basis sets for H to Rn. *Physical Chemistry Chemical Physics* **2006**, *8* (9), 1057-1065.
130. Andrae, D.; Häußermann, U.; Dolg, M.; Stoll, H.; Preuß, H., Energy-adjusted *ab initio* pseudopotentials for the second and third row transition elements. *Theoretica chimica acta* **1990**, *77* (2), 123-141.
131. Bouwman, E.; Reedijk, J., Structural and functional models related to the nickel hydrogenases. *Coord. Chem. Rev.* **2005**, *249* (15-16), 1555-1581.
132. Boer, J. L.; Mulrooney, S. B.; Hausinger, R. P., Nickel-dependent metalloenzymes. *Arch. Biochem. Biophys.* **2014**, *544*, 142-152.
133. Oudart, Y.; Artero, V.; Pécaut, J.; Fontecave, M., [Ni(xbsms)Ru(CO)₂Cl₂]: A Bioinspired Nickel–Ruthenium Functional Model of [NiFe] Hydrogenase. *Inorg. Chem.* **2006**, *45* (11), 4334-4336.
134. Lubitz, W.; Ogata, H.; Rüdiger, O.; Reijerse, E., Hydrogenases. *Chem. Rev.* **2014**, *114* (8), 4081-4148.

135. Ogata, H.; Lubitz, W.; Higuchi, Y., [NiFe] hydrogenases: structural and spectroscopic studies of the reaction mechanism. *Dalton Transactions* **2009**, (37), 7577-7587.
136. Bavykina, A.; Kolobov, N.; Khan, I. S.; Bau, J. A.; Ramirez, A.; Gascon, J., Metal–Organic Frameworks in Heterogeneous Catalysis: Recent Progress, New Trends, and Future Perspectives. *Chem. Rev.* **2020**.
137. Pike, S. D.; Weller, A. S., Organometallic synthesis, reactivity and catalysis in the solid state using well-defined single-site species. *Philos. Trans. R. Soc., A* **2015**, 373 (2037).
138. Yang, D.; Gates, B. C., Catalysis by Metal Organic Frameworks: Perspective and Suggestions for Future Research. *ACS Catal.* **2019**, 9 (3), 1779-1798.
139. Peters, A. W.; Li, Z.; Farha, O. K.; Hupp, J. T., Toward Inexpensive Photocatalytic Hydrogen Evolution: A Nickel Sulfide Catalyst Supported on a High-Stability Metal–Organic Framework. *ACS Appl. Mater. Interfaces* **2016**, 8 (32), 20675-20681.
140. Li, Z.; Schweitzer, N. M.; League, A. B.; Bernales, V.; Peters, A. W.; Getsoian, A. B.; Wang, T. C.; Miller, J. T.; Vjunov, A.; Fulton, J. L.; Lercher, J. A.; Cramer, C. J.; Gagliardi, L.; Hupp, J. T.; Farha, O. K., Sintering-Resistant Single-Site Nickel Catalyst Supported by Metal–Organic Framework. *J. Am. Chem. Soc.* **2016**, 138 (6), 1977-1982.
141. Grosvenor, A. P.; Biesinger, M. C.; Smart, R. S. C.; Gerson, A. R., The Influence of Final-State Effects on XPS Spectra from First-Row Transition-Metals. In *Hard X-ray Photoelectron Spectroscopy (HAXPES)*, Woicik, J., Ed. Springer International Publishing: Cham, **2016**; pp 217-262.
142. Lin, C.; Posadas, A.; Hadamek, T.; Demkov, A. A., Final-state effect on x-ray photoelectron spectrum of nominally d^1 and n-doped d^0 transition-metal oxides. *Physical Review B* **2015**, 92 (3), 035110.
143. Peck, M. A.; Langell, M. A., Comparison of Nanoscaled and Bulk NiO Structural and Environmental Characteristics by XRD, XAFS, and XPS. *Chemistry of Materials* **2012**, 24 (23), 4483-4490.
144. Valente, J. S.; Valle-Orta, M.; Armendáriz-Herrera, H.; Quintana-Solórzano, R.; del Angel, P.; Ramírez-Salgado, J.; Montiel-López, J. R., Controlling the redox properties of nickel in NiO/ZrO₂ catalysts synthesized by sol–gel. *Catalysis Science & Technology* **2018**, 8 (16), 4070-4082.
145. Whelan, C. M.; Smyth, M. R.; Barnes, C. J., HREELS, XPS, and Electrochemical Study of Benzenethiol Adsorption on Au(111). *Langmuir* **1999**, 15 (1), 116-126.
146. Yuan, N.; Majeed, M. H.; Bajnóczi, É. G.; Persson, A. R.; Wallenberg, L. R.; Inge, A. K.; Heidenreich, N.; Stock, N.; Zou, X.; Wendt, O. F.; Persson, I., In situ XAS study of the local structure and oxidation state evolution of palladium in a reduced graphene oxide supported Pd(ii) carbene complex during an undirected C–H acetoxylation reaction. *Catal. Sci. Technol.* **2019**, 9 (8), 2025-2031.
147. Colpas, G. J.; Maroney, M. J.; Bagyinka, C.; Kumar, M.; Willis, W. S.; Suib, S. L.; Mascharak, P. K.; Baidya, N., X-ray spectroscopic studies of nickel complexes, with application to the structure of nickel sites in hydrogenases. *Inorg. Chem.* **1991**, 30 (5), 920-928.
148. Sarangi, R., X-ray absorption near-edge spectroscopy in bioinorganic chemistry: Application to M–O₂ systems. *Coord. Chem. Rev.* **2013**, 257 (2), 459-472.
149. Furenlid, L. R.; Renner, M. W.; Fujita, E., XAS studies of Ni(I), Ni(II), and Ni(III) complexes. *Physica B: Condensed Matter* **1995**, 208-209, 739-742.

150. Barkigia, K. M.; Renner, M. W.; Furenlid, L. R.; Medforth, C. J.; Smith, K. M.; Fajer, J., Crystallographic and EXAFS studies of conformationally designed nonplanar nickel(II) porphyrins. *Journal of the American Chemical Society* **1993**, *115* (9), 3627-3635.
151. Huang, Y. H.; Moura, I.; Moura, J. J. G.; LeGall, J.; Park, J. B.; Adams, M. W. W.; Johnson, M. K., Resonance Raman studies of nickel tetrathiolates and nickel-substituted rubredoxins and desulfuredoxin. *Inorg. Chem.* **1993**, *32* (4), 406-412.
152. Doorn, S. K.; Hupp, J. T., Preresonance Raman studies of metal-to-ligand charge transfer in $(\text{NH}_3)_4\text{Ru}(2,2'\text{-bipyridine})_2^+$. In situ bond length changes, force constants, and reorganization energies. *J. Am. Chem. Soc.* **1989**, *111* (13), 4704-4712.
153. Hadj Romdhane, Y.; Bellamy, B.; De Gouveia, V.; Masson, A.; Che, M., Structure sensitivity: Hydrogenolysis of n-butane and hydrogenation of ethylene on nickel clusters condensed onto amorphous silica. *Appl. Surf. Sci.* **1988**, *31* (3), 383-401.
154. Wang, Q.; Pengmei, Z.; Pandharkar, R.; Gagliardi, L.; Hupp, J. T.; Notestein, J. M., Investigating the effect of metal nuclearity on activity for ethylene hydrogenation by metal-organic-framework-supported oxy-Ni(II) catalysts. *Journal of Catalysis* **2022**, *407*, 162-173.
155. Wang, T. C.; Vermeulen, N. A.; Kim, I. S.; Martinson, A. B. F.; Stoddart, J. F.; Hupp, J. T.; Farha, O. K., Scalable synthesis and post-modification of a mesoporous metal-organic framework called NU-1000. *Nature Protocols* **2016**, *11* (1), 149-162.
156. Huber, G. W.; Iborra, S.; Corma, A., Synthesis of Transportation Fuels from Biomass: Chemistry, Catalysts, and Engineering. *Chemical Reviews* **2006**, *106* (9), 4044-4098.
157. Pang, J.; Yin, M.; Wu, P.; Li, X.; Li, H.; Zheng, M.; Zhang, T., Advances in catalytic dehydrogenation of ethanol to acetaldehyde. *Green Chemistry* **2021**, *23* (20), 7902-7916.
158. Gérardy, R.; Debecker, D. P.; Estager, J.; Luis, P.; Monbaliu, J.-C. M., Continuous Flow Upgrading of Selected C2–C6 Platform Chemicals Derived from Biomass. *Chemical Reviews* **2020**, *120* (15), 7219-7347.
159. Corma, A.; Iborra, S.; Velty, A., Chemical Routes for the Transformation of Biomass into Chemicals. *Chemical Reviews* **2007**, *107* (6), 2411-2502.
160. *Global Acetaldehyde Market - Trends, COVID-19 impact and Growth Forecasts to 2026*. <https://www.chemintel360.com/report-details.php?id=28> (Accessed March 17, 2022).
161. Race, N.; Patel, H.; Sigman, M. S., 5.5 The Wacker Process. In *Catalytic Oxidation in Organic Synthesis*, 1st edition ed.; Georg Thieme Verlag KG: Stuttgart, 2018; Vol. 2017/4.
162. Xue, F.; Miao, C.; Yue, Y.; Hua, W.; Gao, Z., Direct conversion of bio-ethanol to propylene in high yield over the composite of In_2O_3 and zeolite beta. *Green Chemistry* **2017**, *19* (23), 5582-5590.
163. Iwamoto, M., Selective catalytic conversion of bio-ethanol to propene: A review of catalysts and reaction pathways. *Catalysis Today* **2015**, *242*, 243-248.
164. Chakraborty, S.; Pizsel, P. E.; Hayes, C. E.; Baker, R. T.; Jones, W. D., Highly Selective Formation of n-Butanol from Ethanol through the Guerbet Process: A Tandem Catalytic Approach. *Journal of the American Chemical Society* **2015**, *137* (45), 14264-14267.
165. DiBenedetto, T. A.; Jones, W. D., Upgrading of Ethanol to n-Butanol via a Ruthenium Catalyst in Aqueous Solution. *Organometallics* **2021**, *40* (12), 1884-1888.
166. Liu, C.; Li, Y.; Wu, L.; Geng, Z., Synthesis of 1,3-butadiene from ethanol/acetaldehyde over $\text{ZrO}_2\text{-MgO-SiO}_2$ catalyst: The thermodynamics and reaction kinetics analysis. *Chemical Engineering Journal* **2021**, *421*, 127861.
167. Cabello González, G. M.; Villanueva Perales, A. L.; Martínez, A.; Campoy, M.; Vidal-Barrero, F., Conversion of aqueous ethanol/acetaldehyde mixtures into 1,3-butadiene over a

- mesostructured Ta-SBA-15 catalyst: Effect of reaction conditions and kinetic modelling. *Fuel Processing Technology* **2022**, *226*, 107092.
168. Sun, J.; Zhu, K.; Gao, F.; Wang, C.; Liu, J.; Peden, C. H. F.; Wang, Y., Direct Conversion of Bio-ethanol to Isobutene on Nanosized Zn_xZr_yO_z Mixed Oxides with Balanced Acid–Base Sites. *Journal of the American Chemical Society* **2011**, *133* (29), 11096-11099.
169. Rorrer, J. E.; Toste, F. D.; Bell, A. T., Mechanism and Kinetics of Isobutene Formation from Ethanol and Acetone over Zn_xZr_yO_z. *ACS Catalysis* **2019**, *9* (12), 10588-10604.
170. Takei, T.; Iguchi, N.; Haruta, M., Synthesis of Acetaldehyde, Acetic Acid, and Others by the Dehydrogenation and Oxidation of Ethanol. *Catalysis Surveys from Asia* **2011**, *15* (2), 80-88.
171. Wang, Q.-N.; Weng, X.-F.; Zhou, B.-C.; Lv, S.-P.; Miao, S.; Zhang, D.; Han, Y.; Scott, S. L.; Schüth, F.; Lu, A.-H., Direct, Selective Production of Aromatic Alcohols from Ethanol Using a Tailored Bifunctional Cobalt–Hydroxyapatite Catalyst. *ACS Catalysis* **2019**, *9* (8), 7204-7216.
172. Chang, F. W.; Yang, H. C.; Roselin, L. S.; Kuo, W. Y., *Appl. Catal., A* **2006**, *304*, 30.
173. Freitas, I. C.; Damyanova, S.; Oliveira, D. C.; Marques, C. M. P.; Bueno, J. M. C., Effect of Cu content on the surface and catalytic properties of Cu/ZrO₂ catalyst for ethanol dehydrogenation. *Journal of Molecular Catalysis A: Chemical* **2014**, *381*, 26-37.
174. Santacesaria, E.; Carotenuto, G.; Tesser, R.; Di Serio, M., Ethanol dehydrogenation to ethyl acetate by using copper and copper chromite catalysts. *Chemical Engineering Journal* **2012**, *179*, 209-220.
175. Janvelyan, N.; van Spronsen, M. A.; Wu, C. H.; Qi, Z.; Montemore, M. M.; Shan, J.; Zakharov, D. N.; Xu, F.; Boscoboinik, J. A.; Salmeron, M. B.; Stach, E. A.; Flytzani-Stephanopoulos, M.; Biener, J.; Friend, C. M., Stabilization of a nanoporous NiCu dilute alloy catalyst for non-oxidative ethanol dehydrogenation. *Catalysis Science & Technology* **2020**, *10* (15), 5207-5217.
176. Shan, J.; Liu, J.; Li, M.; Lustig, S.; Lee, S.; Flytzani-Stephanopoulos, M., NiCu single atom alloys catalyze the CH bond activation in the selective non-oxidative ethanol dehydrogenation reaction. *Applied Catalysis B: Environmental* **2018**, *226*, 534-543.
177. Shan, J.; Janvelyan, N.; Li, H.; Liu, J.; Egle, T. M.; Ye, J.; Biener, M. M.; Biener, J.; Friend, C. M.; Flytzani-Stephanopoulos, M., Selective non-oxidative dehydrogenation of ethanol to acetaldehyde and hydrogen on highly dilute NiCu alloys. *Applied Catalysis B: Environmental* **2017**, *205*, 541-550.
178. Lu, G.; Li, S.; Guo, Z.; Farha, O. K.; Hauser, B. G.; Qi, X.; Wang, Y.; Wang, X.; Han, S.; Liu, X.; DuChene, J. S.; Zhang, H.; Zhang, Q.; Chen, X.; Ma, J.; Loo, S. C. J.; Wei, W. D.; Yang, Y.; Hupp, J. T.; Huo, F., Imparting functionality to a metal–organic framework material by controlled nanoparticle encapsulation. *Nature Chemistry* **2012**, *4* (4), 310-316.
179. Hardian, R.; Dissegna, S.; Ullrich, A.; Llewellyn, P. L.; Coulet, M.-V.; Fischer, R. A., Tuning the Properties of MOF-808 via Defect Engineering and Metal Nanoparticle Encapsulation. *Chemistry – A European Journal* **2021**, *27* (22), 6804-6814.
180. Gumus, I.; Karataş, Y.; Gülcan, M., Silver nanoparticles stabilized by a metal–organic framework (MIL-101(Cr)) as an efficient catalyst for imine production from the dehydrogenative coupling of alcohols and amines. *Catalysis Science & Technology* **2020**, *10* (15), 4990-4999.

181. Kung, C.-W.; Audu, C. O.; Peters, A. W.; Noh, H.; Farha, O. K.; Hupp, J. T., Copper Nanoparticles Installed in Metal–Organic Framework Thin Films are Electrocatalytically Competent for CO₂ Reduction. *ACS Energy Letters* **2017**, *2* (10), 2394-2401.
182. Platero-Prats, A. E.; Li, Z.; Gallington, L. C.; Peters, A.; Hupp, J. T.; Farha, O. K.; Chapman, K. W., Addressing the Characterisation Challenge to Understand Catalysis in Mofs: The Case of Nanoscale Cu Supported in NU-1000. *Faraday Discuss.* **2017**, *201* (0), 337.
183. Halder, A.; Lee, S.; Yang, B.; Pellin, M. J.; Vajda, S.; Li, Z.; Yang, Y.; Farha, O. K.; Hupp, J. T., Structural reversibility of Cu doped NU-1000 MOFs under hydrogenation conditions. *The Journal of Chemical Physics* **2020**, *152* (8), 084703.
184. Redfern, L. R.; Li, Z.; Zhang, X.; Farha, O. K., Highly Selective Acetylene Semihydrogenation Catalyzed by Cu Nanoparticles Supported in a Metal–Organic Framework. *ACS Applied Nano Materials* **2018**, *1* (9), 4413-4417.
185. Li, B.; Luo, X.; Zhu, Y.; Wang, X., Immobilization of Cu(II) in KIT-6 supported Co₃O₄ and catalytic performance for epoxidation of styrene. *Applied Surface Science* **2015**, *359*, 609-620.
186. Kilo, M.; Weigel, J.; Wokaun, A.; Koeppl, R. A.; Stoeckli, A.; Baiker, A., Effect of the addition of chromium- and manganese oxides on structural and catalytic properties of copper/zirconia catalysts for the synthesis of methanol from carbon dioxide. *Journal of Molecular Catalysis A: Chemical* **1997**, *126* (2), 169-184.
187. Knapp, R.; Wyrzgol, S. A.; Jentys, A.; Lercher, J. A., Water–gas shift catalysts based on ionic liquid mediated supported Cu nanoparticles. *Journal of Catalysis* **2010**, *276* (2), 280-291.
188. Nishikiori, H.; Hizumi, T.; Kawamoto, K.; Teshima, K., Phase transition and crystal growth of a titania layer on a titanium metal plate. *Research on Chemical Intermediates* **2018**, *44* (12), 7539-7555.
189. Miao, B.; Wu, Z.-P.; Xu, H.; Zhang, M.; Chen, Y.; Wang, L., DFT studies on the key competing reaction steps towards complete ethanol oxidation on transition metal catalysts. *Computational Materials Science* **2019**, *156*, 175-186.
190. Kolev, T.; Seidel, R. W.; Koleva, B. B.; Mayer-Figge, H.; Spitteller, M.; Sheldrick, W. S., Polymorphs of 4-(dihydroxymethyl)pyridinium hydrogensquarate – Crystal structures and spectroscopic properties. *Journal of Molecular Structure* **2009**, *931* (1), 45-49.
191. Pang, J.; Zheng, M.; Wang, C.; Yang, X.; Liu, H.; Liu, X.; Sun, J.; Wang, Y.; Zhang, T., Hierarchical Echinus-like Cu-MFI Catalysts for Ethanol Dehydrogenation. *ACS Catalysis* **2020**, *10* (22), 13624-13629.
192. Iyer, J.; Jalid, F.; Khan, T. S.; Haider, M. A., Tracing the reactivity of single atom alloys for ethanol dehydrogenation using ab initio simulations. *Reaction Chemistry & Engineering* **2022**, *7* (1), 61-75.
193. Yu, D.; Dai, W.; Wu, G.; Guan, N.; Li, L., Stabilizing copper species using zeolite for ethanol catalytic dehydrogenation to acetaldehyde. *Chinese Journal of Catalysis* **2019**, *40* (9), 1375-1384.
194. Garcés, J.; Arrué, R.; Novoa, N.; Peixoto, A. F.; Chimentão, R. J., Glycerol Valorization over ZrO₂-Supported Copper Nanoparticles Catalysts Prepared by Chemical Reduction Method. *Catalysts* **2021**, *11* (9), 1040.
195. Yakovenko, A. A.; Wei, Z.; Wriedt, M.; Li, J. R.; Halder, G. J.; Zhou, H. C., Study of Guest Molecules in Metal–Organic Frameworks by Powder X-ray Diffraction: Analysis of Difference Envelope Density. *Crystal Growth & Design* **2014**, *14*, 5397-5407.

196. Díaz de León, J. N.; Ramesh Kumar, C.; Antúnez-García, J.; Fuentes-Moyado, S., Recent Insights in Transition Metal Sulfide Hydrodesulfurization Catalysts for the Production of Ultra Low Sulfur Diesel: A Short Review. *Catalysts* **2019**, *9* (1), 87.
197. Wang, E.; Yang, F.; Song, M.; Chen, G.; Zhang, Q.; Wang, F.; Bing, L.; Wang, G.; Han, D., Recent advances in the unsupported catalysts for the hydrodesulfurization of fuel. *Fuel Processing Technology* **2022**, *235*, 107386.
198. Derouane, E. G.; Pedersen, E.; Clausen, B. S.; Gabelica, Z.; Candia, R.; Topsøe, H., EPR studies on unsupported and alumina-supported sulfided Co–Mo hydrodesulfurization catalysts. *Journal of Catalysis* **1986**, *99* (2), 253-261.
199. Cheng, E.; Notestein, J., Molybdenum oxide and sulfide active sites for isobutane dehydrogenation with methanol as a probe molecule. *Journal of Catalysis* **2022**, *413*, 498-508.
200. Arinaga, A. M.; Ziegelski, M. C.; Marks, T. J., Alternative Oxidants for the Catalytic Oxidative Coupling of Methane. *Angewandte Chemie International Edition* **2021**, *60* (19), 10502-10515.
201. Larson, A. H. A thermodynamic study of the zirconium sulfides. Missouri School of Mines and Metallurgy, Missouri, **1959**.
202. Arinaga, A. M.; Liu, S.; Marks, T. J., Oxidative dehydrogenation of propane over transition metal sulfides using sulfur as an alternative oxidant. *Catalysis Science & Technology* **2020**, *10* (20), 6840-6848.
203. Ziolk, M.; Kujawa, J.; Saur, O.; Lavalley, J. C., Influence of hydrogen sulfide adsorption on the catalytic properties of metal oxides. *Journal of Molecular Catalysis A: Chemical* **1995**, *97* (1), 49-55.
204. Hong, S. T.; Park, D. R.; Yoo, S.-J.; Kim, J.-D.; Park, H. S., Characterization of the active phase of NiMo/Al₂O₃ hydrodesulfurization catalysts. *Research on Chemical Intermediates* **2006**, *32* (9), 857-870.
205. Ishihara, A., Sulfidation State and Sulfur Behavior on Mo-based HDS Catalysts Supported on TiO₂ Using ³⁵S Tracer Methods. *Journal of the Japan Petroleum Institute* **2008**, *51* (2), 73-82.
206. Sugioka, M.; Nakayama, T.; Uemichi, Y.; Kanazuka, T., Promotive effect of H₂S for hydrocarbon conversions over Na zeolites. *Reaction Kinetics and Catalysis Letters* **1990**, *41* (2), 345-350.
207. Colón-Ortiz, J.; Landers, J. M.; Gordon, W. O.; Balboa, A.; Karwacki, C. J.; Neimark, A. V., Disordered Mesoporous Zirconium (Hydr)oxides for Decomposition of Dimethyl Chlorophosphate. *ACS Applied Materials & Interfaces* **2019**, *11* (19), 17931-17939.
208. Yin, C.; Wang, Y., Effect of sulfidation process on catalytic performance over unsupported Ni-Mo-W hydrotreating catalysts. *Korean Journal of Chemical Engineering* **2017**, *34* (4), 1004-1012.
209. Jiang, M.; Wang, B.; Yao, Y.; Wang, H.; Li, Z.; Ma, X.; Qin, S.; Sun, Q., Effect of stepwise sulfidation on a MoO₃/CeO₂-Al₂O₃ catalyst for sulfur-resistant methanation. *Applied Catalysis A: General* **2014**, *469*, 89-97.
210. Zekel, L. A.; Gyulmaliev, A. M.; Batov, A. E.; Visaliev, M. Y.; Kadieva, M. K.; Dandaev, A. U.; Magomadov, E. E.; Kubrin, N. A.; Kadiev, K. M., Sulfidation of a Dispersed Molybdenum Catalyst with Hydrogen Sulfide Formed from Hydroconversion of Petroleum Feedstock. *Petroleum Chemistry* **2021**, *61* (10), 1096-1103.
211. Healy, C.; Patil, K. M.; Wilson, B. H.; Hermanspahn, L.; Harvey-Reid, N. C.; Howard, B. I.; Kleinjan, C.; Kolien, J.; Payet, F.; Telfer, S. G.; Kruger, P. E.; Bennett, T. D.,

- The thermal stability of metal-organic frameworks. *Coordination Chemistry Reviews* **2020**, *419*, 213388.
212. Fang, Y.; Zhu, S.-R.; Wu, M.-K.; Zhao, W.-N.; Han, L., MOF-derived In₂S₃ nanorods for photocatalytic removal of dye and antibiotics. *Journal of Solid State Chemistry* **2018**, *266*, 205-209.
213. Noh, H.; Kung, C.-W.; Otake, K.-i.; Peters, A. W.; Li, Z.; Liao, Y.; Gong, X.; Farha, O. K.; Hupp, J. T., Redox-Mediator-Assisted Electrocatalytic Hydrogen Evolution from Water by a Molybdenum Sulfide-Functionalized Metal–Organic Framework. *ACS Catalysis* **2018**, *8* (10), 9848-9858.
214. Cheng, E.; McCullough, L.; Noh, H.; Farha, O.; Hupp, J.; Notestein, J., Isobutane Dehydrogenation over Bulk and Supported Molybdenum Sulfide Catalysts. *Industrial & Engineering Chemistry Research* **2020**, *59* (3), 1113-1122.
215. Jiang, J.; Gándara, F.; Zhang, Y.-B.; Na, K.; Yaghi, O. M.; Klemperer, W. G., Superacidity in Sulfated Metal–Organic Framework-808. *Journal of the American Chemical Society* **2014**, *136* (37), 12844-12847.
216. Kang, P.; Zhang, S.; Meyer, T. J.; Brookhart, M., Rapid Selective Electrocatalytic Reduction of Carbon Dioxide to Formate by an Iridium Pincer Catalyst Immobilized on Carbon Nanotube Electrodes. *Angew. Chem., Int. Ed.* **2014**, *53*, 8709.
217. Platero-Prats, A. E.; Mavrandonakis, A.; Gallington, L. C.; Liu, Y.; Hupp, J. T.; Farha, O. K.; Cramer, C. J.; Chapman, K. W., Structural Transitions of the Metal-Oxide Nodes within Metal–Organic Frameworks: On the Local Structures of NU-1000 and UiO-66. *Journal of the American Chemical Society* **2016**, *138* (12), 4178-4185.
218. Chen, Z.; Strocio, G. D.; Liu, J.; Lu, Z.; Hupp, J. T.; Gagliardi, L.; Chapman, K. W., Node Distortion as a Tunable Mechanism for Negative Thermal Expansion in Metal–Organic Frameworks. *Journal of the American Chemical Society* **2023**, *145* (1), 268-276.
219. Wong, P. C.; Li, Y. S.; Zhou, M. Y.; Mitchell, K. A. R., XPS Studies of the Stability of a Mixed Zirconium Oxide and Sulphide Thin Film. *Surface Review and Letters* **1995**, *02* (02), 165-169.
220. Ziolk, M.; Saur, O.; Lamotte, J.; Lavalley, J.-C., FTIR study of adsorption and transformation of methanethiol and dimethyl sulfide on zirconia. *Journal of the Chemical Society, Faraday Transactions* **1994**, *90* (7), 1029-1032.
221. Stern, D. A.; Wellner, E.; Salaita, G. N.; Laguren-Davidson, L.; Lu, F.; Batina, N.; Frank, D. G.; Zapien, D. C.; Walton, N.; Hubbard, A. T., Adsorbed thiophenol and related compounds studied at platinum(111) electrodes by EELS, Auger spectroscopy, and cyclic voltammetry. *Journal of the American Chemical Society* **1988**, *110* (15), 4885-4893.
222. Raabe, T.; Rasser, H.; Nottelmann, S.; Groß, A.; Krause, H.; Kureti, S., Mechanistic study on H₂S and subsequent O₂ adsorption on iron oxides and hydroxides. *Applied Surface Science* **2021**, *565*, 150504.
223. Wang, T. C.; Vermeulen, N. A.; Kim, I. S.; Martinson, A. B. F.; Stoddart, J. F.; Hupp, J. T.; Farha, O. K., Scalable Synthesis and Post-Modification of a Mesoporous Metal–Organic Framework Called NU-1000. *Nat. Protoc.* **2016**, *11*, 149.